ESTIMATION OF REGIONAL EVAPOTRANSPIRATION USING REMOTE SENSING DATA IN ARID AREAS

AYOUB AHMED ABDULLAH ALMHAB

UNIVERSITI TEKNOLOGI MALAYSIA

UNIVERSITI TEKNOLOGI MALAYSIA

DECLARATION OF THESIS / UNDERGRADUATE PROJECT PAPER AND COPYRIGHT

Author's full name : **AYOUB AHMED ABDULLAH ALMHAB**

Date of birth : **24 DESEMBER 1972**

Title : **ESTIMATION OF REGIONAL EVAPOTRANSPIRATION USING REMOTE SENSING DATA IN ARID AREAS**

Academic Session : **2008 / 2009**

I declare that this thesis is classified as :

☐	**CONFIDENTIAL**	(Contains confidential information under the Official Secret Act 1972)*
☐	**RESTRICTED**	(Contains restricted information as specified by the organization where research was done)*
√	**OPEN ACCESS**	I agree that my thesis to be published as online open access (full text)

I acknowledged that Universiti Teknologi Malaysia reserves the right as follows :

1. The thesis is the property of Universiti Teknologi Malaysia.
2. The Library of Universiti Teknologi Malaysia has the right to make copies for the purpose of research only.
3. The Library has the right to make copies of the thesis for academic exchange.

Certified by :

SIGNATURE	SIGNATURE OF SUPERVISOR
01542085	**PROF. IBRAHIM BUSU**
(NEW IC NO. /PASSPORT NO.)	NAME OF SUPERVISOR
Date : 15 January 2009	15 January 2009

"I hereby declare that I have read this thesis and in my
opinion this thesis is sufficient in terms of scope and quality for the
award of the degree of Doctor of Philosophy (*Remote Sensing*) "

Signature   : ....

Name of Supervisor I   : IBRAHIM BIN BUSU

Date   : ....

BAHAGIAN A – Pengesahan Kerjasama*

Adalah disahkan bahawa projek penyelidikan tesis ini telah dilaksanakan melalui kerjasama antara

_____ dengan _____

Disahkan oleh:

Tandatangan : _____   Tarikh : _____

Nama : _____

Jawatan : _____
(Cop rasmi)

* _Jika penyediaan tesis/projek melibatkan kerjasama._

BAHAGIAN B – Untuk Kegunaan Pejabat Sekolah Pengajian Siswazah

Tesis ini telah diperiksa dan diakui oleh:

Nama dan Alamat
Pemeriksa Luar   :   **Prof. Madya Dr. Khiruddin Abdullah**
School of Physics
Universiti Sains Malaysia
11800 MINDEN
Pulau Pinang

Nama dan Alamat
Pemeriksa Dalam I   :   **Prof. Madya Dr. Ayob Katimon**
Fakulti Kejuruteraan Awam

Pemeriksa Dalam II   :

Nama Penyelia lain   :
(jika ada)

Disahkan oleh Timbalan Pendaftar di Sekolah Pengajian Siswazah:

Tandatangan : _____   Tarikh : _____

Nama : **EN KHASSIM B ISMAIL**

ESTIMATION OF REGIONAL EVAPOTRANSPIRATION USING REMOTE
SENSING DATA IN ARID AREAS

AYOUB AHMED ABDULLAH ALMHAB

A thesis submitted in fulfilment of the
requirements for the award of the degree of
Doctor of Philosophy (Remote Sensing)

Faculty of Geoinformation Science and Engineering
Universiti Teknologi Malaysia

JANUARY 2009

I declare that this thesis entitled "E**stimation of Regional Evapotranspiration using Remote Sensing data in Arid Areas** "is the result of my own research except as cited in the references. The thesis has not been accepted for any degree and is not concurrently submitted in candidature of any other degree.

Signature　：………………………..
Name　　　：Ayoub Ahmed Almhab
Date　　　：　15/01/2009

*This work is dedicated to my father and family members
who are always giving me encouragement
and support*

*I also wish to dedicate this thesis to all Yemeni farmers, who have
struggled all their lives for a better future.*

ACKNOWLEDGEMENTS

ABSTRACT

Evapotranspiration (ET) constitutes a large portion of the hydrologic cycle and considered as the important parameter in the water budget in the arid areas. Measurement of the water vapour cycle of the land surface is crucial in improving the management of the limited fresh water resources. This study investigates the possibilities of generating a new algorithm for estimating ET in the arid mountainous areas. The modified SEBAL (Surface Energy Balance Algorithm for Land) was developed based on original SEBAL algorithm produced by Bastiaanssen in 1995. A new modified SEBAL is developed to compute ET in three areas. Operational modified SEBAL model estimates ET of mountain areas of Sana'a basin in Yemen using Remote Sensing data from various sensors and appropriate meteorological data. Validation of ET calculated by modified SEBAL model at a local scale was performed by comparing it with several ET estimated using other methods. Generated in this study are, almost all of the model parameters which covers: surface albedo estimation, estimated Leaf area index (LAI) by remote sensing data analyses, effect of elevation on surface temperature, ground heat flux estimation, impact of surface roughness, the estimated of sensible heat flux, windspeed and surface temperature relation and the correction of near surface air temperature difference (dT) in modified SEBAL. The fusion of ET derived from Landsat images and ET derived from NOAA-AVHRR images was also done. Application of modified SEBAL at a regional scale was performed using Landsat TM and NOAA-AVHRR imagery for the Sana'a basin, Yemen. The results indicated that modified SEBAL performed well for predicting daily and monthly ET for mountainous agricultural areas. Some results were obtained for volcanic areas, basalt areas, desert areas and also arid coastal areas, using prediction of surface parameters. Regional decision support system for ET was done in order to select the best or most suitable ET method, finally the proposed model for regional water balance shows good result for monthly data.

ABSTRAK

Proses Sejatpeluhan (ET) mewakili sebahagian besar dalam sesebuah kitaran hidrologi dan diambil kira sebagai parameter penting bagi menghitung kandungan sumber air di kawasan kering. Hitungan terhadap kitaran proses sejatan air di permukaan tanah adalah sangat penting bagi meningkatkan pengurusan sumber air semula jadi yang semakin terhad. Penyelidikan ini tertumpu kepada kemungkinan penghasilan algoritma baru bagi menganggar jumlah ET di kawasan pergunungan kering. Model SEBAL (*Surface Energy Balance Algorithm for Land*) yang dibangunkan oleh Bastiaanssen pada tahun 1995 telah diubah suai bagi menghitung ET pada tiga kawasan berasingan. Model SEBAL yang telah diubah suai bagi meng anggarkan jumlah ET di kawasan pergunungan lembangan Sana'a, Yemen menggunakan imej data Remote Sensing menerusi pelbagai penderia dan data meteorologi yang bersesuaian. Penilaian terhadap model SEBAL yang diubah suai adalah melalui perbandingan beberapa kaedah penganggaran ET pada skala tempatan. Hasil analisis penyelidikan ini meliputi hampir keseluruhan parameter model melibatkan anggaran permukaan albedo, anggaran indeks keluaran permukaan daun (LAI) menerusi penganalisaan data Remote Sensing, kesan ketinggian terhadap suhu permukaan tanah, anggaran aliran haba di permukaan tanah, kesan kawasan permukaan kekasaran, anggaran menggunakan kaedah penilaian haba, hubungkait antara kelajuan angin dengan suhu permukaan tanah dan ketepatan perbezaan suhu udara (dT) berhampiran permukaan tanah melalui penggunaan model SEBAL yang diubah suai. Penggabungan ET dari imej Landsat dan NOAA-AVHRR juga telah dibuat. Aplikasi penggunaan model SEBAL yang diubah suai dijalankan pada skala serantau merangkumi lembangan Sana'a, Yemen menggunakan imej dari Landsat TM dan NOAA-AVHRR. Keseluruhan analisis penyelidikan ini mendapati model SEBAL yang diubah suai memberikan hasil yang baik bagi menganggar jumlah ET berpandukan tempoh sela masa secara harian dan bulanan merangkumi kawasan pertanian di pergunungan. Beberapa hasil analisis juga diperolehi dari kawasan gunung berapi, kawasan berbatuan padat, kawasan gurun dan kawasan kering persisiran pantai menerusi anggaran parameter dipermukaan tanah. Sistem Sokongan Pembuatan Keputusan (DSS) serantau bagi pengukuran ET telah dibangunkan untuk memilih kaedah pengukuran ET yang paling baik dan bersesuaian. Model yang telah dicadangkan juga menampakkan hasil analisis yang baik bagi keseimbangan kandungan sumber air serantau menerusi data tempoh sela masa secara bulanan.

TABLE OF CONTENTS

LIST OF TABLES

LIST OF FIGURE

LIST OF SYMBOLS AND ABBREVIATIONS

AREA	Agricultural Research and Extension Authority
ASTER	Advanced Space borne Thermal Emission and Reflection Radiometer
ASCE	American Society of Civil Engineers
AVHRR	Advanced Very High Resolution Radiometer
$B\uparrow_{24}$	Diurnal Outgoing Black Body Radiation
β	Bowen Ratio
CAMA	Civil Aviation and Meteorological Authority
C_p	Air specific heat at constant pressure
C_s	Soil surface air specific heat at constant pressure
CWSI	Crop Water Stress Index
d_s	Distance Sun-Earth
dT	Soil to atmosphere temperature difference
DSTV	Diurnal surface temperature variation
BT	Difference of temperature between soil skin and air
EDC	Emergence Date of Crop
e_{sat}	Atmospheric saturated vapor pressure
e_{act}	Atmospheric actual vapor pressure
E	Evaporation
EF	Evaporation Fraction
$EFFA$	Experimental Farming Faculty of Agriculture, Sana'a University
ER	Evaporation Ratios
$E\text{-}Pan$	Pan Evaporation
ET	Evapotranspiration
ET_a	Actual Evapotranspiration
ET_{as}	Actual Evapotranspiration calculated by SWAP
ETM	Enhanced Thematic Mapper
ET_o	Grass Reference Evapotranspiration
ET_oF	ET_o fraction
ET_r	Alfalfa reference evapotranspiration
ET_rF	ET_r fraction
ET_s	Seasonal Evapotranspiration
ET_{pot}	Potential Evapotranspiration
FEC	Forced end of crop
g	Gravitational force
G_0	Soil Heat flux

H	Sensible Heat Flux
HG	Hargreaves
Iv	Ivanov
$K\downarrow$	Incident Shortwave Radiation
$K\uparrow$	Reflected Shortwave Radiation
$L\downarrow$	Incident Long wave Radiation
$L\uparrow$	Outgoing Long wave Radiation
LAI	Leaf Area Index
HRV	High resolution visible
MAI	Ministry of agriculture and irrigation
MWE	Ministry of water and environment
MH	Modified Hargreaves
MODIS	Moderate Resolution Imaging Spectroradiometer
N_E	Daily ET hours
NDVI	Normalized Difference Vegetation Index
NOAA	National Oceanographic and Atmospheric Administration
NWRA	National Water Resources Authority
PBL	Planetary Boundary Layer
PM	Penman-Monteith
RY	Republic of Yemen
r_{ah}	aerodynamic resistance for heat transport
R_n	Net Radiation
r_v	Aerodynamic surface resistance to vapor transport
r_s	Bulk surface resistance to evapotranspiration
RS	Remote sensing
SEBAL	Surface Energy Balance Algorithm for Land
SEBI	Surface Energy Balance Index
S-SEBI	Soil Surface Energy Balance Index
SEBS	Soil Energy Balance System
SVAT	Soil Vegetation Atmosphere Transfer Models
SWAP	Soil Water Atmosphere Plant model
SWAT	Soil Water Atmosphere Transfer model
SLURP	Soil Land And Urban Planning
T_s	Land surface temperature
T_a	Air temperature
T_{aero}	Aerodynamic surface temperature
T_{rad}	Radiation surface temperature
T_s	Soil skin Temperature
TSEB	Two-Source Energy Balance algorithm
TM	Thematic Mapper
TEC	Time extent of cropping
u^*_{eff}	The effective fraction velocity
u_z	The wind speed measured at height z
VGM	Van Genuchten Mualem
VITT	Vegetation Index Temperature Trapezoid

VISSR	Visible and infrared spin scan radiometric
VMC	Vegetation Moisture Cofficient
UTM	Universal Transverses Mercator
x	Correction factor for momentum transfer
YEMN	Republic of Yemen
γ	Psychrometric constant
z	The height
z_{oh}	Roughness length for heat
z_{om}	Roughness length for momentum
σ	Stephan Boltzmann constant
Td	Soil surface air specific heat at constant pressure
Λ	Evaporation fraction
λ	Latent heat of vaporization
λE	Latent heat flux
λE_{day}	Daily Latent heat flux
ε_o	Surface thermal emissivity
ρ_o	The surface btoadband albedo
ω_s	Solar angle hour
ϕ_{sun}	Zenith angle of the sun
β	Bowen Ratio
λ	Latent heat of vaporization
$\lambda(ET_{ins})$	Latent Heat Flux
ρ_{air}	Moist air density
ρ_{va}	Atmospheric vapor density
ρ_s	Soil surface air density
ρ_{vs}	Soil surface vapor density
Ψ_h	Psychometric parameter for the atmospheric heat transport
Ψ_m	Psychometric parameter for the atmospheric momentum transport

LIST OF APPENDICES

CHAPTER 1

INTRODUCTION

1.1   General Background

Water is an irreplaceable natural resource that without it human beings cannot exist, and it is also the most widely spread natural substance. However, human beings use only a small portion of this water, i.e. the fresh water, which is about 2% of the total amount of water on this planet. Therefore, the evaluation of water resources of any region, it is the amount of fresh water that is considered (UNESCO, 1970).

In recent years, water resources management has become an important issue. This is especially true with the increased demand and competition for fresh water between different users. Consequently, monitoring the consumption of water has become one of the most popular issues regarding water resources management.

Evapotranspiration (ET) is a collective term of all processes whereby water is lost from the soil surface by evaporation and from plants by transpiration. Both evaporation and transpiration occur simultaneously and there is no easy way of separating the two processes (Dingman, 2002). The actual evapotranspiration is an indicator of how much water the crops and trees need for healthy growth and productivity. Other than the availability of water at the evaporating surface, several other factors affect the evapotranspiration process. These factors include meteorological

parameters such as solar radiation, air temperature, humidity and wind speed. Moreover, type and density of vegetation cover, rooting depth and reflective land-surface characteristics are also are important factors that need to be considered.

A quantitative understanding of evapotranspiration has a great importance in water balance study of the basin in such a way that first, in a long period of time the difference between precipitation and evapotranspiration is the water available for use. Second, most of the food supply is grown in irrigated lands and knowledge of actual ET helps in the use of efficient water without loss required for the plant growth.

Evapotranspiration (ET) is the process that accounts for a large portion of the hydrological water budget. On the land surface, an average about 60% of the precipitation received is returned to the atmosphere through ET (Brutsaert, 1986). However, in the selected study area, it is much higher, which is nearly 80% (Almhab, 2003). Therefore, quantification of ET in the hydrologic budget is essential when planning for the development of water resources of an area, estimating water-supply potential, and understanding the ecological effects of development.

In the Republic of Yemen, irrigation is the largest consumer of fresh water resources. In the main basins 93% of the consumption of fresh water is used for irrigation (NWRA, 2001). In this case, ET from agricultural fields as the major consumption of fresh water is an important factor in water resources management. In order to provide good information for water resources management, a study on the major hydrologic parameter has been proposed.

The areas selected for this study are located in an arid and a semi-arid zone and they comprise of three regions that represent the most important agricultural areas in Yemen. Nonetheless, due to poor management of water resources and water consumption in agricultural fields the water usage efficiency in these areas is very low (NWRA, 2001). On the other hand, because of increasing use of groundwater in the irrigated areas, it is important to determine the amount of available fresh water for agricultural uses and recommend a sustainable method for food production with optimal water use and with minimum losses in water, soil and financial resources.

Taking into consideration the large size of watersheds, the scattering of land parcels and climate variations, modern tools and techniques should be utilized in the

study of water resources management. Remote Sensing (RS), Geographic Information Systems (GISs) and hydrology models may be employed together with agro-climatic data to develop models for assisting planners, researchers, farmers, and decision makers in searching for proper solutions to water resource management problems.

1.2.   Problem Statement

Yemen comprises of arid and semi arid climate zones. The country faces shortages in natural resources particularly water, which in recent years has turned into a water crisis. This is the result of a number of factors such as frequent droughts, poor water management practices and excessive use of water resources. Taking into consideration the large size of the watersheds which make up to 76% of the total area of Yemen, consists of scattered farm lands with climatic variations. The study area is located in the most important agricultural areas in Yemen, where water consumption in agricultural fields is very high with very low water use efficiency, which only about 35-45%. Therefore, ET from agricultural fields needs to be determined as the consumption of fresh water is an important factor in water resource management, but a major improvement in water use has yet to be achieved. For the application in the Republic of Yemen, there is limited basic agro-climate data for estimating the ET which is needed in the formulation of renewable national water balance and crop production strategies.

Modern tools and techniques such as Remote Sensing (RS) and Geographic Information System (GIS) need modifications for use in the study of water resource management in Yemen. However, most of current remote sensing ET estimation methods are either too theoretical, that they are not reasonable to be applied for operational purposes, or too empirical, that it is difficult to apply them in different areas without major modifications. These models, which require ground measurements, reduce the opportunity of applying the models with historical remote sensing data.

Among the several ET estimation methods, remote sensing is regarded as the only technology that can efficiently and economically provide regional and global coverage of actual consumption of groundwater (Kustas and Norman, 1996). Among the current satellite remote sensing models, the Surface Energy Balance Algorithm for Land (SEBAL) has been designed to calculate the energy portioning at the regional scale with minimum ground data (Bastiaanssen, 1995) and has been verified at places in many countries around the world including Spain, Italy, Turkey, Pakistan, India, Sri Lanka, Egypt, Niger, and China (Bastiaanssen, et al., 1998a; Bastiaanssen, et al., 1998b; Bastiaanssen and Bos, 1999). SEBAL is frequently applied in developing countries, because it requires a minimum amount of ground measurements including meteorological information. However, since the SEBAL methodology includes the complete energy balance calculation, it has considerable value in application for developed countries such as the United States and others. In addition, the confidence in the ET estimation using SEBAL is expected to increase with additional meteorological and ground information, when available.

The original SEBAL model does not have the ability to apply to mountainous areas (Bastiaanssen et al., 1998). The $SEBAL_{ID}$ model was developed for Idaho and the western United States conditions and uses Landsat ETM+ data. It was done by refining the SEBAL model. Good weather data sets are required for the implementation of $SEBAL_{ID}$. If weather data is lacking, one must use the original SEBAL method (Tasumi, 2003). Therefore, a large refinement effort was required to extend the SEBAL technology to sloping land surfaces, mountains, and desert areas.

Another refinement which is necessary is to include a better internal calibration procedure in the model. SEBAL was originally produced for developing countries, so that the need for weather data was held to a minimum.

This study involves refining, testing and conducting a sensitivity analysis an operational remote sensing model for ET estimation, based on the SEBAL procedure. The sensitivity of the model is evaluated using traditional models of ET based on hydrological and climate data and applied to the Sana'a Basin, delta Tuban basin and wadi Hadramout basin in the Republic of Yemen.

Currently, no significant studies have been conducted in producing the best model for estimating the ET in different regions in Yemen. The research is proposing an approach of using Remote Sensing data and traditional model which require little dependence on hydro climate data for estimating ET using decision support system (DSS) and GIS technique.

1.3 Justification and Motivation of the Study

This study proposed to apply RS and GIS tools in studies of water resources management problems in Yemen. Due to water crisis, population growth and limited water resources, government and non government bodies put priority on solving these issues. Among the management problems include the following:

a) Lack of basic agro-climatic data for decision makers and investors which they need for formulating crop production strategies and helping them to make economic assessments of production.

b) Lack of vision on aspects of management of water supply and demand for agriculture, which results in a continuous decrease in food production.

c) Limited number of national professional qualified people in RS and GIS inhibits the wide application of these tools in integrated watershed management studies.

In addition to those problems, there are also scientific justifications of the project. It is known that the water resources management sciences are less developed in the Arab regions in comparison to other countries. Therefore, the project has the following scientific justifications:

(a) New techniques and tools used in water Resources management need to be introduced in Yemen .There is a need to educate/ expose national experts in these

fields who will popularize these techniques in the country through teaching and research.

(b) Yemen needs to adopt the principle of integrated water resources management which integrates supply management with demand management. This principle cannot be implemented without using RS and GIS techniques. This is because the areas are too large to be studied properly only by field work studies.

The significance of this study in Yemen can be listed as follows:

- Utilization of RS and GIS tools in providing engineering solution for integrated water resources management problems, especially water balance and irrigation water, through estimation of evapotranspiration and crop water requirement for important crops in different areas of study.

- Introduction of modern techniques and tools in integrated water resources management to the scientific and policy makers' bodies in Yemen.

- This is the first study in Yemen to produce ET maps and Decision Support System (DSS-ET) and the first study on SEBAL in the Arabia peninsula.

- Providing good information for water resources management, a study on the major hydrologic parameter (ET) has been carried out, for Yemen.

- Establishing the main cost factors in relation to the estimated efficiency of the water resources management scheme in Yemen.

1.4   Objectives of the research

The main goal of this study is to develop an optimum model for estimation of ET for arid areas. The goal can be achieved through completing activities that fulfill the following objectives:

a. To investigate the capability of existing SEBAL models for calculating evapotranspiration in mountainous arid areas.

b. To develop a new SEBAL variant for calculating evapotranspiration in mountainous arid areas.

c. To study the reliability of medium and low spatial resolution remote sensing image data for calculating evapotranspiration using new SEBAL variant.

d. To integrate the new SEBAL variant with remote sensing and GIS techniques for a water management, through the implementation of decision support system.

These objectives will provide another approach for the water resource management in mountainous arid areas, with a focus on water balance estimation and irrigation water requirements.

In general this study is planned to encompass the following subject matters:

1. Describing the implementation issues of modified SEBAL whereby the data from remote sensing images can be used to generate ET data, with different processing levels, from NOAA-AVHRR data and from Landsat-5 TM data, to compute spatially distributed ET over an arid and a semi-arid region with mountainous terrain areas in Yemen.

2. To study the feasibility of fused ET result using the new SEBAL variant from medium and low resolution and to compare between the two.

3. To compare and validate the new model ET with traditional hydrology ET models and soil water balance (lysimeter) ET measurements obtained by Dr. Tahir, EFFA for period 1995-1998.

4. Apply the new model to three study areas: Sana'a basin, Wadi Hadramout and Wadi Tuban, Yemen, and assist in transfer of the technology to National Water Resources Authority (NWRA).

1.5   Scope of the study

The scope of this study is defined in such a way that it really focus on the development of an optimum approach for estimations ET in arid areas.

For the remote sensing data the study will be using image data acquired by the Thematic Mapper (TM) on-board Landsat 5 and the Advanced Very High Resolution Radiometer (AVHRR) on-board the NOAA satellites.

A suitable model will be selected and modified for the purpose of estimating of ET in arid area. The models used in the study include modified SEBAL, classical SEBAL, simple energy balance model and biophysical model from remote sensing and FAO Penman- Monteith, Priestley Taylor model, Hargreaves model, modified Blaney Criddle model from conventional hydrology models, and lysimeters from direct measurement (water balance).

The meteorological data of the study area are obtained from existing database mentioned by the National Water Resource Authority (NWRA), Agriculture Research and Extension Authority (AREA) and Civil Aviation and Meteorological Authority (CAMA) in Yemen. Thus, field estimation is kept to a minimum and only carried out for verification purposes. These data are adequate for developing optimum ET calculation model and its verification.

As for the decision support system in water management of the study areas readily available routines for ranking are used in Excel to produce information and weight based on the optimum model (ET) for the study areas. The GIS technology is utilized

as a tool for creating ET maps and creating DSS-ET maps to develop water yield and water balance efficiently in the study area.

1.6 Description of the Study areas

1.6.1 Location and general description of areas

Yemen is located in the south western part of Asia and in the south of the Arabian Peninsula. It is bounded on the north by Saudi Arabia, on the south by the Arabian Sea and the Gulf of Aden, on the east by Oman and on the west by the Red Sea (Figure 1.1)

This study focus on the mountainous arid areas and other study areas are chosen to different regions of the country (Table 1.1). They are located in highland, coastal plain and desert regions. Sana'a Basin, Delta Tuban and Desert Wadi Hadramout respectively figure 1.1 shows the sites.

Table 1.1: General information of the study areas

No.	Name	Region	Latitud N°	Longitud E°	Area km²	Population density p/km²	Mean Temperature	Main crops	Elevation (m)
1	Sana'a Basin,	Highland	15 26 30	44 54 40	3250	60-80	19.27	Plum Grapes	1900-3660
2	Wadi Tuban	Coastal plain	13 22 25	45 16 37	700	30-40	26	Cotton Mango	00- 240
3	Wadi Hadramout	Eastern and Desert	15 45 00	47 53 30	2000	5-15	28.4	Dates	600-800

1.6.1.1   The Site of highland region- Sana'a Basin

The Sana'a Basin is located in the western highlands of Yemen opposite the Red Sea and the Gulf of Aden, (Figure 1.1). It is mostly an intermountain plain surrounded by highlands in the west, south and east. On a regional scale, the basin extends across the central part of the Sana'a Governorate and covers 3250 km. sq. which is about 24% of its total area of 13,550 km. sq.

There is a significant variation in altitude both east-west and north-south. The highest point in the basin is in the south-west end (Jabal An Nabi Shu'ayb) and has an elevation of almost 3660 m above sea level (m.s.l) The lowest point (about 1900 m.s.l.) is in the northern extremity where the Wadi Al Kharid exits the basin towards the main basin by the same name. The predominant climate is arid although semi-arid conditions prevail in certain local areas, particularly along the western highlands. The mean economic activity in the basin is agriculture and it famous by the grapes plantation, Plum, Qat and some irrigated crops and vegetations.

1.6.1.2   The Site of Coastal Region - Wadi Tuban

Wadi Tuban is one of the most important agricultural areas in the Sothern coastal of Yemen. It is located at the North East of Aden city coordinates; Latitude   N 1478469, and Longitude, E 529986, (UTM) system. (Figure 1.1).
 The predominant climate is arid and semi-arid, the mean economic activity is the agriculture, it is famous for its mango plantation and important cash crop like the cotton.
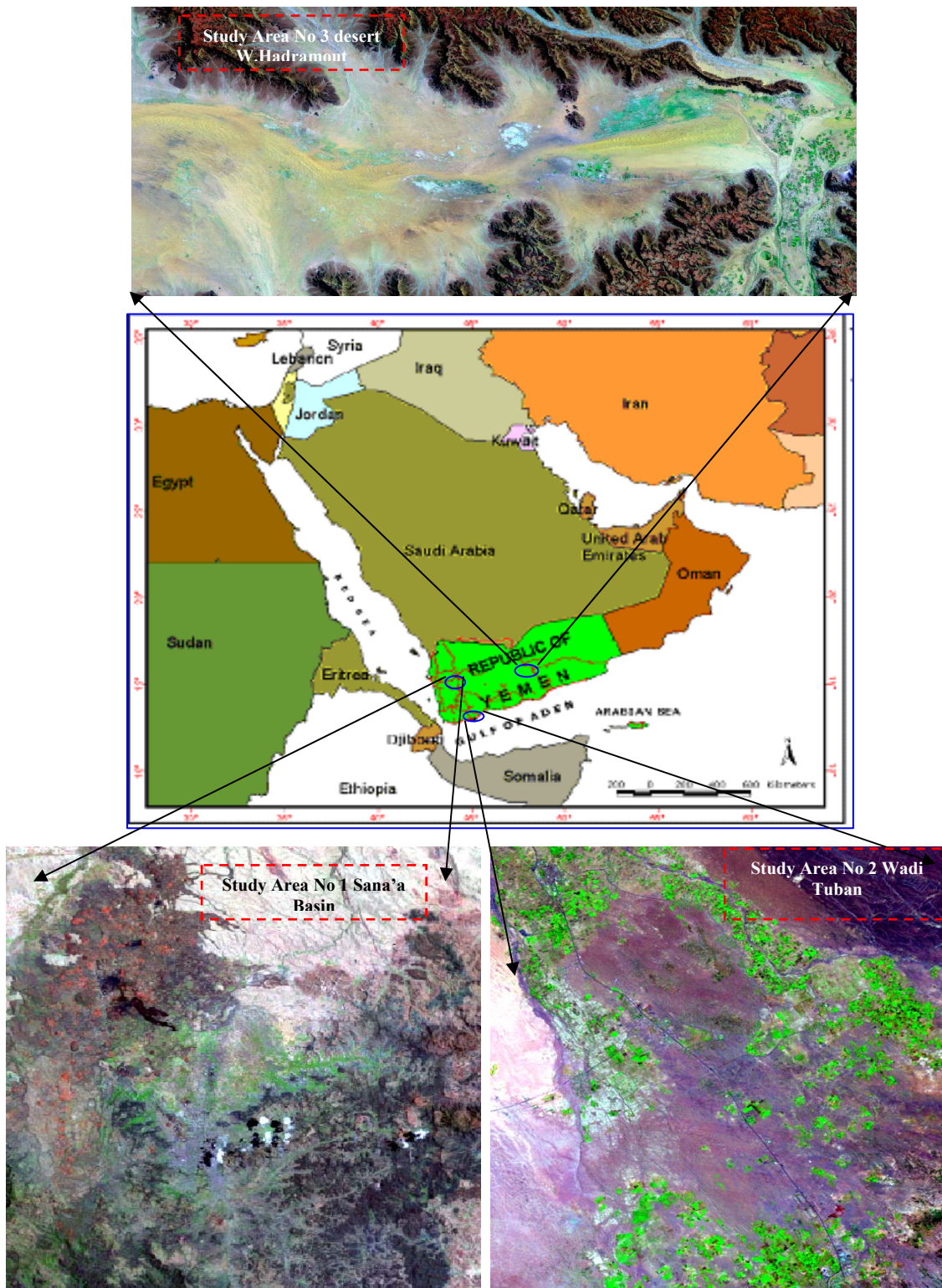
Figure 1.1 General locations of the study areas.

1.6.1.3 The Study area in Eastern Region and Desert- Wadi Hadramout.

Wadi Hadramout is located in the central part of Yemen; it's one of the most important agricultural areas in the eastern and desert region Figure 1.1. The study area covers approximately 2000 km^2, between Heinen (UTM coordinates 921000 E, 1754000 N) and Qasam (930400 E, 1784000 N). The intake part of the watershed starts from the desert named Ramlat Assabateen which has a predominantly arid climate although semi-arid conditions prevail in certain internal of the wadi around Tareem and Syoun local areas, particularly in the middle between the highlands. The mean economic activity is the agriculture and it famous by the Dates plantation and some irrigation crops and vegetations.

1.7 Description of general methodology

The core of the system is mainly composed of three major components namely input data, implementation planning and output data. The system has been named as **Modified-SEBAL** (modified soil energy balance algorithm for land). Figure 1.2 illustrates the conceptual layout of the system.

1.7.1   Input Data

As shown in Figure 1.2, five types of input data are required in the system. It includes the hydro-climate data, the Landsat TM satellite images data, NOAA-AVHRR satellite images data, Digital Elevation Model (DEM) data and GIS data layers. In this study there are some data which have been used for running the model, where three data collection sources have been used. These include satellite images (Section 4.3.1) DEM data (Section 4.3.2), and hydro-climate data (Section 4.3.3). The image data comes from satellite images on board Landsat TM, and NOAA-AVHRR, DEM data comes from SRTM and climate data come from the reference metrological stations; these data are loaded on a database for ArcGIS software then and visualized to raster maps. Later on these raster maps data were saved into a data geospatial database for further use.
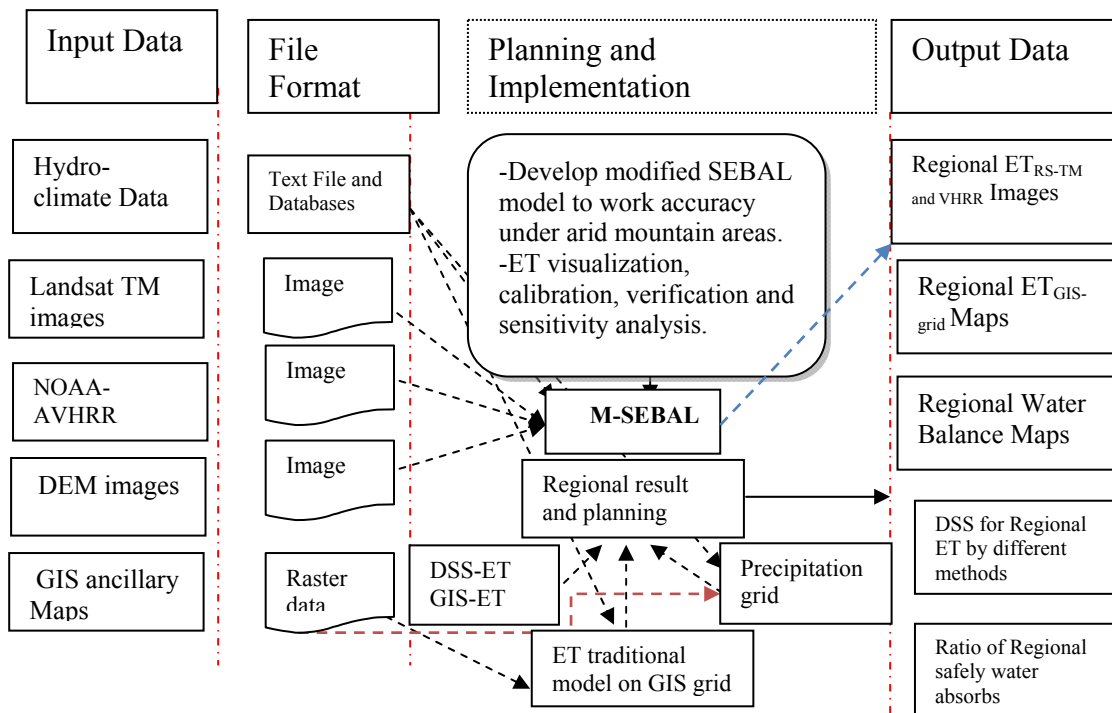
Figure 1.2   Conceptual system layout

1.7.2 Planning and implementation

      The Planning and implementation of this study can be divided into three parts. The intal part of this study is concluding the development of the modified SEBAL model for estimation of ET on the arid mountainous areas. The main focus of this part is the use of remotely sensed image data from Landsat TM as with as from NOAA-AVHRR with minimum ground data. The detail explanation on this part of study is given in chapter 3. The second part consists of modeling techniques for modified SEBAL analysis and development of estimation for the surface parameter, radiations parameter to estimate the evapouration fraction and daily evapotranspiration on the study areas. These algorithms are discussed in Chapter 4. The third part is about the proposal and development of techniques for estimation of regional water balance. An interactive model and method have been proposed and developed to accomplish this task. The details on all these methods are discussed in Chapter 4.

1.7.3   Expected Result of the study (Output Data)

      The output of this study can be expressed in three forms, namely regional ET; instantaneous, daily, monthly images from the satellite which use, regional water balance grid, and analysis reports (Chapter 5). The first type of output data includes regional ET images from TM and AVHRR images. This data is stored in **img** format. If needed, TIF or grid type of data can be converted. On the other hand, the second output data is in the form of regional water balance grid. Mean while the third type of output data consists of various analysis reports generated by the algorithms. These analysis outputs include reports for DSS analysis of ET, and DSS analysis of different ET methods.

1.8   Thesis Organization

This thesis is divided into three parts. The first part comprises of chapter 1 the introduction, and chapter 2 review of literature. The first part gives background information necessary for the understanding of this thesis from the fields of Evapotranspiration modeling, type of the evapotranspiration estimation models and techniques.

The second part includes the research methodology which is presented in chapters 3 and 4. The chapters present techniques that describe the background of the proposed theoretical model and data sets, the methods and materials utilized to conduct the study: including an overview of the data and tools required, the modified SEBAL model, comparison of the modified SEBAL, SEBAL and also another SEBAL variations, and validation of the modified SEBAL. The results are demonstrated in the third part of this work, which comprises Chapter 5 and 6. Figure 1.3 shows structure of the proposed research.

Chapter 1 explains briefly the aim of the study and the rationale for the research work, motivation, background of the study, problem statement, Justification, Motivation of the Study, research objectives, and scope, research contributions, study areas and structure of the thesis.

Chapter 2 is the introductory part of this thesis. It identifies the Evapotranspiration (ET); methods of estimating ET (hydrological modeling, direct measurement and remote sensing**)** then continue to present the mathematical models for ET and Remote Sensing Techniques and capabilities. In this section the ET characteristics of Yemen were reviewed. This chapter also includes with general description of the energy balance, SEBAL techniques models including its general mathematical equation, then, the fusion ET and finally Decision Support System for Estimating Regional Evapotranspiration.

Chapter 3 constitutes the second part of this thesis. It explains basic concepts for Modified SEBAL model; describes the background of the proposed theoretical model

and constitutes the mathematical models to estimate ET, then developing the algorithms for estimation of ET from remote sensing data. The equations and algorithms explains the calculation and use of various factors affecting ET, starting from pre-processing, calibration of the raw satellite data, radiation reflectance correction, topographic correction, the estimation of surface parameters (Albedo, vegetation index, surface temperature, and so on) and calculation of radiation elements (net radiation, soil heat flux and sensible heat flux) are also considered. It presents detailed mathematical model for calculation of various parameters consisted on the modified SEBAL model.

Chapter 4 presents the methods and materials utilized to conduct the study: it includes an overview of the data Selection, Image Processing, instrumentation and tools required, the modified SEBAL model, the development of the parameterization for actual ET, general procedure of modified SEBAL model, and finally estimation of water balance models propose for regional, sub basin and field estimation.

Chapter 5 presents the results of the algorithms and their analysis, calibration, verification, sensitivity analysis, validation and comparisons of the modified SEBAL, comparing the modified SEBAL, SEBAL and another SEBAL variations then application of the modified SEBAL in different areas which consist of mountainous arid areas, volcanic areas, desert areas, coastal arid areas and others on and the proposed approach to estimating regional water balance and overview of the system implementation are also provided.

Chapter 6 is the concluding chapter of this thesis. It summarizes the discussions regarding the research, limitations of the work and final recommendations for future work.

Chapter one	Introduction		1	Background, problem statement, objective, scope and thesis structure
Chapter two	Literature Review		2	Overview of ET, ET models, ET in Yemen, Remote Sensing Techniques and capabilities, estimating ET models, fusion ET.
Chapter Three	Research Methodology		3	Theoretic of the proposed model, System description, mathematical models, and developing algorithms for estimates ET
Chapter Four			4	Data Selection and Image Processing, instrumentation, develop of the parameterization actual ET, general procedure modified SEBAL
Chapter five	Results		5	Results and analysis for ET, calibration, verification, sensitivity analysis, validation and comparisons the modified SEBAL, application modified SEBAL in different areas
Chapter Six	Conclusions		6	System Overview, System Descussion, limetation and future work

Figure 1.3   Summary of the thesis structure

CHAPTER 2

REVIEW OF LITERATURE

2.1. Overview

The study of regional ET using satellite remote sensing included at least three major disciplines: 1) evapotranspiration theory; 2) remote sensing theory and methods; and 3) satellite image processing techniques. The review of literature begins with the key concepts of the ET process and traditional methods of ET estimation. ET characteristics of Yemen were reviewed. Beside the remote sensing theory from field radiometry to satellite image processing techniques were also reviewed. Apart from that, spectral characteristics of vegetation were studied. In addition, the primary parameters that can be derived from remote sensing, vegetation index and surface temperature were then introduced as a link between the ET estimation methods and remote sensing techniques. Furthermore, early works of remote sensing methods for fusion ET estimation from AVHRR and TM were also studied. Finally, the DSS-ET scale consideration in remote sensing and GIS were reviewed.

2.2. Methods of Estimating Evapotranspiration

Gieske (2001) listed some of the methods and models that have currently been applied for monitoring evapotranspiration on global, regional and local scales. He discussed the approaches these models used in estimating the actual and reference evapotranspiration and, they depend on the type of applications and available data. In general the methods can be grouped into: hydrological modeling, direct measurement and remote sensing.

Hydrological models are able to estimate ET spatially and temporally (Kite and Droogers, 2000).

Direct measurement is difficult; it involves specific devices, it is expensive and demanding in terms of accuracy and can only be fully exploited by well trained research personnel (Allen et al., 1998). Owing to the difficulty of obtaining direct measurement of ET, it is commonly estimated by using indirect methods.

Among the various ET estimation methods, the Remote Sensing method is regarded as the best technology that can efficiently and economically provide regional and global coverage of actual consumption (Kustas and Norman, 1996). Doran (1993) reported that the need for measurement of ET over large areas has been a growing concern as efforts to use environmental models at global scales are intensified. ET patterns at a regional scale integrate factors such as change in land use, rainfall distribution and deforestation. The need to monitor ET at a regional scale is becoming realized as an important matter in studies of global change (Curran and Foody, 1994). As Kustas and Norman (1996) mentioned remote sensing is the only method for effectively and economically estimating ET from a wide area with spatial variation.

Methods using Satellite remote sensing data (VIS, NIR, and TIR bands) to derive local, regional and global estimation of turbulent fluxes are a recent development. Among others Surface Energy Balance Algorithm for Land (SEBAL) (Bastiaanssen et al., 1998a), Two-Source Energy Balance algorithm (TSEB) (Norman et al., 1995), Surface Energy Balance Index (S-SEBI) (Roerink et al., 2000), Soil Energy Balance System (SEBS) (Su, 2002) are the most common ones. Among the current satellite remote

sensing models, the SEBAL has been designed to calculate the energy portioning at the regional scale with minimum ground data (Bastiaanssen et al., 1998a).

2.2.1. Physics of the ET Process

Evapotranspiration from land surfaces is the result of several compound processes including radiation exchanges, vapor transport and biological growth operating within a system involving the atmosphere, plants and soil. There are three main factors that influence the process of ET. They are the supply of energy to provide the latent heat of vaporization, the supply of moisture at the evaporative surface, and the ability to transport the vapor away from the evaporative surface.

Since the 1960's, a significant amount of research effort has been devoted to the study of ET. The various methods that have been used to estimate ET can be grouped into four broad categories: energy balance approach, aerodynamic approach, combination approach and instrument measurement (eddy correlation method).

2.2.2 Energy balance approach

Evaporation and transpiration require a large amount of energy at the earth-atmosphere interface. Solar radiation usually supplies 80 to 100 percent of this energy and is often the factor limiting ET. Hence, energy budget is one of the earliest methods used to estimate evaporation. The energy balance equation, in general form, can be expressed as:

$$R_n - \lambda(ET_{ins}) - H - G - P - A_h = \frac{\partial M}{\partial t} \qquad \qquad \text{......(2.1)}$$

where R_n is specific flux of net incoming radiation, $\lambda(ET_{ins})$ is latent heat of evapotranspiration, H is sensible heat flux from the surface to the atmosphere, G is specific flux of heat conducted into the earth, P is energy flux stored as photochemical energy in the process of photosynthesis, A_h is energy advection into the layer as specific flux, $\partial M/\partial t$ is the rate of energy storage per unit area in the layer.

The exact form of several of the terms depends on the type of condition and time for which the energy balance is described. In many practical applications, especially over land surfaces, the terms P, A_h, and $\partial M/\partial t$ are of little consequence, so that Equation 2.1 assumes a much simpler form. The energy balance equation, after simplification, can be expressed as

$$\lambda(ET_{ins}) = R_n - H - G \qquad \qquad \text{......(2.2)}$$

If the net incoming radiation, sensible heat flux, and ground heat flux can be measured or estimated, the evapotranspiration can be solved as

$$ET_{ins} = (R_n - H - G)/\lambda \qquad \qquad \text{......(2.3)}$$

In this formula, λ is the latent heat of vaporization. Equation 2.3 is called the energy balance equation for evapotranspiration.

2.2.3   Aerodynamic approach

Evapotranspiration rate can also be determined by calculating the ability to transport water vapor away from the land or vegetation surfaces. The transport rate is governed by the humidity gradient in the air near the surface and the wind speed across the surfaces using the equation developed by Thornthwaite and Holzman (1939).

$$E = \frac{-\rho_a k^2 (q_{v2} - q_{v1})(u_2 - u_1)}{[\ln(z_2 / z_1)]^2} \qquad \qquad \ldots\ldots(2.4)$$

Where

k is von Karman constant, usually taken as 0.4, p_a is density of air, q_v is specifying humidity, and u is wind speed measured at height z.

2.2.3.1 The Bowen Ratio ß

Evaporation may be computed by the aerodynamic method when there is enough energy supply and by the energy budget method when vapor transport is not a limiting factor. However, under normal conditions, both factors are limiting, so a method considering both factors is required (Chow et al., 1988). Since the atmospheric transport mechanisms of sensible heat are similar to those of water vapor, Bowen (1926) assumed that the sensible heat flux and the latent heat flux are proportional, and the proportionality constant being called the Bowen ratio ß.

$$\beta = \frac{H}{\lambda(ET_{ins})} \qquad \qquad \ldots\ldots(2.5)$$

When net radiation R_n and ground heat flux G are known, the evaporation rate can be written as a combination of the energy budget equation and the Bowen ratio.

$$ET_{ins} = \frac{(R_n - G)}{\lambda(1 - \beta)} \qquad \qquad \ldots\ldots(2.6)$$

The value of ß can be calculated from gradients of air temperature and vapor pressure above the evaporating surfaces by vapor and momentum transport equations expressed as

$$ET_{ins} = \rho_a k_w \frac{dq_v}{dz} \qquad \qquad \ldots\ldots(2.7)$$

$$H = \rho_a C_P k_h \frac{dT}{dz}$$ …….(2.8)

where

ρ_a is density of air, k_w is vapor eddy diffusivity, q_v is specific humidity, T is temperature, C_p is specific heat at constant pressure, and k_h is heat diffusivity.

Campbell (1997) stated that it should be possible to infer evaporation by measuring all of the other terms in the energy budget and taking λE as what is left. Besides he also added that, the problem would be simplified by taking the ratio β= H/λE, called the Bowen ratio (after Bowen, 1926, from Equation 2.7 and Equation 2.8).

$$\beta = \frac{H}{\lambda E} = \frac{\rho_{air} C_P (T_{Z1} - T_{Z2}) r_v}{\lambda (\rho_{v_{z1}} - \rho_{v_{z2}}) r_{ah}}$$ …….(2.9)

Where:

β is the Bowen ratio, H is the sensible heat flux (MJ m^{-2} day^{-1}), $\lambda(ET_{ins})$ is the latent heat flux, being the energy necessary to vaporize water *(W m^{-2})*, ρ_{air} is the air density (mol.m^{-3}), C_p is the specific heat of air (29.3 J mol^{-1} ºC^{-1}), T_{Z1} is the surface temperature in high *z1* (K), T_{Z2} is the surface temperature in high z_2 (K), λ is the latent heat flux, being the energy necessary to vaporize water *(W m^{-2})*, ρ_{v1} is the specific humidity in1, ρ_{v2} is the specific humidity in 2, r_v is the aerodynamic surface resistance to vaporization m/s, r_{ah} is the aerodynamic resistance for heat transport m/s.

The advantage of estimating $\lambda(ET_{ins})$ by the Bowen ratio included into the Energy Budget Equation 2.2 is that it is relatively insensitive to atmospheric transport properties, when β < 1 that is when the energy used for vaporizing water is superior to the energy used in convection, i.e. in wet conditions like an irrigation system Equation 2.5. while the aerodynamic resistance for heat transport is critical for the energy balance studies, the bulk surface resistance and the resistance to vaporization are generally surrounded in practical calculations. The surface resistance controls the passage of moisture from the soil matrix to the overlaying atmosphere. Parodi (2000) stated that

the stomatal and canopy resistance are controlled (in addition to soil moisture) by the shortwave solar radiation, saturation deficit, leaf area index, foliage temperature, leaf age, and leaf mineral nutrients, which all affect the stomatal aperture (Jarvis 1976).

$$\lambda E = \frac{\rho_a C_P}{\psi(r_v + r_s)}\left[e_{sat}(T_O - e_{act})\right] \qquad \qquad ......(2.10)$$

The canopy resistance (for canopies alone) or surface resistance (for mixed canopies and soil elements) relates r_s physic mathematically to $\lambda(ET_{ins})$ (Equation 2.4; Parodi, 2000).

2.2.4 Physics of the Evapotranspiration Process (Traditional ET Estimation)

2.2.4.1 Combination approach

2.2.4.1.1 Penman methods

The Penman equation is an approximate solution of the energy balance equation developed by Penman in 1948 for water surfaces. It was modified by (Monteith, 1965) to account for the surface resistance imposed by different surfaces and vegetations types. The Penman-Monteith equation is given as:

$$\lambda E = \frac{\Delta(R_n - G) + \rho_{air} C_P \dfrac{e_s - e_a}{r_a}}{\Delta + \gamma(1 + \dfrac{r_s}{r_a})} \qquad \qquad ....(2.11)$$

Where:

(e$_s$ - e$_a$) is the vapor pressure deficit of the air at the reference height,

Δ is the slope of the saturation vapor pressure temperature relationship,

γ is the psychometric constant, and r_s and r_a are the (bulk) surface and aerodynamic resistances respectively, between the surface and reference weather measured heights.

2. 2.4.1.2 Penman-Monteith equations

The Penman-Monteith (PM) type equation has the potential for application in many places using publicly available weather data only, with r$_s$ for known or defined surfaces. Modified versions of the Penman and PM equations presented by Wright (1982), Allen et al. (1998), and ASCE-EWRI (2002) have shown the method to accurately estimate actual ET by using the method to calculate reference ET and multiplying by a crop coefficient (Kc). The reference ET is generally defined as ET from well-watered grass (ET$_0$) or alfalfa (ET$_r$). Thus, crop ET is calculated as:

$$ET_c = K_C \times ET_o \qquad \qquad \text{……}.(2.12)$$

where:

ET_c is crop *ET* and K_c is a crop coefficient corresponding to the crop type, growing stages, and surface wetness.

The reference based Penman and Penman-Monteith methods have frequently been used for irrigation planning and management purposes around the world. In this section, the FAO-56 PM and ASCE-PM reference equations are briefly described.

Allen et al. (1998) presented the following simplification of the PM equation.

$$ET_o = \frac{0.408\Delta(R_n - G) + \gamma \dfrac{900}{T_a + 273} u_2 (e_s - e_a)}{\Delta + \gamma(1 + 0.34u_2)} \qquad \text{......(2.13)}$$

where:

ET_o is the reference evapotranspiration for 0.12 m clipped, cool-season grass (mm/day),

R_n is the net radiation at the crop surface (MJ/m^2/day),

G is the ground heat flux density (MJ/m^2/day),

T_a is the mean daily air temperature at 2 m height (°C); u_2 is wind speed at 2 m height (m/s),

e_s is saturation vapor pressure (kPa), e_a is actual vapor pressure (kPa),

Δ is slope of the vapor pressure-temperature curve (kPa/°C), and

γ is the psychometric constant (kPa/°C).

In Equation 2.13, ET$_0$ represents the evapotranspiration occurring from a hypothetical well-watered grass surface having clipped height of 0.12 m, a fixed surface resistance of 70 s/m and an Albedo of 0.23.

2. 2.4.2 Radiation Approach

2. 2.4.2.1 Priestley-Taylor

The Equation used on the Priestley-Taylor method as the following (Priestley and Taylor, 1972):

$$\lambda(ET_P) = \partial \frac{\Delta}{\Delta + \gamma}(R_n - G)$$ ....(2.14)

Where

λ is latent heat of vaporization of water (MJ kg^{-1}), ET_P is potential evapotranspiration (mm day^{-1}), Δ is slope vapor pressure curve (kPa °C^{-1}), γ is psychometric constant (kPa C$^{°-1}$). R_n is net radiation at the crop surface (MJ m^{-2} day^{-1}), G is soil heat flux density (MJ m^{-2} day^{-1}), ∂ is adjustment coefficient ($\partial = 1.26$).

Derivation of some parameters

Parameters G, Δ, γ used in this method can be calculated as FAO56 Penman-Monteith. Latent heat of vaporization of water

$$\lambda = 2.501 - 0.00236T_S$$ ......(2.15)

where:

T_s the surface temperature of the water in degrees Celsius (^{0}C)

2. 2.4.2.2. FAO-24 radiation method

The Equation used on the FAO-24 radiation method as the following:

$$ET_o = a + b\left[\frac{\Delta}{\Delta + \gamma}R_s \right]\frac{1}{\lambda}$$ ......(2.16)

Where

λ is latent heat of vaporization of water (MJ kg^{-1}), ET_o is reference evapotranspiration [mm day^{-1}], Δ is slope vapor pressure curve (kPa °C^{-1}), γ is psychometric constant (kPa C$^{°-1}$). R_s is solar radiation at the crop surface (MJ m^{-2} day^{-1}), a and b regression coefficient.

2. 2.4.3 Temperature Approach

2. 2.4.3.1. Hargreaves Equation

The Equation used on the Hargreaves 1985 method as the fallowing (Hargreaves, 1994):

$$\lambda ET_o = 0.0023 R_a TD^{-0.5}(T+17.8) \qquad ....(2.17)$$

Where:

ET_o potential evapotranspiration [mm day-1], λ latent heat of vaporization of water (MJ kg^{-1}), T average temperature (C^0), R_a extraterrestrial radiation in equivalent evaporation units (mm day^{-1}), TD the difference between mean monthly maximum and mean, monthly minimum temperatures (^0C).

Derivation of some parameters

Monthly or daily values of R_a can be calculated using following equations:

$$R_a = ((24 \times 60)/\pi)G_{SC}d_r\left[(\omega_s)\sin(\varphi)\sin(\delta)+\cos(\varphi)\cos(\delta)\sin(\omega_s)\right] \qquad .....(2.18)$$

Where

ω_s is sunset hour angle in radians, ω_s = arccos (- *tan (δ) tan (φ))*, The argument in above equation must be limited to less than or equal to 2.0 in extreme latitudes (>55 °) during winter months. If the argument is less than −1.0 in extreme latitudes (>55 °) during summer months, then the argument should be set equal to (- tan (δ) tan (φ) -2.0), φ is latitude of the station in radians (negative for southern latitudes), δ is the declination in radians

$$\delta = 0.4093 \sin(2\pi(284+J)/365) \qquad ......(2.19)$$

J is the day of the year (January 1st = 1), d $_r$ is the relative distance of the earth from sun.

$$d_r = 1 + 0.033\cos(2\pi J/356) \qquad \qquad \text{.......(2.20)}$$

G_{sc} is the solar constant, 0.0820 MJm^{-2}min^{-1} (1.959calcm^{-2}min^{-1})

2.2.4.3.2   SCS Modified Blaney-Criddle

The SCS Modified Blaney-Criddle equation use for monthly crop consumptive as follows:

$$ET_m = k_c \cdot k_t \frac{(t)(p)}{100} \qquad \qquad \text{Eq. 2.21}$$

Where: ET_m is a monthly crop consumptive use in inch month^{-1}, t mean monthly air temperature in Fahrenheit (F), p mean monthly percentage of annual daytime hours, k_c mean monthly crop growth stage coefficient, k_t mean monthly climatic (temperature) coefficient F.

Derivation of some parameters

Mean monthly climatic (temperature) coefficient

$$K_t = 0.0173t - 0.314 \qquad \qquad \text{.......(2.22)}$$

Where:

t is monthly air temperature in F, P is mean monthly percentage of annual daytime hours, for any day of the year, j, and the percentage of daily daylight hours is:

$$P = \frac{h_j}{\sum\limits_{i=1}^{365} h_i} 0.0173t - 0.314 \qquad \qquad \text{.......(2.23)}$$

Where:

P the percentage of annual daylight hours for any day of the year,

h_j the number of daylight hours on day *j*,

h_i the number of daylight hours on day *i*.

$$h_i = \omega_s \left(\frac{24}{\pi} \right)$$ …….(2.24)

ω_s is sunset hour angle in radians, ω_s = arccos (- tan (δ) tan (φ)), in above formula:

φ is latitude of the station in radians (negative for southern latitudes); δ is the declination in radians.

$$\delta = 0.4093 \sin(2\pi(284 + J)/365)$$ ……(2.25)

J is the day of the year (January 1st = 1),

The monthly percentage of annual daytime hours as used in the SCS Blaney- Criddle method can be calculated by multiplying the value of *P* for the middle of each month by the number of days in the month. A more accurate approximation would entail integration of above equation over the entire month.

2.2.5. Software of Hydrological models

Hydrological surface flow models such as Soil Water Atmosphere Plant model (SWAP), Soil ,land and urban planning (SLURP) and Soil Water Atmosphere Transfer model (SWAT) simulate the transformation of precipitation into stream flow taking into account all the intermediate processes such as evapotranspiration, interception, infiltration, runoff and groundwater flow and including all the artificial effects of dams, reservoirs, diversions and irrigation schemes. They are therefore able to estimate evaporation and transpiration at many points and at many times (Kite and Droogers, 2000).

2.2.5.1 CROPWAT model

Cropwat for Windows is a computer program to calculate crop water requirements and irrigation requirements from climatic and crop data. Furthermore, this program allows the development of irrigation schedules for different management conditions and the calculation of scheme water supply for varying crop patterns.

The procedure for calculation of the crop water requirements and irrigation requirements is mainly based on methodologies presented in FAO.56 (Allen, 1998) it is a program that uses the FAO Penman-Montieth method for calculating reference crop evapotranspiration.

In this study, CROPWAT model was applied to the calculation of crop water requirements and crop evapotranspiration.

2.2.5.2 Soil Water Atmosphere Plant model (SWAP)

Water flow in the unsaturated zone is predominantly vertical, and can generally be simulated as one-dimensional flow (Romano et al., 1998). Earlier versions of the one-dimensional physically based Soil-Water-Atmosphere-Plant (SWAP) model were developed by Feddes et al., (1978), Belmans et al., (1983), and Kabat et al., (1992). It has been tested for a number of hydrological studies under a wide range of climate and agricultural systems (e.g. Feddes et al., 1988). SWAP has previously been applied and validated for the irrigation conditions in Pakistan, Iran and India (Bastiaanssen et al., 1996; Van Dam and Feddes, 1996; Smets et al., 1997; Beekma et al., 1997, Sarwar et al., 2000 and Droogers et al. 2001). In the present study, particular emphasis has been given to changes of the vertical soil water fluxes with depth.

The SWAP model is based on the Richard's equation, which combines Darcy's Law and the continuity equation for moisture transfer and the advection-dispersion equation for solute transfer (Van Dam et al., 1997; Van Dam and Feddes, 2000). Darcy's law, water movement through a one-dimensional unsaturated, vertical soil column can be written as:

$$q = -K(h) \, dH/dz = -K(h) \, dh/dz - K(h) \qquad ....(2.26)$$

Where: q is soil water flux density (positive upward) (cm d^{-1}), $K(h)$ is unsaturated hydraulic conductivity (cm d^{-1}), h is soil water pressure head or matrix head (cm), and z is the elevation head or vertical coordinate (cm) taken positively upward.

Water balance consideration of an infinity-small soil volume results in the continuity equation for soil water:

$$\partial\Theta/\partial t = -\partial q/\partial z - R_w \qquad ......(2.27)$$

where Θ is volumetric water content (cm^3 cm^{-3}), t is time (d), and R_w is the root water extraction (cm^3 cm^{-3} d^{-1}). Combining Equations 2.26 and 2.27 yields the well-known Richards equation:

$$\partial\Theta/\partial t = C(h) \, \partial h/\partial t = \partial/\partial z \, k(h) \, [\partial h/\partial z +1] - R_w \qquad ....(2.28)$$

where $C(h) = d\Theta(h) \, dh^{-1}$ is the soil water capacity (cm^{-1}).

SWAP solves Equation (2.28) numerically, subject to specified initial and boundary conditions and with known relations between Θh and K. These relationships can be measured directly in the soil, or might be obtained from basic soil data.

SWAP predicts the dynamic interaction between soil, water, atmosphere, and plants on a daily time step. In order to solve these equations, the program uses a finite difference scheme with explicit linearization. In order to apply this finite difference scheme, the soil profile is divided into thin layers and soil horizons of similar hydraulic properties. SWAP may simulate up to three rotating crops in a year and contains three crop growth routines. In this study, a simple crop development model available in SWAP is used which only requires information about the leaf area index (or soil cover fraction), crop height, and rooting depth, all as a function of crop development stage.

2.2.5.3 Geographic Information System (GIS) on regional evapotranspiration

Currently Geographic Information System (GIS) and estimation of technology can do much more than just to make maps. Using GIS databases, information that was initially unavailable can be obtained and estimated using complex analyses. This information can result in a better understanding of the study areas, help make the best choices, or prepare for future events and conditions (Mitchel 1999).

The availability of weather data of acceptable spatial resolution for large-scale irrigation scheduling is an important factor to consider in planning the development and management of irrigation information systems throughout the world (Hashmi et al. 1994).

The spatial distribution of the available weather data is important. It is of special concern in developing countries where the availability of weather stations is limited. The recommended maximum distance between points (weather stations) for least dense networks is 150–200 km, for the intermediate network, 50–60 km for the densest network, 30km (Gandin 1970). Once the data is collected and analyzed using statistics, a surface map can be created using GIS.

Accurate estimation of agricultural water use is of importance to regional water resources management. We are working on a regional evapotranspiration (ET) modeling approach that uses ESRI ArcGIS Arc objects (Zeiler, 2001) modeling environment. Established methods (Jensen et al., 1990) exist to calculate point-specific reference ET from point meteorological data. Here we extend these methods to calculate reference ET field over a region. This approach requires regional meteorological input data such as air temperature and incoming solar radiation. This project focuses on the interpolation of temperature for regional reference ET calculation. ArcGIS provides some two-dimensional spatial interpolation methods; however, these methods may not work well for a spatial variable such as temperature that depends upon topography. The presentation here is therefore focusing on evaluating a set of temperature interpolation schemes (Goovaerts, 1997; Phillips et al., 1992) for use in the GIS–based ET modeling.

2.2.6. Water Balance Approach

2.2.6.1 Lysimeter measurement

This involves an artificially enclosed volume of soil for which the inflow and outflow of water can be measured and commonly changes in storage can be monitored by weighing. This technique is used to determine evaporation in a natural environment by accurately measuring the other water balance components; i.e. soil moisture storage and deep drainage. The lysimeter offers the only absolute way of precisely measuring water loss from soil and crop canopy surfaces. Due to its precise measurement, it can be used for validation of actual evapotranspiration ET_a results obtained with satellite data.

A weighing lysimeter is a container (usually metal) that can measure ET by observing the weight change of the container. Therefore, unlike the above listed energy and bulk transfer methods, lysimeter measurements do not study the energy balance but study the water balance. According to Allen et al. (1998), highly-sensitive weighing or floating lysimeters provide one of the best methods for precisely measuring water loss from soil and crop canopy surfaces, and they have had very important input in the development and testing of the more theoretical micrometeorological methods for estimating ET. They also caution, however, that substantial measurement error occurs with poorly managed or designed lysimeters.

2.2.6.2 Regional Water Balance Approach

A water balance is an accounting of all water volumes that enter and leave a three dimensional (3D) space over a specified period of time. Change in internal water storage must also be considered. Both the spatial and temporal boundaries of a water balance must be clearly defined in order to compute and to discuss a water balance. A complete water balance is not limited to only irrigation water, rainwater or groundwater, etc., but includes all water that enters and leaves the spatial boundaries (Burt 1999).

An important step forward in hydrology for water management is the work on the evapotranspiration flux using satellite data (Bastiaanssen. 1998a). The available amount of water on land (Q) is determined by the amount of rainfall (P) minus the evapotranspiration (ET) (i.e. the water that returns from the land surface to the atmosphere). Thus, in its simplest form, the water balance is:

$$P - ET = Q \qquad \text{.......(2.29)}$$

Where:

P is the precipitations in mm, ET is evapotranspiration and Q is the available amount of water on land.

In the history of hydrology and water management, the spatial distribution of the actual ET term was for a long while a difficult issue and was often considered as a rest term or was subjected to crude estimation methods. It describes where and by how much, water in nature is used by crops and vegetation by wetlands or by soil evaporation. Knowing ET in time and space facilitates not only better determination of the amount of water (Q) in catchments but also performance assessment of the irrigation schemes in terms of water use and crop productivity.

In calculating evapotranspiration, which is an input to the soil water balance model, Penman method or other methods, which take into account a more complete range of meteorological observations, are recommended by (Donker 1987).

2. 2. 7.   Potential ET and Reference ET

Potential ET is defined as the quantity of water evaporated from an extensive free water surface as dictated by existing atmospheric conditions (Shuttleworth, 1993). A concept similar to potential ET is reference ET. Reference ET is defined as ET from a well watered reference crop maintained at a given standard height. Therefore, potential ET can be defined exclusively from meteorological conditions, while reference ET is dependent on the reference crop selected. Typically grass is used as the reference crop. However, other crops, such as alfalfa, have also been used (Jensen et al., 1990). Numerous studies have been devoted to the estimation of ET from meteorological observations. Jensen et al. (1990) Studies on ET estimation method were conducted by Brutsaert (1982) and Rosenberg et al. (1983). These authors have each provided an extensive review of a range of potential ET estimation methods.

The review of literature begins with the key concepts of the ET process and traditional methods of ET estimation show in the (Allen.et.al 1998). The FAO Penman-Monteith approach of reference crop evapotranspiration as relatively accurate and has consistent performance in both arid and humid climates. Thus, it is recommended as the sole standard method in the evapotranspiration estimation (Allen.et.al 1998). Evapotranspiration of any crop could be estimated by multiplying the reference crop evapotranspiration with crop coefficient of the crop of interest.

Estimated monthly average Reference crop evapotranspiration using FAO Penman-monteith approach has been used to estimate the crop potential evapotranspiration and actual evapotranspiration in the Thornthwaite and Moistures soil water balance procedure. In this study focus for the point which ET equal PET equal ETr, in the field of lysimeter, and good irrigated fields, near from the gauging stations in different places in the study area in Sana'a basin, Yemen.

2. 2. 8.   Evapotranspiration Studies in Yemen

In Yemen, the unevenly distributed rainfall and ET has been well recognized (NWRA, 2001). Countrywide rainfall averages 96 billion cubic meters per year and average ET is estimated to be about 81.2 billion cubic meters per year with the rate being the highest in southern highland Yemen and lowest in the coastal and eastern areas of the country (Jac, et al.. 1995; Bruggement, 1997; NWRA, 2001). A study of potential ET characteristics in Yemen conducted by Jac, et al. (1995) concluded that the annual potential ET using the Penman model, Doorenbos and Pruitt (1984) in different zones in the country ranged between 1800-2700 mm for coastal zones and foothills and ranged between 1500-2500mm at the mountain zones of western Yemen, yet 2000-3500mm at arid zones of the interior. The variation in potential evapotranspiration (PET) during the year is illustrated in the Figure 2.1a&b. Precipitation (P) is shown in the same graphs, in order to highlight the degree of aridity of the sites.

Bruggement (1997) estimated the reference evapotranspiration (ET_O) have been calculated according the Penman-Monteith method (FAO, 1990). It is the rate of evapotranspiration from an extensive surface 8 – 15 cm tall green grass cover, actively growing and not short of water. As for the calculation mean monthly, values of the climate parameters have been used. The PET used in determining the length of growing period the rate of ET of sorghum and maize during the period of full crop development and not short of water has been selected. The PET for sorghum/ maize during the period of full crop development is comparable to the ETo.

The PET is a function of the following climatic and location parameters:

- Climate parameters contains: temperatures (minimum, maximum, and average), windspeed, sunshine or solar radiation and relative humidity;

- Location parameters contains: altitude and latitude (which influence the radiation, temperature and maximum sunshine duration).

The variation of PET during the year follows the variation of temperature, with the maximum heat during early summer. The annual PET (Figure 2.1) ranges from less than 1200 mm (Ibb) to around 2000 mm (Al-Jowf), while daily values vary between 2.9 to 3.7 mm/day for Ibb and 3.6 to 7.8 mm/day for al Jowf (Bruggement, 1997). The PET greatly exceeds the average rainfall. Since soil water is usually severely lacking during the greater part of the year, the actual evapotranspiration is only a minor fraction of the potential evapotranspiration.

Evapotranspiration from local and water basin studies within Yemen also showed high spatial and temporal variability. Almhab et al. (2004a) study the evapotranspiration for Sana'a basin using Penman, FAO penman, Thornthwaite, Blaney-Criddle, Penman-Monteith FAO, Hargreeves and water budget methods in the Sawan small watershed Area. They concluded that the Penman-Monteith FAO method provided the closest prediction while water balance and the Blaney-Criddle method could be used for limited data availability. ET data requirements in Yemen were reported by Jac, et al. (1995) and the results showed that the PET in related to elevation, although there is a tendency for PET to decrease at increasing elevations. However, the relation is certainly not as well-defined as relation between temperature and elevation. Thus factors other than average temperature must have a notable influence on the PET variations. Analysis that shows the large part of the variation is explained by differences in wind speed, which possibly reflects local rather than regional effect. The two prominent 'outliers' in the graph are the data for Marib and Nugub; low relative humidity is the main case of their anomalous position.
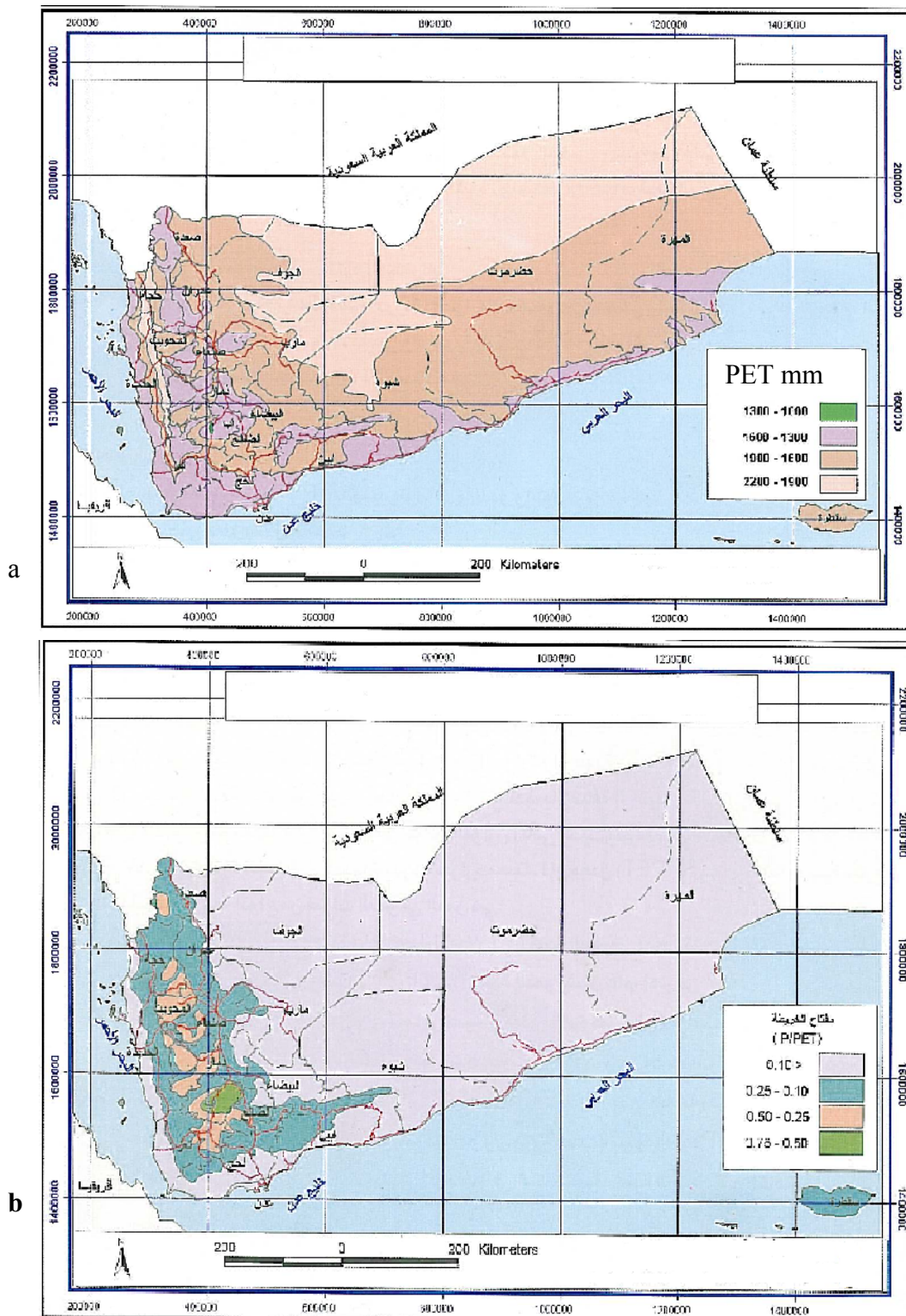
Figure 2.1a,b   The annual PET and the annual P/PET in Yemen after (Bruggement, 1997)

2.3 Remote Sensing Techniques and capabilities

Remote sensing by means of its large coverage and high data frequency should be able to provide ample data and information to determine regional ET. Satellite remote sensing equipped with suitable sensor provides suitable data for the ET estimation.

2.3.1 Spectral responses of vegetation

A leaf is built of layers of structural fibrous organic matter within which there are pigmented, water-filled cells and air spaces. Each of the three features (pigmentation, physiological structure, and water content) has an effect on the reflectance, absorption, and transmittance properties of a green leaf. Leaf physiology determines infrared reflection by means of discontinuities in the refractive index within the leaf. Four primary pigments are contained in higher plants, namely, chlorophyll a, chlorophyll b, carotene and xanthophy ll, all of which absorb visible light for photosynthesis. Chlorophyll a absorbs at wavelengths of 0.43 μm and 0.66 μm and chlorophyll b at wavelengths 0.45 μm and 0.65 μm. The carotenoid pigments, carotene and xanthophy ll, both absorb blue to green light at a number of wavelengths (Wittingham, 1974; Curran, 1983). It is the combined effects of the leaf pigments and the physiological structure that produce the characteristic reflectance property for vegetation. The spectral character of light reflected by a normal plant leaf is controlled by two groups of cells (Figure 2.2). The long, narrow cells below the upper epidermis are the palisade cells. They contain many chloroplasts with chlorophyll pigments that absorb most blue and red light for photosynthesis and efficiently reflect green light. The chlorophyll absorption features are centered at 0.43 μm and 0.68 μm, while the area between the two features falls within the portion of the visible spectrum which results in

the green color of plants. Leaf reflectance is reduced also as a result of absorption by three major water absorption bands that occur near wavelengths of 1.4 μm, 1.9 μm and 2.7 μm and two minor water absorption bands that occur near wavelengths of 0.96 μm and 1.1 μm (Curran, 1983). Table 2.1 shows the relationship between multispectral reflectance and vegetation amount for five wavebands as defined by Tucker and Maxwell (1976) for a grass canopy. These relationships provide indications for the detection of vegetation amount by remote sensor in different wavelengths.

The vegetation spectral reflectance curve also provides a good indication for monitoring vegetation condition. The steep rise in reflectance of vegetation beyond 0.8 μm is called the red edge of the chlorophyll band (Horler et al., 1983) and the slope of the red edge has been related to chlorophyll concentrations in the leaves (Horler et al.. 1983).
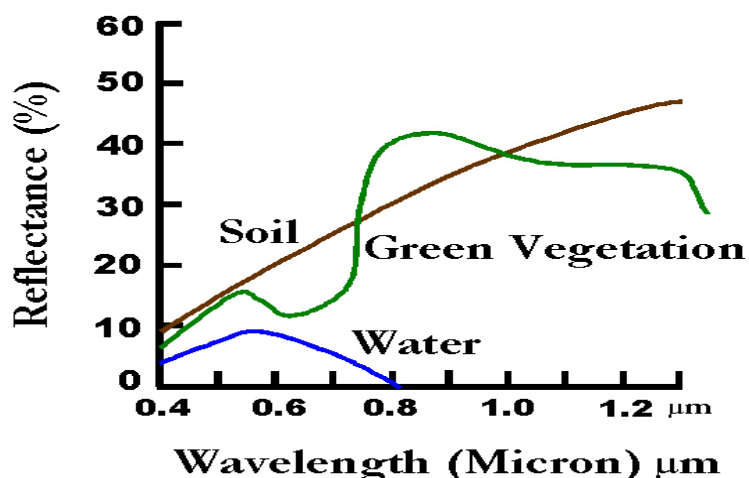
Figure 2.2   spectral reflectance of vegetation, soil, water in the visible, near infrared and middle infrared portion EM radiation (adapted from http://landsat.usgs.gov/ resources/remote_sensing/remote_sensing_ applications.php, 29-10-2007).

As vegetation becomes senescent, the infrared reflectance does not significantly decrease (Wooley, 1971; Sinclair et al.. 1973). However, the breakdown of plant pigments causes a rise in blue and red reflectance. This results in a positive relationship between all wavelengths and vegetation amount. If the vegetation is diseased, the cell wall structure is damaged and the high Albedo between 0.7 and 1.3 μm is reduced, which provides a diagnostic remote sensing technique for assessing the condition of plants. The abrupt and characteristic change in the reflectance of vegetation at about 0.7

μm is the basis of a number of techniques for assessing the amount of vegetation present in a remotely sensed image (Hobler et al., 1983).

Table 2.1 : The Multispectral reflectance and vegetation characteristics and their relationship to vegetation amount.

Waveband	Characteristics	Relationship to vegetation amount*
Ultraviolet/blue 350-500 nm	Strong chlorophyll and carotenoid absorption	Strong negative
Green 500-600 nm	Reduced level of pigment absorption	Weak positive
Orange/red 600-700 nm	Strong chlorophyll absorption	Strong negative
Far red 700-740 nm	Transition between strong absorption and strong reflectance	Weak negative
Near infrared 740-800 nm	High vegetation reflectance	Strong positive

* adapted from Tucker and Maxwell, 1976 and Tan, 1998.

Spectral reflectance curves of vegetation can also be used for early stress detection. When a healthy plant becomes strained by some type of stress in its environment changes occur in its spectral curves. These stresses include moisture deprivation, prolonged inundation by flood water, nutrient deficiency, plant diseases, and concentration of soil salts (Murtha, 1978). Figure 2.3 illustrates the changes in the typical reflectance properties of a plant leaf as it progresses from a healthy state through different stages of damage.
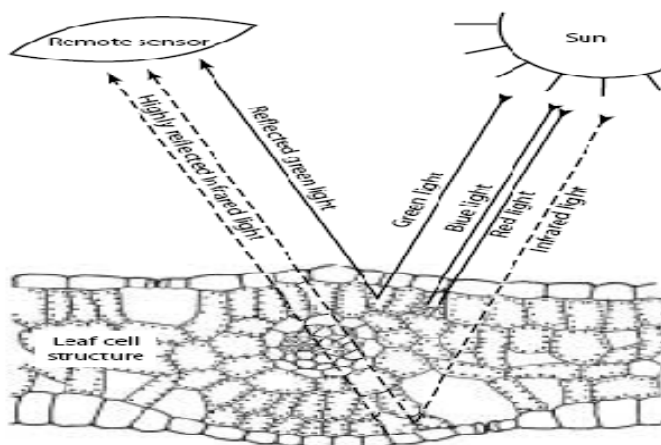
Figure 2.3 Reflectance of a typical green leaf in cross-section; chloroplasts reflect the green light and absorb red and blue light for photosynthesis (Harrison and Jupp 1989)

2.4 Remote Sensing in Evapotranspiration (ET) Estimation

Since the beginning of Earth remote sensing from satellites, remotely sensed observations of the Earth's surface provide a promising source of data for synoptically examining characteristics over land surfaces. Hydrologists and agricultural meteorologists have been searching for techniques to calculate ET from data provided by satellites. The studies involving remote sensing techniques and ET estimation can be divided into four major categories: 1) empirical methods; 2) simplified energy balance methods; 3) Biophysical estimation ET model; 4) Temperature and Vegetation Index Method; 5) Full energy balance methods.

2.4.1 Empirical Methods

Empirical relationship between the quantities that can be measured from a satellite and evapotranspiration has been recognized early. Idso et. al. (1975) found a linear relationship between evaporation and net thermal radiation. Menenti (1979) obtained evapotranspiration as a bilinear function of the remotely estimated temperature and surface Albedo. Seguin and Itier (1983) have shown that, at a given location, there exists a good correlation between the midday surface temperature and daily evapotranspiration. Kerr et al. (1989) found a close relationship between the Normalized Difference Vegetation Index (NDVI). derived from NOAA High Resolution Picture Transmission (HRPT) data, and the actual evapotranspiration with a time lapse of 20 days.

2.4.2 Simplified Energy Balance Methods

Various researchers have related satellite derived surface temperature in a simplified energy balance equation for ET estimation. Heliman et al. (1976) used airborne sensors derived surface temperature in combination with ground-measured solar radiation, wind speed, air temperature, and crop growth condition parameters to calculate daily ET based on an energy balance equation. Jackson et al. (1977) simplified the energy balance equation in which the daily evapotranspiration value is given as a function of the instantaneous value of the difference between the surface temperature and the air temperature both measured near midday (T_s - T_a). Their equation is expressed as:

$$ET = R_d - G_d - B(T_s - T_a) \qquad\qquad ......(2.30)$$

where R_d is the daily value of the net radiation, G_d is the daily value of the soil heat flux and B is a constant depending primarily on surface roughness and wind speed.

This approach was used in various studies (Seguin and Itier, 1983 and Moran et al., 1994). The soil heat flux G_d was assumed to be zero when the daily average was used. Using equation (2.30) with instantaneous remote sensing imagery requires further assumptions, because G_d can be relatively large and R_d may vary from location to location. As a first approximation, equation (2.30) was rewritten in the following format:

$$ET = A - B(dT) \qquad\qquad ......(2.31)$$

Where A = R_d - G_d, which is sometimes termed the "available energy". Parameters A and B can be determined empirically using ground data.

The advantage of Equation 2.31 is its simplicity, which requires minimal amounts of ground-based meteorological data (net radiation and temperature).

2.4.3   Biophysical estimation evapotranspiration model

Reference ET (ET_o) was calculated from meteorological data with the FAO Penman–Monteith equation 2.13 (Allen. et al., 1998). ET_o was calculated as a daily total ET (mm/d) from an imaginary grass reference crop (Jones, 1983). The equation adjusts the equation for mainly stomata resistance (rs) as a constant, whereas the rs of plants respond in complex ways to environmental factors in natural environments (Jones, 1983; Osmond et al., 1980). Potential evapotranspiration was also calculated by the Blaney-Criddle method (ET_o-BC) (Brower & Heibloem, 1986) for comparison purposes. This method is based mainly on mean monthly temperature.

Empirical methods based on Vegetation Indexes (VIs) for estimating ET are modifications of the crop coefficient method (Jensen & Haise, 1963) for estimating water demand by irrigated crops. Crop coefficients (K_c) are empirical ratios relating crop ET (ETc) to a calculated reference-crop ET (ET_o) that is based on atmospheric water demand (Jones, 1983) over a crop cycle or to actual ET measurements, as in the present study. A Kc curve gives the seasonal distribution of Kc as a function over time or a time-related index, such as growing degree-days. In this form, however, Kc cannot account for variations in crop growth from field to field, as affected by soil type, nutrition, uneven water distribution, or other agronomic factors.

As an alternative, Kc can be adjusted throughout the crop cycle to take into account changes in the fraction of absorbed solar radiation (FARs) by the plant canopy (estimated by VIs) as the crop develops. A time-series of VI measurements is correlated with measured *ETc* or ETo to develop a *VI–Kc* curve over the crop cycle. Once calibrated, these VI-based Kc curves can provide close estimates of ET_c within 10% of measured values among fields with different growth characteristics ((Hunsaker et al., 2003).

Choudhury et al. (1994) used a heat balance and irradiative transfer model to study relations among transpiration coefficients *(T_c)* and *VIs*. They provided a theoretical

basis for estimating transpiration from no stressed crops from VI and T_a data. Based on the relationship between ET and LAI and the relationship between LAI and VI, they developed an equation in the form:

$$ETc = ETo\left[1 - \frac{V\operatorname{Im}ax - VI}{V\operatorname{Im}ax - V\operatorname{Im}in}\right]^{n}$$
........(2.32)

The term $\left[1 - \frac{V\operatorname{Im}ax - VI}{V\operatorname{Im}ax - V\operatorname{Im}in}\right]^{n}$ converts VI to a scaled value (0–1) and is derived from the light extinction curve through a canopy as estimated by VIs.the $VImax$ is the maximum value of the vegetation index and $VImin$ is the minmemum value of the vegetation index. The exponent ^{n} depends on the crop and the VI used. The effects of soil evaporation and crop stresses added scatter and uncertainty into the ET estimates.

2.4.4   Surface Temperature and Vegetation Index Method

Many studies on radiometric surface temperature have focused on the widely observed negative correlation between surface temperature and remotely sensed measurements of actively transpiring vegetation such as NDVI (Hope et al.. 1992; Nemani and Running, 1989; and Moran et al., 1994). Shuttleworth and Wallace (1985) adapted the Penman-Monteith equation (Monteith, 1981) to account for energy partitioning between crop and soil.

Gilles et al. (1995) used a relation between NDVI and surface temperature derived from multispectral aircraft measurements to define surface fluxes. Over a large area, a plot of NDVI versus surface temperature forms a triangular distribution that is due to the distribution of soil moisture and vegetative cover.   Schmuggee and Becker (1991) also observed the NDVI and surface temperature relationship with ET. Humes et al. (1994) showed that points of both low NDVI and surface temperature correspond to areas of high soil moisture.

Price (1990) developed a method for relating contextual information (the slope of the vegetation index - surface temperature line and the slope of the wet soil - dry soil line) in AVHRR data to large area evapotranspiration. Carlson et al. (1990) found that spatial variations in surface radiometric temperature are related to variations in the vertical variation of soil water content modulated by fractional vegetation cover. Based on theoretical and experimental evidences, Moran et al., (1994) proposed a concept termed the vegetation index/temperature trapezoid, which combines vegetation indices with composite surface temperature measurements to allow application of Crop Water Stress Index (CWSI) theory to partially vegetated fields without knowledge of foliage temperature.

Much effort is now concentrated into increasing the accuracy of radiant fluxes. Although, surface albedo can easily be estimated by common sensors (enabling the calculation of the shortwave net radiation), it takes more specific sensors to estimate the longwave component of the radiation balance. Surface Albedo and temperature can also be the basis for estimates of the upwelling components, while the down welling components are based on meteorological data (Moran et al., 1989). The parameterization of turbulent fluxes is having a large part of research in itself, two main parameters are used generally, the Leaf Area Index (LAI, inferred from NDVI) and the aerodynamic resistance (r_{ah}, for momentum and for heat transport). Menenti (2000) concludes that relatively simple models of heat transfer at the land atmosphere interface can be sufficiently accurate if a few key variables can be determined with sufficient accuracy and capturing the fundamental physics of the process, as in the case of the difference between the aerodynamic and radiation surface temperatures (T_{aero}-T_{rad}).

Lastly, some methods exploit image context (Price, 1990; Bastiaanssen, 1995), albeit having certain advantages (like taking advantage of range availability for deriving equations) these methods are also restrictive to areas and often contextual to image conditions, making automation of processes a major constraint.

2.4.5   Full energy balance method

The Radiation coming from the sun can be split into longwave and shortwave (Figure 2.4). The Long wave radiation heats particular ground features that will eventually be released after a certain amount of time. The Shortwave radiation is instantaneously reflected by ground features according to their Albedo characteristics.

$$Rn = K^{\downarrow} - K^{\uparrow} + L^{\downarrow} - L^{\uparrow} \qquad\qquad \ldots\ldots(2.33)$$

Where: $K^{\downarrow}$ is incoming short wave radiation, $K^{\uparrow}$ is outgoing short wave radiation, $L^{\downarrow}$ is incoming long wave radiation, and $L^{\uparrow}$ is outgoing long wave radiation.

This rather simple system of radiation balance is considering the ground elements as a layer of a given height, responding uniformly to a radiation stimulus. This concept has two direct advantages, the first one is to simplify in-layer structural ground element interactions, and the second one is that it is very well fitting the ideal description of a satellite remote sensing and its ground sampling unit: the pixel.
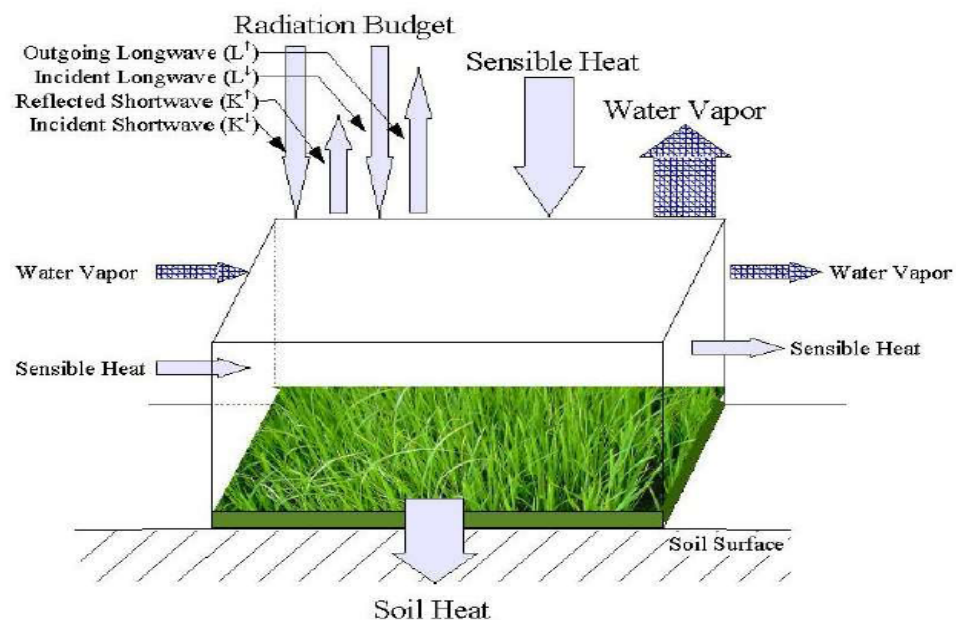
Figure 2.4   The energy balance components (Chemin, 2003)

The Energy Balance partitioning (Figure 2.4) is summarized at an instant time t (at the time of satellite overpass) by the following equation:

$$Rn = G + H + \lambda E \qquad\qquad ……..(2.34)$$

Where

Rn is the net radiation emitted from the Earth surface $(W\ m^{-2})$,

G is the soil heat flux $(W\ m^{-2})$,

H is the sensible heat flux $(W\ m^{-2})$,

$\lambda(ET_{ins})$ is the latent heat flux, being the energy necessary to vaporize water $(W\ m^{-2})$.

Generally lateral fluxes are not considered when dealing with Remote Sensing images because of their spatial cover capturing the instantaneous energy balance system. Even when transforming the energy balance components for a daily extrapolation of the values, lateral exchanges between pixels are found either in one pixel or in the neighboring ones, extrapolation does not expose lateral values yet encompasses them.

$$G = \frac{\rho_s C_s (T_0 - T_s)}{r_s} \qquad\qquad ……(2.35)$$

Heat flow into the soil, G, is driven by a thermal gradient in the uppermost topsoil (Parodi, 2000). It is a conduction flux through the soil matrix. This gradient varies with the state of the vegetation covering the soil that is influencing the light interception by the soil surface. The irradiative heating of the topmost layer is then directly modifying the surface temperature and thermal gradient in the top layer. The Sensible Heat flux (H) is a convection flux through the atmosphere layers, coming from the surface skin boundary layer with the topmost soil/vegetation layer.

$$H = \frac{\rho_{air} C_p (T_0 - T_a)}{r_{aH}} \qquad\qquad ……..(2.36)$$

The energy necessary to vaporize water under given atmospheric conditions is especially ruled by the resistance to vaporization parameter (r_v)

$$\lambda E = \lambda \left(\frac{\rho_{vs} - \rho_{va}}{r_v} \right) \qquad\qquad …….(2.37)$$

The use of satellite remote sensing data (VIS, NIR, and TIR bands) to derive local, regional and global estimation of turbulent fluxes are considered recent developments. Among others SEBAL (Soil Energy Balance Algorithm for Land) (Bastiaanssen et al., 1998), TSEB (Two Sources Energy Balance) (Norman et al., 1995), S-SEBI (Roerink et al., 2000), SEBS (Su, 2002) are the most common ones. Among the current satellite remote sensing models, the SEBAL has been designed to calculate the energy portioning at the regional scale with minimum ground data (Bastiaanssen et al., 1998). SEBAL has been verified at many places around the world including Spain, Italy, Turkey, Pakistan, India, Sri Lanka, Egypt, Niger, and China (Bastiaanssen, et al., 1998a; Bastiaanssen, et al., 1998b; Bastiaanssen and Bos, 1999).

2.4.5.1 SEBAL Remote Sensing Technique

The SEBAL algorithm as illustrated in Figure 2.5 is a parameterization of the energy balance and surface fluxes based on spectral satellite measurements (Bastiaanssen et al. 1998).

SEBAL requires visible, near-infrared, and thermal infrared input data, which means that applications of Landsat Thematic Mapper (TM) and NOAA Advanced Very High Resolution Radiometer (AVHRR) sensors are useable.

SEBAL estimates ET by tracking the land surface energy balance at the satellite image time (satellite image acquisition time). Satellite images basically provide energy balance information for the image time only. After the instantaneous ET flux is estimated using a satellite image, the flux is empirically extrapolated to the 24-hour integrated ET (mm/day) and seasonal integrated ET (mm/season) using ratios to reference ET based on weather data from local weather stations.

SEBAL

Visible Near infrared Thermal infrared	Surface albedo Vegetation index Surface temperature	Conversion	-Net Radiation flux density Rn -Soil heat flux density Go -Sensible heat flux density H -Latent heat flux density LE	-Bowen-ratio -Evaporation fraction -Pristly& Taylor coef. -Surface resistance
Satellite radiances	**Surface parameters**	Land surface parameterization	Surface energy balance	Moisture indicator

Figure. 2.5 Principal components of the Surface Energy Balance Algorithm for Land (SEBAL) which converts remotely measured spectrally emitted and reflected radiance's into the surface energy balance and land wetness indicators Bastiaanssen (1998a).

Figure 2.6 show the main steps of the technique used to estimate instantaneous energy balance calculation and ET in SEBAL model after (Bastiaanssen, 1995).
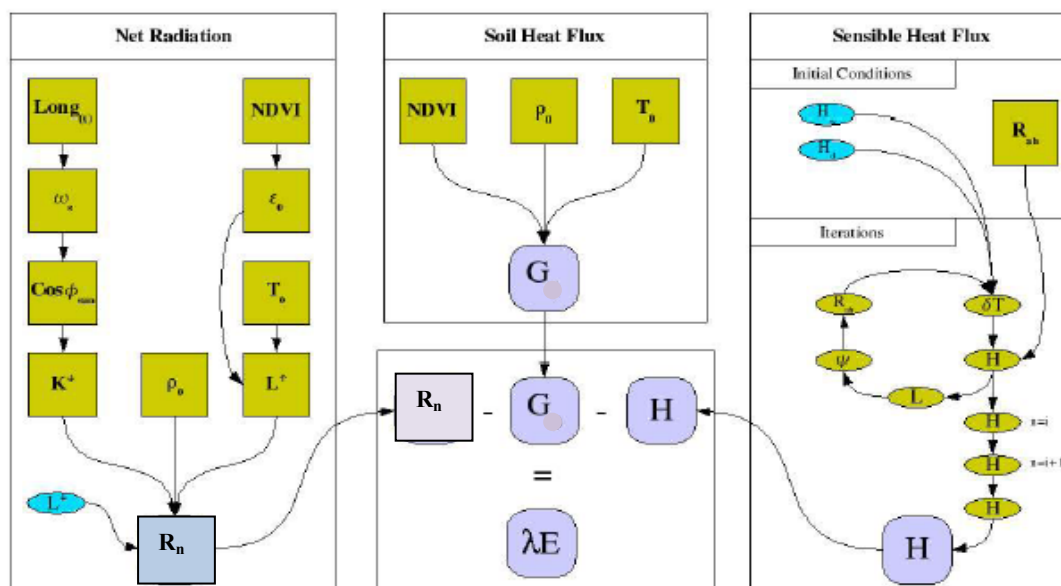
Where : *Rn* is the net radiation, *G* is the soil heat flux, *H* is the sensible heat flux, λE is the latent heat flux, being the energy necessary to vaporize water .

Figure 2.6 Main steps of instantaneous energy balance: (Bastiaanssen ,1995 and Chemin, 2003)

2.4.5.2 SEBAL$_{ID}$ model

Tasumi (2003) developed remote sensing model named SEBAL$_{-ID}$, which estimates evapotranspiration (ET) from satellite images. The operationally usable remote sensing model was developed for Idaho and western United States conditions by refining the SEBAL (figure 2.7).
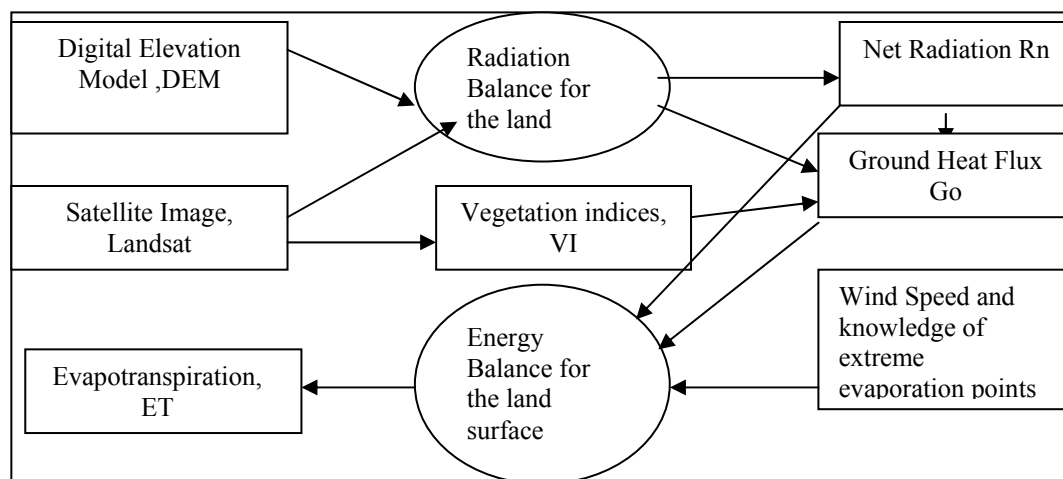
Figure 2.7   general computational processes for determining ET using SEBAL$_{ID}$

The estimation of ET_{24} in SEBAL $_{ID}$ partitioning (Figure 2.7) is summarized by the following equation:

$$ET_{24} = ET_r F \bullet ET_{r24} \qquad \text{........(2.38)}$$

Where : *ET_{24} is 24 hour* Evapotranspiration. ET_{r24} is Alfalfa reference evapotranspiration, $ET_r F$ is ET_r fraction calculation by equation 2.39, and ET_{ins} instantaneous Evapotranspiration

$$ET_r F = \frac{ET_{ins}}{ET_r} \qquad \text{.......(2.39)}$$

During the period between January 2000 and February 2005, Idaho University (IU) has been working on original SEBAL. In the studies SEBAL was significantly modified into METRIC (Mapping Evapotranspiration with High Resolution and Internalized Calibration) which uses Landsat ETM+ data, under Idaho station conditions in the, western USA (Allen et al., 2005).

2.5. Fusion of multispectral information

2.5.1. Overview

Working in the field of multi-sensor image fusion, the evaluation of the achieved results becomes relatively complex because of the different sources of data that are involved (Pohl and Van Gendren, 1998). It is even more difficult when multi-date composite data are used for data fusion. One of the possibilities is to validate findings from fused data by comparing with actual data sets or ground truth (Pohl and Van Gendren, 1998). Data fusion is a very wide domain, and Pohl (1996) provide the following definition: "data fusion combines data from multiple sensors, and related information from associated databases, to achieve improved accuracy and more specific inferences than that could be achieved by the use of single sensor alone". The purposes of data fusion should be that the information obtained should at least improve image visualization and interpretation. There are several fusion approaches, based on the stage at which the fusion is performed. Pixel based approaches have commonly been used for satellite imagery, where data are merged on a pixel-by-pixel basis. In this study, appropriate pixel-based fusion methods were developed to extract detailed information from multi-temporal NOAA-AVHRR 10-day composite data and Landsat TM data at a regional scale. When considering quantitative information, like the evapotranspiration, the first concern is to keep the volumes of water constant through the scales, or said differently, the sum of water volume evapotranspiration from small size pixels should be equal to the water volume in the large pixel of another satellite that encompasses the smaller pixels.

Low cost techniques are required, which are of sufficient accuracy to allow correct identification of ET over a range of climatic conditions ranging from clear sky - arid to cloudy tropical and over physical scales from small holder to large contiguous irrigation schemes. With a single data set, it is rather difficult to study ET and its dynamic signatures.

2.5.2 The Fusion model

The simple fusion model was applied to satellite images from both the National Oceanic and Atmospheric Administration-Advanced Very High Resolution Radiometer (NOAA-AVHRR) and Landsat satellite images. NOAA-AVHRR images are characterized by a relatively high temporal resolution (once a day), but a low spatial resolution of approximately 1 km. Landsat images have a high spatial resolution of 30 meter, but a low temporal resolution of 16 days. An analysis of the growing season solely based on Landsat images is practically impossible as the chance of almost all acquisitions during the season being cloud-free is very low in most farming areas. On the other hand, an analysis using only NOAA-AVHRR images would not give sufficient spatial detail. Therefore, the advantages of both sensors are combined in this methodological framework where high and low resolution products are integrated to calculate total seasonal evapotranspiration.

$$ET_{fusion} = ET_{NOAA} * ET_{TM}/ET_{TM\text{-}mean} \qquad …..(2.38)$$

$$ET_{fusion} = \sum i=1 i=3 (ET_{NOAA,i} * ET_{TM,j} / ET_{TM,i}) \quad m^3 ha^{-1} \quad ….(2.39)$$

Where:

i is the NOAA period and j is the corresponding Landsat image. The same method to calculate ET_{season} is applied to calculate seasonal biomass production (bioseas) from NOAA-AVHRR and Landsat biomass production maps:
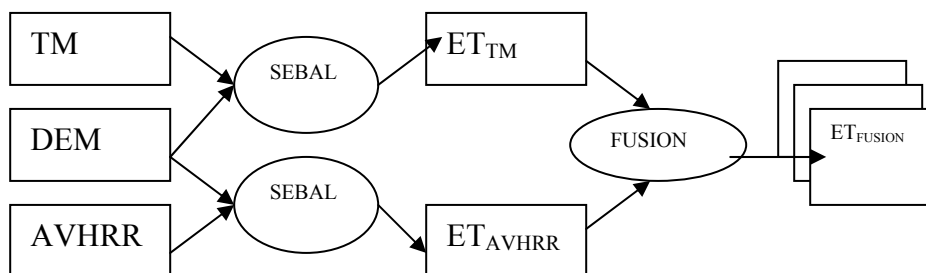
Fig. 2.8   Scheme for generating daily high resolution maps: mapping individual temporal values on the classification image. (Spatial resolution enhancement)

2.6 Decision Support System for Estimating Regional Evapotranspiration

The performance of different ET estimation methods varies with climatic conditions and availability of data. The data requirements vary from method to method. Furthermore, ET estimations depend upon the quality of the meteorological data.

Therefore, it is very difficult for users to decide upon an appropriate ET estimation method among the different available methods for a particular station given the available data. Thus, there is a need to develop a tool not only for estimating the ET but also to decide on the best ET method for given data availability and climatic conditions. Many scientists have studied the reliability of the Penman- Monteith method for estimating the reference ET (McNaughton and Jarvis 1984; Allen 1986; Allen et al. 1989; Chiew et al.1995). Jensen et al. (1990) analyzed the performance of 20 different methods against the lysimeter measured ET for 11 stations around the world under different climatic conditions. The Penman-Monteith method ranked as the best method for all climatic conditions. However, the subsequent ranking of other methods varied with climatic condition. A study comparing nine ET equations using lysimeter data from six locations in Europe was performed by Choisnel et al. 1992. The results of the study supported use of the Penman-Monteith equation for ET estimation.

Amatya et al. 1995 compared the efficiency of five ET estimation methods against the Penman-Monteith method at three sites in North Carolina.

The purpose of this research was to developing a decision support system for estimating the ET (DSS-ET) under different data availability and climatic conditions, using eleven ET estimation methods against the Penman- Monteith method, and also tested for three locations in Sana'a basin, Yemen.

2.6.1 Model Base

The model base consists of the eleven most commonly used and internationally accepted ET estimation methods based on combination theory, radiation, temperature, and remote sensing along with an algorithm based decision-making model. The different methods in each group are selected according to a ranking method.

Recently, the Food and Agriculture Organization of the United Nations FAO suggested use of the FAO Penman-Monteith method for estimation of ETo. However, ET estimation methods included in FAO 24 are still widely used and popular. Therefore, one FAO 24 method is included in the combination, temperature, radiation, and Remote Sensing group.

2.6.1.1 Combination Methods

Earlier ET estimation methods were based on either energy balance or mass transfer approaches. The combination methods were developed by combining the energy balance, heat, and mass transfer approaches. These methods combine fundamental physical principles and empirical concepts based on standard meteorological observations and have been widely used for estimation of ET from climatic data.

Penman (1948) first derived the combination equation by combining components of energy balance and aerodynamics. Later many scientists modified the Penman equation by incorporating stomata resistance, modifying the wind function and vapor pressure deficits Penman 1963; Monteith, 1965; Wright and Jensen 1972; Doorenbos and Pruitt 1977; Wright 1982. The present DSS model consists of two combination methods, namely, FAO-24 Penman, and FAO-56 Penman-Monteith (section 2.2.4.1.2).

2.6.1.2 Radiation Methods

Since solar radiation provides the energy required for the phase change of water and often limits the ET process where water is readily available, a number of ET estimation methods have been developed based on energy balance (Makkink 1957; Turc, 1961; Priestley and Taylor, 1972; Doorenbos and Pruitt, 1977). In the DSS, two radiation methods, namely, the Priestley-Taylor, and FAO-24 radiation methods, (section 2.2.4.2) are included in chapter two.

2.6.1.3 Temperature Methods

One of the earliest methods of estimating ET involved the use of air temperature. Many scientists have established relationships between air temperature and ET, Lowry and Johnson (1942); Thornthwaite (1948). Blaney and Criddle (1950) developed a simplified formula for estimating consumptive use of crops for the arid western regions of the United States by correlating mean monthly temperature and daylight hours. Doorenbos and Pruitt (1977) presented the most fundamental revision of the Blaney- Criddle method. Hargreaves and Samani (1985) proposed a method for estimating the reference ET that requires only maximum and minimum air temperatures. In the present DSS model two temperature methods, the SCS Modified Blaney-Criddle and the Hargreaves methods are included. The governing equations and time scale of calculation of each method are given in (section 2.2.4.3) chapter two.

2.6.1.4 Remote Sensing Methods

Many studies have reported that remote sensing techniques cannot measure evapotranspiration directly (Tasumi, 2003). However, ET can be indirectly estimated by applying remote sensing techniques by extending point measurements or empirical relationship to much larger areas, or by estimating ET as a residual of the energy and moisture balance, where other energy fluxes are estimated from the satellite data (Engman, 1995). The empirical approach, which is one of the most widely applied approaches, is to correlate instantaneous radiometric temperature to the daily energy balance. This method was pioneered by Jackson et al. (1977) and cited by Kustas and Norman (1996) section 2.4.2 in this study methods similar to equation 2.31 have been proposed by Seguin and Itier (1983), and Nieuwenhuis et al. (1985) cited by Kustas and Norman (1996). Kerr et al. (1989) and Smith and Choudhury (1990) established empirical relations between evaporation and NDVI Choudhury, 1991) section 2.4.3 in this study. In some conditions, NDVI has good correlation with ET. However, this method does not have good ability to detect low ET for conditions of high vegetation but low soil moisture. The relations are generally not valid for daily or even weekly ET estimation but for longer periods (i.e. annual ET) (Tasumi, 2003). Regarding the above two empirical methods, numerous studies have found a significant negative correlation between vegetation indices and Trad over different surfaces (Goward et al., 1985; Hope and McDowell, 1992; Nemani and Running, 1989; Nemani et al., 1993), Kustas and Norman (1996).

As for the energy balance approach the basis of this approach is the same as the energy balance method described in Section 2.2.2 Energy balance components are estimated using satellite data supplemented with ground-based weather data. In this approach, $\lambda(ET_{ins})$ is estimated as the residual of the energy balance equation (Equation 2.2).

Among the several ET estimation methods, the remote sensing method is regarded as the only technology that can efficiently and economically provide regional and global

coverage of actual consumption (Kustas and Norman, 1996).

Among the current satellite remote sensing models, the Surface Energy Balance Algorithm for Land (SEBAL) methodology includes the complete energy balance calculation (Tasumi, 2003). In the United States, the IDWR/UI group has applied SEBAL in the western US from 2000 (Morse et al. 2000 and 2001). Dr.Hendrickx and Dr.Small, New Mexico Tech., began applying SEBAL under a program of the NSF Center for Sustainability of semi-Arid Hydrology and Riparian Areas (SAHRA) in 2001 (http://www.sahra.arizona.edu/).

The detailed procedure for the original SEBAL method is explained by Bastiaanssen (1995 and 2000) and Bastiaanssen et al. (1998a). Modifications by the IDWR/UI group were described in Tasumi et al. (2000a and 2000b).

SEBAL$_{-ID}$ model was developed for Idaho and western United States conditions by refining the SEBAL. Additionally, the confidence in the ET estimation is expected to increase with additional meteorological and ground information, when available (Tasumi, 2003). SEBAL$_{-ID}$ can apply when good weather data is available. If not the original SEBAL must be used (Tasumi, 2003).

In this study Modified SEBAL for arid mountain areas was developed by the refinement and calibration the original SEBAL model to adapt it to work under local arid mountain, and desert conditions, to obtain a good accuracy to estimated ET. The Remote Sensing methods explain above Simplified energy balance method (section 2.4.2), biophysical model (section 2.4.3), original SEBAL (section 2.4.5.1), SEBAL$_{-ID}$ (section 2.4.5.2), and Modified SEBAL proposed by this research was included in the DSS-ET model.

CHAPTER 3

MODIFIED SEBAL MODEL THEORY AND ESTIMATION

3.1   Overview of the model

The main computation steps for modified SEBAL model which was proposed by this study can be referred from Figure 3.1. There are seven steps which are necessary for applying SEBAL spatially in mountainous arid areas. The firest step was input of data: satellite image from NOAA-AVHRRR and Landsat TM and local weather data; The second step was data preprocessing: geometric; The third step was generation of DEM: slop/aspect and cosine solar zenith angle; While forth step was calculation of surface reflectance; After that the fifth step was generating model parameters surface Albedo , vegetation indices , emissivity and surface temperature, from this step the original SEBAL start. The sixth step was determining of radiations; net radiation, soil heat flux and sensible heat flux. The final step was calculation of latent heat flux, evaporation fraction, instantaneous ET, daily ET and monthly.

```
                        ┌─────────────┐
                        │    Start    │
                        └─────────────┘
                               │
                               ▼
        ┌──────────────────────────────────────────────────┐
        │   Input data: satellite data, local weather data  │
        └──────────────────────────────────────────────────┘
                               │
                               ▼
        ┌──────────────────────────────────────────────────┐
        │         Data preprocessing: geometric             │
        └──────────────────────────────────────────────────┘
                               │
                               ▼
        ┌──────────────────────────────────────────────────┐
        │      Generation of DEM: slop/aspect and theta     │
        └──────────────────────────────────────────────────┘
                               │
                               ▼
        ┌──────────────────────────────────────────────────┐
        │         Calculation of surface reflectance        │
        └──────────────────────────────────────────────────┘
                               │
                               ▼
        ┌──────────────────────────────────────────────────┐
        │           Generating model parameters             │
        └──────────────────────────────────────────────────┘
                               │
                               ▼
        ┌──────────────────────────────────────────────────┐
        │           Determination of radiations             │
        └──────────────────────────────────────────────────┘
                               │
                               ▼
        ┌──────────────────────────────────────────────────┐
        │         Calculation of ET: daily, monthly         │
        └──────────────────────────────────────────────────┘
                               │
                               ▼
                        ┌─────────────┐
                        │     End     │
                        └─────────────┘
```
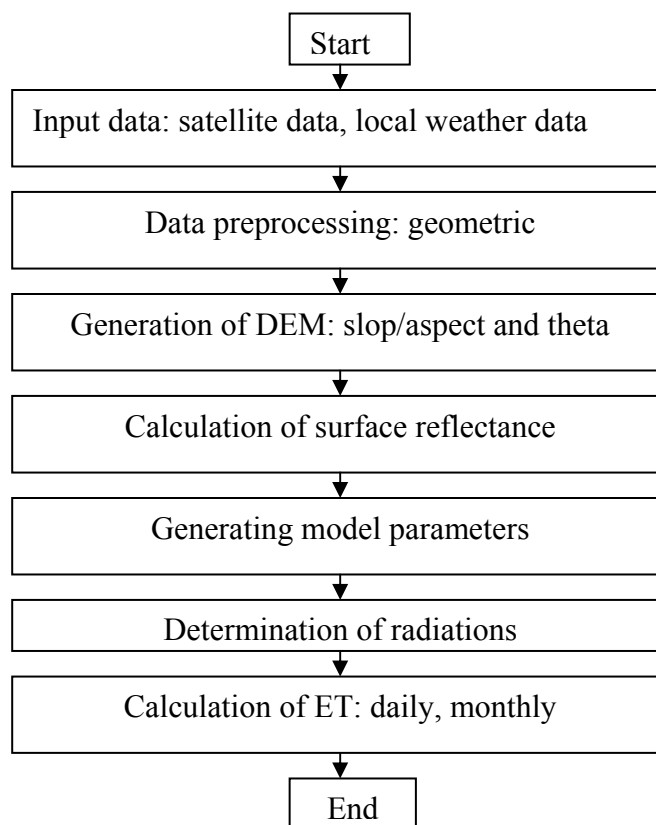
Figure 3.1   General flowchart of the modified SEBAL

The proposed ET estimation model known as a "modified SEBAL", as detailed in this chapter, estimates evapotranspiration from land surfaces by tracking the land surface energy balance using information generated from the satellite image data, a digital elevation model (DEM) and meteorological data from weather stations. These references should be referred to it ones are looking for the original SEBAL methodology Bastiaanssen (1995 and 2000) and Bastiaanssen et al. (1998a and 2005), Tasumi et al (2000a), Tasumi (2003) and Chemin and Ahmed (2000). Modified SEBAL was developed for application with NOAA-AVHRR images and Landsat 5 TM images. However, most of the theory and much of the procedures are satellite-type independent and therefore the technique can be used with other satellite images having thermal bands such as Vegetation SPOT, MODIS, ASTER, etc. with little modification.

Satellite images basically provide energy balance information for the image acquisition time only. After the instantaneous ET flux is estimated using a satellite

image, the flux is empirically extrapolated to the 24-hour integrated ET (mm/day) and seasonal integrated ET (mm/season).

At the land surface, substantial energy is supplied (or lost) as radiation. The primary sources of radiation are shortwave solar radiation and longwave radiation emitted by the atmosphere. The radiation balance at the land surface is described by:

$$R_n = R_{s\downarrow} - R_{s\uparrow} + R_{L\downarrow} - R_{L\uparrow} \qquad \dots\dots(3.1)$$

where,

$R_{s\downarrow}$ is incoming short wave radiation, $R_{s\uparrow}$ is outgoing short wave radiation,

$R_{L\downarrow}$ is incoming long wave radiation, and $R_{L\uparrow}$ is outgoing long wave radiation.

The net radiation (R_n) at the earth's surface is basically redistributed in three processes. A portion of the net radiation is used to heat the near-surface air (this flux is called sensible heat flux, H), a portion of R_n is used to evaporate water (this flux is called latent heat flux, $\lambda(ET_{ins})$), and the remaining R_n is absorbed or conducted into the soil or water and results in a change in soil temperature. This flux is called ground heat flux, G. Equation3.2 figure 3.2 shows the energy redistribution process at the earth's surface:

$$R_n = G_0 + H + \lambda(ET_{ins}) \qquad \dots\dots(3.2)$$

Where

R_n is the net radiation emitted from the Earth surface *(W m⁻²)*,

G_0 is the soil heat flux *(W m⁻²),and* H is the sensible heat flux *(W m⁻²)*,

$\lambda(ET_{ins})$ is the latent heat flux, being the energy necessary to vaporize water *(W m⁻²)*.
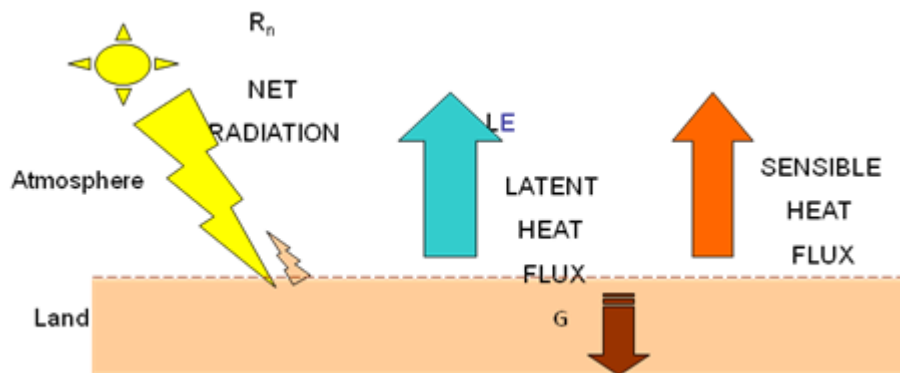
Figure 3.2 Energy balance at the earth's surface

In modified SEBAL, ground heat flux (G) is empirically calculated by vegetation indices derived from the satellite image and sensible heat flux (H) is estimated by employing unique assumptions concerning near surface temperature differences and point measurements of windspeed. The latent heat flux $\lambda(ET_{ins})$, is calculated as the residual of the energy balance. Latent heat flux is readily converted into the equivalent amount of ET as:

$$ET_{inst} = 3600 * \frac{\lambda(ET_{ins})}{\lambda} \qquad \qquad ......(3.3)$$

Where

ET_{inst} is instantaneous ET flux at the satellite image time (mm/hr equivalent),

3600 is the conversion from seconds to hours $(W\ m^{-2})$,

$\lambda(ET_{ins})$ is in $W\ m^{-2}$, and λ is latent heat of vaporization (J/kg) representing the energy required to evaporate a unit mass of water, calculated as (Harrison, 1963):

$$\lambda = (2.50 - 0.00236(T_S - 273.16)) * 10^6 \qquad \qquad ......(3.4)$$

Where

T_s is surface temperature in Kelvin.

3.2 Pre-Processing and Calibration of the images

The aim of the calibration of the bands in the visible, is to get radiance values at the earth skin surface as per power in a certain area ($W\ m^{-2}$) being the physical basis for all the Remote Sensing processing to be implemented. Once this is done, a reflectance value is extracted as being the reflected amount of radiation over the total radiation received. Reflectance values are the basis of most of the remote sensing calculation in the visible bands.

The top of atmosphere reflectance is:

$$\rho^{TOA}{}_i = \frac{L^{TOA}{}_i}{K^{\downarrow}{}_i} \qquad \ldots\ldots(3.5)$$

With:

ρ^{TOA} being the planetary spectral reflectance at the top of the atmosphere, L_i^{TOA} the spectral radiance at the top of the atmosphere, $K_i^{\downarrow}$ the incoming spectral radiance
i is the band number of the satellite (band 1, 2, 3, 4, 5 and 7) for landsat image and (band 1and2)for NOAA -AVHRR .

In order to get to L_i^{TOA}, first is to go to the two components of the ratio. Let us start with L_i^{TOA}, then finishing with $K_i^{\downarrow}$.

The spectral radiance at the top of the atmosphere L_i^{TOA} is:

$$L^{TOA}{}_i = \left(\frac{DN_i - I_i}{G_i}\right) \times \pi \qquad \ldots\ldots(3.6)$$

With:

L_i^{TOA} the spectral radiance at the top of the atmosphere for band $_i$, G_i the gain (-) and the I offset, *(b-a)* the gain (-) and *a* the offset, DN $_I$ the Digital Numbers , $_i$ is the band number of the satellite . The gain and offset values for Landsat 5TM satellite images have been considered constant in that study, so the formula become as the fallowing:

$$L^{TOA}{}_i = \frac{\left(a + (b-a) \times DN_i\right)}{255} \qquad \ldots\ldots(3.7)$$

With:

L_i^{TOA} the spectral radiance at the top of the atmosphere for band $_i$, *(b-a)* the gain (-) and

a the offset, DN_I the Digital Numbers , $_i$ is the band number of the satellite.

The coefficients *a, b* are taking from the work of Markham and Baker (1987) as show in the table 3.1 below.

Table 3.1 : *a - b* the gain and the offset, to correct the L_i^{TOA} Landsat 5TM , after Markham and Baker (1987)

band	a	b
Band 1	-0.15	15.21
Band 2	-0.28	29.68
Band 3	-0.12	20.43
Band 4	-0.15	20.62
Band 5	-0.037	2.719
Band 7	-0.015	1.438

The gain and offset values for Landsat 7ETM+ satellite images are extracted from the header files available with each CD ROM product delivered. This also can be made to the web site of Landsat 7ETM+, for the updated Calibration Parameters Files (CPF).

The gain and offset values for NOAA satellites are varying according to the NOAA satellite number, NOAA-14 images was used in this study. Calibration parameters for G_i and I_i .The gain and offset for NOAA satellites are given by the following set of equation:

$$G_i = a_i t + b_i \qquad\qquad ……(3.8)$$
$$I = c_i t + d_i$$

with:

t being the number of days after launch of NOAA ,*i* the band number (band 1 and 2) and a_i, b_i, c_i, d_i coefficient varying with t after satellite launch and with the band number.

Table 3.2 : *a – b-c-d* the constant, to correct the L_i^{TOA} NOAA-14 Channel 1 and 2 after chemin (2003).

a)NOAA-14 Channel 1

Date	Day post launch	a	b	c	d
30/12/94	0	0.000e-04	1.795	0.000e-04	41.0
01/01/95	2	-3.527e-04	1.795	0.000e-04	41.0
01/01/96	367	-3.047e-04	1.778	0.000e-04	41.0

b)NOAA-14 Channel 2.

Date	Day post launch	a	b	c	d
30/12/94	0	0.000e-04	2.364	0.000e-04	41.0
01/01/95	2	-6.161e-04	2.364	0.000e-04	41.0
01/01/96	367	-5.088e-04	2.324	0.000e-04	41.0

NOAA-14 (December 30, 1994)

3.2 1   Drifts correction of the spectral radiance with $K^{\downarrow}_i$.

The spectral reflectance ρ^{TOA} can be obtained after specifying the incoming radiance

$$K^{\downarrow}_i = \frac{K^{\downarrow}_{exoi}\cos\phi_{su}}{\pi d_r^{\,2}} \qquad\qquad \text{......(3.9)}$$

With: $K^{\downarrow}_i$ being the incoming radiation W.m^{-2}.µm^{-1} for band *i*, the $K^{\downarrow}_{exoi}$ exo-atmospheric irradiance for band *i* ,ϕ_{su} the Zenith angle*(rad),* d$_r$ Earth-Sun distance, *i* is the band number of the satellite .

Table 3.3 **:** The $K^{\downarrow}_{exoi}$ exo-atmospheric irradiance (W.m^{-2}.μm$^{-1)}$ is fixed for: a)Landsat 5TM , b)ETM+ and c) NOAA-AVHRR

Band no. / satellite type.	Landsat 5TM	Landsat 7ETM+	NOAA11	NOAA14
For band 1	195.8	1970	195.8	195.8
For band 2	182.8	1843	182.8	182.8
For band 3	155.9	1555	-	-
For band 4	104.5	1047	-	-
For band 5	K 21.91	227.1	-	-
For band 7	7.457	80.53	-	-

d_r is calculated as follows (Duffie and Beckman, 1991, Allen et al., 1998):

$$d_r = 1 + 0.033\cos(DOY\frac{2\pi}{365})$$

......(3.10)

The value for d_r is dimensionless, and *DOY* is the sequential day of year. The unit of the angle argument (DOY 2л/365) is in radians. The annual averaged value of d_r is 1.0, and it ranges from about 0.97 to 1.03.

3.2 2 Determination of the Solar Zenith angle θ
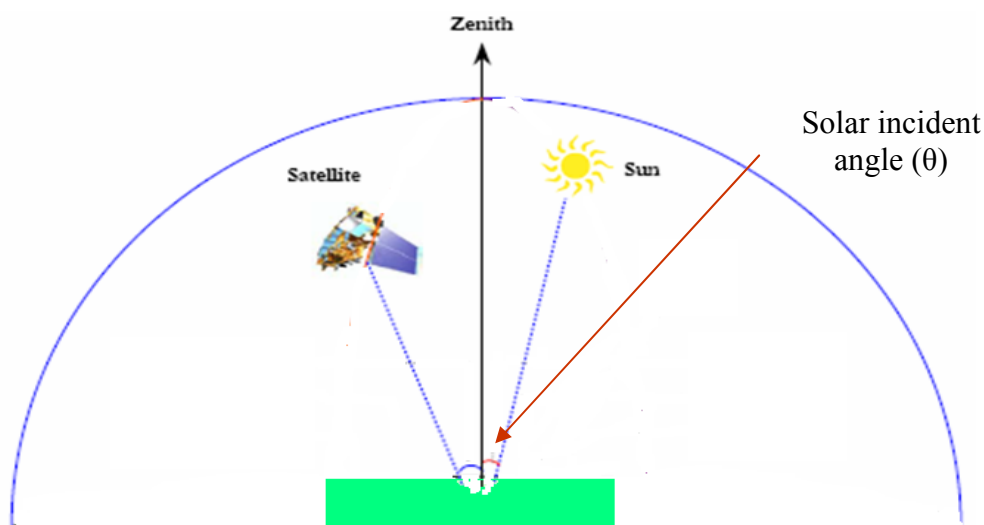
Figure 3.3   Solar incident angle (θ)

When land surface is flat or does not have slopes, the cosine of the solar Zenith angle is simply derived from the sun elevation angle provided in the header file of Landsat images:

$$\cos\theta = \cos(\frac{\pi}{2} - \varphi)$$

......(3.11)

where:

φ is sun elevation angle in radians.

On a sloped land surface, the solar incident angle changes with surface slope and aspect. The ERDAS Field Guide gives the equation to compute the cosine of the incidence angle as follows (ERDAS Field Guide p383 "Lambertian Reflectance Model"):

$$Cos\theta = cos(90-\theta_s)cos\theta_n + sin(90-\theta_s)\, sin\theta_n\, cos(\phi_s-\phi_n)$$

......(3.12)

Where:

θ_s is the elevation of the sun above the horizon, ϕ_s is the azimuth of the sun, θ_n is the slope of each surface element, ϕ_n is the aspect of each surface element.

Equation 3.12 gives the cosine of the incidence angle for a particular date and time. However, one must integrate the equation for daily time steps by tracking the sun. Equation 3.12 is not suitable for integration because the location of sun is not an independent constant in this equation. Therefore, the following general equation for calculation of incident angle is applied (Duffie and Beckman, 1991):

$$
\begin{aligned}
cos\,\theta_{unadjusted} = {} & sin(\delta)sin(\phi)cos(s) - sin(\delta)cos(\phi)sin(s)cos(\gamma) \\
& + cos(\delta)cos(\phi)cos(s)cos(\omega) \\
& + cos(\delta)sin(\phi)sin(s)cos(\gamma)cos(\omega) \\
& + cos(\delta)sin(\phi)sin(s)sin(\omega)
\end{aligned}
\qquad\text{......(3.13)}
$$

Where

$cos\,\theta_{unadjusted}$ is the cosine of the solar incident angle for the land surface,

δ is solar declination (positive in summer in the northern hemisphere) calculated by equation 3.14,

ϕ is latitude of the pixel (positive for northern hemisphere) in radians,

s is ground slope in radians, where "s = 0" is horizontal and "s = л/2" represents a vertical surface (s is always positive and represents an upward/downward slope in any direction),

γ is the surface aspect angle in radians, γ is the deviation of the projection of the normal to the surface from the local meridian, where y = 0 for aspect that is due south, γ is negative for east and positive for western aspect, γ = -л/2 for an east facing slope and γ = +л/2 for a west facing slope, γ = -k or γ = n represents a north facing slope,

ω is the hour angle of the sun, calculated by Equation 3.15. to ω = 0 at solar noon, where to is negative in morning and positive in afternoon.

In Equation 3.13, surface slope and aspect for each pixel of the image can be derived from a digital elevation model (DEM). The parameters δ and ω are calculated by Equations 3.14 and 3.15 (Duffie and Beckman, 1991, Allen et al., 1998): Solar declination δ is calculated by

$$\delta = 0.409 \sin(\frac{2\pi}{365} * DOY - 1.39)$$
...... (3.14)

Where:

DOY is the sequential day of year.

Sun hour angle is calculated by (Duffie and Beckman, 1991, Allen et al.., 1998):

$$\omega = \frac{\pi}{12}\left[(t + \frac{L_z - L_m}{15} + S_c) - 12\right]$$
...... (3.15)

Where:

t is standard local time when the satellite image was taken (daylight savings time should not be applied), L_z is longitude of the center of the local time zone (degrees east of the Greenwich), L_m is longitude of the measurement site (degrees east of the Greenwich), and S_c is seasonal correction for solar time calculated by equation 3.2.8 (Duffie and Beckman, 1991).

$$S_c = 0.1645 \sin\left(\frac{4\pi(DOY - 81)}{364}\right) - 0.1255 \cos\left(\frac{2\pi(DOY - 81)}{364}\right) - 0.025 \sin\left(\frac{2\pi(DOY - 81)}{364}\right)$$
...... (3.16)

Satellite images have a certain pixel size. For example, Landsat shortwave bands generally have 30m*30m (or 28.5mx28.5m) pixel size. However, this does not mean that the corresponding land surface area for a pixel is 30mx30m = 900m^2, since the satellite does not regard the effect of surface slope. Radiation observed by a satellite sensor for a 30mx30m pixel having a 40° sloped surface is reflected from a land surface area of 900/cos(40°) = 1175m^2. To keep the energy balance calculation consistent, modified SEBAL calculates the energy balance on a "horizontal equivalent". For this reason, the cosθ value derived by equation 3.13 is adjusted to the horizontal equivalent by the following equation:

$$\cos\theta = \frac{\cos\theta_{unadjusted}}{\cos(s)}$$
...... (3.17)

Where: *cos(s)* is the cosine of the land surface slope. The minimum value for cosθ is limited to 0.1, in order to account for diffuse solar radiation.

3.3   Generation of DEM Intermediate files

Digital elevation map of the area was prepared using shuttle Radar Topography Mission (SRTM) with a resolution of 30 m^2 and DEM was processed usind DEM height converter in ERDAS imagine software.

3.3.1   Correction of slope/aspect and cos theta on DEM

In this section, the sine and cosine of the surface slope and aspect are made for each pixel of the image. These outputs are used for slope/aspect correction in modified SEBAL.

3.3.1 1   Slope *(s)* calculation

The surface slope is made for each pixel of the image .These outputs are used for slope correction in modified SEBAL. The procedures used in this step are relatively simple.

In degrees (not in percent or in radians) the range of values in the image is from 0° to 90°.0° means that there is no slope (0= flat), and 90° means that the land surface profile is vertical. The output, Sin (slope) and cos(slope) : The range of the output image is from 0 to 1. In ERDAS imagine, the slop at each pixel is calculated using 3x3 pixel

moving window. For a pixel at location X,Y, having an elevation e, elevation values a,b,c,d,f,g and i of the pixels around it are used to calculate slope as shown below.

a	b	c
d	e	f
g	h	i

For a given pixel, the average change in elevation per unit distance in the x and y direction (Δx and Δy) are calculated using the following expression:

Δx1 =c-a   **......(3.18a)**   Δy1 =a-g **......(3.18b)**

Δx2=f-d   **......(3.18c)**   Δy2=d-h **......(3.18d)**

Δx3=i-g   **......(3.18e)**   Δy3=c-i **......(3.18f)**

$$\Delta x = (\Delta x1 + \Delta x2 + \Delta x3) / 3xs \qquad ......(3.18g)$$

$$\Delta y = (\Delta y1 + \Delta y2 + \Delta y3) / 3ys \qquad ......(3.18h)$$

Where

a…i : elevation value 3×3 window

xs   : x pixel size or horizontal distance between the centers of two pixels

ys   : y pixel size or vertical distance between the centers of two pixels.

The slop at pixel x,y is calculated as:

$$s = \frac{\sqrt{(\Delta x)^2 + (\Delta y)^2}}{2} \qquad ......(3.18i)$$

And slop in degrees =

$$s_{deg\,ree} = \frac{\tan^{-1}(s) * 180}{\pi} \qquad ......(3.18j)$$

3.3.1.2.   Aspect *(γ)* calculation

The surface aspect for each pixel of the image is represented in degrees, where North is zero, and with values increasing positively in a clockwise direction. There is no sense of aspect when the slope of the surface is zero. The number 361 is given to the pixels that have no slope. Therefore, the range of values in the images is from 0° to 361°. 0° indicates a north facing slope, 90° indicates an east facing slope, 180° is a south facing slope, 270° is a west facing slope, and 361° indicates that there is no aspect, since there is no slope. The output of Sin(aspect) and Cos(aspect) was defined as the aspect in the output as South=0, West= positive. Therefore, the range of aspect is from -180 to 180 degrees.

As with slop calculations, for pixel x,y, the average changes in elevation in both x and y directions are calculated first.

$$\Delta x = (\Delta x1 + \Delta x2 + \Delta x3)/ 3 \quad \textbf{......(3.19a)}$$

$$\Delta y = (\Delta y1 + \Delta y2 + \Delta y3)/ 3 \quad \textbf{......(3.19b)}$$

If $\Delta x = 0$ and $\Delta y = 0$, then the slope is zero and aspect is undefined. Otherwise θ is calculated as:

$$\theta = \tan^{-1}\left(\frac{\Delta x}{\Delta y}\right) \qquad\qquad ......(3.20)$$

Then aspect is $180 + \theta$ (in degrees), where Δy is not zero. If Δy is zero thus aspect is also undefined since there is no division by zero.

The input file with the above defined units can be automatically derived from a DEM using ERDAS's Topographic Analysis function. If the available input files have a different definition for units, then the user must modify the model to obtain output files having the appropriate definition for units.

3.3.1.3 .   Cosine of solar incidence angle (*cosθ*).

This section discusses slope and aspect corrections in SEBAL. The slope/aspect correction is carried out based on an assumption that the land surface acts as a Lambertian reflector. The solar incidence angle θ is the angle between the solar beam and a vertical line perpendicular to the land surface. If the land surface is horizontal, then the solar incidence angle θ is computed by equation 3.11 and in slop area by equation 3.12. However, it is not suitable for integration because the location of sun is not an independent constant in this equation. Therefore, in modified SEBAL the equation 3.13 is used, with cosine of the incidence angle for a particular date and time. However, one must integrate the equation for daily time steps by tracking the sun.

The value of cosθ calculated by equation 3.13 is divided by the cosine of the slope, *cos(s)* equation 3.17. *Cosθ* is used for the calculation of incoming solar radiation for each band of the Landsat TM , ETM+ and NOAA-AVHRR (Rs↓) equation 3.41, and the reflectance is calculated from the reflected radiation observed by the satellite.

Usually the incoming and outgoing solar radiation for a band ($Rs_{i↓}$, $Rs_{i↑}$) or reported as a whole ($Rs_↓$, $Rs_↑$)) are expressed as energy per unit area, *W m⁻²*. For incoming radiation, the unit area is expressed along a plain parallel to the sloped surface.

Since outgoing radiation is observed by the satellite's sensors for an essentially flat surface, the intensity of outgoing radiation is redefined as energy per unit area where the unit area is in a horizontal equivalent. In modified SEBAL, the factor cosθ that represents the effect of the solar angle is divided by cos(s) to adjust the incoming solar radiation to energy per unit area where the area is a horizontal equivalent.

All of the fluxes that are computed for the energy balance, including radioactive fluxes, are analyzed on a horizontal equivalent basis in SEBAL.

3.4   Calculation of Spectral reflectance (unadjusted for transmittance)

In this section, spectral reflectance is calculated for all pixels of each band 1-5 and 7 (band 6 is the thermal band) for LANDSAT satellite images, and band 1 and 2 for NOAA-AVHRR images (band 3, 4 and 5 is the thermal bands),the reflectance of *a* band is computed by the formula (3.5) is the outgoing energy (radiation) of the band measured at the top of atmosphere by the satellite, and incoming energy (radiation) of the band at the top of atmosphere. The outgoing energy is recorded by the satellite's sensors is computed by the equation (3.6), and incoming energy is based on theoretical values for various wave lengths of solar radiation. Incoming energy (band) is computed by the equation (3.9) . Cosθ is the cosine of the solar incident angle derived in equation 3.11and d_r is inverse relative distance Earth-Sun. The value for d_r averages 1.0 and ranges from about 0.97 to 1.03. Outgoing energy (band) is computed by the equation (3.10). In equation 3.10, inverse squared relative distance Earth-Sun d_r is computed as FAO56 (Allen et al., 1998).

3.5   Generating model parameters

3.5.1   Albedo at the top of atmosphere, *a* TOA

Albedo is the ratio of reflected to incident solar radiation at the surface and is computed initially as

$$\alpha = \frac{R_{s\uparrow}}{R_{s\downarrow}} \qquad\qquad ......(3.21)$$

Where:

a is Albedo, $R_{s\downarrow}$ is incoming short wave radiation (solar radiation) and $R_{s\uparrow}$ is outgoing short wave radiation. Short wave radiation is defined as the wave-lengths between 0.17 and 4 micrometers.

In this section, Albedo was calculated as observed at the top of atmosphere (unadjusted for transmittance) using the reflectance of each band calculated in the previous section. This Albedo at the top of the atmosphere is converted into a surface Albedo in the following step. The interpretation of Equation 3.21 is basically same as Equation 3.5. The only difference is in the range of the wavelengths used. Equation 3.5 targets whole range of short wave radiation, by essentially adding the magnitudes (k_{out}) of the individual short-wave bands.

The basic concept of calculating a_{TOA} is to use weight coefficients on the summation of individual bands:

$$\alpha_{TOA} = \sum (C_{band} * \rho_{band}) \qquad \ldots\ldots(3.22)$$

Where:

$C_{(band)}$ is weighting coefficient for a particular band and ρ_{band} is Radiation (band) in equation 2.23.

The ratio of potential incoming energy in each band is determined by the ratio of solar constant Gsc in each band (See. Table3.4). Therefore,

$$C_{band} = \frac{G_{SC(BAND)}}{\sum G_{SC(BAND)}} \qquad \ldots\ldots(3.23)$$

Where, $C_{(band)}$ is the weighting coefficient for the band given in Table 2.1 For example, since $G_{sc(band)} = 668.4$, c1 = 195.7 / 668.4 = 0.293

Table 3.4. Weighting coefficients $G_{sc(band)}$ ($W\ m^{-2}$/μm) and $C_{(band)}$ for shortwave Landsat bands (Markham and Barter, 1986 for Landsat 5, and Landsat 7 Science Data Users Handbook, 2002)

		Band	Band 2	Band 3	Band 4	Band 5	Band 6	Band 7	Total
Landsat5 TM	$G_{sc(band)}$	1957	1829	1557	1047	219.3	—	74.52	6683.8
	$C_{(band)}$	0.292	0.2736	0.2330	0.1566	0.0328		0.0111	1
Landsat7 ETM+	$G_{sc(band)}$	1969	1840	1551	1044	225.7	:	82.02	6711.7
	$C_{(band)}$	0.293	0.2741	0.2311	0.1555	0.0336		0.0122	1

3.5.2   Transmittance (τ_{sw})

A general value for the one-way transmittance in clear-sky can be predicted for clear, relatively dry atmospheric conditions as:

$$\tau_{SW} = 0.75 + 2*10^{-5}*z \qquad \qquad ……(3.24)$$

where, z is elevation above sea level in m. (Allen et al.,1998(FAO56)). More complicated expressions are available for transmittance in FAO56 and elsewhere (Allen, 1996) considers that sun angle and absorption by water vapor. Transmittance can also be determined for a locality using measurements of solar radiation on clear days. However, it is important for the pyranometer used to be well-calibrated and maintained.

As an example for the Sana'a Basin application, two-way transmittance is the square of one-way transmittance, if the elevation is 1800m, $\tau_{sw} = 0.75 + 2 * 10^{-5} * 1800 = 0.786$, then, $\tau_{sw}^2 = (0.786)^2 = 0.618$.

3.5.3   Surface Albedo (α)

In this step, SEBAL estimates surface Albedo, α, from the "surface Albedo at the top of atmosphere, a_{TOA} that was calculated in the previous section.

Since the atmospheric transmittance is not taken into account in a_{TOA}, the adjustment of the Albedo value by transmittance is the task in this step.

Therefore, surface Albedo is calculated as

$$\alpha = \frac{\alpha_{TOA} - \alpha_{path\_radiance}}{\tau_{SW}^2} \qquad \qquad ......(3.25)$$

Where:

$a_{path\_radiance}$ is Albedo path radiance, and $\tau_{sw} \times \tau_{sw}$ is the two-way transmittance. Usually, a path radiance has a value between 0.025 to 0.04.

3.5.4 Vegetation indices (VI)

Although Vegetation indices (VI) is not components of the energy balance, it is briefly described in this section since these indices are frequently used to estimate various components of the energy balance.

Healthy green vegetation generally reflects 40% to 50% of the incident near-infrared energy (0.7 to 1.1 µm), with the chlorophyll in the plants absorbing approximately 80% to 90% of the incident energy in the visible (0.4 to 0.7 µm) part of the spectrum (Jensen, 1983). Therefore, vegetation indices are often derived from satellite images using the contrast between visible (especially the red band) and near infrared bands. For Landsat Thematic Mapper (TM) and Enhanced Thematic Mapper Plus (ETM+) images, a comparison of bands 3 and 4 (0.63 to 0.69pm and 0.76 or 0.78 to 0.90pm respectively) are generally used, and for NOAA-AVHRR, bands 1 and 2 (0.58 to 0.68pm and 0.725 to 1.10pm, respectively) are used.

Some of the energy balance components in SEBAL are difficult to estimate theoretically. Vegetation indices such as Normalized Difference Vegetation Index (NDVI), Soil Adjusted Vegetation Index (SAVI) and Leaf Area Index (LAI) give a general idea of land surface and near land surface conditions. These indices are applied in modified SEBAL, to help empirically estimate the energy balance components.

3.5.4.1   Normalized difference vegetation index (NDVI)

NDVI was developed by Tucker in 1979, and has been the most popular Vegetation Index:

$$NDVI = \frac{IR - R}{IR + R} \qquad\qquad \ldots\ldots(3.26)$$

Where:

IR is near infrared band and *R* red band, that mean the reflectance's of bands 4 and band 3 of Landsat TM/ETM+ and reflectance's of bands 2 and 1 of NOAA-AVHRR computed in Equation 3.26.

The *NDVI* values used in modified SEBAL are derived using reflectance's that are corrected for atmosphere.

3.5.4.2   Soil adjusted vegetation index (SAVI)

Huete et al. (1985) found that at intermediate levels of vegetation cover, significant scattering and transmission of near infrared flux through the canopy produces a soil-reflected spectral signal that strongly resembles vegetation spectral signatures. This soil-induced influence depends on soil moisture content, and roughness and can hinder the detection of the actual vegetation condition.   After analyzing a series of vegetation isolines in near infrared-red wavelength space, Huete (1988) found that a shifting of the origin of the reflectance spectra will account for first order soil-vegetation interactions and he proposed a soil adjusted vegetation index:

$$SAVI = \left(\frac{IR - R}{IR + R + L} \right) \times (1 + L) \qquad \qquad \ldots\ldots(3.27)$$

Where

L is an adjustment factor, for very low vegetation densities $L=l$, intermediate vegetation densities $L=0.5$, and higher density $L=0.25$. Huete also stated that a single value of $L=0.5$ can reduce soil noise considerably throughout the range in vegetation densities.

3.5.4.3 Leaf Area Index (LAI)

Leaf Area Index (LAI) is the cumulative area of leaves (one side) per unit area of land at nadir orientation, and is commonly used in agricultural science. In remote sensing, LAI is often estimated from SAVI, for example using the form by Bastiaanssen (1998):

$$LAI = \frac{\ln\left(\frac{c_1 - SAVI}{c_2} \right)}{c_3} \qquad \qquad \ldots\ldots(3.28)$$

where c_1, c_2 and c_3 are empirical constants.

Bastiaanssen (1998) has reviewed many VIs include NDVI, SAVI, and LAI. Also, Huete et al. (1997) reported the results of comparison of many VIs.

3.5.5   Thermal infrared surface emissivity (ε_o)

Emissivity of an object is the ratio of the energy radiated by that object at a given temperature to the energy radiated by a blackbody at the same temperature. Since the thermal radiation of the surface is observed in the TM thermal band (band 6) the surface temperature can be computed from band 6 if the emissivity of the land surface is estimated.

In SEBAL, surface emissivity is estimated using NDVI and an empirically-derived method:

$$\varepsilon_o = 1.009 + 0.047 \ln(NDVI) \qquad \qquad \dots\dots(3.29)$$

Where:

NDVI > 0. Otherwise, emissivity is assumed to be zero (for example, for water).(Ref. Van de Griend and Owe (1993))

3.5.6   Surface temperature (T_S)

3.5.6.1   Surface temperature (T_S) from landsat satellite images.

In this step, surface temperature is estimated by Band 6 (thermal band). The Stefan-Boltzman law explains the relationship between temperature and radiation of an object:

$$B = sT^4 \qquad \qquad \textbf{......(3.30)}$$

Where:

B is radiation from a black body, s is the Stefan Boltzman constant $5.67 * 10^{-8}$ (W m^{-2}/K^4), and T is surface temperature of a black body.

However, the thermal band of Landsat TM is too narrow to use as a representation of B in equation 3.30. The range of the radiation used in the Stefan Boltzman relationship is 3.0 – 300 µm, and the range of TM band 6 is 10.4 – 12.4 µm. Therefore, SEBAL uses the Plank equation which is given in the following equation:

$$B_\lambda = \frac{2\pi h c^2}{\lambda^5 \times \exp\left(\frac{hc}{k\lambda T}\right) - 1}$$ ......(3.31)

where

B_λ is intensity of radiation which has a wave length λ ($W\ m^{-2}$),

h is the Plank constant $6.626*10^{-34}$ Js, c is speed of light $2.998*10^8$ m s^{-1},

k is Boltzman constant $1.381*10^{-23}$ J/K,

T is surface temperature of the black body in K.

From equation 3.31, the following equation is derived with a modified Plank constant for TM band 6 from Landsat 5 (coefficients for Landsat 7 are different):

$$T = \frac{1261}{\ln\left(\frac{60.8}{L6} + 1\right)\varepsilon_o^{0.25}}$$ ......(3.32)

where, $L6 = 0.0056322DN + 0.1238$ ......(3.33)

DN is a digital number of band 6 (Wukelic,et al., 1989, for equation 3.31 and 3.32)

Surface temperature T_s is then calculated by T and ε_o with the following equation:

$$T_S = \frac{T}{\varepsilon_o^{0.25}}$$ ......(3.34)

From the equation 3.31 to 3.32, the surface temperature T_s can finally be calculated for Landsat.

3.5.6.2 Surface temperature (T_S) from NOAA-AVHRR satellite images.

The surface temperature from NOAA-AVHRR image was estimation in this section, after (Chemen and Ahmed ,2000) the surface emissivity image processed from NDVI as equation 3.29. Linear calibrations of the Band 4 and 5 are included in the import procedure of ERDAS Imagine.

Calculation of the surface temperature through the standard split-window technique should go through these inverse-Planck functions per band (POD Guide, 1998):

$$T_{b6}{}^{TOA} = \frac{1.4388 \times \lambda_4}{\ln\left(\dfrac{(1.1910 \times 10^{-5}) \times \lambda_4}{B4} + 1\right)} \qquad \ldots\ldots(3.35)$$

$$T_{b5}{}^{TOA} = \frac{1.4388 \times \lambda_5}{\ln\left(\dfrac{(1.1910 \times 10^{-5}) \times \lambda_5}{B5} + 1\right)} \qquad \ldots\ldots(3.36)$$

With:

$T_{bi}{}^{TOA}$ is the Top of Atmosphere brightness temperature for band i *(K)*

B_4 is the digital number corrected linearly   (cm^2 *Sr m mW)*

λ_5 is the specific 290-330 K central wavelength (i.e. NOAA 14 = 929.5878) *(cm^{-1})*

The split-window equation for the Skin Surface Temperature without emissivity correction (considered as "A" in the following) is after Coll and Caselles, (1997):

$$T_S = [\ \frac{(A)^4}{\varepsilon_o}\ ]^{0.25} \qquad \ldots\ldots(3.37)$$

With

$$A = [0.39 \text{ x } (T_{b4}^{TOA})^2] + (2.34 \text{ x } T_{b4}^{TOA}) - (0.78 \text{ x } T_{b4}^{TOA} \text{ x } T_{b5}^{TOA}) -$$
$$(1.34 \text{ x } T_{b5}^{TOA}) + [0.39 \text{ x } (T_{b5}^{TOA})^2] + 0.56 \qquad \ldots\ldots(3.38)$$

With:

T_s is the surface temperature estimation *(K)*

$T_{bi}{}^{TOA}$ is the Top of Atmosphere brightness temperature for band *i (K)*

ε_o is the surface emissivity *(-)*

3.5.7 DEM adjusted temperature ($T_{S\text{-}DEM}$)

Apparent Surface Temperature for a Reference Elevation for calculating of sensible heat flux, generally, air temperature decreases $6.5C^{o}$ when elevation increases by 1 km under neutral stability conditions. Since surface temperatures are in strong equilibrium with air temperature, one can usually observe similar decrement in surface temperature. In the prediction of the surface-to-air temperature difference (*dT*) during estimation *H*, SEBAL assigns a value for *dT* as a function of surface temperature.

However, the surface temperature that is used needs to be uniformly adjusted to a common reference elevation for accurate prediction of *dT*. Otherwise, high elevations that appear to be "cool" may be misinterpreted as having high evaporation. Therefore, in this step, a "lapsed" (and artificial) surface temperature map is made for purposes of computing surface-to-air temperature differences by assuming that the rate of decrease in surface temperature by the orographic effect is the same as that for a typical air profile. Elevation data are taken from SRTM, Digital Elevation Model (DEM) data. The "fictitious" lapse-adjusted surface temperature is referred to as a DEM corrected surface temperature.

The DEM corrected surface temperature is calculated using the following equation;

$$T_{S-DEM} = T_S + 0.0065 \Delta z \qquad \qquad \text{......(3.39)}$$

Where:

Δz is the difference of a pixel's elevation from the datum in meters. The term Δz is positive if the elevation of a pixel is higher than the datum.

3.6 Determination of radiations

3.6.1. Net radiation (R_n)

Net radiation is given by the surface radiation balance by the following equation:

$$R_n = (1-\alpha)R_{s\downarrow} + \varepsilon\ R_{L\downarrow} - R_{L\uparrow} \qquad \ldots\ldots(3.40)$$

Where:

R_n is the net radiation $(W\ m^{-2})$ which is the net energy gained by the Earth surface,

$R_{s\downarrow}$ is incoming shortwave radiation (=solar radiation) reaching the earth's surface ($W\ m^{-2}$), α is the Albedo at the surface, ε is broad-band emissivity of the surface,

$R_{L\downarrow}$ is incoming longwave radiation reaching the surface,

$R_{L\uparrow}$ is outgoing longwave radiation emitted from the surface

In Equation 3.40, Albedo is the ratio of reflected shortwave radiation to incoming solar radiation at the surface, and broad-band emissivity is the ratio of the energy radiated by the land surface at a given temperature to the energy radiated by a blackbody (which is the perfect emitter) at the same temperature. In modified SEBAL, $R_{s\downarrow}$ is measured or empirically estimated, and a, ε, $R_{L\downarrow}$ and $R_{L\uparrow}$ are estimated from satellite image data. Figure 3.4 shows a breakdown of radiation balance at the earth's surface.
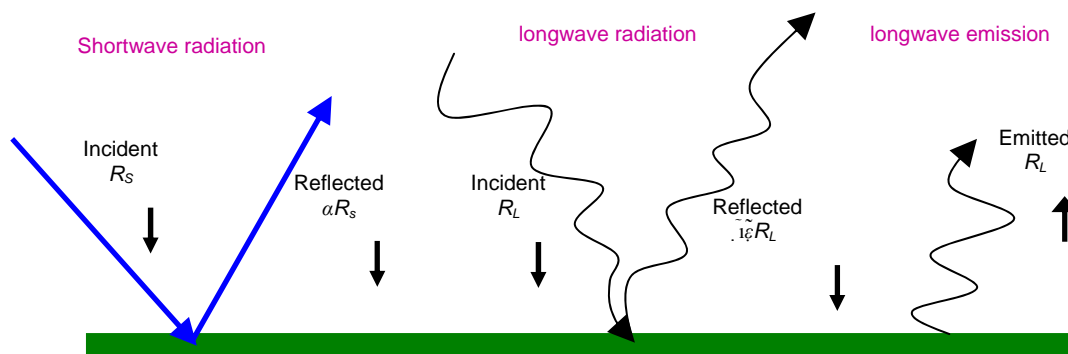
Figure 3.4   Radiation balance at the earth's surface

3.6.1.1   Shortwave radiation (R_s)

The incoming short wave radiation ($R_s\downarrow$) in equation 3.41, is predicted, assuming cloud-free conditions, in this study as follows (Fu 1998, Tasuni et al. 2000) in which the diffuse radiation was neglected:

$$R_{s\downarrow} = \frac{G_{sc}}{d_r^{\,2}} \cos\theta \times \tau \qquad \qquad \ldots\ldots(3.41)$$

where G_{sc} is the solar constant (1367 W m^{-2}), d_r is the relative Earth-Sun distance (dimensionless) given by equation 3.10, cosθ is the cosine of the solar zenith angle calculated by equation 3.11. In the sloping and mountainous terrain areas (as in the present study) the solar incident angle changes with surface slope and aspect. Therefore the equation suggested by Duffie and Bekman,(1991) is applied. The equations are 3.13and 3.17 and τ is a one-way transmittance.

3.6.1.2   Longwave radiation (R_L)

In Equation 3.42, the Stephan Boltzman equation is applied for long wave components $R_{L\downarrow}$ and $R_{L\uparrow}$.

$R_{L\downarrow}$ is calculated by the following equation from Bastiaanssen et al. (1998a) for cloud-free conditions:

$$R_{L\downarrow} = \varepsilon_a s T_a^4 \qquad\qquad \text{......(3.42)}$$

where,

$$\varepsilon_a = 1.08\ (-\ln\ \tau_{sw})^{\ 0.265} \qquad\qquad \text{......(3.43)}$$

T_a is the surface temperature at a reference point, generally selected to be a well-watered pixel so that surface temperature and air temperature are similar.

Since $R_{L\uparrow}$ is the long wave radiation from the surface, it is calculated by applying Equations 3.44:

$$R_{L\uparrow} = \varepsilon_o s T_s^4 \qquad\qquad \text{......(3.44)}$$

However, in equations 3.41 to 3.44, surface reflectance of incoming long wave radiation is not taken into account. This reflectance is estimated as $(1 - \varepsilon_o)\ R_{L\downarrow}$. Therefore, Equation 3.40 becomes:

$$R_n = (1- a)\ R_s{\downarrow} + (R_L{\downarrow} - R_L{\uparrow}) - (1 - \varepsilon_o)\ R_L{\downarrow} \qquad\qquad \text{......(3.45)}$$

3.6.2 Soil heat flux (*G*)

Ground heat flux *G* is given by the soil heat conduction as equation:

$$G = \lambda_s \left(\frac{\partial T_s}{\partial Z} \right) \qquad\qquad \text{......(3.46)}$$

Where:

T_s is the temperature of the soil and

λ_s is the thermal conductivity of the soil.

Z is the depth in the ground.

G is dependent on soil moisture and the amount of vegetative cover (figure3.5) thus the ground-based measurements of the soil heat flux cannot be extrapolated to large

areas. In the energy budget equation, the soil heat flux utilizes a very small quantity of available energy during daytime and this is almost balanced with night-time radiation loss.

Figure3.5.   Soil Heat Flux (G)

An alternative approach to calculate soil heat flux from remote sensed data is to make it proportional to another term in the energy balance equation. Indeed, many researchers (Choudhury et al., 1986; Reginato et al.. 1985; Idso et al., 1975), have indicated that the magnitude of G is highly related to the net solar radiation. R_n. Idso et al. (1975) found that the ratio of soil heat flux to net solar radiation is about 0.5 for dry soils and 0.3 for wet condition for vegetation surfaces under full cover. Monteith (1973) suggested values for the ratio would most likely be between 0.05 and 0.1. Reginato et al. (1985) reported that the soil heat flux was approximately 10% of net radiation for bare soil and sparse canopies and less than 10% under a well developed plant canopy. The empirical relationship between G/R_n, and crop height, h, obtained by Reginato et al. (1985) as equation:

$$G = (0.1 - 0.042h)R_n \qquad \qquad ……(3.47)$$

Choudhury et al. (1986) expressed the ratio as an exponential function of leaf area index (*LAI*) yielding a correlation of 0.9. For regional energy balance studies, typically little information about crop height and leaf area is available. In this case, the fore mentioned two methods cannot be directly applied to the calculation of G by remote sensing methods. However, there are indications that remote sensed vegetation indices may be a good replacement for plant phytomass, leaf area index and percent cover (Holben et al., 1980; Ormsby et al., 1987; Price, 1992). In fact, Kustus et al. (1990)

obtained a linear relationship between G/R_n, and the normalized difference vegetation index (*NDVI*) from observations of different vegetation types and soil surface conditions.

$$G = (0.325 - 0.208 NDVI) R_n \qquad \qquad ......(3.48)$$

Soil heat flux is usually measured with sensors buried just beneath the soil surface. A remote measurement of G is not possible but several studies have shown that among other factor the day time ratio of G/R_n is related to the amount of vegetation present Bastiaanssen (2000) proposed G as an empirical fraction of the net radiation using surface temperature, surface Albedo (α) and *NDVI* and was adopted in this study to compute G as:

$$G = R_n \left(\frac{T_s}{\alpha} \right) * \left(0.0038 \, \alpha + 0.0074 \, \alpha^2 \right) * \left(1 - 0.98 \, NDVI^4 \right) \qquad ......(3.49)$$

Where

T_s is the surface temperature, α is the Albedo, *NDVI* is the normalized difference vegetation index.

3.6.3 Sensible heat flux (*H*)

Sensible heat flux (*H*) is the energy which is directly transferred to the air via convection. Similar to the ground heat flux (*G*), sensible heat flux is generated by a temperature gradient, but in this case between the earth's surface and air:

$$H = \frac{\rho_{air} c_p dT}{r_{ah}} \qquad \qquad ......(3.50)$$

Where

ρ_{air} is air density (kg/m3) which is a function of atmospheric pressure, c_p is the heat capacity of air (1004 J/kg/K), r_{ah} is aerodynamic resistance to heat transport (s/m), and dT is explained in SEBAL as $(T_1 – T_2)$ where T_1 and T_2 are air temperatures at heights z_1 and z_2 above the zero plane displacement height in Kelvin (See. Figure 3.6).
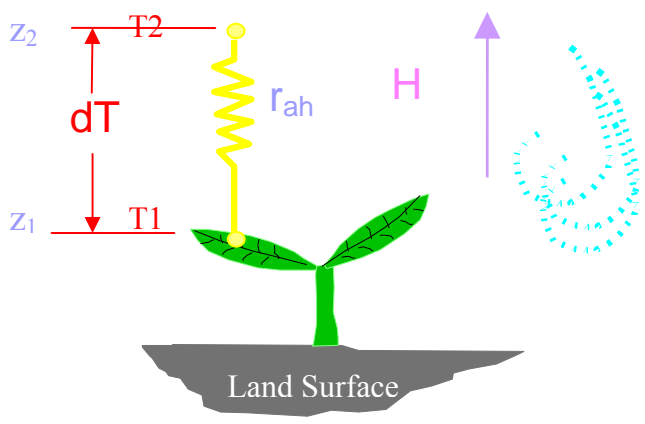
Figure 3.6 Sketch of aerodynamic heat transfer (Allen, 2005)

3.6.3.1   The aerodynamic to heat transport (r_{ah})

The aerodynamic resistance to heat transport (r_{ah}) between z_1 and z_2 is calculated using the following equation:

$$r_{ah} = \frac{\ln\left(\dfrac{z_2}{z_1}\right)}{u^* \times k} \qquad \ldots\ldots(3.51)$$

Where

z_1 and z_2 are the two heights (m) given in the Figure 3.6, u^* is friction velocity (m/s), and k is von Karman's constant (= 0.41).

3.6.3.2 The friction velocity (u*)

The friction velocity ($u*$) in Equation 3.52 is given as:

$$u* = \frac{ku_x}{\ln\left(\dfrac{z_x}{z_{om}}\right)} \qquad \ldots\ldots(3.52)$$

Where

z_x is a height above surface in meters (e.g. 2m), u_x is windspeed (m/s) at height z (m), and z_{om} is surface roughness for momentum transport (m).

As shown in Equation 3.52, windspeed and surface roughness values must be assigned "pixel by pixel", to calculate the friction velocity with spatial variation. SEBAL estimates a pixel based value for friction velocity by extrapolating downward from a common value for windspeed determined at a blending height at around 200 m where it is assumed that windspeed is independent of the surface roughness by equation 3.53. The windspeed of the blending height is extrapolated upward from an observed windspeed at a weather station then assigned "pixel by pixel" using the equation 3.54.

$$u_{200} = u^* \frac{\ln\left(\dfrac{z_{200}}{z_{om}}\right)}{k} \qquad \ldots\ldots(3.53)$$

$$u^* = \frac{ku_{200}}{\ln\left(\dfrac{z_{200}}{z_{om}}\right)} \qquad \ldots\ldots(3.54)$$

3.6.3.3   Surface roughness for momentum transport (z_{om})

Surface roughness for momentum transport (z_{om}) is defined as the height above the zero-plane displacement height, d, where the zero-origin for the wind profile just begins to show for a surface or vegetation cover visualized in Figure 3.7.

This z_{om} is very difficult to estimate by Landsat or NOAA-AVHRR images. The general estimation equation for agricultural areas has been presented by Allen et al. (1996).

$$z_{om} = 0.12h \qquad\qquad ……(3.55)$$

Where

z_{om} is in meters, and h is crop height in meters.

Alternative method to estimate z_{om} by correlating with *NDVI* has been described in Bastiaanssen et al. (1998a) , Tasumi et al., (2000a) and Tasumi ., (2003).

3.6.3.4   Surface Roughness for Momentum Transport in Mountains

In modified SEBAL, the impact of terrain on aerodynamic roughness is empirically adjusted by estimating a sort of "geometrical" z_{om} for mountain areas. There are two main reasons to correct z_{om} for sloped terrain especially in mountain areas: (1) acceleration of windspeed is generated when a vertical component of movement is created by the land surface (Oke, 1987), and (2) sloping surfaces have a larger land surface area for a unit pixel (horizontal 30mx30m pixel), and therefore, the process of heat transportation by wind is enhanced.

The following equations were developed assuming that z_{om} increases 10% for every 10° of surface slope increment. This adjustment is applied only where the surface slope is 5° or more.

$$z_{om\_adj} = c_{zom}.z_{om\_adl} \qquad\qquad ......(3.56)$$

Where:

$z_{om\ -adj}$ is the adjusted z_{om} that accounts for geometrical roughness (m), z_{om} unmade is z_{om} unadjusted for the geometrical roughness (m), c_{zom} is a coefficient calculated as:

$$c_{zom} = 1 + \frac{S-5}{20} ....(Slope > 5°) \qquad\qquad ......(3.57)$$

Where:

S is surface slope in degrees.

Surface roughness for momentum transport (z_{om}) is defined as the height above the "zero-plane displacement" that the zero-origin for the wind profile just begins within the surface or vegetation cover.

In modified SEBAL, surface roughness is estimated from *NDVI* using an empirical equation:

$$z_{om} = \exp(a \times NDVI) + b \qquad\qquad ......(3.58)$$

Where:

a and b are constants.

The constants a and b are derived by values of *NDVI* and z_{om} for sample pixels representing specific vegetation types.

The following conditions were considered in selection of the heights z_1 and z_2.
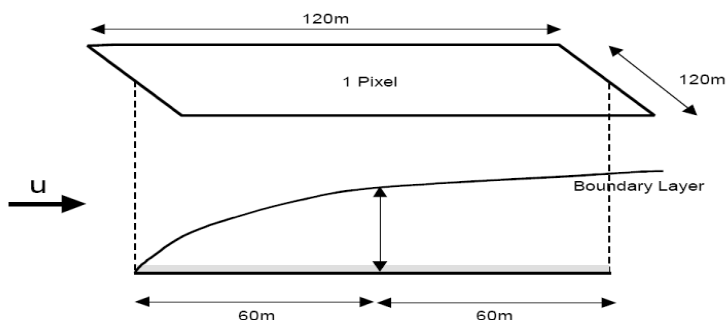
Figure 3.7.　　Boundary layer (Tasumi et al., 2000a)

As shown in Figure 3.7, a boundary layer develops above the land surface downwind of each change in surface characteristics. The information from TM band 6 only indicates

the environment of the surface that is operating below the boundary layer. The height of the boundary layer is assumed to be 0.01 to 0.02 of the distance (fetch) from the beginning of a change in vegetation in a downwind direction. (e.g. if the fetch is 60m, the height of the boundary layer is 0.6 m to 1.2 m). In this situation, the boundary layer height tends to be higher when the surrounding pixels have similar vegetation and water-status environment.

Ideally, heights z_1 should be defined as being just above the mean height of the crop canopy, and height z_2 should be defined as being just below the height of the boundary layer. For consistency of the calculation, z_1 and z_2 are assigned values of 0.01 m and 2.0 m respectively. The value of rah is calculated using Equation 3.51 based on these two heights.

3.6.3.5   Correct of Friction velocity (u^*)

The friction velocity u^* is an index that explains the intensity of the turbulence of air. If u^* value is high (which means that the intensity of turbulence is strong), the resistance r_{ah} becomes smaller and H becomes larger, since surface energy is transferred to the air more effectively by the strong turbulence.

The value of u^* can be calculated with the Equation 3.52, but only at the location of the weather station where observed windspeed data are available. SEBAL estimates u* for each pixel by employing an assumption that windspeed at some blending height at about 200 m above the land surface is uniform over an image. By accepting this assumption, u^* for each pixel can be estimated using the procedure shown in Figure 3.8 (1) First, estimate u* at the weather station (weather station does not necessarily have to be within an image) sing Equation 3.52 with the height z as the wind measurement height, (2) calculate windspeed at 200 m using the inverse of Equation 3.53 with $z =$

200 m, assuming that u* is constant with height over the weather station. The calculated windspeed at the 200 m blending height is assumed to be applicable for the entire image. Then, (3) calculate u* for each pixel by Equation 3.54 using z_{om} values for each pixel, and assuming that u* based on the z_{om} at a pixel is constant between the surface and 200 m.

1. Estimation u* at the weather station using measured wind speed (at 2m) and $z_{om.}$
2. Estimate u* at 200 m above the wither station and assume u_{200} is constant over the image
3. Estimate u* for each pixel from u_{200} using a z_{om} image.
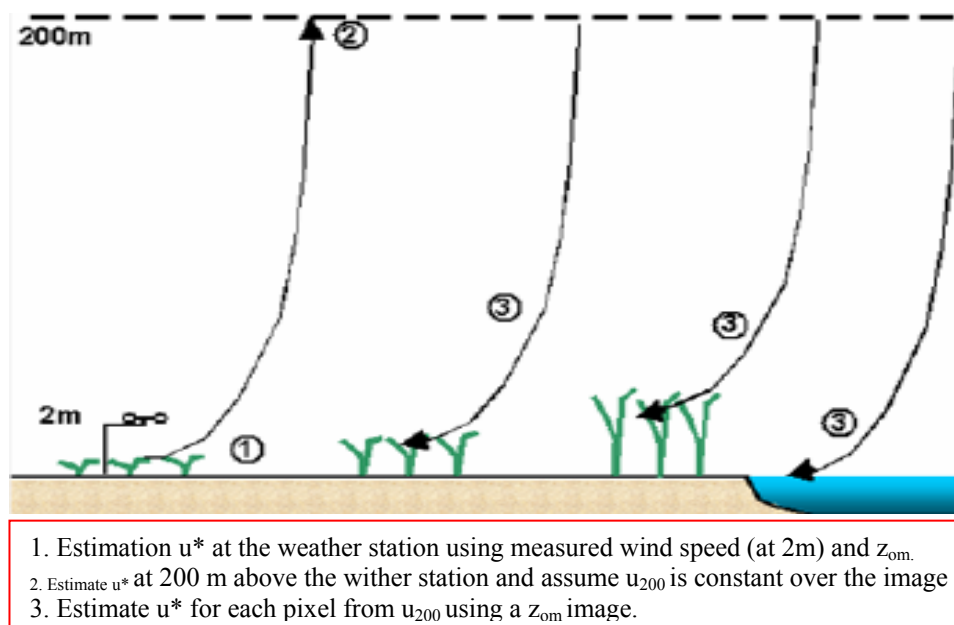
Figure 3.8   The friction velocity ($u*$) estimation procedure in SEBAL

The assumption of constant wind speed at 200 m would probably not be true in mountainous regions where Venture effects tend to increase the average windspeed (Oke, 1987). Therefore, in modified SEBAL, we attempt to adjust the average windspeed using elevation:

$$u_{200\_ADJ} = c_{wind} . u_{200\_unadj} \qquad ......(3.59)$$

Where:

u_{2oo_ADJ} is windspeed at 200 m height (m s^{-1}) adjusted by accounting for effects,

u_{2oo_unadj} is windspeed at 200 m (m s^{-1}) above the weather station, and c_{wind} is the adjustment coefficient calculated by:

$$c_{wind} = 1 + 0.1 \frac{z - z_{station}}{1000} \qquad ......(3.60)$$

Where:

z (m) and $z_{station}$ (m) are elevations for each pixel and for the weather station where windspeed is measured. Equation 3.60 presumes a 10% increase in windspeed for each 1000 m gain in elevation (Tasumi , 2003).

3.6.3.6 Temperature difference near surface (*dT)* function and "cold/hot pixel"

The temperature difference between z_1 and z_2 is predicted in order to estimate H from Equation 3.50. In the Equation 3.50, *H* and *dT* are both unknown factors, but are directly related to one another, and also the value for r_{ah}.

$$dT = \frac{H \times r_{ah}}{\rho_{air} Cp_{air}}$$

......(3.61)

Therefore, during the SEBAL process, *dT* can be calculated at two extreme "indicator" pixels (endpoints) by assuming values for *H* at the reference pixels. The reference pixels are carefully chosen so that, at these pixels it can assume that, *H = 0* at a very wet pixel (i.e., all available energy *(R_n – G)* is converted to ET), and that $\lambda(ET_{ins})= 0$ at a very dry pixel, so that *H = R_n – G.* These assumptions from the selected pixels provide endpoints for values and locations for *H,* so that a relationship for *dT* can be established.

The selection of the wet and dry pixels is somewhat subjective, but necessary to solve the energy balance.

The selection of wet and dry pixels where *ET = R_n – G* and where *H = R_n - G* is easier compared to pixels that lie in between these endpoints, since conditions favoring these two endpoints are generally straight-forward to identify.

Under conditions of similar available energy *(R_n – G),* a wet pixel will have a lower temperature than a dry pixel. The lower the temperature, relative to other pixels, the more likely that *ET* approaches *Rn – G* so that *H* approaches *0.* Therefore, to find a very

wet pixel, one should search for the coldest pixel that is located in an agricultural setting (if possible). The assessment should be done using the DEM adjusted surface temperature image so that lapse effects do not mask the wet pixels see figure 3.9 "cold/hot pixel" estimation.
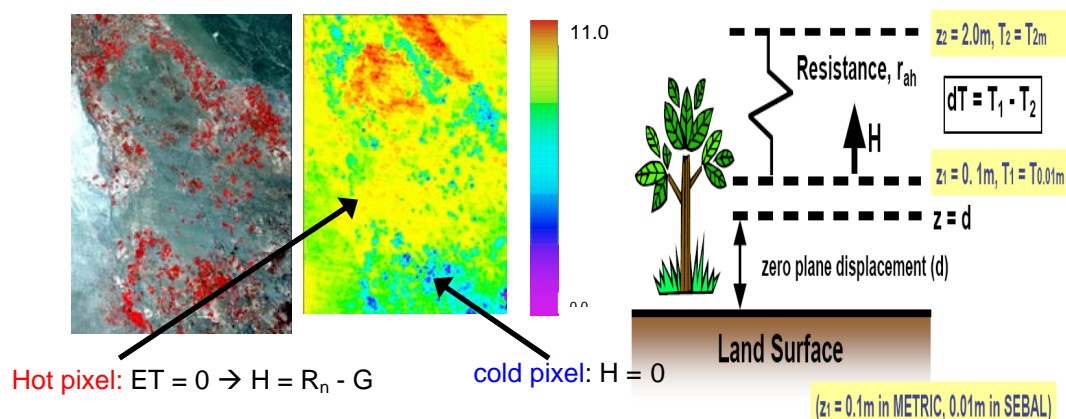
Figure 3.9   The *dT* function and "cold/hot pixel" estimation procedure in SEBAL

The value of *dT* is presumed to be zero at the wet pixel (T_{cold}). This assumption is generally true in a wide range of climates, except perhaps, in extremely arid regions where regional advection of sensible heat energy into irrigated projects can cause ET to exceed *Rn – G*. This results in negative values for H, since according to Equation 3.66, dT may become negative. If this type of highly adjective situation is known to occur, then the SEBAL user can make an assumption concerning the ratio of *ET/(Rn-G)* at the "wet" pixel and can then determine H and subsequently dT for the pixel. In the winter time, the coldest pixel might be below 273K (0 C°). However, the coldness may not necessarily indicate wetness, but is from being snow covered, or from the ground being frozen. In such situations, a very wet pixel might have a surface temperature during midmorning (during the Landsat overpass) and under sunlit conditions of approximately 273.1 K. Since the DEM corrected surface temperature is not the actual temperature, but a fictitious lapse corrected temperature, the actual surface temperature *T* must also be referred to in order to judge the actual, underlying conditions and relative wetness.

It is often more difficult to find a very dry pixel at which one can assume $\lambda(ET_{ins})$ is zero. This is especially difficult in a semi humid or humid climate having substantial

rainfall since even bare soil has some evaporation flux. Additionally, since the driest pixel has a large value for dT as compared to the coldest pixel in SEBAL, a good estimation is required. As an initial guess, a very hot pixel is a good sample for locating the driest place within the image. Within the hotter pixels, man-made places such as airports or highways are more likely to be dry than a naturally vegetated location or location having bare soil. Man-made surfaces are less desirable than natural or agricultural surfaces because of larger uncertainties in the estimate for G and aerodynamic transport. A steeply sloped place should be avoided due to uncertainties in total energy. One can refer to the DEM adjusted surface temperature in the very dry pixel selected as T_s hot.

The UTM coordination of the driest pixel must be recorded since they are required later. Once the driest pixel is identified, the value of H at the pixel is calculated from the values of R_n and G in the R_n and G images since $H = R_n - G$ for the pixel. Then dT of the pixel can be calculated with the equation 3.61 assuming an initial value for aerodynamic resistance, r_{ah} .

In SEBAL, it is assumed that dT has a linear relation to T_s at all pixels:

$$dT = aT_s + b \qquad\qquad ……(3.62)$$

Where:

a and b are calibration constants.

The constants a and b must be determined in equation 3.62, using the T_s and dT values of the wettest and the driest pixels that have been chosen for the image.

Once dT is determined, H is calculated by Equation 3.50. However, the result is only a preliminary estimation.
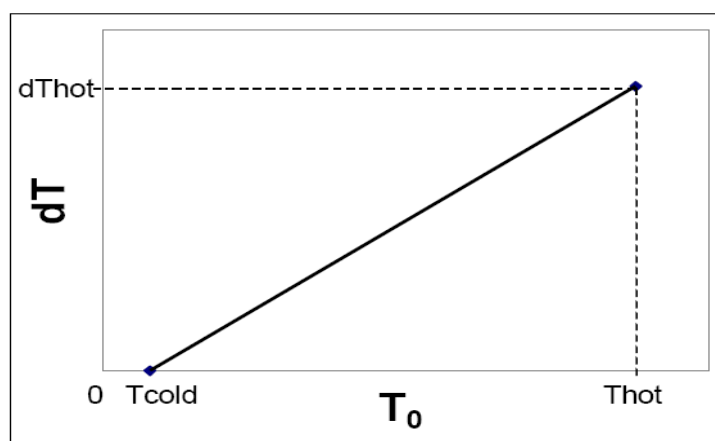
Figure 3.10 Concept of dT (temperature difference between surface and air) prediction in SEBAL

3.6.3.7 Atmospheric Stability corrections for momentum and heat transport

Air has three stability conditions; unstable, neutral, and stable. Stability conditions must be considered during the computation of sensible heat flux (H) since they affect the aerodynamic resistance to heat transport (r_{ah}). In SEBAL, stability corrections are applied using the Monin-Obukhov length (L) as the parameter.

The three stability conditions are illustrated in Figure 3.11 taken from Kondo (2000) and Tasumi (2003). Generally, air temperature decreases by about 6.5 C° when elevation increases by 1 km under neutral stability conditions (i.e., 0.65C° per 100m). In the places where positive sensible heat flux (H) is available, the decrement of temperature with elevation becomes smaller since the air mass is heated by positive H. In this condition, vertical air movement is easier and therefore aerodynamic resistance becomes smaller as H becomes higher. This condition is called an "unstable" condition

Figure 3.11. In general, air is in a neutral condition over a well-watered agricultural field and in an unstable condition over a dry surface at noon-time. The stable condition will most likely occur at night and sometimes in the afternoon over irrigated areas surrounded by desert. The details of stability corrections equations are described below.
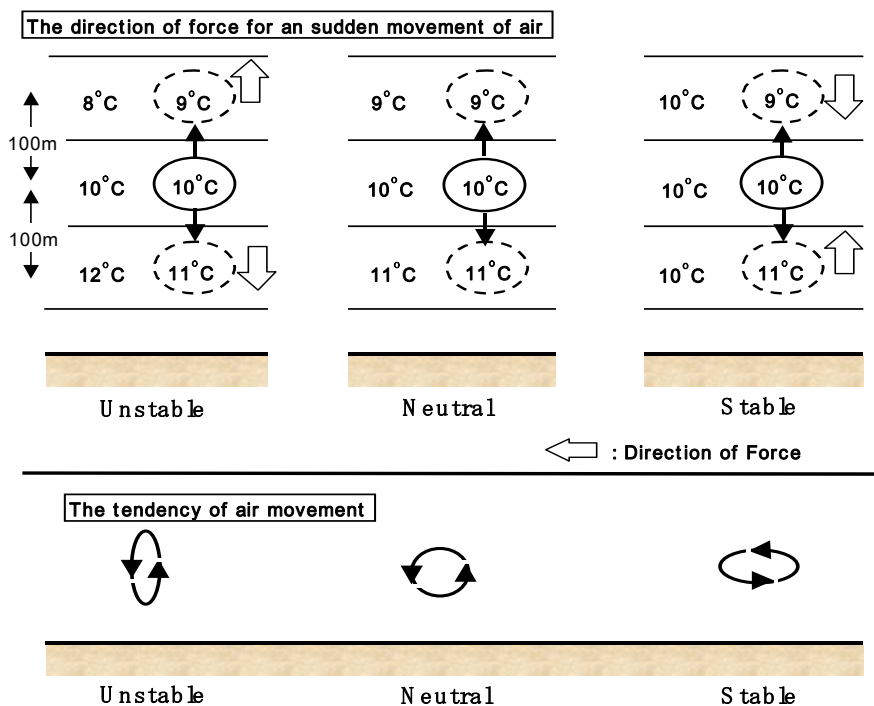
Figure 3.11 . Stability condition Correction after (Kondo, 2000).

SEBAL must internally repeat the calculation of *H* at least five times, as explained in this section this step is necessary there is a need to employ corrections to the estimates for r_{ah} due to instability (buoyancy) effects within the lower atmosphere caused by surface heating Figure 3.12.

In the steps of repeating the calculation of *H*, the Monin-Obukov method is applied to estimate updated values for r_{ah}. The stability corrected r_{ah} is calculated as:

$$r_{ah} = \frac{\ln\left(\dfrac{z_2}{z_1}\right) - \psi_{h(z2)} + \psi_{h(z1)}}{u^* k} \qquad \ldots\ldots(3.63)$$

Where:

z_1 and z_2 are the two heights (m) given in the Figure 3.7 , k is von Karman's constant (=0.41), u^* is friction velocity (m/s), ψ_h is the stability correction factor for atmospheric heat transfer for two heights, where $\psi_{h(z1)}$ is ψ_h for the height z_1 and $\psi_{h(z2)}$ is ψ_h for the height z_2.

In the application of SEBAL, the component $\psi_{h(z1)}$ is ignored since the value is very small. Therefore, Equation 3.51 is modified as:

$$r_{ah} = \frac{\ln\left(\dfrac{z_2}{z_1}\right) - \Psi_{h(z_2)}}{u_* \times k}$$

......(3.64)

In equation 3.52, an updated value for u^* is computed during each successive iteration and for each pixel as;

$$u^* = \frac{u_{200}k}{\ln\left(\dfrac{200}{z_{om}}\right) - \Psi_{m(200m)}}$$

......(3.65)

Where

u_{200} is wind speed at 200 (m) if a different height is used for the reference wind speed, then the wind speed at the reference height must be specified in Equation 3.65 instead of 200 (m), z_{om} is surface roughness for momentum transport (m), $\psi_{m(200m)}$ is stability correction factor for atmospheric momentum transport for height 200m.

The stability correction factor for atmospheric heat transfer ψ_h is calculated for negative values of L (i.e., for unstable conditions) as:

$$\Psi_{h(Z2)} = 2\ln\left(\frac{1 + x_{(z_2)^2}}{2}\right)$$

......(3.66)

Where

$x_{(z2)}$ is a parameter (x) based on the z_2 height. The value for x is defined in Equation 3.70. For nonnegative values for L, the equation for stable conditions is:

$$\Psi_{h(Z2)} = -5\left(\frac{z_2}{L}\right)$$

......(3.67)

The stability correction factor for atmospheric momentum transport ψ_m is defined for $L < 0$ (unstable boundary layer) as:

$$\psi_{m(200m)} = 2\ln\left(\frac{1+x_{(200m)}}{2}\right) + \ln\left(\frac{1+x_{(200m)^2}}{2}\right) - 2ARCTAN(X_{200M}) + 0.5\pi \quad \ldots(3.68)$$

Where

x is defined in Equation 3.70. As for stable conditions $(L = 0)$, the equation is:

$$\psi_{m(200m)} = -5\left(\frac{z_2}{L}\right) \quad \ldots\ldots(3.69)$$

Where

The *200m* represents the elevation height where u_{200} is calculated.

The x used in Equations 3.66 and 3.68 is calculated for $L < 0$ as:

$$x_{(height)} = \left[1 - 16\frac{(hieght)}{L}\right]^{0.25} \quad \ldots\ldots(3.70)$$

Where

(height) is the corresponding height z_2 or *200m*, L is the Monin-Obukov length parameter given by equation 3.71. For $L = 0$, x(height) = 1.

The Monin-Obukov length parameter L is

$$L = -\frac{\rho_{air} Cp_{air} u^{*3} T_s}{kgH} \quad \ldots\ldots(3.71)$$

Where

ρ_{air} is air density in kg m^{-3}, Cp_{air} is heat capacity of air (= 1004 J/kg/K), T_s is in K, k is von Karman's constant (=0.41), g is gravitational acceleration (= 9.81 m s^{-2}), H is sensible heat flux in W m^{-2}.
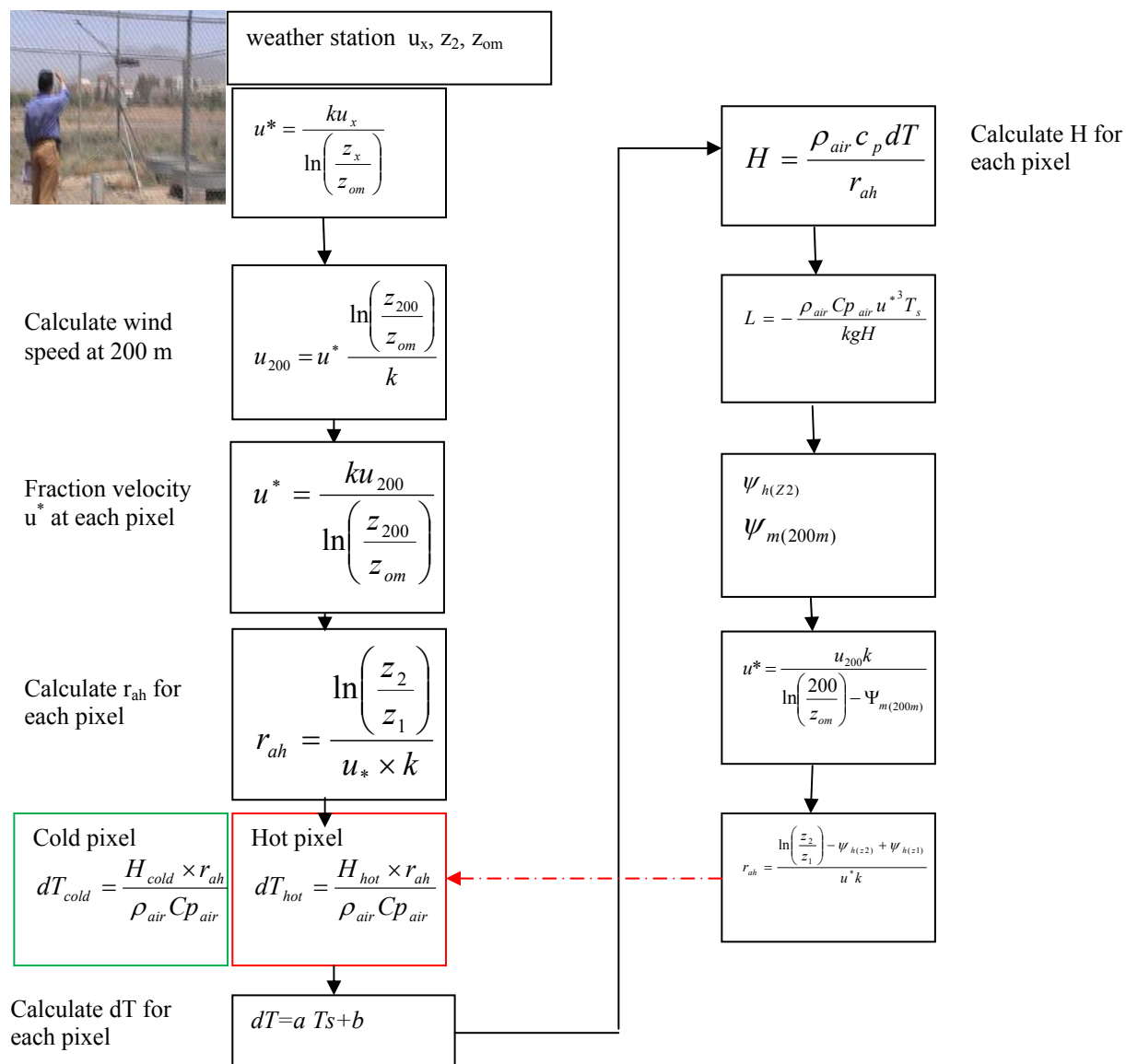
Figure 3.12   Iterative Process to Compute H

3.7   Evaporative fraction, EF and Latent heat flux $\lambda(ET_{ins})$

3.7.1   Evaporative fraction (*EF*)

Once the final (relatively stable) values for H are calculated (repeat the calculation four to five times), the latent heat flux $\lambda(ET_{ins})$ can be calculated from Equation 3.74 using values for H, G and R_n. This $\lambda(ET_{ins})$ represents the instantaneous evapotranspiration at the time of the satellite overpass.

Following the computation of the evaporative fraction (*EF*) at each pixel of the image, one can estimate the 24-hour evapotranspiration for the day of the image by assuming that the value for the *EF* is constant over the full 24-hour period. In this step, the *EF* is calculated for the instantaneous values in the image as:

$$EF = \lambda(ET_{ins}) \; / \; R_n - G_o \qquad\qquad ……(3.72)$$

Equation 3.72 can be rewritten as

$$EF = (R_n - G - H)/R_n - G \qquad\qquad ……(3.73)$$

Where the values for R_n, G and H are instantaneous values taken from processed images. Units for all flux parameters are expressed as W m^{-2}.

3.7.2   Latent heat flux $\lambda(ET_{ins})$

Latent heat flux at the satellite image time can be calculated as the residual of Equation 3.2 namely:

$$\lambda ET_{ins} = R_n\text{-}H\text{-}G \qquad\qquad \ldots\ldots(3.74)$$

Where: all fluxes are in $W\ m^{-2}$.

The calculated latent heat flux can be converted to the equivalent ET value with the Equation 3.75, using the correction for actual area difference in one pixel. As discussed in the $\cos\theta$ calculation in section 3.2.2, all energy balance calculations in modified SEBAL are conducted on a horizontal-equivalent. Therefore, the calculated $\lambda(ET_{ins})$ $(W\ m^{-2})$ is not the flux in unit watts for a square-meter of sloping surface but the flux in unit watts for an equivalent square-meter of apparent horizontal surface. This unit can be re-converted to the actual $W\ m^{-2}$ of the slope, by multiplying by the cosine of surface slope. As for calculating ET per actual unit of area, Equation 3.3 is rewritten as:

$$ET_{inst} = 3600\frac{\lambda(ET_{ins})}{\lambda} \times \cos(s) \qquad\qquad \ldots\ldots(3.75)$$

Where:

ET_{ins} is in *mm/hour*, λ is latent heat of vaporization calculated by Equation 3.4 (J/kg), *cos(s)* is cosine of land surface slope, and *3600* is the conversion from seconds per hour.

3.7.3   Twenty-four hour actual evapotranspiration estimation (ET_{24})

The 24 hour actual evaporation is calculated by the following equation:

$$ET_{24} = \frac{86400\, EF\, (R_{n24} - G_{24})}{\lambda} \qquad\qquad \ldots\ldots(3.76)$$

Where:

R_{n24} is daily net radiation, G_{24} is daily soil heat flux , *86400* is the number of seconds in a twenty-four hour period, *EF is* evaporative fraction and λ is the latent heat of vaporization (J/kg).

The latent heat of vaporization allows expression of ET_{24} in mm/day.

In equation 3.76, G_{24} can be approximated as zero for vegetative and soil surfaces at the soil surface. This is because, on average, the energy stored in the soil during the daytime is released into the air at night. The value for G_{24} of snow can also generally be approximated as zero. As for a water body, especially in deep lakes, G_{24} does not become zero because of the high heat storage capacity of water.

Assuming that the evaporative fraction (*EF*) is constant over the day the daily average sensible heat (H_{24}) can be derived from *EF* and the daily average net radiation (R_{n24}) can be calculated as follows:

$$H_{24}= (1-\ EF)\ R_{n24} \qquad\qquad \ldots\ldots(3.77)$$

This leads to the improved daily net radiation parameterization scheme and daily actual evapotranspiration.

3.7.4 Daily Net Radiation (R_{n24})

The daily net radiation can be expressed as:

$$R_{n,24} = (1-\alpha)R_{s,24} + R_{L,24} \qquad\qquad \ldots\ldots(3.78)$$

Where $R_{s,24}$ is the daily solar radiation and $R_{L,24}$ is the daily net long wave radiation (W m^{-2}).

As the terrain of our study area is complex with undulations, the impact of topography, i.e., the impact of the slope and azimuth of the surface, the available radiation should be considered pixel by pixel in the calculated instantaneous and daily net radiation, the shaded areas (pixels) were excluded from imageries with the model maker in the

ERDAS imagine software package. Through importing parameters of solar azimuth and solar elevation at the satellite overpass time. The daily net radiation is estimated by an integral of equation (3.41) transmittance for one-way transmittance τ with $(c+dn/N)$:

$$R_{s,24} = (c + d\frac{n}{N}) \int_{-\pi}^{+\pi} \left[\frac{G_{sc}}{d_r^2} a\sin\delta + b\cos\delta\cos\omega + \cos\delta\sin s\sin\gamma\sin\omega \right] d\omega$$
(3.79)

$$R_{s,24} = (c + d\frac{n}{N}) \int_{\omega 1}^{\omega 2} \left[\frac{G_{sc}}{d_r^2} a\sin\delta + b\cos\delta\cos\omega + \cos\delta\sin s\sin\gamma\sin\omega \right] d\omega$$
(3.80)

$$R_{a,24} = (c + d\frac{n}{N}) \frac{G_{sc}}{2\pi d_r^2} \left[a\sin\delta(\omega_2 - \omega_1) + b\cos\delta(\sin\omega_2 - \sin\omega_1) - \sin s\sin\gamma\cos\delta(\cos\omega_2 - \cos\omega_1) \right]$$
(3.81)

Where:

$$a = \sin\phi\cos s - \cos\phi\sin s\cos\gamma$$
$$b = \cos\phi\cos s + \sin\phi\sin s\cos\gamma$$
......(3.82)

$$N = \frac{12(\omega_2 - \omega_1)}{\pi}$$
......(3.83)

Where c and d are coefficients of the solar radiation depending on the latitude, climate and other factors of the study area, respectively; $c+d$ is the fraction of exterritorial radiation reaching the Earth on clear sky days. n is the actual sunshine duration, N the potential sunshine duration, ω_1 and ω_2 are the sunrise and sunset angle, respectively. The difficulty in retrieval of the daily solar radiation focuses on calculation of the sunrise and sunset angle for the tilted surfaces.

The sunrise and sunset angles for horizontal surfaces are given by Tasumi *et al.* (2000)

$$\omega_H = \cos^{-1}(-\tan\phi\tan\delta)$$
......(3.84)

The sunrise and sunset angle for tilted surfaces can be obtained by simple mathematical manipulation from equation (3.13) by setting cosθ=0, leading to

$$\omega = \cos^{-1}\left(\frac{-ab\tan\delta \pm \sin\gamma\sin s\sqrt{1-a^2\left(1+\tan^2\delta\right)}}{1-a^2}\right) \quad \ldots\ldots(3.85)$$

The positive or negative sign in the numerator of this equation is determined by

$$\omega = \sin^{-1}\left(\frac{-a\sin\gamma\sin s\tan\delta \pm b\sqrt{1-a^2\left(1+\tan^2\delta\right)}}{1-a^2}\right) \quad \ldots\ldots(3.86)$$

Let ω_{s1} and ω_{s2} are the roots of Eq 3.86, where $\omega_{s1} > \omega_{s2}$. Note that the surface receives the solar radiation only if *cos θ* in equation (3.13) is greater than 0. Several relationships are given below to determine the sunrise and sunset angles (ω_1 , ω_2),

- if $\omega_{s1} \leq \omega \leq \omega_{s2}$ and cosθ ≥0, then $\omega_{s1} \geq \omega_{s2}$, $\omega_{s2} \leq \omega_{s1}$;

- if $\omega \leq \omega_{s1}$, $\omega_{s1} > \omega_{s2}$ and cosθ>=0 then $\omega_1 \leq \omega_{s1}$,$\omega_2 \geq \omega_{s2}$.

- Meanwhile, the sunrise and sunset angles for tilted surfaces must also satisfy the condition that sunrise is no earlier and sunset is no later than those for horizontal surfaces. Namely $\omega_1 \geq$ - $\left|\omega_H\right|$, $\omega_2 \geq \omega_{s2} \leq \left|\omega_H\right|$.

The calculation of daily net long wave radiation is given by the equation:

$$R_{L,24} = \varepsilon_a\sigma T_a^4 - \varepsilon_s s T_s^4 \quad \ldots\ldots(3.87)$$

where ε_a is the daily average atmospheric emissivity (Campbell and Norman, 1998) and T_a is the daily mean atmospheric temperature (K). The surface temperature determined at 3.30 can be taken to represent the daily average surface temperature for estimation of the surface daily long wave radiation (Granger, 2000).

CHAPTER 4

METHOD AND DATA REQUIREMENTS

4.1 Overview

Based on chapter 2 and chapter 3, the main requirement is to develop a remote sensing model that is capable of estimating ET from satellite images on the ERDAS Imagine software package depending on soil energy balance (see appendix A). Basically, this chapter describes the data required and research methodology needed to fulfill the research objective. The expected outcome at each stage of the research will be presented and at the end of this chapter the assumptions and the limitations of this research will be also presented.

ET is estimated by modified SEBAL using the theory described in the previous chapter. This chapter describes the more detailed procedure of modified SEBAL based on image from NOAA-AVHRR and Landsat-TM for a highland region, a coastal region and a desert region, in the Republic of Yemen.

The application of modified SEBAL requires a satellite image having a thermal band for surface temperature and ground based weather data. Digital elevation model (DEM) is also required due to the need for a correction for surface slope/aspect in the steeply sloping areas.

The overall intention of this research was to improve the means for generating ET maps for the central mountains of Yemen, an area that has more than 3200 square km of farmland. An operational remote sensing model is desired for routine application by the National Water Resources Authority (NWRA) as a means for predicting ET over large areas, modeling ground water, and performing a better management of the water resources and new projects in the regions.

The Surface Energy Balance Algorithm for Land (SEBAL) was selected as the basis to develop a model that can be adapted to the prevailing conditions of the study area. In order to validate and refine SEBAL in this work, concurrent satellite imagery and measured ET values were used. ET data were provided by NWRA , CAMA and AREA(AlIrra) stations and some measurements of ET at the soil water balance (lysimeter) site in the Experimental Farming – Faculty of Agriculture (EFFA), Sana'a University performed by Tahir (2006). ET data are available for a wide range of weather conditions, surface covers, and crop types. In addition, measurements of net radiation, soil heat flux and plant canopy parameters were made near the lysimeter. This dataset provides valuable information to evaluate and refine the accuracy of SEBAL for instantaneous ET values as well as to verify procedures for extrapolating remote sensing algorithms over various time scales and for various types and categories of land cover. With regard to remote sensing data for the application of SEBAL, from NOAA-AVHRR and Landsat 5 TM imagery was utilized.

4.1.1   Site Description

The study area is located in the central mountains of Yemen. The site comprises of a variety of surfaces such as mountain agricultural lands, arid land, a desert wadi Hadramout and arid coastal Tuban. Details of the study areas were described in chapter one and depicted in figure 1.1.

4.2.   Satellite Selection for Regional ET Study

The data required for evapotranspiration study must fulfill three major conditions: First, they must provide spatial quality that is sufficient for good spatial resolution to identify the land use/cover on the ground. Second, the information must also meet the temporal quality that satisfies the need for frequent observation. Third, they should have spectral bands in the visible and thermal range in order to provide vegetation and temperature properties simultaneously. Regional scale evapotranspiration studies, due to their highly temporal variation and low spatial requirement, are often carried out using sensors with higher time frequency data and intermediate spatial resolution such as the Landsat 5 and AVHRR of the NOAA satellite.

4.2.1   Data requirements

The necessary input to energy balance calculations are showing in the Table 4.1.

Table 4.1 :   Input necessary for remote sensing ET calculations

Symbol	Description	Symbol	Format	Description
d_r	Distance Sun Earth	$u*$		The effective friction velocity (m/s)
t_{GMT}	Time of satellite overpass converted to GMT	z_{om}	Raster	Roughness length for heat (m)
Lat	Latitude (dd)	NDVI	Raster	Normalized Difference Vegetation Index (-)
lon	Longitude (dd)	a_0	Raster	The Surface Broadband Albedo (-)
$K\!\downarrow_{sun}$	Sun external atmosphere Radiation ($W\,m^{-2}$)	T_0	Raster	Land surface temperature (K)
$R_L\!\downarrow$	Incident Longwave Radiation ($W\,m^{-2}$)	ε_0	Raster	Surface thermal emissitivity
ϕ_{sun}	The Solar Declination (rad)	τ_{sw}		Atmospheric transmissivity single way
σ	Stephan Boltzmann constant ($W\,m^{-2}/K^4$)			

4.2.2. Image Resolution Degradation

A geo-rectified Landsat Thematic Mapper (TM) image taken on June 1, 1998 used to study optimal spatial resolution. The spectral bands and ground resolution of Landsat TM are listed in Table 4.2.

Table 4.2   Spectral band, wavelength, spectral location, and ground resolution of Landsat Thematic Mapper (Lillesand and Kiefer, 1987)

Band	Wavelength(µm)	Spectral location	Ground Resolution, (m)
1	0.45-0.52	Blue	30
2	0.52-0.60	Green	30
3	0.63-0.69	Red	30
4	0.76-0.90	Near Infrared	30
5	1.55-1.75	Mid Infrared	30
6	10.4-12.5	Thermal Infrared	120
7	2.08-2.35	Mid Infrared	30

The primary environmental sensor for the NOAA satellite series is the Advanced Very High Resolution Radiometer (AVHRR) which is a five channel scanning radiometer sensing in the visible, near infrared, and thermal infrared window regions.   The channel width and features are tabulated in Table 4.3.

Table 4.3 : NOAA/AVHRR spectral ranges.

Band	wave length µm	Description
1	0.58-0.68	visible (red)
2	0.725-1.05	reflected infrared
3	3.55-3.92	mid infrared
4	10.3-11.3	thermal infrared
5	11.5-12.5	thermal infrared

AVHRR channels 1 and 2 were designed to discern clouds, land-water boundaries, extent of snow and ice, the inception of snow/ice melting, and to monitor terrestrial vegetation employing the computation of the vegetation indices. Channels 3, 4, and 5 were designed to be used to measure the temperature of clouds and the sea surface and for night time cloud mapping. Current applications have far exceeded these original objectives.

4.2.3   Procession of AVHRR and TM Data

Information collected via satellite sensors generates large amounts of data and is transmitted in complex formats. Raw AVHRR and TM data come with auxiliary data such as calibration coefficients, solar zenith angles, earth locations, and images in packed 8-bit radiometric resolution. The raw images contain both radiometric and geometric errors which have to be removed in order to quantitatively analyze and overlay other data sets. A schematic diagram of the preprocessing of AVHRR and TM data is illustrated in figure 4.1.

4.2.4. Image and data extraction

The AVHRR/TM images obtained from NOAA/class website and from the Earthsat Company respectively contained about 8 images AVHRR and about 5 images TM (Table 4.4). The recorded satellite pass consisted of all five-channel AVHRR and seven channel for TM.   The data was digitized to 10-bit precision and ordered in band

interleaved by element format. The solar zenith angle and earth location data (latitude and longitude) were embedded in the data record.
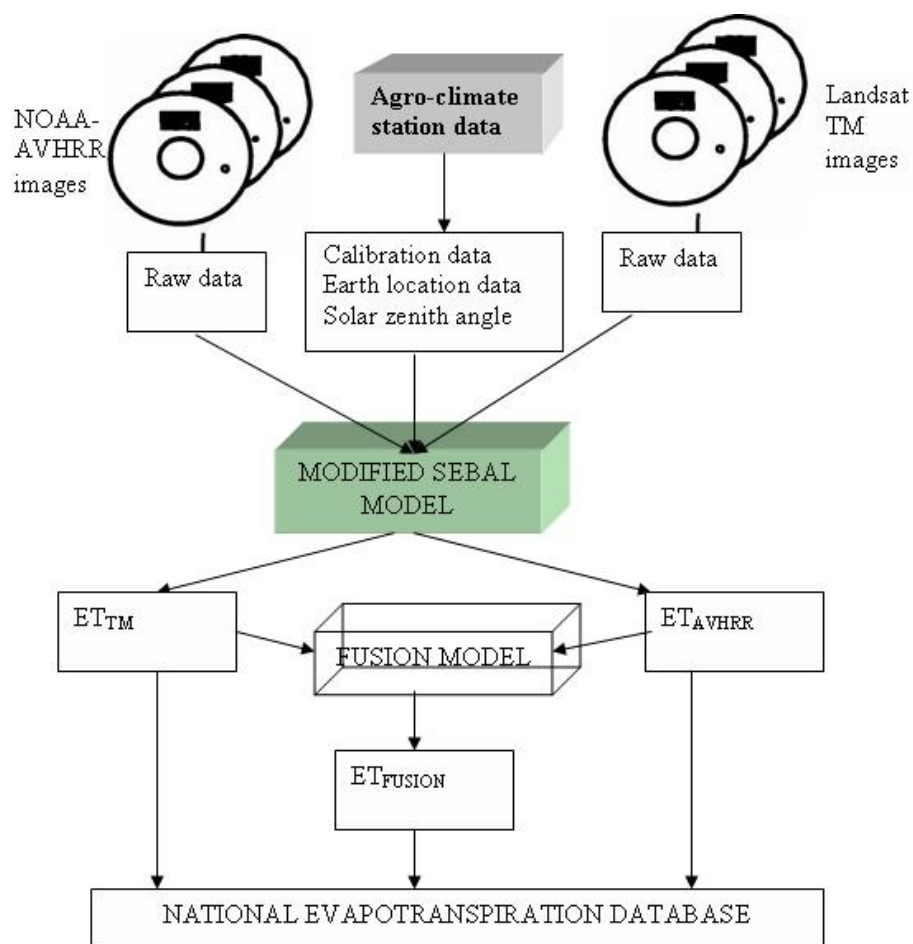
ET$_{TM}$, is the evapotranspiration estimated from landsat TM images, ET$_{AVHRR}$ is the evapotranspiration estimated from NOAA-AVHRR images, and ET$_{FUSION}$ is the evapotranspiration estimated from fusion ET from TM and AVHRR.

Figure4.1.   Schematic diagram of AVHRR/ TM data is preprocessing procedures

4.3   Data preparation

Two datasets which were used, include the high spatial resolution made of a combination of Landsat TM data and the low spatial resolution from NOAA-AVHRR imagery.

The Digital Elevation Model (DEM) was obtained from Shuttle Radar Topographic Mission images (SRTM) of 30 m^2.

4.3.1.   Remote Sensing Data

The sensor characteristics of NOAA-AVHRR are listed in Table 4.3. The images were obtained from the NOAA website. http://www.ngdc.noaa.gov/ngdcinfo/ newdownloads.html.

Landsat 5 TM imagery and NOAA-AVHRR were used as the source of remote sensing data for this study. Landsat imagery was selected because it has the finest resolution (28.5 to 30 m shortwave pixel size) of all satellite sensors equipped with a thermal band and NOAA-AVHRR has the finest image temporally every day. The best image, of course, is for a totally clear sky over all portions of the image. ET cannot be estimated for cloud-covered land surfaces and for the shadowed area of clouds due to effect on surface temperature. A Table 4.4 shows the detail of the images used in this study.

For Landsat 5 images, all seven bands are used and for NOAA-AVHRR image only four bands 1,2,4,5 were used in SEBAL.

The header file of the satellite image contains important information that is necessary for processing the image. Currently, purchasing a Landsat image with "NLAPS format" provides the best header file information. The following information must be obtained

from the header file or elsewhere: The satellite overpass date and time, Lat./Long. of the image, Sun elevation at the satellite overpasses time. Image date and time are supplied in GMT (Greenwich Mean Time) by which users can convert to local time or solar time (solar time is time relative to the time when noon is defined as when the sun is exactly south). These values are used to calculate instantaneous and 24-hour solar radiation. The sun elevation described in the header file is used for the modified SEBAL model, while sun angle information is not used because the relative sun angle to each land surface is calculated pixel by pixel, using slope and aspect of the land surface.

Table 4.4 : Date, overpassing time and type of the image from Landsat TM and NOAA AVHRR data used in this study

Landsat TM Images date	Overpassing time (GMT)	NOAA 14 Images date	Overpassing time (GMT)	NOAA 14 Images date	Overpassing time (GMT)
1 June 1998	12:12:00	10 June 1998	18:54:56	08-24-2006	19:17:45
-	-	20 October 1998	19:10:46	09-09-2006	18:54:56
20 May 1995	10:08:15	31 May 1995	19:24:57	09-28-2006	19:10:46
12 December 1995	12:15:12	20 December 1995	19:18:10	11-30-2006	19:24:57

4.3.2   Elevation data

A Digital Elevation Model (DEM) is necessary for the image area when the modified SEBAL model is applied. The units of the DEM should be in meters and the DEM should have the same pixel size as the satellite image and the area of coverage by the DEM file must be same as or larger than TM image. Otherwise, there will be divide by zero error in later steps. In this research SRTM images resolution 30m^2 was used and obtained from, ftp://e0srp01u.ecs.nasa.gov/srtm/version2/.

4.3.3   Weather data

Meteorological data collected at the study areas were used as the main source of weather data for validation of SEBAL. The high quality of the collected data and the location of the station are valuable in describing land-atmosphere related parameters. In addition, data from the weather stations, such as the National Water Resources Authority (NWRA), Agriculture research Extension Authority (AREA) and Civil Aviation &Meteorological Authority (CAMA), adjacent to the CAMA Sana'a airport weather station were utilized. Four of the stations were available from CAMA database previously collected from the Directorate of meteorology and the remaining stations were collected from NWRA - Ministry of Water and Environment, and AREA- Ministry of Agriculture And Irrigation, meteorology section, the testing and collect data from the stations was don during the field study see figure 4.2, and some data collect as a hard copy and transferred into a soft copy form.

Weather data included air temperature, wind speed and direction, dewpoint temperature, and solar radiation at all the mentioned stations. In addition, at the lysimeter micrometeorological station, net radiation and soil heat flux were recorded.

SEBAL requires measured windspeed data at the satellite image time. Generally, wind speed at only one representative location is needed per satellite image. However, if a wide variation in windspeed across an image is known to exist, using windspeed data from multiple locations is advised. In this situation, SEBAL may need to run separately for each wind zone.

In addition to the windspeed data, in application of modified SEBAL, solar radiation, air temperature and humidity are required. Solar radiation (Rs) is also useful for adjustment of transmissivity at the image time, and for predicting the occurrence of clouds during the day. Precipitation records provide an idea of the relative "wetness" of the image. Also, the precipitation record allows the application of a simple water balance model during the modified SEBAL process to improve the quality of ET

estimation. This is important especially for images that have received rain within less than five days before the image date.

Table 4.5 : Weather Station Description

	Region	Station name	Elevation m	Latitude N UTM(km)	Longitude E UTM(km)	Time scale	Data available
1	Mountain Sana'a basin	CAMA	2216	1697.100	415.100	daily	Temp., RH, solar radiation, and wind velocity
2	Mountain Sana'a basin	AREA (Al-Irra)	2200	1546.053	411.795	Daily	humid Temp., RH, wind velocity, sunshine hours, and pan evaporation
3	Mountain Sana'a basin	EFFA	2285	1698.736	412.418	daily	Temp., RH, wind velocity, and pan evaporation
4	Mountain Sana'a basin	NWRA	2275	1696.500	412.400	daily	Temp., RH, wind velocity, and sunshine hours
5	Eastern desert	Seiyun	700	1762.679	278.761	daily	humid Temp., RH, wind velocity, and sunshine hours
6	Eastern desert	Marib (CAMA2)	1000	1705.000	535.000	daily	humid Temp., RH, wind velocity, and sunshine hours
7	Coastal	Lahij (CAMA3)	129	1442.689	487.351	daily	Temp., RH, wind velocity, humid andsunshine hours
8	Coastal	K-Makser (CAMA4)	4	1410.872	503.617	daily	Temp., RH, wind velocity, and sunshine hours

The processing follows the methodology setup by Bastiaanssen (1995) to calculate the soil and sensible heat fluxes. In order to address the data requirements from Table 4.6 a set of instruments were set up.

Table 4.6 : Instruments description

Instrument	Measurement
Meteorological station	Wind speed, temperature, relative humidity, precipitation, shortwave incoming radiation $(0.31.1\mu$ m).
dT system	Difference of temperature at heights $z = 0.3$ & 2m
Net Radiometer	Net radiation (Rn) at surface $(0.330 \mu$ m).
Lysimeter	Water balance (soil moisture and ET)

A

B
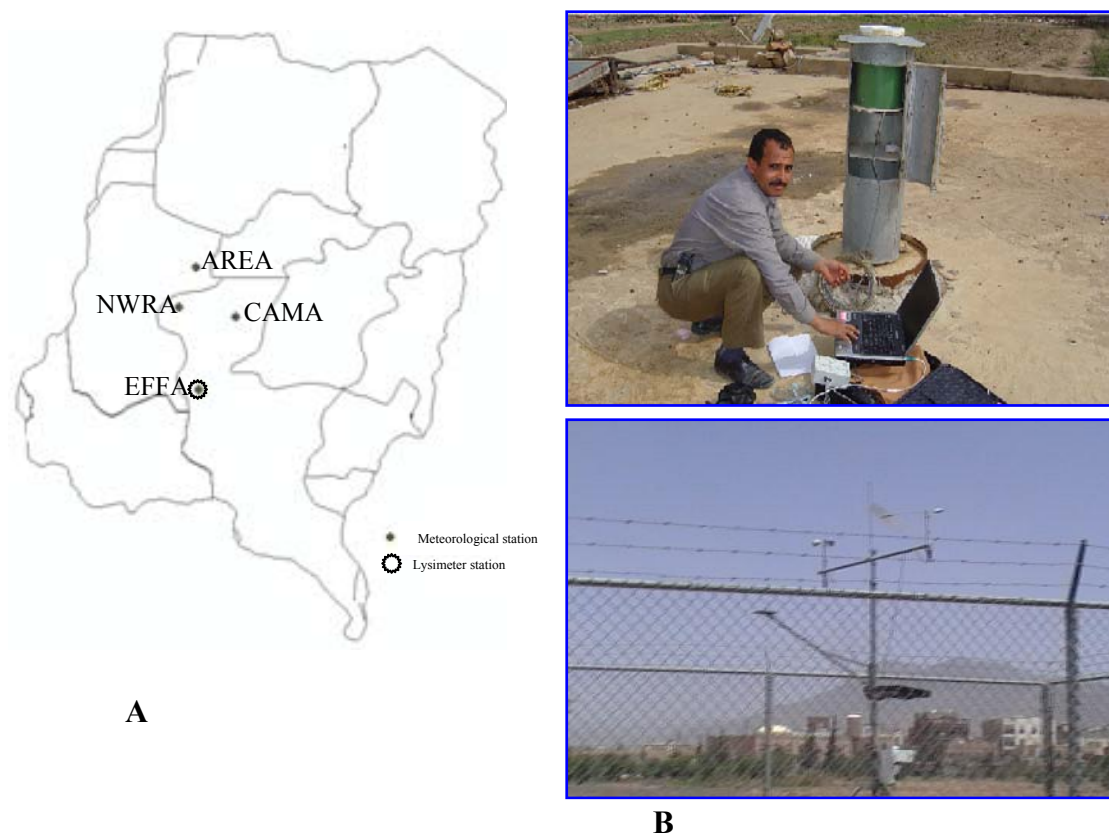
Figure 4.2.   Location map of the Meteorological gauge stations in Sana'a basin (A) and pictures during gathering data 2006 (B)

4.3.4   Geometric rectification and geo-referencing

Satellite images are subjected to different geometric deformations due to the Earth's rotation, oblateness, curvature, speed, attitude, and altitude variation of the satellite. The scan skew and the projection of spherical surface on a flat image also contribute to geometric errors. Those deformations, if not properly accounted for, will prevent meaningful comparison among data from ground-truthing and images acquired from different sources, and will also hinder further applications of the geographical information system.

4.4. Development of the parameterization of actual ET

4.4.1 Overview

Previous work with SEBAL has shown it to be an effective predictor of ET in Africa and Asia (Bastiaanssen et al, 1998b) and in the United States in Bear River Basin, Idaho, North America (Tasumi. et al, 2000). The results of the work in Yemen-Sana'a Basin, while somewhat equivocal, indicate that SEBAL can perform well in Yemen, as well. Further research on SEBAL is needed if SEBAL is to become an operational tool in Yemen's water resources projects. SEBAL as formulated by Bastiaanseen, et al. (1998a) assumes all vegetation is growing on a relatively flat surface. In applying SEBAL to entire watersheds, especially those in Yemen, this assumption clearly is not valid, and affects the ET estimates.

SEBAL is an emerging technology, and suffers from some uncertainties that should be eliminated or reduced if SEBAL is to become operational. These uncertainties are in the form of :

I. Uncertainties created by the need to refine SEBAL to account for slope, aspect, and elevation, in mountains area in Yemen,

II. Uncertainties created by the need to refine SEBAL to account for Desert areas,

III. Uncertainties created by the need to refine SEBAL to account for coastal plain in arid and semi arid region in Yemen.

4.4.2   The General procedure of the Modified SEBAL Model.

A Modified SEBAL model was developed by introducing some changes into the existing SEBAL model. Notably these were the inclusion of terrain, mountains and deserts effect into calculations of surface radiation. The main steps in M-SEBAL are: (1). generation DEM, (2).calculation surface reflectance correction, (3).generating model parameter (4).determination of radiation finally (5).calculation ET daily monthly. The steps (1) and (2) modified by Modified SEBAL model to prepare the image to use in SEBAL model to work in the Aride Mountains. The steps (3) and (4) have some modification for step 3 the estimation of the Albedo and $T_{s\text{-}DEM}$, and the step (4) the estimation of G and step of estimation H was modified also and change from original SEBAL to Modified SEBAL. The main computation steps for the Modified SEBAL Model (Figure 4.3) follow the methodology laid down by Bastiaanssen (1995). The latent heat flux is the resulting partition of the energy balance at the time of the satellite overpass (typically 10.00 -10.30AM for Landsat and 12 pm NOAA-AVHRR). Eventually, the latent heat flux ($W\ m^{-2}$) is converted into an instantaneous actual Evapotranspiration (mm). Low-resolution information from NOAA-AVHRR will be given preference, since georeferencing issues are less than for Landsat TM has improved georeferencing accuracy and could be used as a backup sensor. The satellite Aqua has a midday local overpass time, and is preferred for a better partitioning of H and $\lambda(ET_{ins})$.

There are several hurdles to solve the energy balance. The main issue is that the sensible heat flux parameterization requires information depending on itself (in the MoninObukov Length parameterization). Bastiaanssen (1995), solved this issue by using an iteration technique that is initialized with ($T_{s\,/}\,T_{air}$) information in desert and farming areas (or so called "dry" and "wet" pixels), selected from the image and assumed to have specific properties in the energy balance.

Because of this, the model developed by Bastiaanssen is not automatized. Among the parameters that are iteratively optimized with the sensible heat flux itself is the aerodynamic resistance to heat transport, related to the vegetation height.
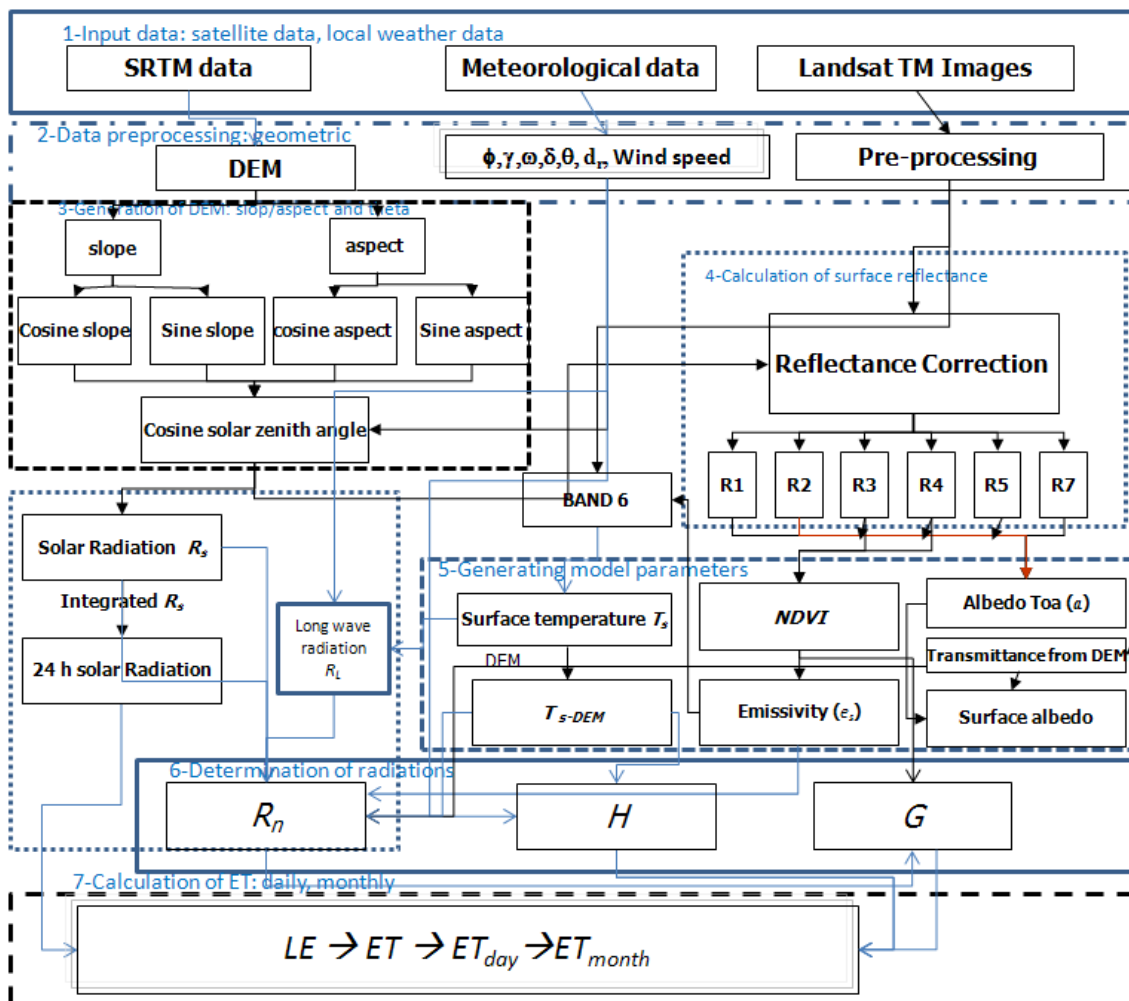
Figure 4.3 The general flowchart of correlations between modified SEBAL model parameter

4.4.2.1 Input data: satellite data, local weather data

The proposed modified SEBAL method is for the application in the three different regions in Yemen the mountains, coastal and desert regions in Sana'a Basin, Wadi Tuban and Wadi Hadramout Yemen. The difference between the SEBAL and

modified SEBAL is whether the slope/aspect/elevation corrections are applied or not. Before preparing data, the user must decide whether the surface slope/aspect correction is needed in modified SEBAL.

The modified SEBAL model is more complicated although the basic structure is the same as for the SEBAL model. With the modified SEBAL model, slope/aspect/elevation corrections in the radiation balance, and corrections for surface temperature and windspeed are made. With the modified SEBAL model, the energy balance calculation in sloping terrain is theoretically improved, although some future study is required to provide more confident prediction by this model on mountainous areas.

4.4.2.2 AVHRR Data Calibration

Calibration is a process that converts the digital number in the image to meaningful surface characteristics. AVHRR visible data values (Channels 1 and 2) may be converted to Albedo and AVHRR thermal data values (Channels 4 and 5) may be converted to temperature values.

4.4.2.2.1 Visible Channel Calibration

AVHRR visible channels (channel 1 and channel 2) are designed to provide conversion between the digital numbers and surface reflectivity (Albedo). The

percent Albedo measured by the sensor channel i is computed as a function of the input data value as follows:

$$A_i = S\,C + I \qquad\qquad\qquad ……(4.1)$$

where A_i is the percent Albedo measured by channel i, C is the input data value, and S, and I, are the scaled slope and intercept values, respectively. The scaled slopes and intercepts were calculated from the calibration coefficients extracted from HRPT data file (Kidwell, 1991).

4.4.2.2.2 Thermal Channel Calibration

The thermal channels (channel 4, and 5) are designed and calibrated before launch as well as in space to provide direct conversion between digital numbers and radiant temperature. The conversion of radiant temperature from energy is performed using the inverse of Plank's radiation equation:

$$T_i(E_i) = \frac{C_2 v}{\ln\left(\dfrac{C_1 v^3}{E_i} + 1\right)} \qquad\qquad ……(4.2)$$

where T = radiant temperature (K) for the energy value E_i,

    v = central wave number of the channel filter (cm^{-1}),

    C_1= constant (1.1910695* 10^{-5} milliwatts/m^2 -steradian-cm^{-4}),

    C_2= constant (1.438833 cm-K),

    E_i = energy measured by the sensor (channel i), and E_i =SC + I

    S and I are scaled slope and intercept described above.

The temperature obtained by this procedure is radiant temperature, which needs further correction for atmospheric attenuation and surface emissivity. The

atmospheric correction of brightness temperature was performed by the water-body calibration technique.

The atmospherically-corrected radiant temperature is the actual surface temperature only when the emissivity is equal to 1.0. For most surfaces, where the emissivity is not equal to 1.0, a further adjustment needs to be undertaken. Emissivity values were assigned to each of the study areas in the Yemen.

4.4.2.3 Landsat TM & ETM+ Data Calibration and Image Processing

Albedo is calculated by a weighted average of the reflectance of shortwave bands (band 1-5 and 7). A satellite sensor observes total radiation of each specific wavelength band, and records the strength as digital number 0 (or 1) to 255. The Digital Number (DN) must be converted into radiance for calculating the reflectance of each band. Although the thermal band (Landsat TM/ETM+ Band6) is not used in the surface Albedo calculation, the thermal band must also be converted to radiance for use in a future step.

The recommended computation methods are different between Landsat 5 TM and Landsat 7 ETM+. For Landsat 5 TM images, the following equation is used (Markham and Barker, 1986):

$$L_\lambda = \left(\frac{LMAX - LMIN}{255} \right) DN + LMIN \qquad \text{.......(4.3)}$$

Where

L_λ is sensor observed radiance for band in W m^{-2} sr^{-1} μm^{-1}, LMAX and LMIN are constants given in Table 4.7, and DN is a digital number recorded in the satellite image.

Table 4.7 : L_{MIN} and L_{MAX} values for Landsat TM after 15 Jan 1984 (Markham and Barter, 1986)

Bands	L_{MIN}	L_{MAX}
	W m^{-2} sr^{-1} μm^{-1}	W m^{-2} sr^{-1} μm^{-1}
1	-1.50	152.10
2	-2.80	296.80
3	-1.20	204.30
4	-1.50	206.20
5	-0.37	27.19
6	1.24	15.60
7	-0.15	14.38

The calibration constants in Table 4.8 were published in 1986, and the constants L_{MIN} and L_{MAX} change over time because of sensor degradation. For recent Landsat 5 TM images, the following calibration constants are recommended for use by (Tasumi, 2003).

Table 4.8 L_{MIN} and L_{MAX} for Landsat 5 TM, year 2000 (Note that the Band 6 calibration constants are from Markham and Barker, 1986)

Bands	L_{MIN}	L_{MAX}
	W m^{-2} sr^{-1} μm^{-1}	W m^{-2} sr^{-1} μm^{-1}
1	-1.76	178.94
2	-3.58	379.05
3	-1.50	255.69
4	-1.76	242.30
5	-0.41	30.18
6	1.24	15.60
7	-0.14	13.16

Note that more than a 20% error in Albedo estimation can occur for general land surfaces, if the old constants in Table 4.7 are applied to a recent Landsat 5 image (Tasumi, 2003).

4.4.3. Calculation of surface reflectance

Once the radiance is obtained, the reflectance of each band can be calculated by equation 3.5 with $k^{\downarrow}_{exoi}$ given in the Table 3.3 and cosine of solar incident angle (cosθ), calculated by Equation 3.13 for the modified model on the mountain. Note that the cosθ given in Equation 3.13 is not a constant but must be calculated separately for each pixel.

4.4.4 Generating model parameters

After the reflectance calculation, the albedo at the top of the atmosphere (a_{T0A}) is computed from Equation 3.22, with weighting coefficients given in the Table 3.4.

The transmittance is either derived from actual observation of solar radiation and from equations 3.24. Then the surface albedo is calculated by Equation 3.25.

Table 4.9 shows typical albedo values for many different land use types. This table can be compared against albedo derived from modified SEBAL to ensure that modified SEBAL is functioning correctly.

The Vegetation indices (VI) estimation: NDVI is calculated by Equation 3.26. SAVI is calculated by Equation 3.27, and LAI is calculated by Equation 3.28, which was verified using agricultural data for Sana'a Yemen. However, it is an empirical equation and may not give reasonable estimates for other conditions. The Surface Emissivity (ε_o) is estimated using the formula 3.29 after Bastiaanssen et al. (1998a) and Tasumi et al, (2000a).

The Surface temperature (Ts) was estimated and corrected using Equations 3.32 to 3.34 for Landsat 5&7 and equations 3.35 to 3.38 for NOAA-AVHRR with narrowband.

Table 4.9 Typical Albedo values (Horiguchi, 1992 and Tasumi, 2003).

Black soil	0.08-0.14
Clay	0.16-0.23
White-yellow sand	0.34-0.4
Gray-white sand	0.18-0.23
Paddy field (rice)	0.17-0.22
Grass or pasture field	0.15-0.25
Maize field	0.14-0.22
Forest (coniferous)	0.1-0.15
Forest (deciduous)	0.15-0.2
Water (solar elev. = 10°)	0.348
Water (solar elev. = 30 °)	0.06
Water (solar elev. = 50 °)	0.025
Water	0.025 – 0.348

4.4.5   Determination of radiations

4.4.5.1   Net Radiation

The net radiation is comprised of two main radiation can presents usually shortwave radiation and longwave radiation, the following sections explained both radiation types in detail.

4.4.5.1.1   Shortwave radiation (solar energy(R_s))

    In the last step, the reflectance of the short wave radiation was corrected and calculated for all pixels of each band 1-5 and 7 (band 6 is the thermal band) for Landsat images, and band 1 and 2 for NOAA-AVHRR images (band 3, 4 and 5 is the thermal bands). The reflectance of a band computed by the Equation (3.21) is the ratio of the outgoing energy (radiation) of the band measured at the top of atmosphere by the satellite, and the incoming energy (radiation) of the band at the top of atmosphere. The outgoing energy is recorded by the satellite's sensors, and the incoming energy is based on theoretical values for various wave lengths of solar radiation. The incoming energy (band) is computed by the equation (3.41). $cos\theta$ is the cosine of the solar incident angle derived in equation 3.13 and d_r is the inverse relative distance Earth-Sun. The value for d_r averages 1.0 and ranges from about 0.97 to 1.03 calculate by equation 3.10 after Allen et al., (1998).

4.4.5.1.2   Longwave radiation (R_L)

    For completing the radiation balance calculation, the incoming and outgoing longwave radiation must be determined. The outgoing longwave radiation $R_{L\uparrow}$ can be calculated by Equation 3.44 using the broad-band emissivity calculated by Equation 3.29.

    The incoming longwave radiation ($R_{L\downarrow}$) calculation requires the surface temperature of a well-watered agricultural field expressed as T_s (cold pixel). In the modified SEBAL process, the cold pixel and hot pixel introduced in Section 3.6.3.6 are selected at this point. The total incoming longwave radiation can be calculated by

Equation 3.42, using the surface temperature of the selected cold pixel (from T_s after corrected by DEM). Finally, the net radiation R_n for each pixel is calculated using Equation 3.45.

Figure 4.4 showing the flow chart of the steps and the images is used for determin of net surface radiation

```
┌─────────────┐              ┌─────────────┐
│ NDVI        │              │ Spectral    │
│ SAVI        │              │ Radiance    │
│ LAI         │              │ Lλ          │
└─────────────┘              └─────────────┘
```

$$R_n = (1-\alpha)R_S{\downarrow} + R_L{\downarrow} - R_L{\uparrow} - (1-\varepsilon_0)R_L{\downarrow}$$
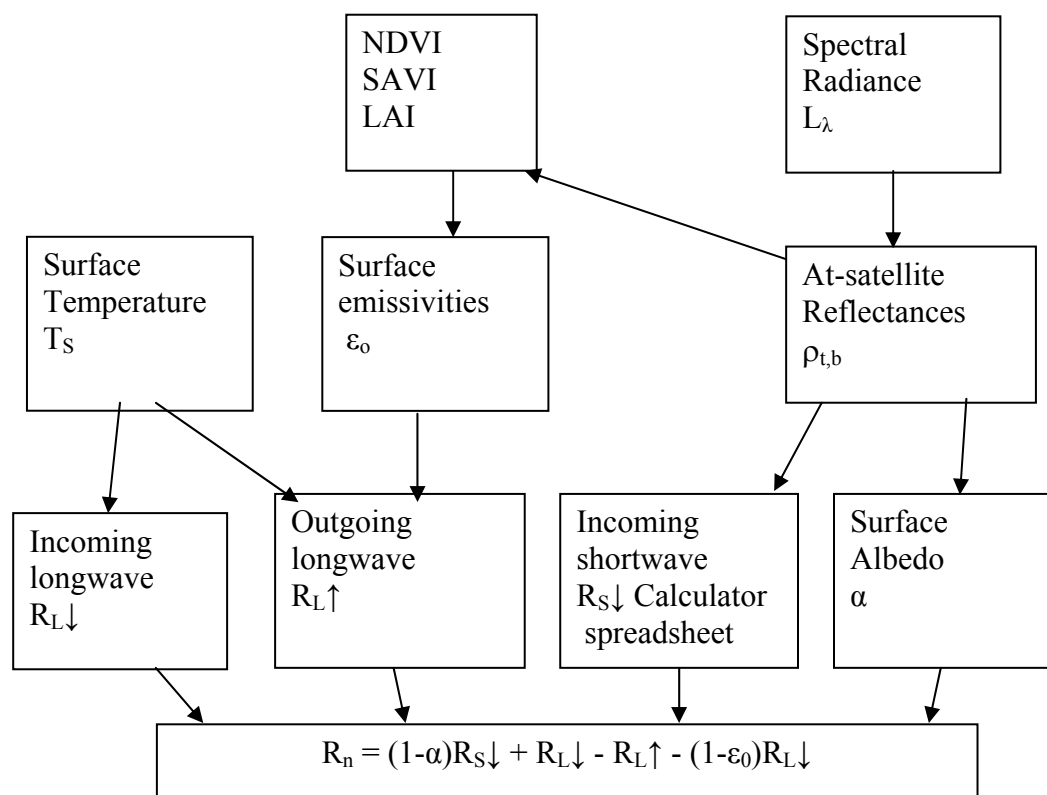
Figure 4.4   Flow Chart of Net Surface Radiation Estimation

4.4.5.2   **Ground heat flux (G)**

As described in Chapter 3 (Section 3.6.2), the ground heat flux G is calculated by Equation 3.49 using the albedo, temperature, and *NDVI*. This equation by Bastiaanssen was verified under Sana'a basin, Yemen mountain conditions by a totally independent method for general agricultural land uses by measuring the G and R_n from the field station and comparing versus the value of the *NDVI* from the images data in the same point and date. However, it is uncertain whether this equation works well for other land use types such as cities and desert areas.

One should locally calibrate and probably modify the G equation used in SEBAL, especially if land conditions are different from agriculture. For example, several studies have shown that the G/R_n ratio for water surfaces can be totally different from other land use types (Yamamoto and Kondo 1968, Amayreh 1995, Burba et al., 1999). The G/R_n ratio for water surfaces can be quite large, since the solar radiation penetrates into the water. The ratio might mostly depend on the turbidity and the depth of the water body, and seasonal differences occur especially in clear deep lakes, where the water body acts as a large heat storage reservoir.

Table 4.10 : G/R_n values for Various Surfaces (after Tasumi, 2003)

Surface Type	G/R_n
Deep, Clear Water	0.5
Snow	0.5
Desert	0.2 – 0.4
Agriculture	0.05 – 0.15
Bare soil	0.2 – 0.4
Full cover alfalfa	0.04
Clipped Grass	0.1
Rock	0.2 – 0.6

These values represent daytime conditions.

In modified SEBAL, the ground heat flux (G) is empirically calculated by vegetation indices derived from the satellite image Equation 5.6.

4.4.5.3   **Sensible heat flux (*H*)**

4.4.5.3.1   **Surface Roughness for Momentum (*z_{om}*)**

For modified SEBAL operation, an empirical relation between crop height and NDVI was developed. This relationship is for general agricultural crops and fits most observations for Yemen mountains crops. Equation 3.58 is most accurately applied to fields having general agricultural crops. For other land use types, it is recommended that one use a constructed land use map with assigned general value of *z_{om}* (surface roughness for momentum transport (m)) versus NDVI relationships for each land use. Also, an alternative method to estimate z_{om} by correlating with NDVI has been described in Bastiaanssen et al. (1998a) and Tasumi et al., (2000a).

In modified SEBAL, the impact of terrain on aerodynamic roughness is empirically adjusted by estimating a sort of "geometrical" z_{om} for mountain areas. There are two main reasons to correct z_{om} for sloped terrain especially in mountain areas: (1) acceleration of windspeed is generated when a vertical component of movement is created by the land surface (Oke, 1987), and (2) sloping surfaces have a larger land surface area for a unit pixel (horizontal 30 m x 30 m pixel), and therefore the heat transportation process by wind is enhanced (after Tasumi, 2003) by using equations 3.59 and 3.60.

Sensible heat flux is calculated using equations 3.50, 3.51 and 3.52 with *dT* calculated by equation 3.61. However sensible heat estimation requires some iteration process, since the intensity of the stability correction is unknown at the beginning.

Table 4.11 :. Surface roughness for each land use type (Tasumi, 2003).

Land use	z_{om} (m)
Agriculture	0.018LAI (z_{om}MIN = 0.005)
Water	0.0005
City	0.2
Forest	0.5
Desert Grassland	0.02
Desert Sage Brush	0.1
Salty Soil	0.002
Basalt Rock	0.07
Mountain Bare Soil or Grass	0.05
Mountain Forest	0.5
Snow	0.005

Windspeed at 200 m above the selected weather station is estimated using an actual point windspeed measurement from a local weather station Equations 3.53. During the extrapolation, surface roughness surrounding the weather station must be determined by the user. Many weather stations do not have large "fetch". Namely, the measured windspeed generally includes the effect of surfaces somewhat further upwind, and therefore, surface roughness of the weather station should not be determined only by looking at the surface condition of the weather station itself. For the agricultural weather stations in Sana'a Yemen, a value of z_{om} = 0.03 m was estimated to be an average value that considered upwind agricultural fetch of the stations. The 0.03 m reflects an average vegetation height of 0.25m if the relation in Equation 3.55 is applied. The u_{200} at the weather station can be determined by using Equation 3.53 assuming a neutral stability condition. The calculated u_{200} is applied for the entire Landsat image in the flat Model. For our model in the Mountain, u_{200} for each pixel is adjusted by the DEM using equation 3.59 before use to predict u^* for the pixel Equation 3.52 (after Tasumi, 2003).

4.4.5.3.2   H estimation

Sensible heat flux (H) is estimated through an iterative process for aerodynamic stability correction. First, r_{ah} and $u*$ are calculated for each pixel assuming a neutral stability condition, so that the stability correction terms are all zero, and equations 3.51 and 3.52 become:

$$u*_{(1st)} = \frac{u_{200} k}{\ln\left(\dfrac{z_{200}}{z_{om}}\right)} \qquad \ldots\ldots(4.5)$$

$$r_{ah(ist)} = \frac{\ln\left(\dfrac{z_2}{z_1}\right)}{u*_{(1st)} \times k} \qquad \ldots\ldots(4.6)$$

Where

$r_{ah(1st)}$ and $u*_{(1st)}$ are the first estimates of r_{ah} and $u*$ assuming a neutral stability condition.

The first estimates for "a" and "b" in the dT function (Equation 3.62) is derived using the cold and hot pixel dT values back calculated by Equation:

$$dT_{(cold\_1st)} = \frac{H_{(cold)} . r_{ah(cold\_1st)}}{\rho_{air(1st)} . Cp} \qquad \ldots.(4.7)$$

And

$$dT_{(hot\_1st)} = \frac{H_{(hot)} . r_{ah(hot\_1st)}}{\rho_{air(1st)} . Cp} \qquad \ldots..(4.8)$$

where the subscripts "cold" and "hot" represent the values at the cold and hot pixels, the subscript "1st" stands for the first estimation which is calculated assuming a neutral stability condition. The first estimate for air density (ρ_{air}) uses standard air temperature 20°C, since there is no information on air temperature. This is improved in later iterations. H values for cold and hot pixels are determined by equation 3.50.

The first estimate of H, $H_{(1st)}$ for each pixel is calculated by Equation 3.50, using the first estimate for dT and r_{ah}. The air density (kg/m³) used in Equation 3.50 is calculated as (Allen et al., 1998):

$$\rho_{air} = \frac{100 \times P}{1.01 \times T_s \times 287} \qquad \text{......(4.9)}$$

Where

T_s is surface temperature in Kelvin, and P is air pressure (kPa). Usually, air temperature is used in Equation 4.11 instead of surface temperature. However, surface temperature is used in modified SEBAL for the reason described in Equation 3.34 and 3.37. Air pressure P (kPa) is calculated by Equation 4.11. However, air temperature is unknown and therefore, a rough estimation of air temperature is applied:

$$T_a' = T_s - dT \qquad \text{......(4.10)}$$

Where

T_a' is a rough estimation of the air temperature (K) and dT is temperature difference (K) calculated by Equation 3.61. The equation for P calculation (Equation 4.11) is relatively insensitive to temperature.

$$P = 101.3 \left(\frac{T_a - 0.0065z}{T_a} \right)^{5.26} \qquad \text{.......(4.11)}$$

The T_a' from Equation 4.10 represents air temperature but not at z2 (Figure 3.7, which is 2m above d), because the estimated dT is not the temperature difference between land surface and air at z_2, but between z_1 and z_2. Since the z_1 in dT estimation (Figure 3.6) is 0.01 m above the zero plane displacement height and is generally higher than the surface roughness of heat transfer, z_{oh}, the T_{air}' in Equation 4.10 takes on an air temperature value somewhere between the land surface and air at 2m above the surface. This rough estimation is not a problem in modified SEBAL because (1) the air density equation is not very sensitive to the temperature, and (2) the evaporation and heat transfer processes occur very near the surface (so one could argue that using a

temperature value somewhere between the surface and 2m is better than using air temperature at 2m).

After the $H_{(1st)}$ calculation, a second estimates for $u*$ and r_{ah} are calculated with stability correction applied. The Monin-Obukov length parameter L is applied as the indicator of air stability (Monteith and Unsworth (1990)):

Figure 4.5 showing the flow chart of the steps and the images is used for compute sensible heat flux (H) and their iterative process to make the atmospheric stability corrections for momentum and heat transport.

```
                    ┌─────────┐
                    │  Start  │
                    └─────────┘
                         │
                         ▼
        ┌────────────────────────────────────┐
        │ Calculate u* at weather station     │
        └────────────────────────────────────┘
                         │
                         ▼
        ┌────────────────────────────────────┐
        │ Calculate wind speed at 200 m       │
        └────────────────────────────────────┘
                         │
                         ▼
        ┌────────────────────────────────────┐
        │ Calculate z_om for each pixel        │
        └────────────────────────────────────┘
                         │
                         ▼
        ┌────────────────────────────────────┐
        │ Calculate u* for each pixel         │
        └────────────────────────────────────┘
                         │
                         ▼
        ┌────────────────────────────────────┐
        │ Calculate dT for each pixel         │
        └────────────────────────────────────┘
                         │
                         ▼
        ┌────────────────────────────────────┐
        │ Calculate R_ah for each pixel        │
        └────────────────────────────────────┘
                         │
                         ▼
        ┌────────────────────────────────────┐
        │ Calculate H for each pixel          │
        └────────────────────────────────────┘
                         │
                         ▼
 ┌───────────────────────────────────────┐      ┌────────────────────────┐
 │ Calculate stability parameter for     │◄─────│ Update H for each pixel│
 │ each pixel                            │      └────────────────────────┘
 └───────────────────────────────────────┘                  │
                         │                                   ▼
 ┌───────────────────────────────────────┐            ┌──────────┐
 │ Correct u* according to stability     │            │   H_5    │
 │ parameter for each pixel              │            └──────────┘
 └───────────────────────────────────────┘                  │
                         │                                   ▼
 ┌───────────────────────────────────────┐            ┌──────────┐
 │ Correct R_ah according to the         │───────────►│   End    │
 │ parameter for each pixel              │            └──────────┘
 └───────────────────────────────────────┘
```
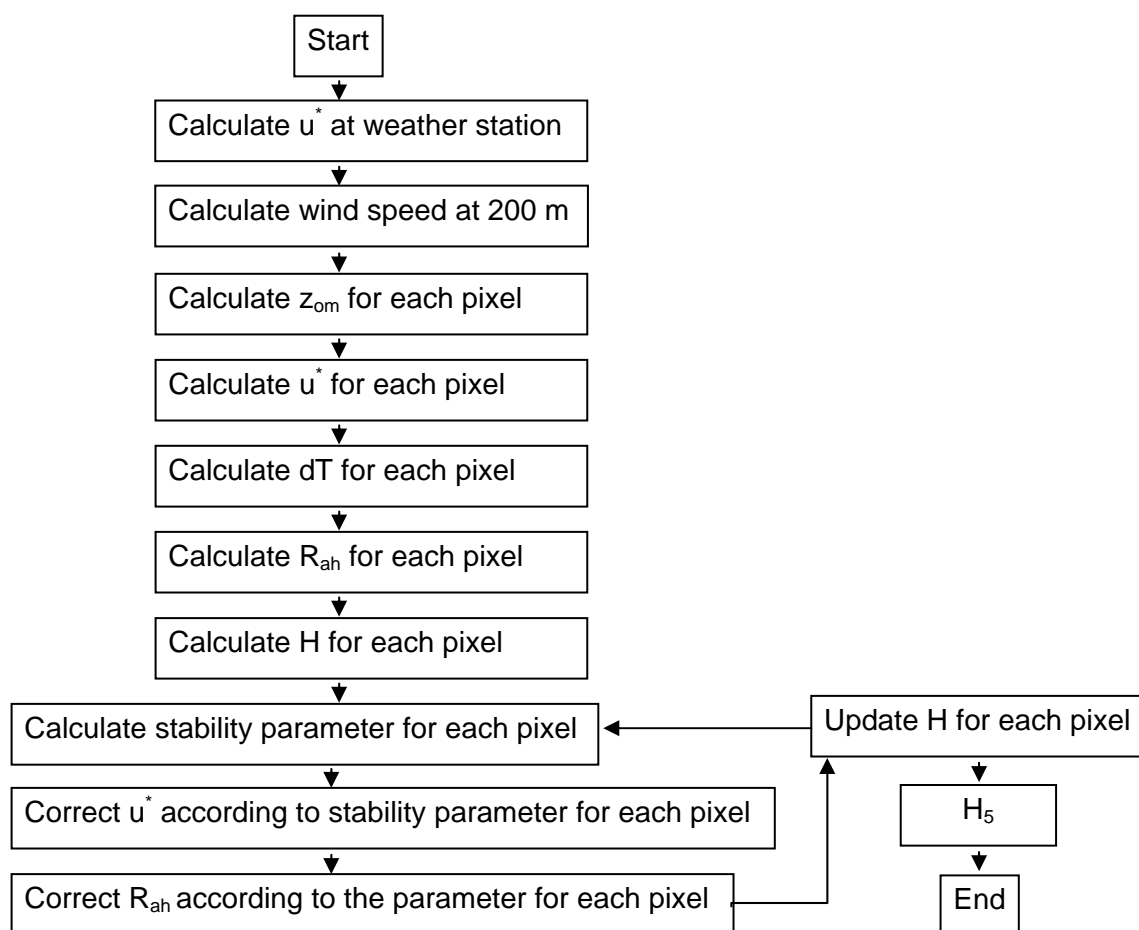
Figure 4.5   Iterative Process to Compute Sensible heat flux (H)

4.4.6 Calculation of ET: daily, monthly

4.4.6.1 Latent heat flux $\lambda(ET_{ins})$, instantaneous *ET* and 24-hour *ET*

Latent heat flux λ is calculated by Equation 3.4. Instantaneous *ET* (for satellite image time) is calculated by Equation 3.3 with *EF* calculated by Equation 3.72. The estimated instantaneous ET can be extrapolated to 24-hour ET using Equations 3.76.

4.4.6.2 Daily and Monthly ET estimation

Depending on the time scale chosen, different time integrations of (R_n- G) need to be obtained. For time scales of one day or longer, *G* can be ignored and net available energy (R_n-*G*) reduces to net radiation (R_n). For the daily time scale, ET_{24} (*mm d^{-1}*) is formulated as:

$$ET_{24} = \frac{86400 * 10^3}{\lambda \rho_w} EF * R_{n24} \qquad \ldots\ldots(4.12)$$

where R_{n24} (W m^{-2}) is the 24-h average net radiation, λ (J kg^{-1}) is the latent heat of vaporization, and ρ_w (kg m^{-3}) is the density of water.

For time scales longer than one day Eq. 4.12 becomes:

$$ET_{int} = \frac{(dt86400 * 10^3)}{\lambda \rho_w} EF * R_{n24} \qquad \ldots\ldots(4.13)$$

where ET_{int} (mm interval^{-1}) is actual evapotranspiration during interval *dt*, R_{n24t} (*W m^{-2}*), is the average R_{n24} value for the time interval *dt* measured in days. R_{n24t} is usually

lower than R_{n24} because R_{n24} is taken from clear-sky satellite overpass days and R_{n24t}, also includes cloud-covered days. The chief assumption in the SEBAL model is that the evaporative fraction specified in Eq. 3.72 remains constant for the time interval between each satellite image. Experimental work has demonstrated that this holds true for environmental conditions where soil moisture does not significantly change (e.g. Shuttleworth et al., 1989; Brutsaert and Sugita, 1992; Nicols and Cuenca, 1993; Kustas et al., 1994; Crago, 1996; Franks and Beven, 1997). Farah (2000) found that the accumulated evapotranspiration for a period of 10 to 20 days can be predicted satisfactory from Eq. 4.13, but that the computation of $\lambda(ET_{ins})$ for a particular day within a 10-day period using the constant value of EF obtained for the time of the satellite overpass is not accurate. This has an important implication: $\lambda(ET_{ins})$ estimates for days with no satellite images can be erroneous, but the temporally integrated value for a week can be sufficiently accurate using a temporally constant value of EF. Apparently, there are some systematic errors that cancel out over longer periods of time (Ahmed, 2003).

4.4.6.3   Seasonal ET estimation

Seasonal ET estimation employs a similar assumption to the one that is made for 24-hour ET estimation. This assumption is that daily evaporative fraction $EF_{(24)}$ for a satellite image date can approximate EF for a certain time period between images. However, since this assumption is not true, especially if a time period represented by one satellite image is long, one should estimate seasonal ET using the most satellite images possible.

4.5   Verification and validation methods

Verification of satellite derived regional ET is difficult due to the lack of ET records representing areas large enough to compare with satellite derived values. Traditional ET estimation methods, regardless of complexity, still represent point estimation. In fact, the remote sensing ET estimation method in this study still utilized traditional ET methods with ground measured meteorological data for potential ET estimation. Only the complex, surface-dependent crop coefficients (vegetation and moisture index), which are difficult to measure by traditional methods, were determined by remote sensing methods. Based on these limitations, verification of the model was by comparing point ET at weather stations determined by the 4 tradition ET estimation method (FAO-56 Penman-Monteith FAO, FAO-24 corrected Penman, FAO-24 Radiation, Priestley-Taylor, Hargreaves and SCS Blaney-Criddle) with ET determined by the remote sensing method.

4.5.1   Verification with Traditional ET Methods

The meteorological data from 3 stations, including pan evaporation, solar radiation, air temperature, relative humidity, atmospheric pressure, and wind speed, were obtained from the NWRA, AREA and CAMA. The ET rates estimated by remote sensing SEBAL method were compared with those by traditional ET estimation methods. ET estimated by the FAO Penman Monteith method was used to compare the results from the remote sensing method. The crop coefficients were assigned for each weather station based on its land use/cover type in the Sana'a Basin, land cover map (NWRA, 2001).

4.5.2 Verification with lysimeter ET

ET estimated by the remote sensing method was compared with the lysimeter ET at EFFA to monitor the actual ET and vegetation growth, the lysimeter were used to simulate ET from a large homogeneous area. The lysimeters were installed within EFFA areas with the vegetation, meteorological condition and fetch being the same as surrounding vegetation. Lysimeter (1698736.264 N; 412418.726 E). Located in EFFA, was a wheat plantation area. See Appendix D for more detail on the EFFA lysimeter. The lysimeters were placed inside their respective environment in order to provide sufficient fetch and minimize oasis effect. The main component of the lysimeter is a 3.54 m diameter and 0.9 m deep polyethylene tank. Data was stored manually. ET of the lysimeters was computed by the water balance equation expressed Appendex C equation (c.1)

A weather station was installed southeast from the lysimeter to monitor the meteorological parameters in the experimental farm. Solar radiation, net radiation, air temperature, relative humidity, atmospheric pressure, wind speed and rainfall were recorded at 5 hour intervals.

Because there was no satellite image available for the same date with the field experiment lysimeter data for 2006, so we recommend doing this verification in the future.

4.5.3 Comparison the simulation and observation data.

The measured and simulated is compared, the relative error is calculated as:

$$\mathrm{Re}\,lativeError = \frac{|\,simulation - observation\,|}{observation} \qquad\qquad .....(4.14)$$

The absolute error is calculated as (mm/day):

$$AbsoluteError = | simulation - observation |$$ ……(4.15)

The average of the relative error and the absolute error was also calculated.

This was conducted to determine whether a day was water-stressed in alfalfa field. The non-stressed (alfalfa , mm/day) calculated by FAO Penman-Monteith equation and was compared to the corresponding observation which was obtained from Yemen NWRA Climate Center. The Grape orchard was always well-irrigated and non stressed.

Intercomparison of different methods also used for validation and verification the developed model on the three climatic stations NWRA, CAMA and AREA, was done. The reference ET values were estimated by all applicable methods using the spreadsheet on Microsoft Excel for this research. The FAO24-Penman method resulted in alfalfa reference evapotranspiration ET_r which were adjusted to ETo by dividing the ET_r values by 1.15. The ETo values obtained by different methods were multiply by the crop coefficient planting in the same data (in this study the grapes) to obtain ET_c or ET, then the result compared with the FAO-56 Penman-Monteith ET estimate and SEE values were calculated as follows:

$$SEE = \left[\frac{\sum (Y_i - Y'_i)^2}{n-1} \right]^{0.5}$$ ……(4.16)

Where:

SEE is standard error of the estimate; Y is ET estimated by the standard method Penman-Monteith method; $Y\hat{} =$ corresponding ET estimated by the comparison method; and n is total number of observations. The SEE gives equal weight to the absolute differences between the standard method and the comparison method. It is a measure of the goodness of fit between the ET values estimated by the different methods and the standard method. The SEE has units of mm/day and n-1 degrees of freedom.

Linear regression analysis was performed between the *ET* estimates by the standard and comparison methods as follows:

$$ET_{Penman\text{-}Monteith}=b *ET_{method} \quad …… (4.17)$$

Where:

b=regression coefficient.

Regression through the origin was selected to evaluate the goodness of fit between the ET method estimates and the Penman-Monteith estimates because both values should theoretically approach the origin when the actual ET is zero.

4.6   Comparison of NOAA AVHRR and Landsat TM

Spectral reflectance of the red and near infrared bands were extracted to compare with the band 1 (red) and band 2 (near infrared) reflectance of the NOAA AVHRR data, and the band 3 and band 4 for Landsat TM data. In order to match the red-band range of the NOAA AVHRR, red band reflectance of the Landsat TM was obtained by averaging the reflectance range from 0.58 to 0.68 μm. And similarly, near infrared reflectance was obtained by averaging the range from 0.73 to 1.05 μm to match the near infrared band of the NOAA AVHRR. The reflectances of grass, cattail and open water on the aforementioned dates were used in the comparison. Satellite reflectances were acquired from the calibrated bands 1 and 2 of NOAA AVHRR images at the Sana'a basin bare soil and vegetations area. Three vegetation indices, IR/R ratio, NDVI, and SAVI, were also generated from the red and near infrared reflectances.

4.7   **Fusion of multispatial information**

Working in the field of multi-sensor image fusion, the evaluation of the achieved results becomes relatively complex because of the different sources of data that are involved (Pohl and Van Genderen, 1998). It is even more difficult when multi-date composite data are used for data fusion. One of the possibilities is to validate findings from fused data by comparing with actual data sets or ground truth (Pohl and Van Genderen, 1998).

The fusion model was applied to satellite images from both the National Oceanic and Atmospheric Administration-Advanced Very High Resolution Radiometer (NOAA-AVHRR) and Landsat satellite images. NOAA-AVHRR images are characterized by a relatively high temporal resolution (once a day), but a low spatial resolution of approximately 1 km. Landsat images have a high spatial resolution of 30 meter, but a low temporal resolution of 16 days. An analysis of the growing season solely based on Landsat images is practically impossible as the chance of almost all acquisitions during the season being cloud-free is very low in most wheat areas.

$$ET_{fusion} = ET_{NOAA,i} \times ET_{TM,j} / ET_{TM\text{-}mean} \qquad \text{.......(4.18)}$$

Where:

i is the NOAA period and j is the corresponding Landsat image. The same method to calculate ET_{season} is applied to calculate seasonal biomass production from NOAA-AVHRR and Landsat biomass production maps.

4.8 Evapotranspiration Estimation by other Remote Sensing Methods

4.8.1 Simplified energy balance model

During an intensive field campaign in Sana'a basin, remote sensing images from satellite sensors were also acquired with spatial resolutions of 30m. Ground in situ measurements of surface temperatures, evaporative water losses, sensible heat fluxes, and the available incoming solar radiation, along with other meteorological variables, were conducted at three sites: one being with dominated by grape vines trees, one with plum trees, and another one with grasses.

The evapotranspiration (ET) or evaporative water losses to the atmosphere were estimated based on the basic water balance equation balance equation(2.30) which modified by (Jackson et al., 1977) as a function of the temperature difference between the surface and the air above dT equation 2.31. Thus ET values can be estimated with the differential temperature dT which can be obtained from remote sensing images (see Appendix E1 for more detail).

4.8.2 Biophysical estimation evapotranspiration model

Reference ET (ETo) was calculated from meteorological data with the FAO Penman–Monteith equation (mm/d) (Allen. et al., 1998). And Empirical methods based on VIs for estimating ET are modifications of the crop coefficient method to develop a VI–Kc curve over the crop cycle. They found close estimates of ET using the relationship between ET and LAI and between LAI and VI, using equation 2.32.
Thus ET values can be estimated with the differential vegetation indexes Vis and Kc which can be obtained from remote sensing images see Appendix E2 for more detail.

4.9 Decision Support System (DSS) Model Design (Planning Model)

The decision support system (DSS) is an integrated assemblage of models, data, interpretative routines, and other relevant information that efficiently processes input data, runs the models, and displays the results in an easy to interpret format. The system makes the support accessible to decision-makers. The DSS developed for ET estimation includes a model base with decision making capabilities, Microsoft excel, ArcGIS software and a database management system DBMS see Appendix B for more detail.

The performance of five Remote sensing ET estimation methods and six traditional methods based GIS table 4.12 .

Table 4.12. : Different ET estimation methods, governing equations

Grope	Approach	Method of ET estimation	Equations used No.	Reference
Remote Sensing (RS)	Remote Sensing (RS) (energy balance)	SEBAL	Eq. 4.12 and 4.13.	(Basteaanssen et al ,1998)
RS	RS (energy balance)	SEBAL$_{-ID}$	Eq. 2.38 to 2.39	(Tasumi. Et al, 2000)
RS	RS (energy balance)	modified SEBAL (M-SEBAL)	Eq. 3.75 and 3.76	this study
RS	RS Vegetation index	Biophysical	Eq. 2.32	Kustas and Norman (1996)
RS	RS Surface temperature	Simplified energy balance	Eq.2.31	Jackson et al. (1977),
*Hydrology modeling (H) based GIS	Combination	FAO-56 Penman-Monteith FAO	Eq.2.13	FAO-56(Allen. Et al,1998)
*H-GIS	Combination	FAO-24 corrected Penman	Eq.2.11	FAO-24 Doorenbos and Pruitt (1977)
*H-GIS	Radiation	FAO-24 Radiation	Eq.16	FAO-24 Doorenbos and Pruitt (1977)
*H-GIS	Radiation	Priestley-Taylor	Eq.2.14	Priestley and Taylor, 1972
*H-GIS	Temperature	Hargreaves	Eq. 2.17	Hargreaves and Samani (1985)
H-GIS	Temperature	SCS Blaney-Criddle	Eq. 2.21	Doorenbos and Pruitt (1977)

*This models have calculate reference ET (ETo) which was multiplied by crop coefficient (Kc) map of the study area in order to estimate the actual crop evapotranspiration. While the remote sensing methods estimate the actual evapotranspiration direct.

Despite numerical discrepancies, most of the available ET methods can effectively capture the time series structure, which can avail in the ET record, slowly because, the inherent characteristics of most methods contain a radiation component in their model structure, which is noted to cause three-fourth of water loss through evaporation (Moges et al, 2002).

Three climatologically stations in Sana'a basin, namely, CAMA, NWRA, and AREA (Al-irra) figure 4.2, were selected for this study based on the location characteristics and data availability. The description of the different weather stations along with the data available and time scale is given in Table 4.5.

4.10   Methods used to compute the water balance

Several methods for estimated water balance was developed and published. This method depended on the study areas and the purposes of these studies. In this study two methods for water balance were investigate and propose for estimating water balance using remote sensing and GIS techniques' and support for future work, these method are : Regional water balance in watershed and water balance in the field irrigation.

4.10.1 Regional Water Balance in Watershed.

The water balance of a particular region represents a measure of the inputs to the hydrology system and outputs from that system over a specified period of time. In this case where a daily water balance is desired, therefore a decision was made to partition

the study area into incremental drainage units based on the location of stream gauge stations.

The equation for calculate the water balance of each gauging station zone is:

$$dS/dT = I - Q \qquad \qquad \text{......(4.19)}$$

Where:

dS is the change of the volume of water stored in each gauging station zone, dT is the change of the time index, and I and Q are inflow to the gauging station zone and outflow from the gauging station zone, respectively. The term on the right (I-Q) can be rewritten to account for the area of the gauging station zone:

$$I - Q = (P - E)A + SQ_{in} - Q_{out} \qquad \qquad \text{......(4.20)}$$

Where P is the rate of precipitation, E is the rate of evaporation, A is the area of the gauging station zone, SQ_{in} is the sum of the inflows recorded at gauges whose flows enter the zone and Q_{out} is the outflow at the downstream end of the zone.

The change in storage (ΔS) can be found by combining equations 4.19 and 4.20 and integrating each term over a time interval of one day (Δt):

$$\Delta S = P\Delta tA - E\Delta tA + SQ_{in}\Delta t - Q_{out}\Delta t \qquad \qquad \text{......(4.21)}$$

In order to express ΔS in terms of average depth over the gauging station zone area, equation 4.21 can be rewritten as the following $(\Delta y = \Delta S/A)$;

$$\Delta y = P\Delta t - E\Delta t + (I/A)[SQ_{in}\Delta t - Q_{out}\Delta t] \qquad \qquad \text{......(4.22)}$$

Where:

Δy is the change in storage depth per unit area of gauging station zone.

The values of Δy were computed on daily basis (1 June 1998 to 9 August 1998) for each zone.

Precipitation values obtained from the NWRA daily file were treated in a similar manner to the stream flow data. A total of 3 climate stations were mapped.

The Arc-GIS GRID function "zonal average" was subsequently used to obtain an average value of precipitation depth, as evapotranspiration (ET), over the gauging station zones.

These grids were created by subtracting Q_{out} from the sum of Q_{in}, and dividing the answer by the area of the gauging station zone. The final map series involves a combination of all of the preceding maps. Daily storage change Δy grids were produced using the map algebra function in ARC/INFO GRID and equation 4.22. essentially, the equation changed to:

$$S\ Grid = P\ Grid - E\ Grid + (I/A)[NS\ Grid], \qquad …..(4.23)$$

Where S Grid is grid of daily storage depth change, P Grid is a daily precipitation grid, E Grid is a daily evaporation grid, and NS Grid is a daily net stream flow grid. Maps of cumulative storage depth were obtained by summing the grids. The resultant 4 grids show the water storage depth of each gauging station zone in the study area on a daily basis. See Appendix F for more detail

4.10.2 Propose water balance estimation method in the field irrigation using remote sensing.

Precipitation provides part of the water crops need to satisfy their transpiration requirements. The soil acts as a buffer, stores part of the precipitation water and returns it to the crops in times of deficit. In humid climates, this mechanism is sufficient to ensure satisfactory growth in rainfed agriculture. In arid climates or during extended dry seasons, irrigation is necessary to compensate for the evaporation deficit due to insufficient or erratic precipitation. Net irrigation water requirements in irrigation are

therefore defined as the volume of water needed to compensate for the deficit between potential evapotranspiration and effective precipitation over the growing period of the crop. For a given period, the primary crop water balance is calculated as follows (Faures et al 2002).

$$IWR = K_C . ET_o - P \qquad \qquad ......(4.24)$$

Where:

IWR is the net irrigation water requirement needed to satisfy crop water demand

Kc is a coefficient varying with crop type and growth stage, ET_o is the reference potential evapotranspiration, depending on climatic factors, P is the precipitation.

Using remote sensing techniques the *IWR* was calculated for different cultivated crops in the study area. Since, the equation (4.24) has used just two main components of water balance model of an irrigated area, *ET* or ET_c *(Kc*ET$_o$)* can be estimate from remote sensing by M-SEBAL model and *P* can be measure by gauge station and chang to grid using ARC-GIS see Appendix F for more detail.

CHAPTER 5

RESULTS AND DISCUSSION

5.1   Overview

In general the discussion and presentation of results are presented in several parts. The **first** part is the overview. The **second** part is related to the Derivation of parameters in modified SEBAL model, calibration, sensitivity analysis and refinement the surface parameter from the remote sensing model, which was done by comparing with measured surface parameter and ET with estimated ET using Landsat 5 and NOAA-AVHRR imagery. The **third** part of the presentation includes the validation of the modified SEBAL by comparing measured ET with estimated ET using Landsat 5 and NOAA-AVHRR imagery. Then the **fourth** part discusses the comparison of ET using NOAA-AVHRR and Landsat-TM Images, and comparing estimates of actual evapotranspiration from satellites, hydrological Models, and water balance model (lysimeter) field data : a case study from mountains region Yemen. The years used for model validation were 1995 and 1998 which were used to sincere with the lysimeter reading in the area of Sana'a basin, Yemen. The **fifth** part fusion ET from medium spatial resolution, low temporal resolution. Landsat images with low spatial resolution, high temporal resolution, NOAA-AVHRR using fused model. The **sixth** part include Analysis of behavior modified SEBAL in different areas study, this present result of application modified

SEBAL using Landsat 5 TM and NOAA-AVHRR images, in mountains (territorial, agricultural, volcanic and basalt), desert and coastal regions in the central-Western mountains of Yemen, central-Eastern part of Yemen and in the Southern coastal of Yemen.

The **seventh** part include the Difference between modified SEBAL, SEBAL and other SEBAL's variants. The **eighth** part is include Regional DSS-ET maps for Sana'a basin, Yemen. And the last part showing the Regional Water balance propose model.

Figure 5.1 shows an illustrative map of estimated daily ET predicted for the Landsat 5 TM (A) and NOAA-AVHRR (B) scene corresponding to 1st and 10th June 1998 for the Sana'a Yemen. Maps were created for three dates during 1995-1998 when concurrent micrometeorological data, and cloud free satellite images were available.

A   B
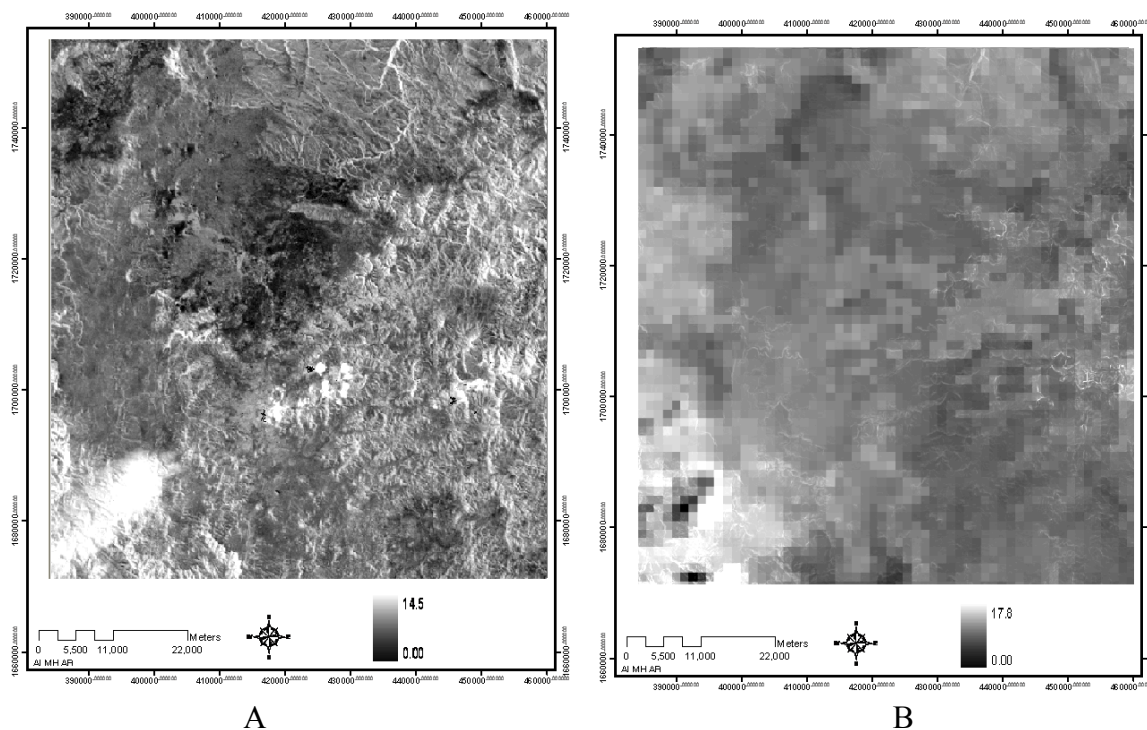
Figure.5.1   estimated daily ET predicted for the Landsat(A) and NOAA-AVHRR(B) images Dec.1995

5.2   Derivation of parameters in modified SEBAL model

This section describes results of calibration, verification, and sensitivity analysis of modified SEBAL. A large amount of model development work focused on arid mountain applications. In this study, no verification has been made for arid mountainous regions due to lack of suitable data and time constraint, thus, further improvements are definitely needed. However, this study has provided some directions for estimating ET from mountain areas. The effects of the series of corrections to the energy balance for mountains are demonstrated in this section. The results are mostly from the modified SEBAL application for 1995 and 1998 images. The modified model is more complicated than classical SEBAL but more comprehensive. The following sections illustrate how the modified SEBAL model and classical SEBAL model calculate energy balance of mountain areas.

5.2.1.   Estimation of surface Albedo (α)

The estimated Albedo by the method described in section 4.4.4, have agreed well with the general values given in Table 4.9. Figure 5.2 shows estimated Albedo in agricultural areas. The low NDVI indicates an essentially bare soil condition and high NDVI indicates an essentially full covered crop condition. The estimated Albedo for field bare soil varies from 0.018 (dark volcanic areas and bare soil fields) to 0.51 (possibly bright rocks in the north of the basin) from landsat TM images and from NOAA-AVHRR images data varied from 0.084 to 0.793. The soils in the study area are mostly silt loams and sandy loams. As for bare soil fields, there are no appropriate reference values shown in Table 4.9 However, the estimated Albedo range 0.018 - 0.51 is similar to the reference values for black soil in the minimum (0.08 - 0.14) and similar

to the reference white –yellow sand in the maximum values, and comparing with the result reported by Brutsaert (1982) and Tasumi(2003).

The estimated Albedo from full covered crop fields is ranging from 0.15 to 0.25, from both Landsat 5 and NOAA-AVHRR images in figure 5.2. The major crops in this area are pasture, grapes, plum, wheat, potatoes, corn and mostly alfalfa. The estimated values 0.15-0.25 agreed very well with the reference values of pasture (0.15-0.25) and Maize (0.14-0.22) in Table 4.9.

A   *B*
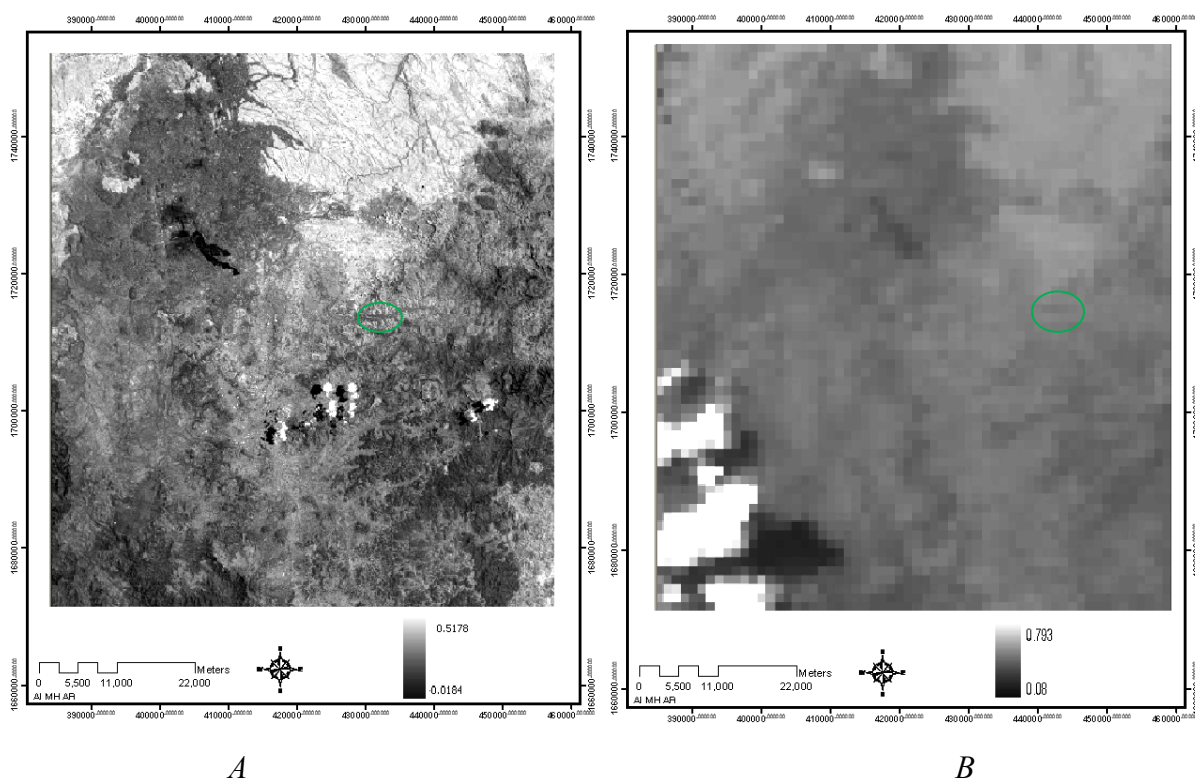
Figure 5.2   Estimated Albedo values of agricultural landuse, by Landsat 5 image(A 6/01/1998) and NOAA-AVHRR image (B, 6/10/1998).

Several studies have shown that the ratio of Albedo (*a)* is related to factors such as the normalized difference vegetation index (NDVI). In this study, equation (5.1) was adapted using actual measured data from the field observation, for agricultural fields around Sana'a basin, Yemen. The regression equation relating surface Albedo and NDVI of the study area is shown in figure 5.3.
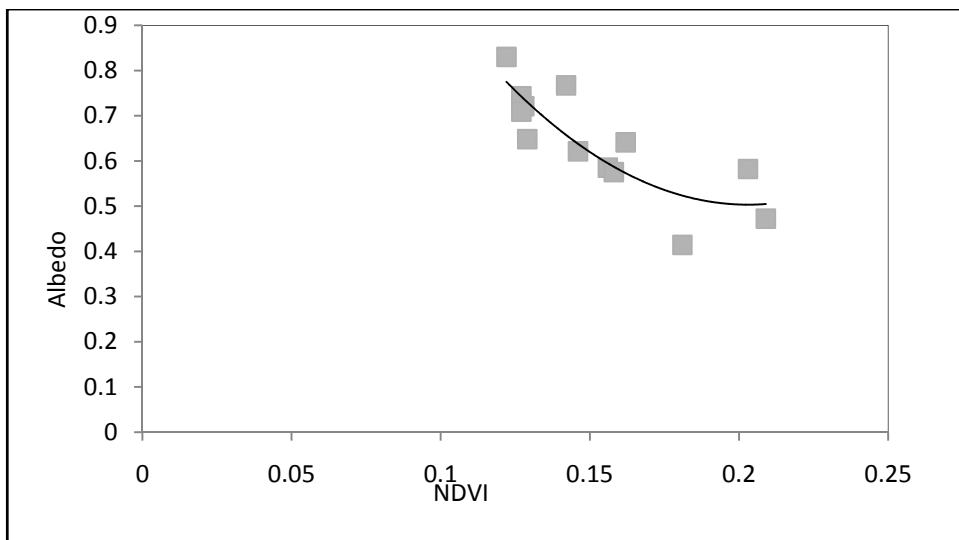
Figure 5.3   Surface Albedo versus of Normalize vegetation index from Landsat 5 image (6/01/1998)

$$a_s=41.398NDVI^2 - 16.811NDVI+2.2099 \quad …………(5.1)$$

The figure 5.4 shows the estimated Albedo values for desert wadi Hadramout. The values range from 0.06 to 0.56; although no reference value is available in Table 4.9, however, this may be because of the mixed between the Black Mountain and white and yellow sand soil in the desert from the images from 1998.
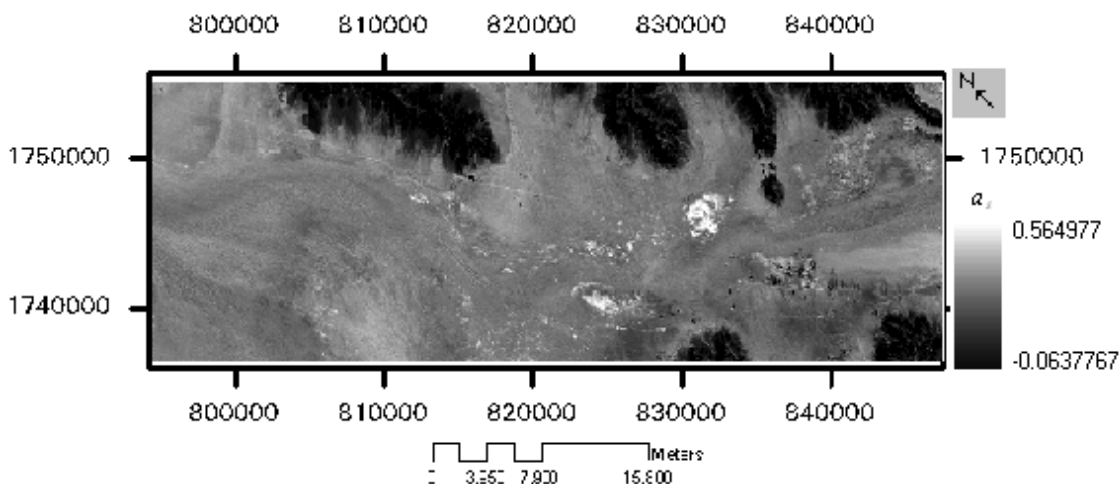
Figure 5.4   Estimated albedo values of desert Wadi Hadramout surface, by Landsat 5 image08/16/1998

Figure 5.5 shows the estimated Albedo value of salty surfaces in *Wadi Tuban* ranged from 0.096 to 0.37and there were no confirmation with the values given in Table 4.9.
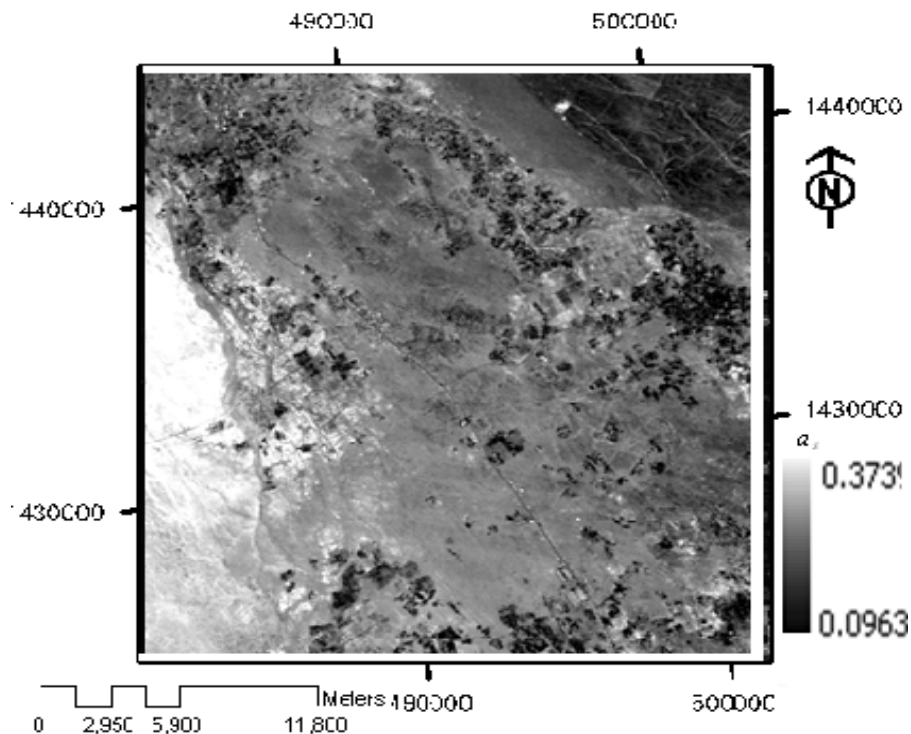
Figure5.5   Estimated albedo values of Wadi Tuban, by Landsat 5 image
(4/21/1998)

Albedo value at Surfaces, from thirteen samples in total from agriculture areas using
Landsat 5 TM and same number from NOAA-AVHRR .

Figure 5.6 shows Albedo value at Surfaces, from thirteen sample points taken from
agriculture areas using Landsat 5 TM and also from NOAA-AVHRR images data.

A
B
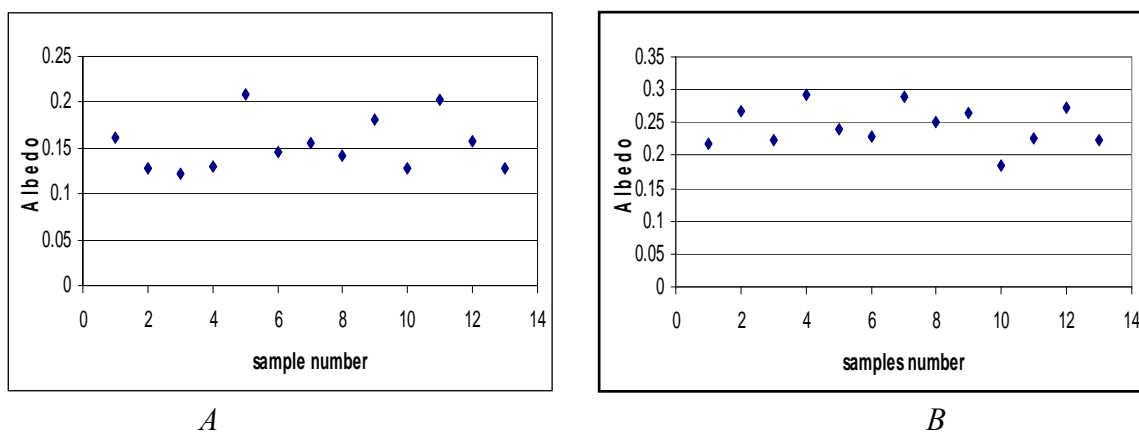
Figure.5.6   Estimated Albedo values of agriculture areas, by (A) from Landsat 5
image 06/01/1998 and (B) from NOAA-AVHRR 06/10/1998

5.2.1.1   Sensitivity of modified SEBAL to Topographic Correction for Shortwave Radiances

Through sensitivity of SEBAL for the use of topographic corrected radiances for the shortwave bands it was found that, even though the surface albedo values were different; These differences did not have a substantial effect on the final estimation of ET. In Figure 5.7 comparison between SEBAL estimates of ET using albedo calculated from equation 3.25 and SEBAL estimates of ET using topographic corrected reflectances is displayed.
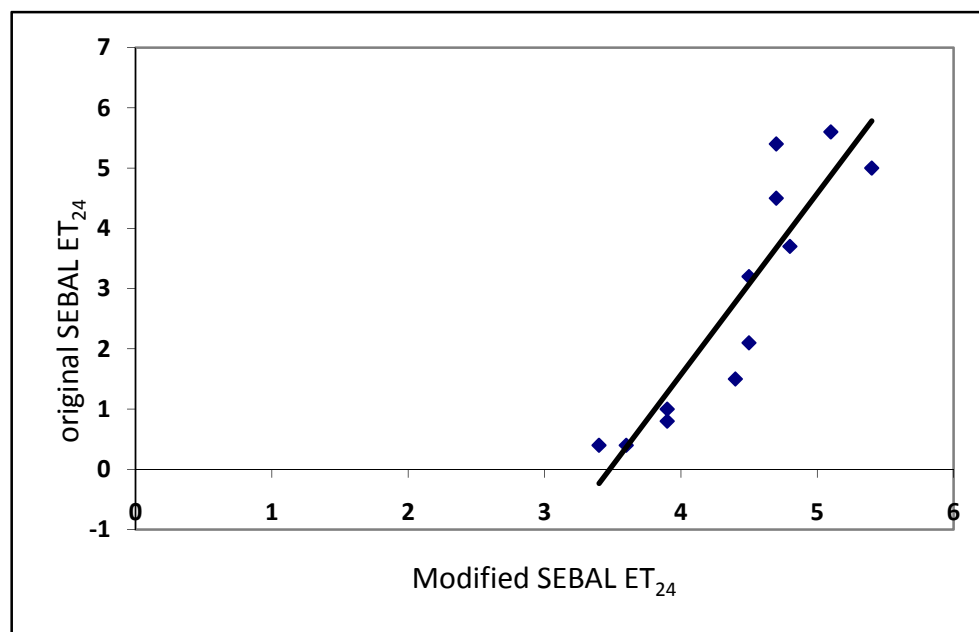
Figure 5.7   Comparison of SEBAL ET_{24} estimates using Albedo from Bastiaanssen, et al.1998b Eq(3) and using Corrected Reflectance in modified SEBAL Eq.(3.25). Equation of fitted line is y = 3.008x - 10.46 with R^2 = 0.816

In Figure 5.7 it can be seen that the normalized differences between estimates of ET in agricultural areas are not significant. Consequently it could be concluded that the definition of ET at the hot and cold pixel is controlling part of the biases and errors introduced for the application of equation 3.24 which a considers a broadband transmittance for shortwave radiation.

5.2.2. Derivation Vegetation index (NDVI) and Leaf Area index (LAI) function

During the model development, it was concluded that using L = 0.9 in SAVI equation 3.27 efficiently eliminated the soil background information for Sana'a Basin Yemen conditions. Figure 5.8 is a plot of an analysis showing that L = 0.9 works well for bare soil conditions in Sana'a basin Yemen. The optimal L value can be changed according to the availability of vegetation information (Huete, 1988 and Tasumi, 2003). This high L value derived by this analysis compared to the generally used value 0.5, probably explains the uniformity of soil type within one Landsat TM and AVHRR images.
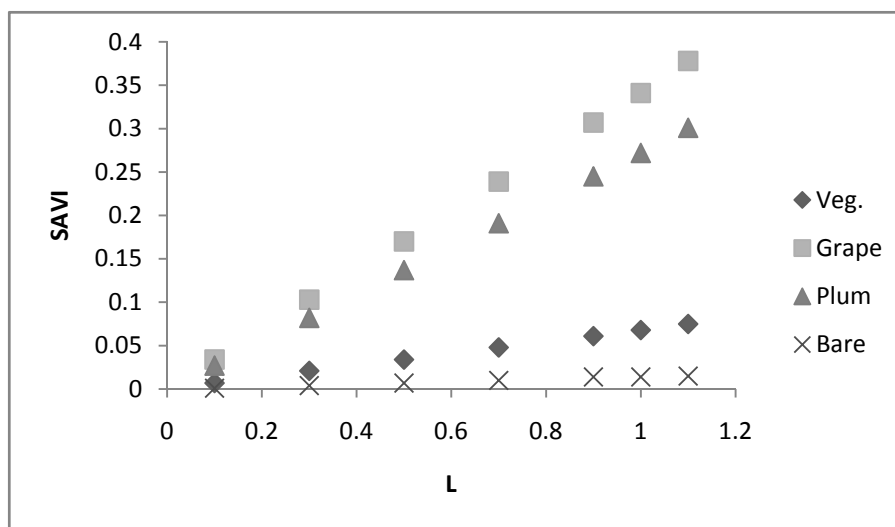
Figure 5.8.   Change in SAVI value with various L values for 6 soil and bare soil conditions in Sana'a basin Yemen.

Figure 5.9 shows the comparison of LAI values estimated by Equation 3.28 using NOAA-AVHRR and Landsat TM images. Overall, the estimated LAI value agreed well with the observed value. It was also confirmed during the modified SEBAL application that the estimated LAI gives reasonable values in most case of agricultural fields.

However, the LAI estimation equation has not been tested for other areas and other landuse types, or with other ground-based LAI data.
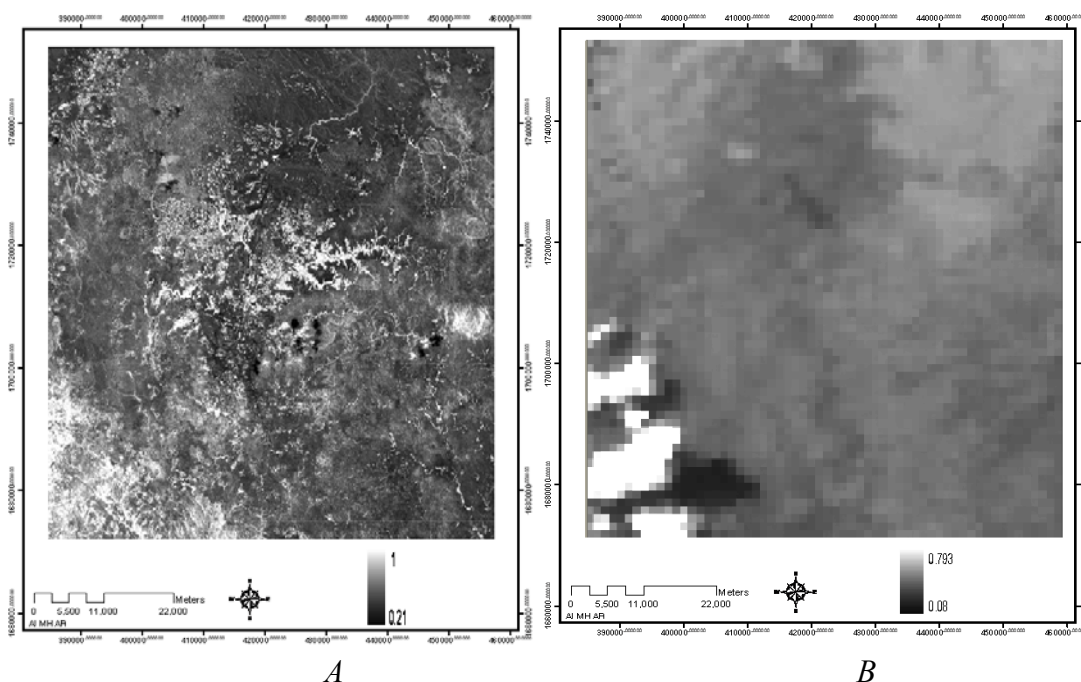
Figure 5.9.   Estimated LAI from Landsat TM (A) and from NOAA-AVHRR (B) images

To avoid confusion with the general SAVI computed using L = 0.5, the SAVI computed using L - 0.9 is termed SAVI. From Equation 3.27, SAVI is:

$$SAVI = \left(\frac{IR-R}{IR+R+0.9}\right) x (1+0.9) \qquad \ldots\ldots\ldots(5.2)$$

LAI is the ratio of green leaf area to a unit area of land surface. It is dimensionless (i.e., units of m^2/m^2). Bastiaanssen (1998) summarized the method for calculating LAI from SAVI, and the following its equation for general agricultural crops, see regression figure 5.10:

$$LAI = 2.006 * SAVI - 0.102 \qquad \ldots\ldots..(5.3)$$

Equation 5.4 is derived by an analysis of LAI predicted by Equation 3.28 for fields in Sana'a Basin, Yemen, indicated LAI calculated using SAVI with L = 0.5 did not agree with actual measurements of LAI. The estimation was in much better agreement when SAVI was

used in Equation 5.4 where the SAVI constant L is 0.1 . Use of SAVI did not require modification in any of Bastiaanssen's original coefficients.

$$LAI = \frac{\ln\left(\frac{0.7 - SAVI}{0.6}\right)}{0.9} \qquad \ldots\ldots(5.4)$$

The relation between SAVI and LAI can changed depending on the location and soil/crop types. Equation 5.4 is empirical and is not considered to be a universal equation. Tasumi, (2003) was developing two different equation called $SAVI_{ID}$ and LAI_{ID} to work under Idaho, USA condition.
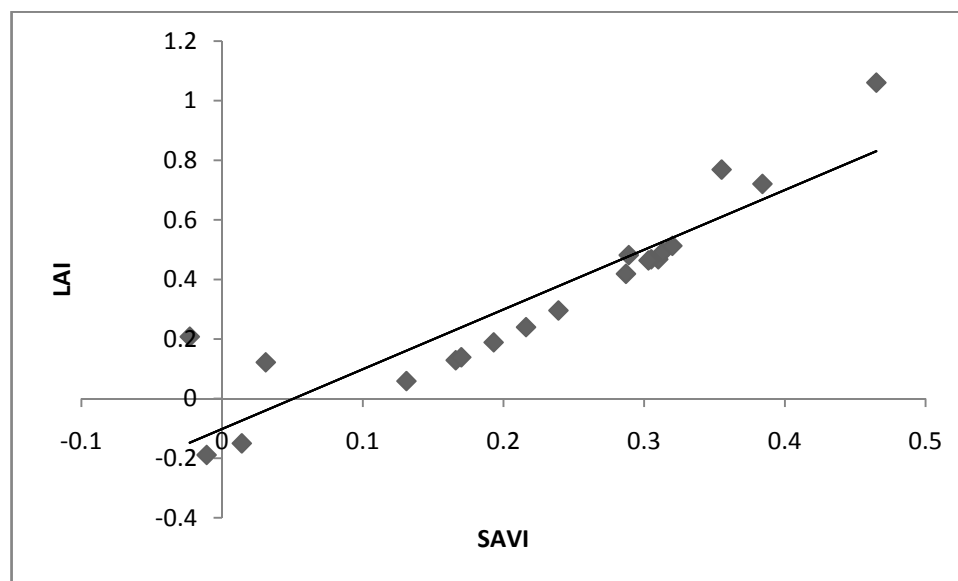
Figure 5.10 shows the correlation between LAI and SAVI under different land use in Sana'a basin Yemen. Equation of fitted line is y = 2.006x - 0.102 with R² = 0.823

5.2.3   Surface temperature, T_s

Corrected surface temperature is referred to as a DEM was calculated using Equation 3.39 was applied to modified SEBAL application in Yemen Mountain. Figure 5.11 shows the surface temperature maps estimation from Landsat TM (A) and NOAA-AVHRR image (B). Figure 5.12 show the effect of surface temperature correction was small over the area. However, the effect became larger when the land surface was hotter. As in 1st and 10th June 1998 images.

A   *B*
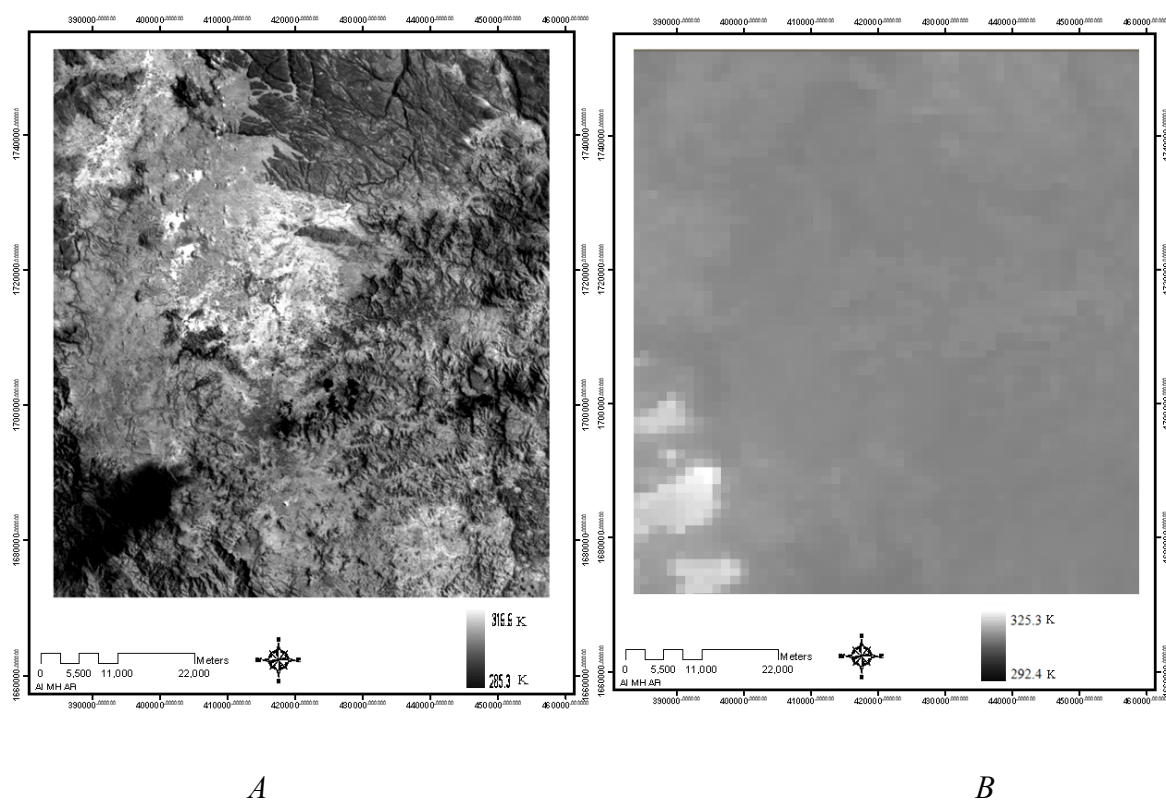
Figure 5.11   Estimation of surface temperature (K) from Landsat TM (A) and NOAA-AVHRR images (B)
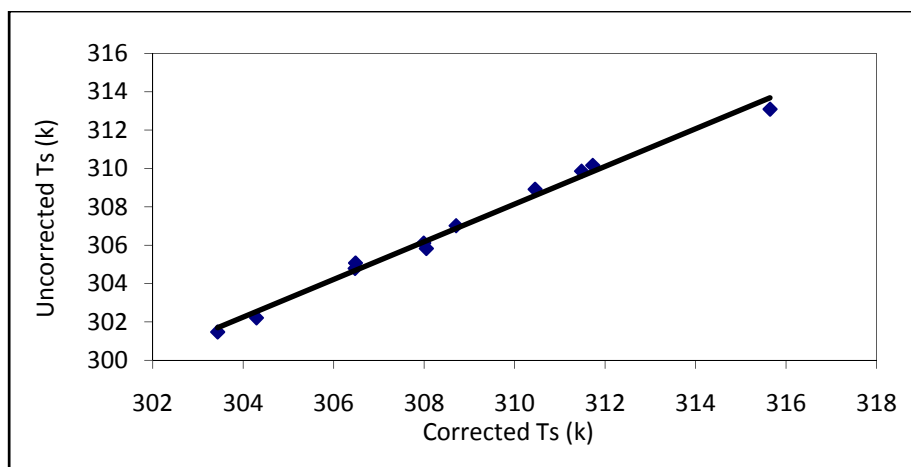
Figure 5.12 Corrected and uncorrected surface temperature for different landuse types
Equation of fitted line is $y = 0.981x + 3.752$ with $R^2 = 0.990$

Fortunately, modified SEBAL is not sensitive to these errors. This agrees with the result from Tasumi, (2003). When uncorrected surface temperature is used, the error in surface temperature estimation is absorbed at the dT estimation and therefore a bias does not appear in the final ET estimation, although uncorrected temperature generates small random error (Figure5.13). In Figure 5.13, slope of ET which predicted the corrected T_s was compared to ET without T_s correction and $R^2 = 0.83$ indicated little error impact at all ranges of ET. Some errors occur in the R_n calculation due to error in $R_{L\uparrow}$. However, many of this error impacts are calibrated into the dT function at the cold and the hot pixels.
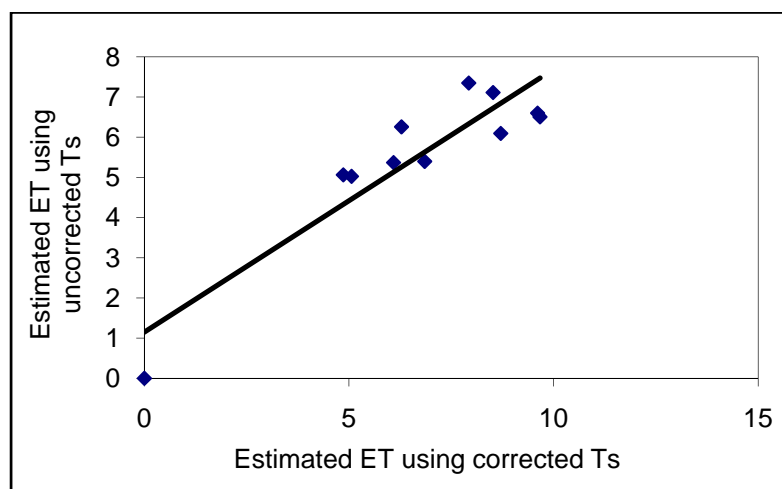
Figure 5.13. ET 24-hour by corrected and uncorrected T_s for all landuse types
Equation of fitted line is $y = 0.653x + 1.151$ with $R^2 = 0.832$

The error becomes high when only agricultural fields are focused as shown in Figure 5.14. This is because the "bias" for the uncorrected surface temperature is nearly perfectly eliminated by the dT function.
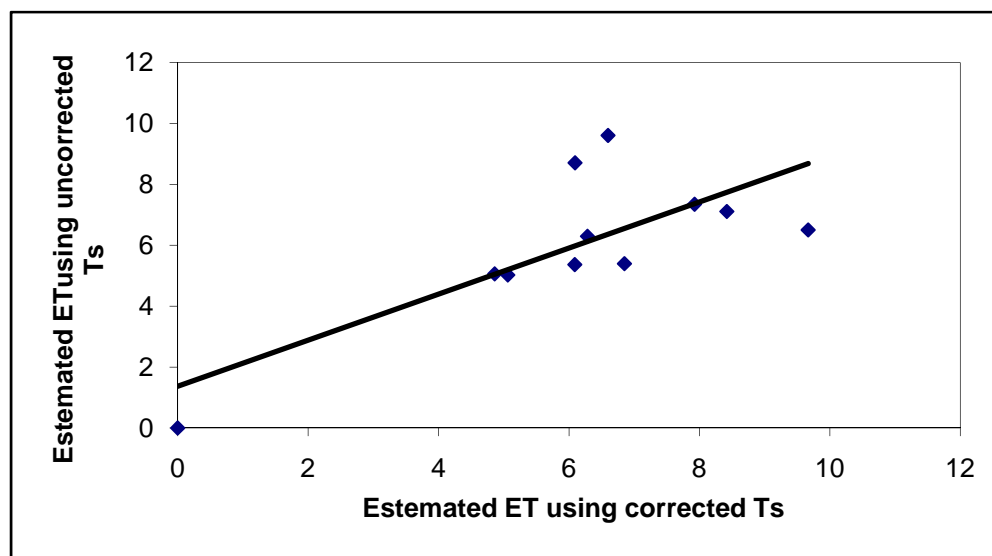
Figure 5.14. Estimated 24-hour ET by corrected and unconnected T_s for agricultural landuse Equation of fitted line is y = 0.756x + 1.370 with R^2 = 0.570

5.2.4 Derivation of DEM adjusted surface temperature $T_{s\text{-DEM}}$

The lapse rate of surface temperature was assumed to be 6.5°C/km, which is a general lapse rate for moist air (Roberson and Crowe, 1997). Figure 5.15 is an example of the trend of T_s and calculated $T_{S(DEM)}$ for the mountainous areas. It seems that by applying the 6.5°C/km lapse rate, the distribution of $T_{S(DEM)}$ becomes random with elevation. This indicates that $T_{S(DEM)}$ efficiently eliminates the elevation effect from the surface temperature. Most of the variation in $T_{S(DEM)}$ after correction for lapse was due to slope and aspect of the surfaces in the mountains as shown in figure 5.15 images

A,B,and C show the change of surface temperature influenced by elevation and also by the surface aspect.

| | A | B | C |
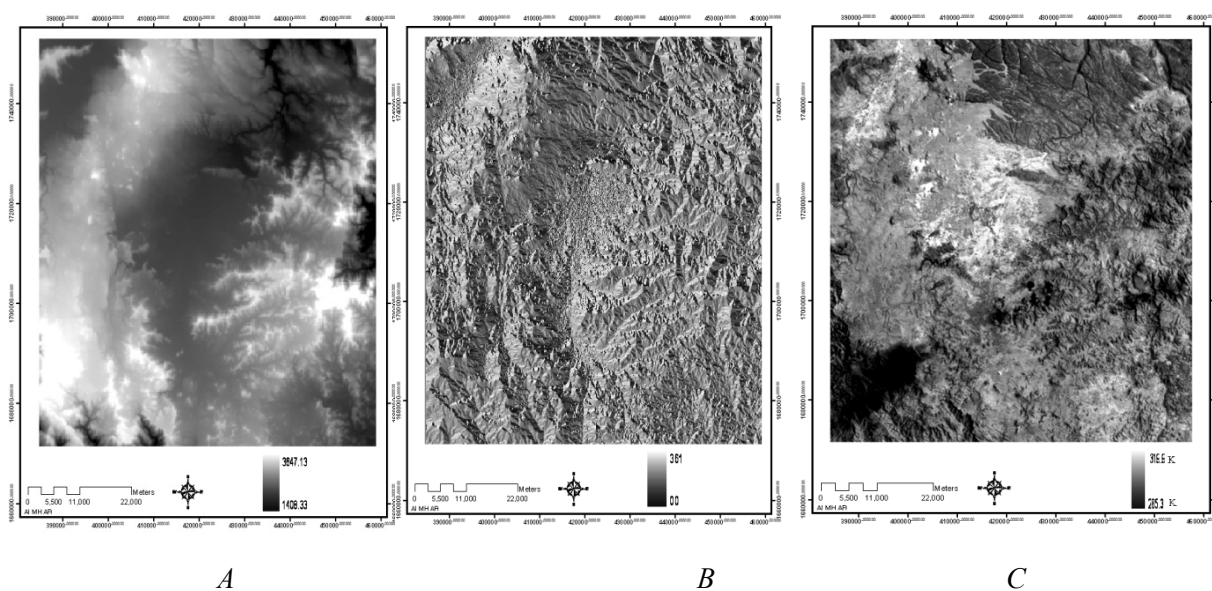
Figure 5.15 Digital Elevation Model (DEM) (A) compared to surface aspect angle (B) and instantaneous Ts (C) for the study area images

5.2.4.1 Sensitivity of modified SEBAL to Surface Temperature

Energy balance calculations in modified SEBAL make use of radiometric surface temperature in nearly every component of the surface energy balance. Net radiation calculations use T_s to compute outgoing and incoming longwave radiation (as shown in equation 3.42, and 3.44). Later the ratio G/R_n uses surface temperature if Equation 3.49 is applied. Finally the computation of sensible heat requires the definition of a T_s versus dT linear relationship Equation 3.62. This dependence of modified SEBAL on radiometric surface temperature indicates that the model needs a really accurate estimation of T_s. This argues for the need to correct radiometric surface temperature measurements taken by satellite for atmospheric interactions. Fortunately, in modified SEBAL the use of two

indicator pixels (cold and hot pixels), that define the sensible heat for two extreme conditions of the dT functions, makes modified SEBAL, less sensitive to the use of corrected radiometric surface temperatures. This is because the specification of H on these two pixels incorporates biases present in the T_s layer. In Figure 5.13 estimated values for 24 hour ET using corrected radiometric surface temperature are compared with estimated 24 hour ET using uncorrected (apparent) surface temperature for all land use area and for agricultural pixels only on the basis of Figure 5.14, it is concluded that the way modified SEBAL defines the sensible heat flux at the cold and hot pixels, substantially offsets the biases introduced by using uncorrected surface temperatures. The slope and intercept of the plot of estimated ET, with and without corrections of T_s, shows that the use of thermally corrected surface temperatures is not a strong requirement in modified SEBAL. This is an extremely valuable attribute of modified SEBAL and illustrates the importance and value of specifying energy components at known pixels (cold and hot pixels).

5.2.5   Ground heat flux, G

Soil heat flux is usually measured with sensors buried just beneath the soil surface. A remote measurement of G is not possible but several studies have shown that the day time ratio of G/Rn is related to factors such as, the normalized difference vegetation index (NDVI). In this study, equation (5.6) was adapted using actual measured data from the field study, for agricultural fields near gauging satiations in Sana'a basin, Yemen, and comparing it with the value of the NDVI from the images data in the same point. The following equations were adapted, the figure 5.16 showing the regression equation.
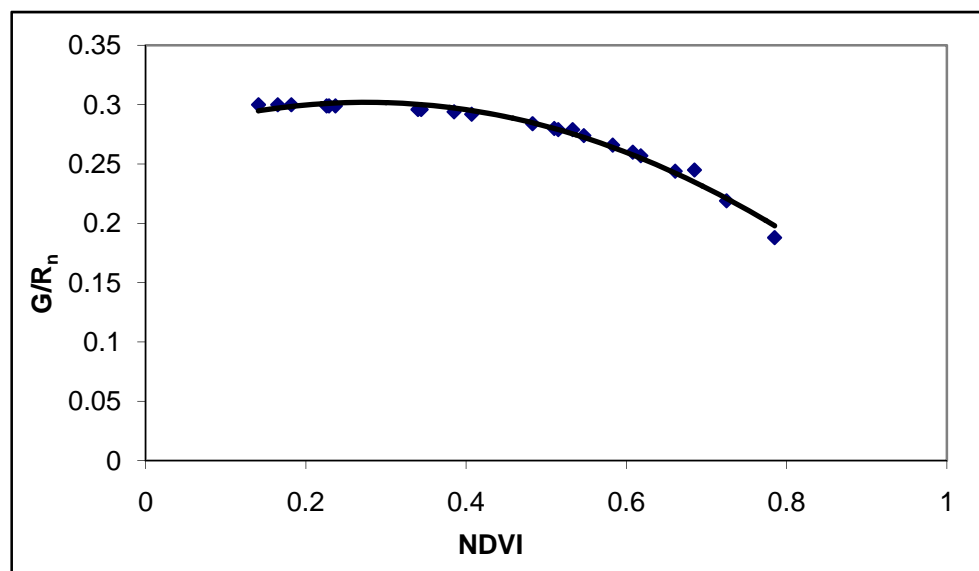
Figure5.16. the regression equation for *G/R$_n$*. Equation of fitted line is $y = -0.400x^2 + 0.220x + 0.271$ with $R^2 = 0.981$

G as an empirical fraction of the net radiation using surface temperature, surface Albedo (α) and NDVI and was adopted here to compute G as:

$$G = R_n\left(-0.4005\,NDVI^2 + 0.2207\,NDVI + 0.2715\right) \qquad \text{......(5.6)}$$

Where:

NDVI is the normalized difference vegetation index, is calculated as the equation 3.26.

The estimated G value from equation 5.6 was not much different from the estimated values from Bastiaanseen's equation 3.49. The results of the comparison are shown in Figures 5.17. The estimated G values by equations 5.6 tend to be lower in crop covered conditions and higher in bare soil conditions over a wide range of land conditions. This means that estimated G by Equation 5.6 has reasonable accuracy in modified SEBAL at least in agricultural fields in Yemen mountainous area. The agreement with prediction by Equations 5.6 constitutes a completely independent validation for agricultural areas. Equation 3.49 was kept in modified SEBAL instead of equations 5.6 because the first equation is more widely used by many SEBAL users in

many landuse types including agricultural fields and deserts, where Equations 5.6 was developed only with agricultural data.
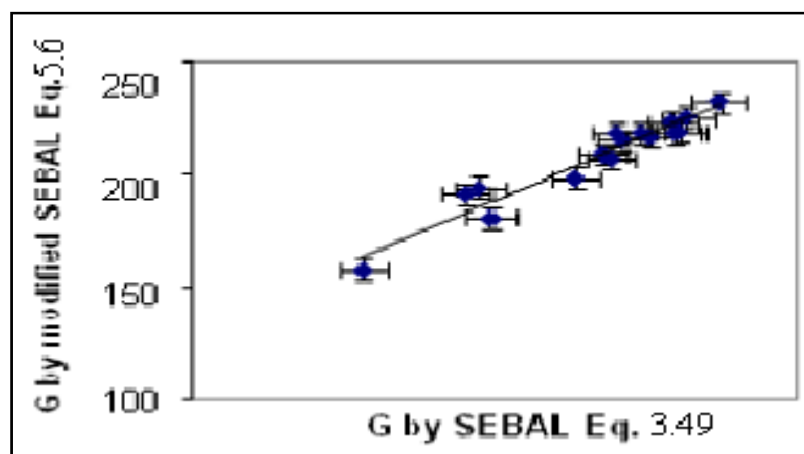
Figure 5.17. Comparison of Eq. 3.49 (SEBAL) and modified SEBAL Eq.5.6 for G estimation. Equation of fitted line is y = 0.811x + 42.81 with R² = 0.932

5.2.6   Surface roughness of momentum transport (Z$_{OM}$)

According to the section 3.6.3.4, the z_{om} for each pixel is calculated by a regression equation according to the pixel value. The equation is obtained by three pairs of known values of z_{om} and $NDVI$. This study used the Plum (maturity growing) has z_{om} =1.1 m and NDVI=0.464, for alfalfa z_{om} =0.03 m and NDVI=0.248, and bare agricultural field z_{om} =0.00 m and NDVI=0.113, then a regression equation for z_{om} Figure 5.18 was obtained.
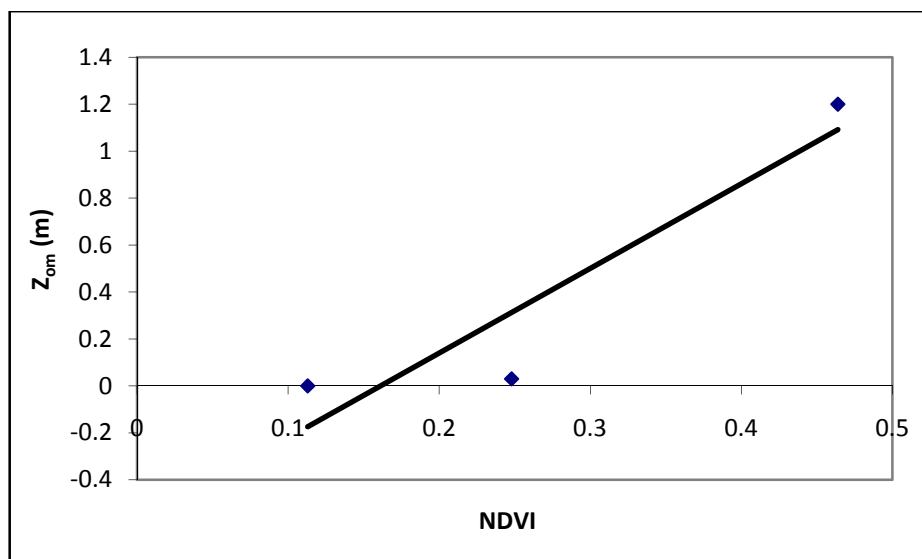
Figure 5.18   One example of a regression equation for z_{om} from NDVI.
Equation of fitted line is y = 3.604x - 0.581with R^2 = 0.869

$$z_{om}=3.6047\ NDVI-0.5813 \qquad\qquad \text{.......(5.7)}$$

The estimation of z_{om} is a weak point in modified SEBAL. Especially, the accuracy of z_{om} estimation for landuses apart from agriculture is limited. However, ET estimation is not so sensitive to z_{om}. Therefore, the low quality of z_{om} estimation in modified SEBAL does not cause large error in ET. This is especially true for areas having high ET where H is small. In agricultural areas, estimated ET is not impacted even if z_{om} is doubled or halved Figure 5.19. This is because that z_{om} value is used as log of $200/z_{om}$ in u* estimation Equation 3.52.
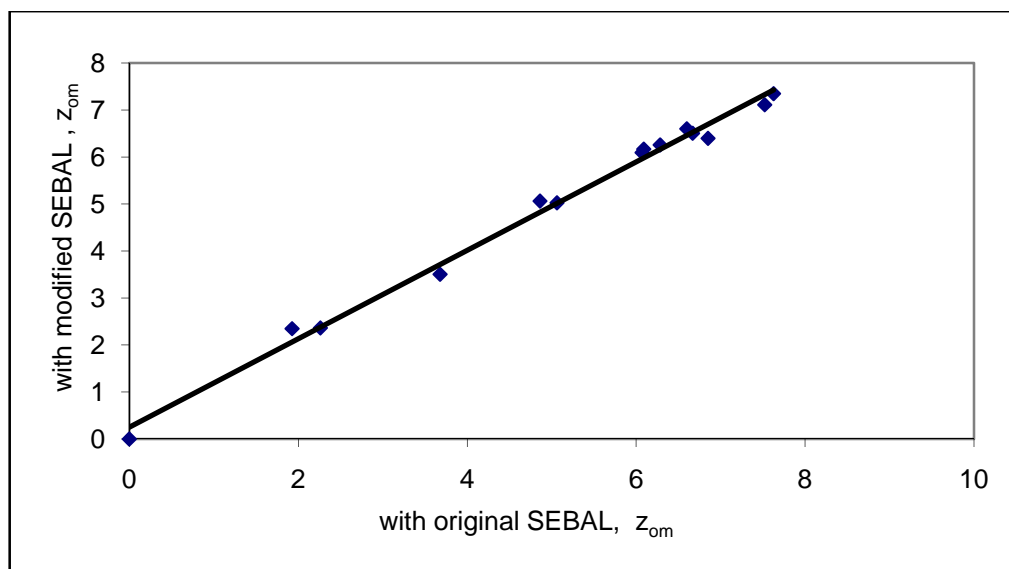
Figure 5.19.   Impact of error in z_{om} values on estimated ET, from agricultural areas.
Equation of fitted line is $y = 0.941x + 0.249$ with $R^2 = 0.992$

However, in urban areas, the quality of estimated z_{om} is much lower compared to agricultural areas, and therefore the high uncertainty in z_{om} values affects ET estimation. ET can be impacted to some extent if the estimated z_{om} value is far from the actual value. In order to improve the ET estimation for landuses besides agricultural areas, one should consider developing a better z_{om} map for modified SEBAL should be considered.

5.2.7.   Heights (z_1 and $z_{2)}$ for calculation of H

In SEBAL z_1 and z_2 presented in Figure 3.6 are determined as 0.01 m and 2 m respectively. The height z_1 should be low enough to approximate very near surface air temperatures, but must be higher than the surface roughness of heat transport z_{om}. The height 0.01 m above zero plane displacement height has been selected as the best height

to satisfy these requirements for z_1. Tasumi (2003) used $z_1 = 0.1$ m and Bastiaanssen (2000) used $z_1 = 0.01$ m. However, this is probably below the z_{om}, for tall vegetation such as forests, and therefore violates the physical principles. The height z_2 should be high enough to obtain sufficient resolution in dT and r_{ah}, but must be lower than surface boundary layer. Unfortunately, in satellite remote sensing, the surface boundary layer is vague since each pixel gives "averaged" information from a unit area. The 2 m height is used as an appropriate value for general condition.

The heights z_1 and z_2 are more theoretical heights and do not have a strong meaning in modified SEBAL operation. The height z_1 and z_2 controls the r_{ah} calculation in Equation 3.51. If r_{ah} value was doubled because of a larger distance between z_1 and z_2, then the estimated dT is doubled, since the dT for both cold and hot pixels will be doubled using the Equations 4.7 and 4.8. The doubled r_{ah} and dT values are totally compensated in the H calculation Equation 3.50, so that the change of heights z_1 and z_2 are not reflected in the H estimation. However, large changes in heights z_1 and z_2 affect the estimation of air density values and this somewhat impacts the H estimation. The z_1 and z_2 values are not very important from operational aspects, but one should not give unrealistic values for z_1 and z_2. The separation of z_1 and z_2 should be large enough to provide good numerical resolution for dT and r_{ah}.

5.2.8. Relationship between surface temperature (Ts) and near-surface air temperature difference (dT)

The application of SEBAL and modified SEBAL involves the definition of T_s versus dT relationship for every image Equations 3.62. The T_s versus dT function is representative for the time that satellite image was taken. In every processed image, a cold and hot pixel was defined, and the corresponding T_s and dT were used to define the linear relationship.

The cold pixel was always taken from a full-cover agricultural field in the Sana'a area having lower temperature compared to similar pixels, which was taken as an indication of the presence of a non-stressed crop having wet surface conditions. Hot pixels were taken from bare agricultural soils having higher temperatures than other similar fields, which were taken as an indication of substantial lack of soil moisture.
Figure 5.20 shows a plot of LAI versus surface temperature corresponding to several agricultural pixels. The location of cold and hot pixels is also displayed.

As can be seen in Figure 5.20, the cold pixel was located in the zone of maximum LAI (full cover conditions) and lowest surface temperature (indication of a non-stressed crop). On the other hand the hot pixel was located in the zone of minimum LAI (bare soil conditions) and highest surface temperature (indication of dry conditions). In both cases extreme low and high temperatures were avoided because they might not be representative of the general conditions of the soils in the study area.
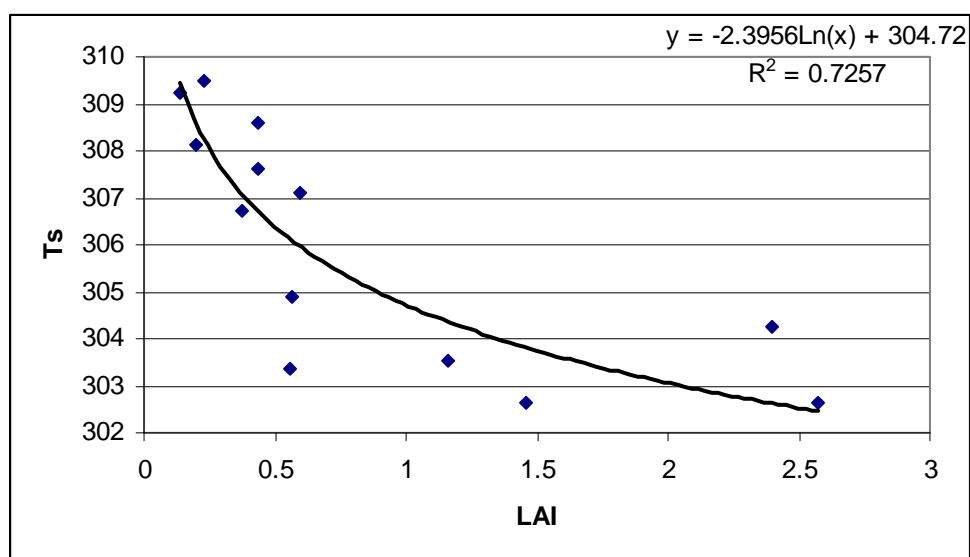
Figure 5.20   Plot of LAI versus Surface Temperature for Several Agricultural Pixels on the scene corresponding to 06/01/1998. Equation of fitted line is $y = -2.3956x + 304.72$ with $R^2 = 0.7257$

dT at the hot pixel was always greater than dT for the cold pixel. In SEBAL dT is used to predict the sensible heat, thus hot pixels will have greater H. As for the image corresponding to 06/01/98, dT at the cold pixel was negative, because the

predicted H at that pixel was negative, indicating the presence of adjective conditions at the cold pixel, produced by transport of sensible heat into the cold pixel, which made predicted ET greater than the available energy.

5.2.8.1 Temperature difference near surface (dT) function and the effect of windspeed on surface temperature

In modified SEBAL, ET estimation is somewhat sensitive to the windspeed input. For example, the estimated windspeed at 200 m above the weather station was estimated to be 5.3 m/s in 6/01/1998, based on a measurement at 2 m at NWRA, Sana'a Yemen. However, estimated ET does not change even if the windspeed input is double the actual measurement (Figure 5.21 and 5.22). This is due to the effect of strong internal calibration of energy balance at the cold and the hot pixels.
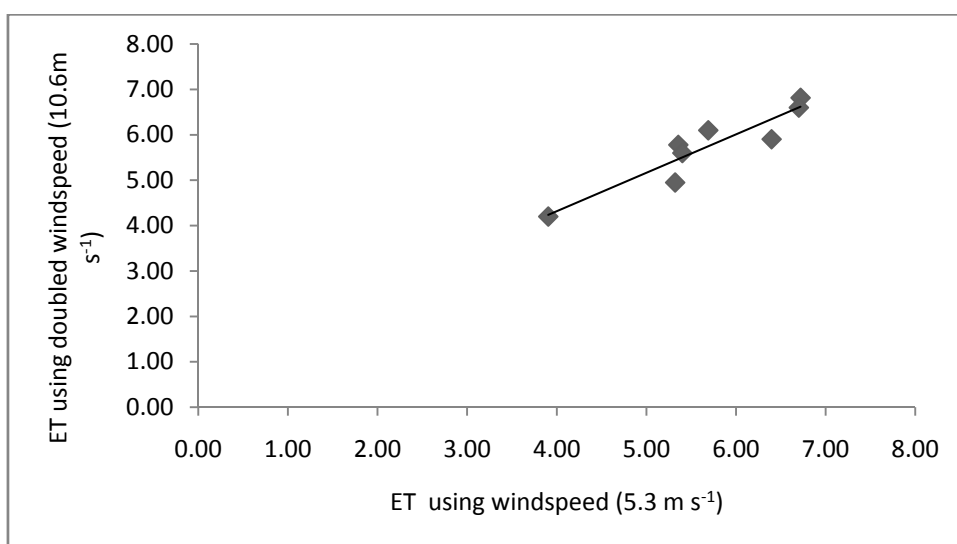
Figure 5.21.   Estimated ET values using the measured windspeed (x axis), and using doubled windspeed (y axis) as input, for all landuse types. Equation of fitted line is y = 0.846x + 0.933 with R² = 0.861
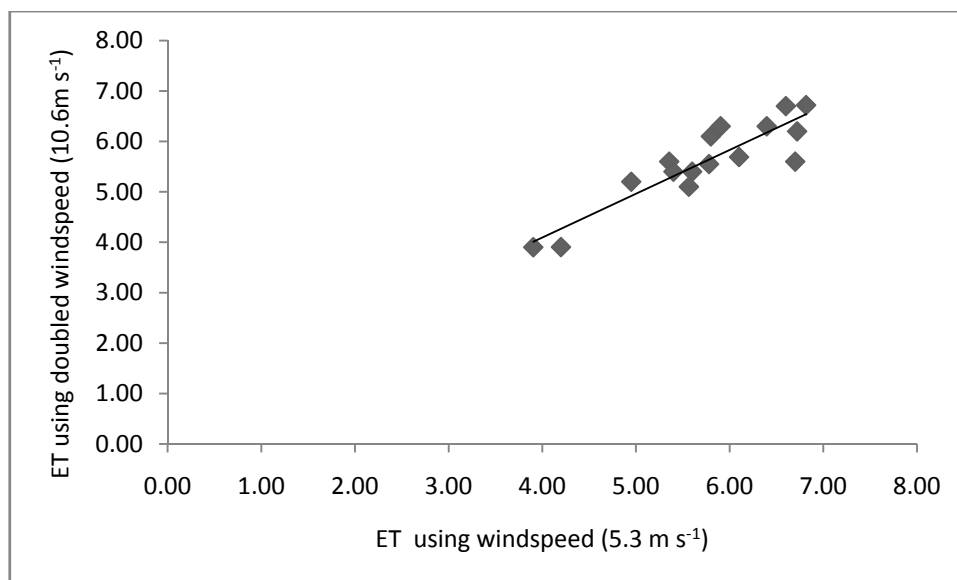
Figure 5.22   Estimated ET values using the measured windspeed (x axis), and using doubled windspeed (y axis) as input, for agricultural fields only. Equation of fitted line is y = 0.869x + 0.617 with R² = 0.809

The H estimation procedure in modified SEBAL is quite stable and was little effected by the overestimation of windspeed. However, modified SEBAL can be somewhat sensitive to the underestimation of windspeed due to numerical reasons in the stability correction. In the case of 6/01/1998 image, the H estimation process fails to converge if windspeed input is half of the actual value. In 6/01/1998, the estimated H at the selected cold pixel was -32 $W\ m^{-2}$ which means that the surface temperature at the cold pixel is colder than the air temperature because of the effect of regional advection. In case, the artificially calm windspeed created on the aerodynamic resistance that was too large to allow the transfer of negative 32 $W\ m^{-2}$ of H, and therefore the H iteration process became numerically diverged.

These evaluations for overestimation and underestimation of windspeed are caused if windspeed of entire area of interest are equally over/under estimated. As presented in Figure 5.21, modified SEBAL is insensitive to windspeed input unless the iteration process of stability correction becomes numerically diverged.

The most challenging problem would occur when windspeed changes with locations within an image. In this case, the problem is complicated because surface

temperature and dT may change with windspeed. Windspeed, which affects r_{ah} estimation, and the dT function exhibit the same interrelation (See, Equation 3.61). If we assume for example, that "Area 1" in Figure 5.23 has a general windspeed condition of $u_2oo = 5.3$ m/s, and "Area 2" has much higher wind speed of $u_2oo = 10.6$ m/s, the problem is not only with windspeed but with the dT function. This is because the dT function is developed for only one of the windspeed conditions (Area 1 or Area 2).

Returning to the problem illustrated in Figure 5.23, not only the windspeed condition but also the surface temperature condition may be different between Areas 1 and 2, consequently, the appropriate dT function can be different. The error generated by the windspeed difference should be greater in "dry" areas than in "wet" areas, since the windspeed primarily affects the H estimation. In such cases, the most appropriate solution is to separate an image into two sub-areas based on the weather condition, and operate modified SEBAL separately, using different cold and hot pixels and weather data. Generally, one can regard the windspeed condition as similar if the hot pixel candidates over the area of interest which have a similar surface temperature range.
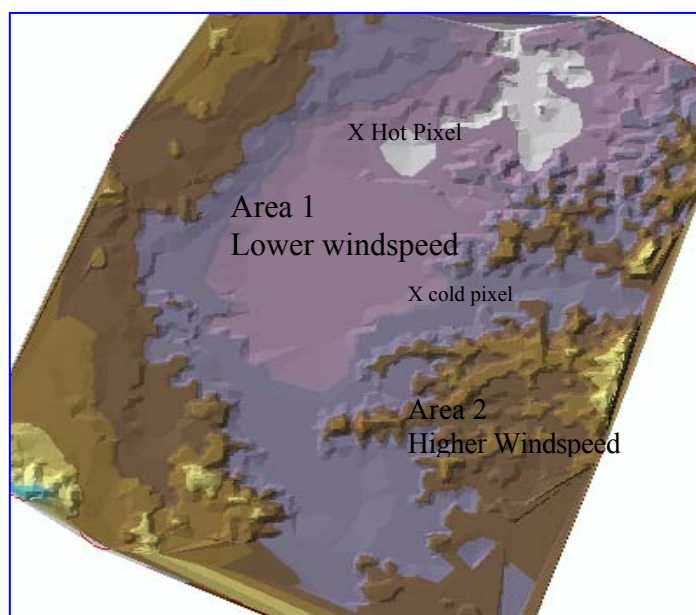
Figure 5.23.   Sketch of two different weather conditions within one image.

5.2.8.2   **Estimation related temperature difference near surface (dT)**

The problem in the study is compute the air temperature maps using only remote sensing data. However, it would be problem to estimate air temperature without available meteorological stations. In order to solve this problem, it is appropriate to propose to replace the temperature gradient between soil and air by a linear function of dT.

$$dT = T_s - T_{air} = a \times T_s + b \qquad ....(5.8)$$

Where:

T_S is surface temperature, T_{air} is air Temperature, a, b is experimental constants obtain daily maps of T_s at the chosen scale.

The computation of daily maps of T_s and T_{air} was made by using only satellite data, it is proposed to replace the gradient of temperature by a linear function of $\Delta T = T_s - T_{air} = a\ T_s + b$.

Simultaneous measurements of T_{air} and T_s have been collected during a field-trip and a linear regression has been achieved to obtain the following relation, equation 5.9 and 5.10, figure 5.24 and 5.25

$$dT = T_s - T_{air} = -0.149 \times T_s + 46.95 \qquad ....(5.9)$$

and $T_{air} = T_s + dT$

$$T_{air} = T_s - dT \qquad ....(5.10)$$

with a correlation coefficient of $r^2 = 0.873$.
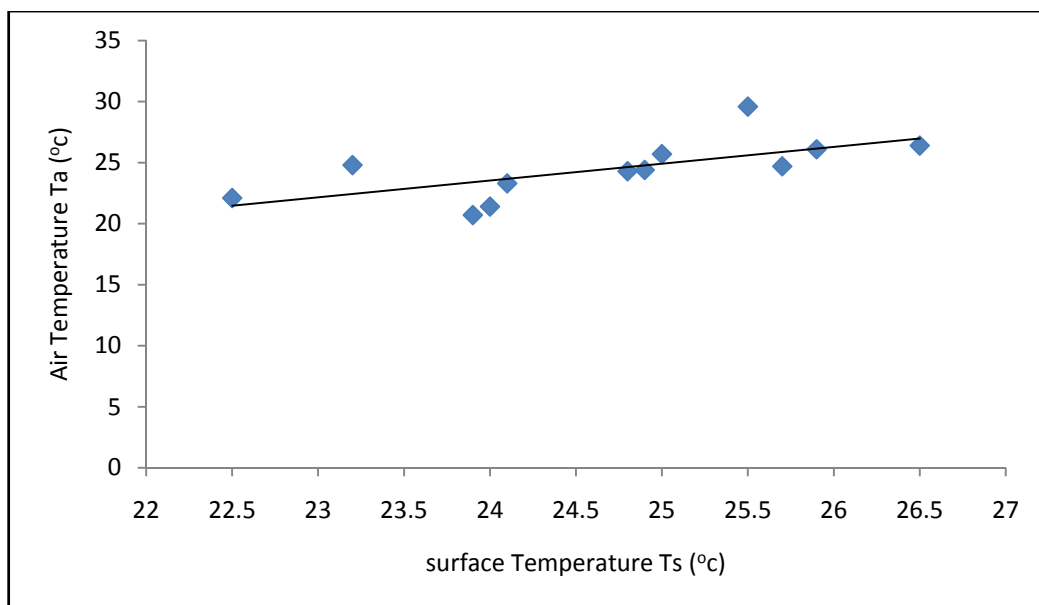
Figure 5.24   Air Temperature (T_a) versus Surface Temperature (Ts) for the sample areas. Equation of fitted line is y = 1.376x - 9.493
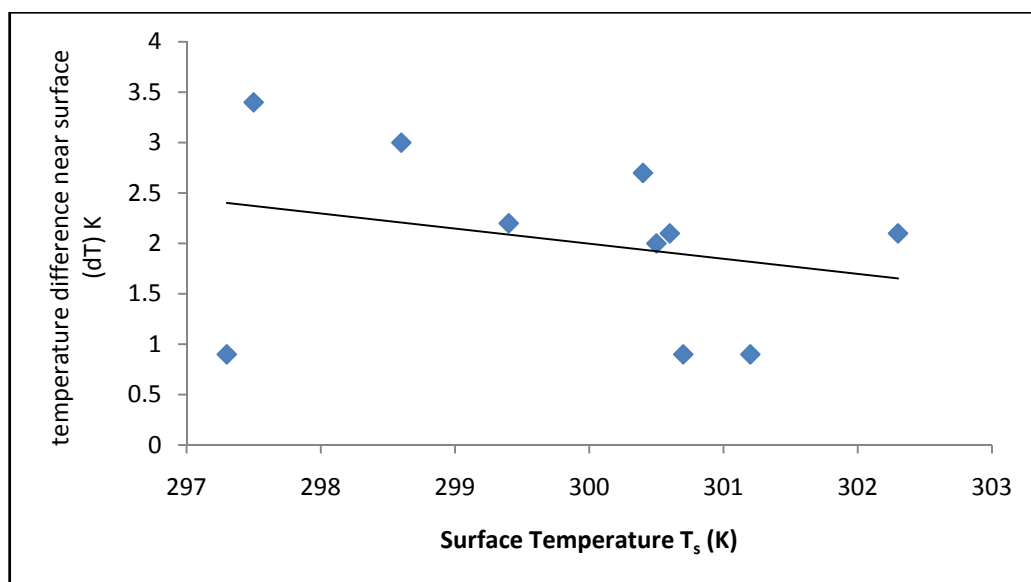
Figure 5.25.   Surface Temperature T_s versus temperature difference near surface (dT) for the sample areas. Equation of fitted line is *y = -0.149x + 46.*

5.2.9   Relations of elevation to wind speed

In mountainous areas, lapse corrected surface temperature was almost independent of elevation as shown in figure 5.15. If windspeed affects on the surface temperature as, the results from Figures 5.21 and 5.22 indicate, that effect of windspeed on T_s is almost independent of elevation in mountain areas (or error in lapse rate for the surface temperature is affected by the actual trend of windspeed with elevation).

It is likely that windspeed is not a strong function of elevation in mountainous regions. Essentially, windspeed increases when elevation increases from the base (Oke, 1987). However, windspeed is a strong function of the shape of terrain and the direction of windspeed, for a specific land surface (Oke, 1987, and Kaimal and Finnigan, 1994). Therefore, in mountainous areas, windspeed should be a strong function of the wind direction and surface aspect angle rather than elevation itself. Namely, the upwind surface of a mountain has tronger wind but the opposite side might be calm. Although one should expect some windspeed increase with elevation in mountains due to the Ventura effect and closer proximally to upper air streams, the general increase appears to be too small to be discussed accurately from the surface temperature data.

5.2.10.   Instantaneous and 24-hour ET

Modified SEBAL and SEBAL assume that the instantaneous evaporation fraction (EF) values are the same as the 24-hour values. As shown in Figure 5.26, field observations indicated that EF_{ins} was almost the same with EF_{24} most days for agricultural fields. Figure 5.26 shows the comparison of EF_{ins} and EF_{24} for sorghum and grass fields for all satellite image dates evaluated. The sorghum field images include a dry bare soil

condition (12/12/95), wet bare soil condition (5/20/95), and crop growing period (6/1/98). For all conditions, EF_{24} was close to EF_{ins} this result strongly supports this assumption used in modified SEBAL.
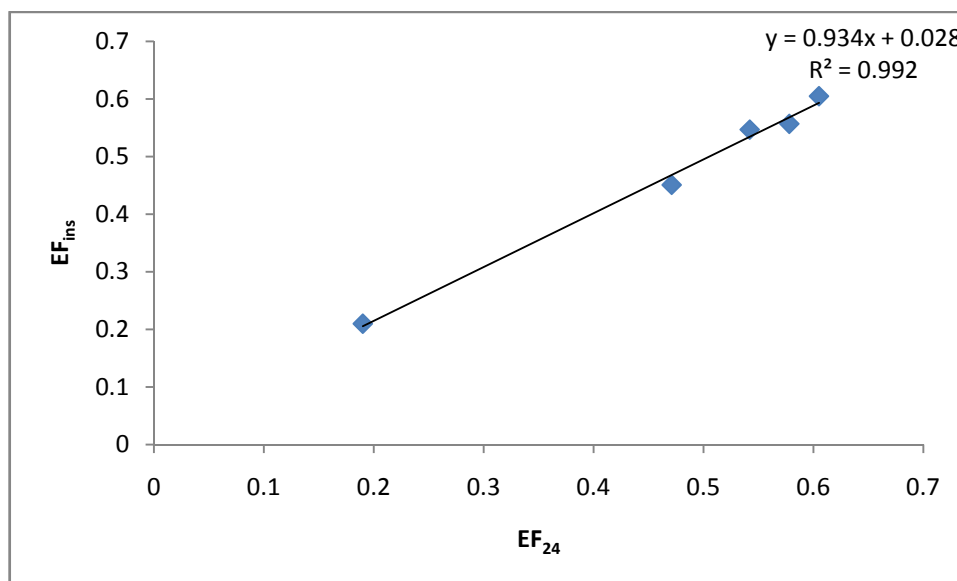
Figure5.26 Instantaneous EF_{ins} (at satellite image time) values varsus EF_{24} from the meteorological station data, Sana'a basin, Yemen.

Figure 5.27 shows that daily ET is increased from bare soil to where Vegetation indices are high, the daily ET distribution from Landsat 5 TM june 1st 1998 (0.0– 11.8 mm day^{-1}) .
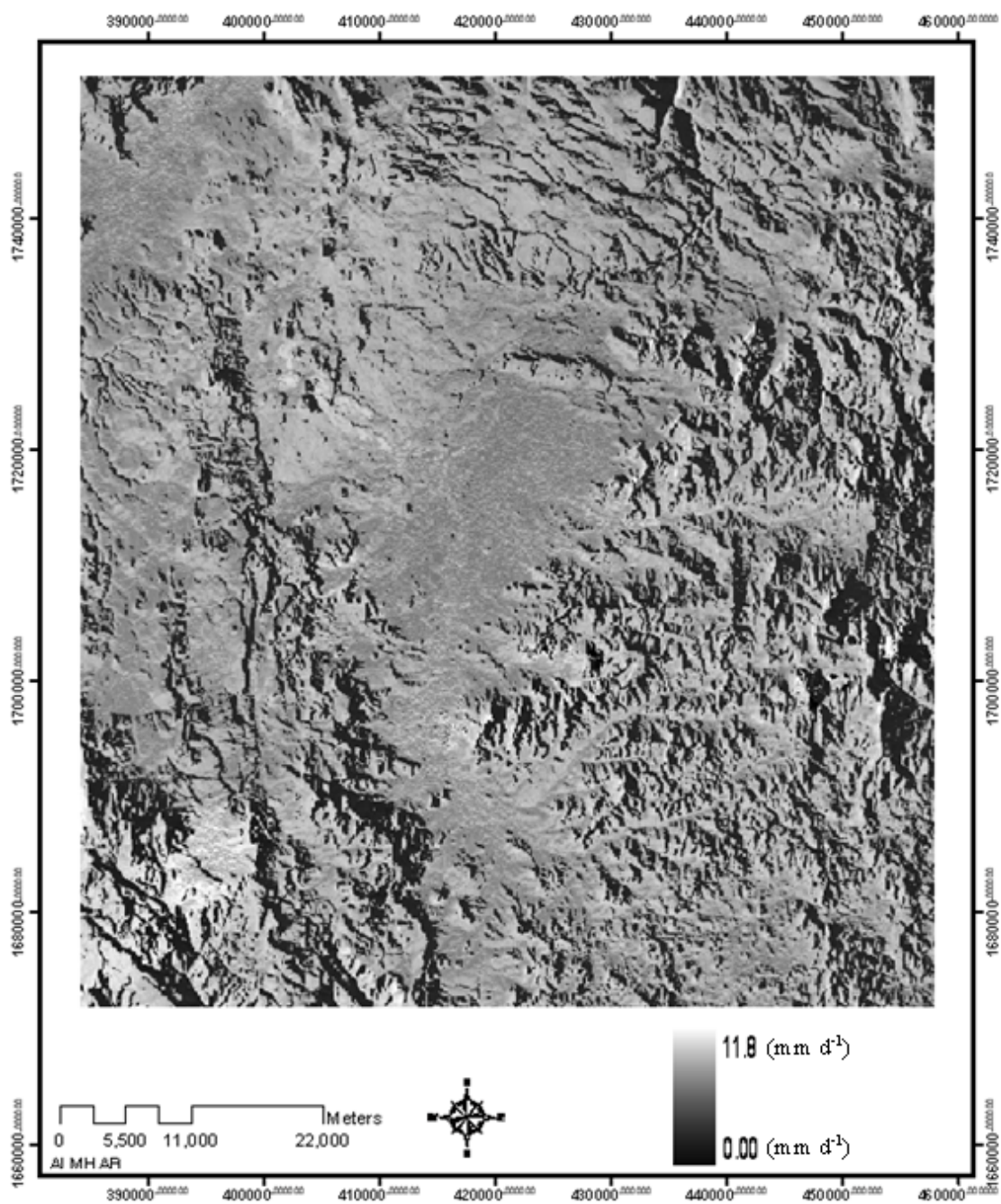
Figure 5.27 24-hour ET values for the Sana'a basin, Yemen

5.2.11.   24-hour ET and monthly ET

Modified SEBAL has been successfully used to predict 24-hour ET and monthly ET in agricultural situations. In 1998, a pre-version of modified SEBAL was applied to the Sana'a *Basin,* and the error in monthly ET as compared against Penman Monteith FAO ET was 4.3% (see Figure 5.28).
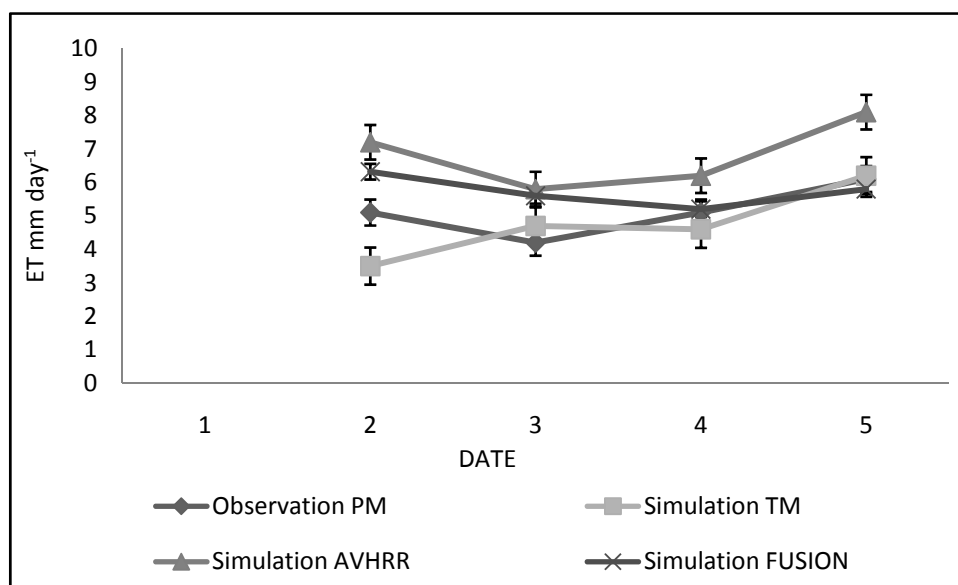
Table 5.28   Summary of modified SEBAL and PM-derived ET values for mean monthly periods at Sana'a NWRA, Yemen

Through the modified SEBAL application documented, a second verification was provided using lysimeter measured ET values from a EFFA lysimeter Sana'a Yemen, field using data Table 5.2. of the two years. The error in estimated seasonal ET was 2.5% for a 3 month period. This result supports the conclusion that modified SEBAL can accurately estimate ET for agricultural conditions.

5.3 Validation modified SEBAL model

5.3.1 Overview

In this section the modified SEBAL validated the accuracy of estimation ET by utilizing different methods in the study area. The methods used include:

- Validation modified SEBAL ET using Landsat TM by comparison with ET from the lysimeter data in the Experimental Farming – Faculty of Agriculture (EFFA), gauge station in Sana'a basin.
- Validation modified SEBAL ET using Landsat TM by comparison the ET from the lysimeter with the ET from metrological data.
- Validation modified SEBAL ET using Landsat TM by comparison with ET from four traditional methods using metrological data in four gauge station (NWRA, CAMA, AREA and EFFA) in Sana'a basin.
- Comparison ET, Ts and NDVI from Landsat TM and NOAA-AVHRR in the date which available TM images and estimated the error in the pixel which have the lysimeter data, then
- Comparison the ET during 2006 from the lysimeter with the ET from metrological data.

The original SEBAL model was modified as described in Chapter 3 and 4 to improve the estimation of various components for agricultural fields in mountains, terains and slope areas.

This version of SEBAL, termed modified SEBAL was implemented in ERDAS-Imagine software and general description of the coding is included in appendix A1.

Model validation focused on the comparison of daily values of ET (ET_{24}), measured with the EFFA lysimeters, with estimates from modified SEBAL. This comparison was limited by the fact that the spatial resolution of the Landsat 5 thermal band (band 6) is 90 x 90 m, (see Fig. 5.29), and the area of the Lysimeter field was 130 x 190 thus, in most cases, it was

impossible to have a "pure thermal pixel" NOAA-AVHRR inside the lysimeter fields, that represents only those fields.

The challenge of obtaining a thermal pixel representative of the lysimeter fields all bands for NOAA-AVHRR ware especially difficult for Lysimeter , since during the 2006-2007 period the northern and the southern area of the field were used to plant other crops instead of wheat. This meant that the actual dimensions of Lysimeter field were 190 m east-west, and only 63 m north south. During 2006 the northern section of the field was planted with alfalfa and the southern area was planted with sorghum. Therefore, it was impossible to obtain all pixels that had a high percentage of wheat.

The contamination of thermal pixels introduces significant errors in modified SEBAL, because all energy balances components: net radiation, sensible heat and soil heat fluxes use surface temperature information, which is derived from the NOAA-AVHRR thermal band.

The integrity of the lysimeter data was evaluated using the known methodology.

5.3.2 Results of modified SEBAL model validation for prediction of ET_{24} values

After applying modified SEBAL for each image, results from four 30x30 pixels around the lysimeter site were taken and averaged. A geo-rectified Spot image (taken in 2006) was utilized to provide the lysimeter approximate location. In Figure 5.29 the Spot image of the lysimeter location, and details of Landsat and NOAA-AVHRR are shown.

NOAA-AVHRR pixels are not square because of revamping done during geo-rectification and Spot image to true North-South. As mentioned before, the low spatial resolution of NOAA-AVHRR bands introduces uncertainties in the calculation of some energy balance components of SEBAL. On the other hand, Figure 5.29 shows a case where the NOAA-AVHRR pixels inside the lysimeter were "contaminated" by

surrounding areas. The lysimeter field on 06/01/98 contained information from 8 pixels Landsat TM, however none of them completely inside of it.   Therefore, estimation of radiometric surface temperature, and all components of modified SEBAL that are derived from it, is expected to be hampered by the mixing of thermal information.

The accuracy of modified SEBAL strongly depends on the quality of the thermal information which is used to retrieve the radiometric surface temperature of the pixel. Table 5.1 shows a summary of the results obtained in the model validation. ET values from modified SEBAL were obtained averaging results from four 30 m x 30 m pixels approximately centered at the lysimeter site. Table 5.1 includes the values of daily ET estimated from modified SEBAL, and corresponding daily ET measured at the lysimeter site.
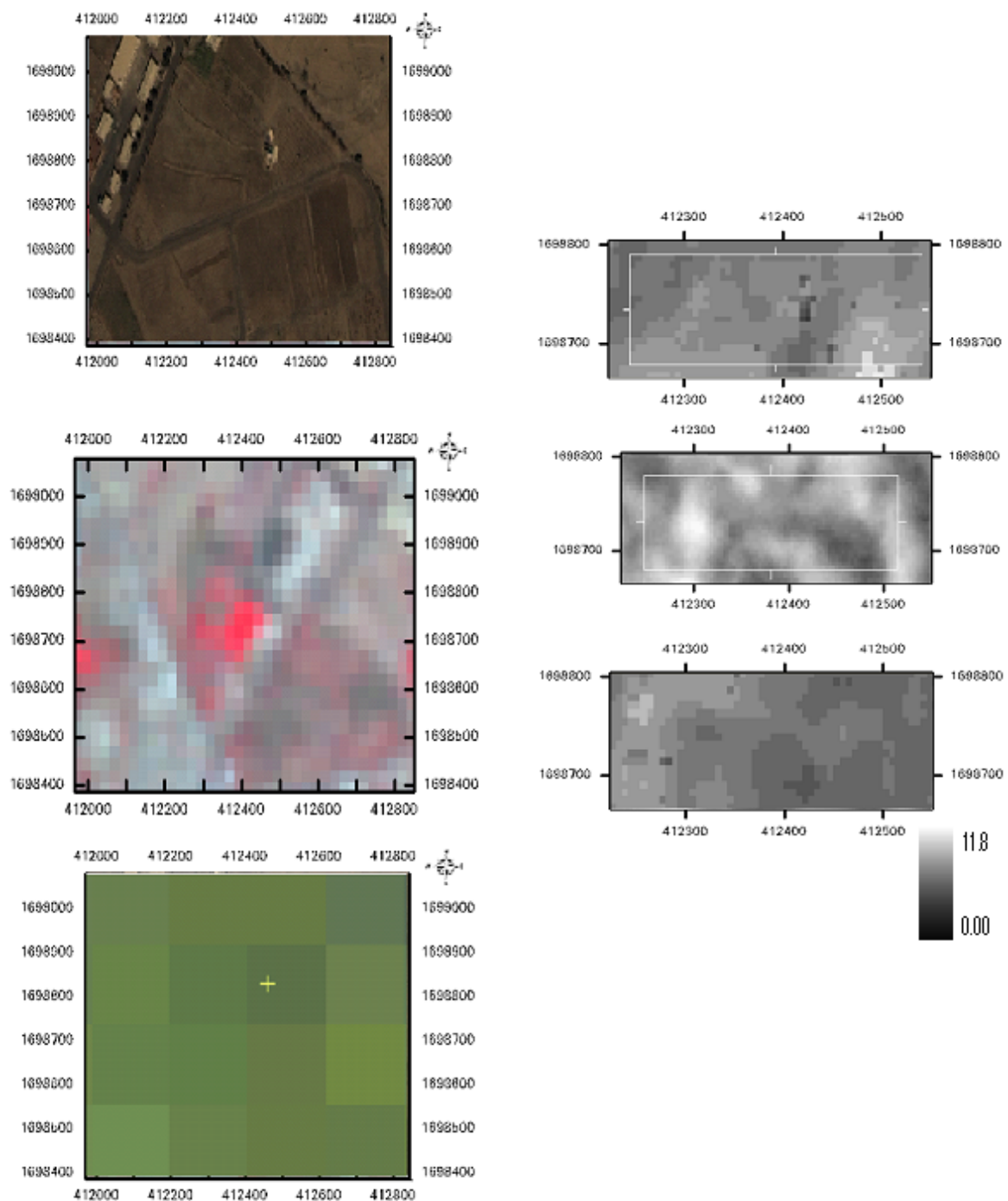
Figure 5.29 Picture of Lysimeter Field. SPOT image (above) Landsat TM (center), and
NOAA-AVHRR (bottom) (left). Image ET $_{RS-TM}$ for the three date (right).

5.3.2.1. Validation modified SEBAL ET using Landsat TM by comparison with ET from the lysimeter data in the EFFA gauge station in Sana'a basin.

The accuracy of modified SEBAL strongly depends on the quality of the thermal information which is used to retrieve the radiometric surface temperature of the pixel. Table 5.1. shows a summary of the results obtained in the model validation. ET values from modified SEBAL were obtained averaging results from four 30 m x 30 m pixels approximately centered at the lysimeter site. Table 5.2 includes the values of ET_{24} (around the five days to the satellite overpass time) estimated from modified SEBAL, and corresponding ET_{24} measured at the lysimeter site. In addition, the corresponding values of reference ET are included for comparative purposes.

Table 5.1. : Summary of ET Comparison for 1998 (sorghum), 1995 (alfalfa), and 1995 (peas) EFFA by ET calculated by modified SEBAL model using Landsat TM images

date	$ET_{-Lysimeter}$ (mm d^{-1})	ET_{-TM} (mm d^{-1})	AE (mm d^{-1})	RE	A	NE
1st JUNE1998	6.91	5.281	1.629	0.235	0.764	76
12th december1995	4.05	3.414	0.636	0.157	0.842	84
20th MAY1995	7.98	5.91	2.07	0.259	0.740	74

$ET_{-lysimeter}$ = Measured ET values were provided by EFFA archive, 2006
ET_{-TM} = ET calculated by modified SEBAL model using Landsat TM images
AE= The Absolute Error.
RE= The Relative Error.
A= Difference ET_{-PM} / $ET_{-Lysimeter}$ (linear regression coefficient).
NE= Normalized error was calculated as 100*Difference
Negative value in ET difference indicates that ET-TM was lower than the lysimeter ET.
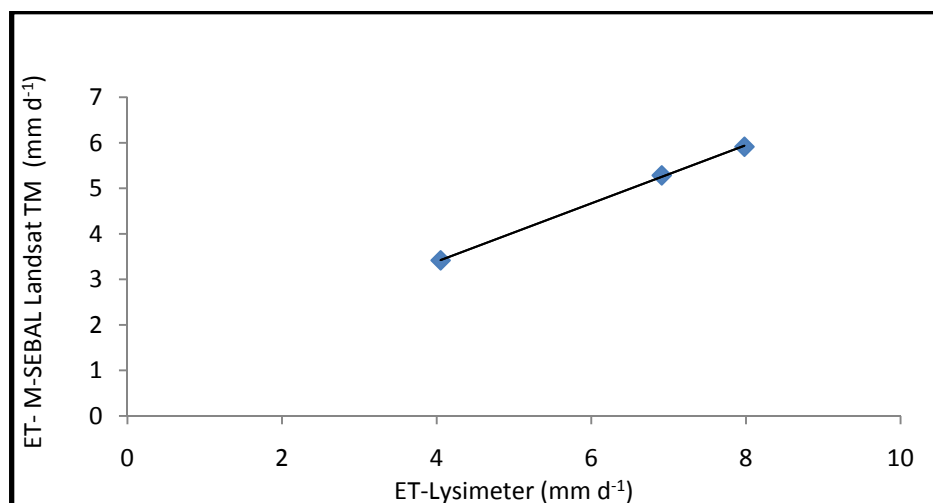
Figure 5.30   Remote sensing estimated ET were compared with the lysimeter water balance ET. Equation of fitted line is y = 0.638x + 0.835 with R² = 0.999

The accuracy of modified SEBAL strongly depends on the quality of the thermal information which is used to retrieve the radiometric surface temperature of the pixel. Table 5.1. shows a summary of the results obtained in the model validation. ET values from modified SEBAL were obtained averaging from four 30 m x 30 m pixels approximately centered at the lysimeter site.

The ET estimated by the remote sensing method versus ET estimated by lysimeter water balance ET on the three days is shown in Figure 5.30. Their relationship can be shown as;

$$ET_{TM} = 0.638\ ET_{lysimeter} - 0.835, \qquad r^2 = 0.999\ ....(5.11)$$

where ET_{TM} is the remote sensing method ET modified SEBAL model using Landsat TM images, and $ET_{lysimeter}$ is the lysimeter water balance method ET. The correlation coefficient indicate a strong relationship between the remote sensing ET and the lysimeter water balance ET.

As shown in Table 5.1, the Absolute error of the estimate of remote sensing , Landsat TM recorded ET and lysimeter water balance ET was 1.629 and 2.07for EFFA station may20[th] 1995 and 1st June1998 , respectively. The largest Normalized error (84%) was with the EFFA lysimeter on 12th december1995. The smallest Normalized error (74%) was with the EFFA lysimeter on may20[th] 1995.

5.3.2.2 Comparison the ET from the lysimeter with the ET from metrological data.

Average monthly ratios of actual to potential ET in a long term lysimeter study from EFFA area in Sana'a basin could provide a more reliable monthly $\lambda(ET_{ins})$ for the ET estimation in Sana'a basin, Yemen. This result supports the conclusion that modified SEBAL can accurately estimate ET for agricultural conditions.

Table 5.2 includes the values of ET24 estimated from FAO Penman-Monteith equation, and corresponding ET24 measured at the lysimeter site.

Table 5.2. : Summary of ET Comparison for 1998 (sorghum), (peas) 1995, and (alfalfa) 1995 by ETc calculated by FAO Penman-Monteith equation in EFFA.

Date	ET-Lysimeter (mm d^{-1})	ET-PM (mm d^{-1})	AE (mm d^{-1})	RE	A	NE
1st june1998	6.91	5.8	1.11	0.160	0.839	84
12th december1995	4.05	6.723	2.673	0.397	0.602	60
20th may1995	7.98	5.3	2.68	0.335	0.664	66

ET-lysimeter $^{=}$ Measured ET values were provided by EFFA archive, 2006
ET-PM= ET calculated by FAO Penman-Monteith equation
AE= The Absolute Error.
RE= The Relative Error.
A= Difference ET-PM / ET-Lysimeter (linear regression coefficient).
NE= Normalized error was calculated as 100*Difference

The ET estimated by the lysimeter water balance ET method versus ET estimated by traditional (FAO Penman-Monteith) method at EFFA weather stations on the three days is shown in Table 5.2 . The correlation coefficient indicates a strong relationship between the lysimeter water balance ET and the tradition method ET.
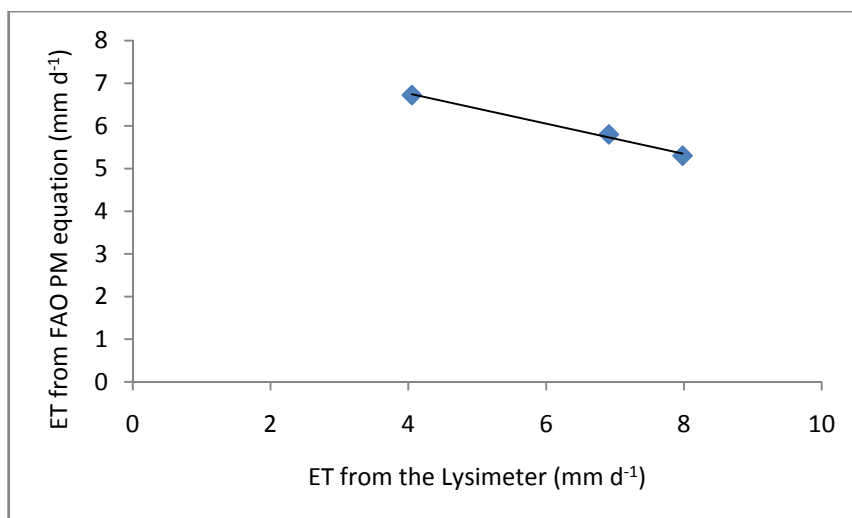
Figure 5.31 the measurement lysimeter ET compared with ET calculated by FAO Penman-Monteith equation in EFFA. Equation of fitted line is $y = -0.354x + 8.175$ with $R^2 = 0.992$

5.3.2.3 Comparison the modified SEBAL ET with ET from traditional methods using metrological data.

The relationship of modified SEBAL ET and the traditional method ET was re-evaluated excluding the four traditional methods ET; The relationship between the methods are shown in table 5.3 presented bellow.

Table 5. 3 : Comparison of ET from Remote Sensing models and four hydrological models and water balance model in four gauge stations and three satellite images in Sana'a basin, Yemen.

a) SANAA-RS-Jun98

	ET-TM		ET-PM	ET-FAO-P	ET-PT	ET-HAR	AVERAG	SEE
EFFA	5.281		5.8	6.6	5.5	6	5.84	1.12
NWRA	7.095		6.6	6.5	5.8	5.9	6.47	0.28
IRAA	5.254		5.8	5.8	5.3	5.7	5.57	0.29
CAMA	7.351		6.55	5.1	5.5	5.8	6.06	0.49

b) SANAA-RS-DEC95

	ET-TM		ET-PM	ET-FAO-P	ET-PT	ET-HAR	AVERAG	SEE
EFFA	3.414		4.05	3.64	3	3.8	4.10	1.28
NWRA	6.68		4.13	3.66	2.3	4	4.30	-0.03
IRAA	7.89		3.8	3.8	1.8	4.6	4.25	-0.72
CAMA	7.97		4	4.02	2.4	4	4.48	-0.60

c) SANAA-RS-MAY95

May-95	ET-TM		ET-PM	ET-FAO-P	ET-PT	ET-HAR	AVERAG	SEE
EFFA	5.91		5.3	5.7	5.3	5.4	5.93	0.84
NWRA	6.171		5.8	5.7	5.8	5.8	5.96	-0.07
IRAA	7.677		7.8	6.6	5.5	6	6.55	1.36
CAMA	8.107		5.3	6.5	5.3	5.9	5.77	-1.15

SEE=standard error of the estimate

As shown in Table 5.3a, 5.3b and 5.3c, the standard error of the estimate of remote sensing , lysimeter recorded ET and hydrological models ET for NWRA station December 95 and IRAA station may 95 , was -0.03 and 1.36 respectively. The largest estimation error 0.84 was with the EFFA gaug station on May, 1995. On that date, the satellite image pixel at the EFFA station location was not identified as cloud-contaminated while the alfalfa pixel was grown. However, the NDVI of the EFFA was significantly lower than the average NDVI from other dates. The cause of the low NDVI value might be due to the existence of thin cloud which was not detected by the cloud screening algorithm.   The low NDVI resulted in a low EF and consequently a low estimated ET.
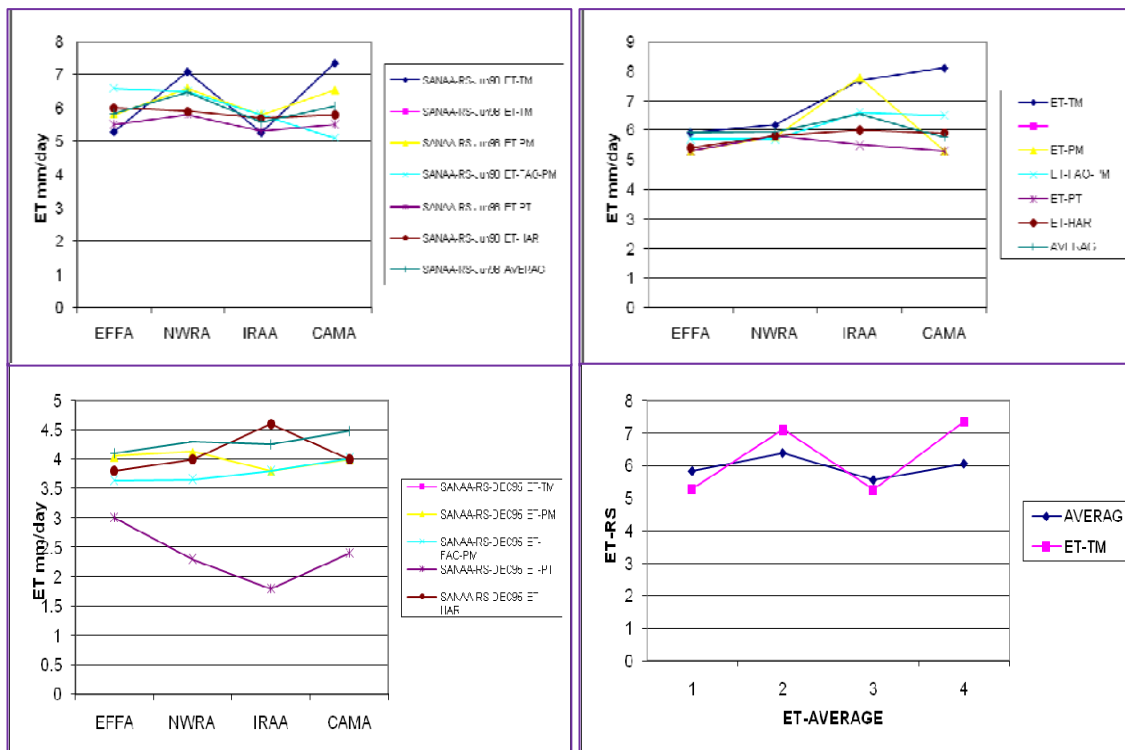
Figure 5.32   Comparison of ET by Remote Sensing models with four traditional hydrological using metrological data from four gauge station (NWRA, CAMA, AREA and EFFA) in Sana'a basin, Yemen.

5.3.3   Comparison of surface parameter using AVHRR and TM Images

The relationship of surface parameter application of modified SEBAL from NOAA-AVHRR and Landsat-TM Images will be compared and table 5.4 shows the surface parameter (NDVI, Ts and ET) in three dates, over EFFA area.

Table 5. 4 : Comparison of surface parameter using NOAA-AVHRR and Landsat-TM Images EFFA

DATE	DATA	TM	AVHRR	AE	RE	A	NE
June 1998	NDVI	0.54	0.27	0.27	0.5	0.5	50
	Ts	307.9	314.7	6.8	0.022	0.978	98
	ET	6.28	4.833	1.447	0.230	1.299	130
December 1995	NDVI	0.415	0.324	0.091	0.219	1.281	128
	Ts	307.2	315.2	8	0.026	0.9759	97
	ET	3.8	3.77	0.03	0.008	1.008	101
May 1995	NDVI	0.59	0.324	0.266	0.451	1.821	182
	Ts	309	314.5	5.5	0.018	0.982	98
	ET	4.85	4.22	0.63	0.129	1.149	115

AE= the Absolute Error.
RE= the Relative Error.
A= Difference $ET_{(PM)}$ / $ET_{(LYSI)}$ (linear regression coefficient).
NE= Normalized error was calculated as 100*Difference

The Absolute error of the estimate of remote sensing , Landsat TM recorded ET and NOAA-AVHRR ET for EFFA station December 1995 and may 1995 , was 0.03 and 1.447 respectively. The largest Normalized error 130% was with the EFFA lysimeter on June 1st 1998. On that date, the NOAA-AVHRR satellite image pixel at the EFFA lysimeter location was not identified as cloud-contaminated while the sorghum pixel was. However, the NDVI of the EFFA was significantly lower than the average NDVI from other dates. The cause of the low NDVI value might be due to the existence of thin cloud which was not detected by the cloud screening algorithm. The low NDVI resulted in a low FE and consequently a low estimated ET.

The latent heat flux $\lambda(ET_{ins})$ values of the three EFFA of the NDVI -Ts are important in determining $\lambda(ET_{ins})$ at each pixel. Average monthly ratios of actual to potential ET in a long term lysimeter study from EFFA area in Sana'a basin could provide a more reliable monthly $\lambda(ET_{ins})$ for the ET estimation in Sana'a basin, Yemen.

5.3.4 Comparison the ET from lysimeter data with the ET from the meteorological data calculated by FAO Penman-Monteith equation in year 2006.

The integrity of the lysimeter data was evaluated using the known meteorological data. Table 1c in the aappendex C provides comments on the general soil and crop conditions present in the EFFA Lysimeter. Most of the dates included in table 5.5 correspond to 2006, where lysimeter field EFFA was planted with wheat. The wheat was planted on June 12 and was harvested on November 28. Full cover conditions for the wheat were reached around August 21st to 7th September.

Table 5.5 : Summary of daily ET Comparison for 2006 (wheat) at EFFA station

Date	Crop	ET-Lysimeter	ET-PM	A	AE	RE	NE
06/18/2006	Wheat	5.544	6.2	1.118326	0.656	0.105806	112
07/04/2006	Wheat	6.396	6.3	0.984991	0.096	0.01524	98
07/20/2006	Wheat	5.355	5.8	1.0831	0.445	0.076724	108
08/05/2006	Wheat	5.4	5.4	1	0	0	100
08/21/2006	Wheat	6.72	6.2	0.922619	0.52	0.08387	92
09/07/2006	Wheat	6.7	5.6	0.835821	1.1	0.19643	84
09/23/2006	Wheat	5.565	5.1	0.916442	0.465	0.09118	92
11/25/2006	Wheat	3.904	3.9	0.998975	0.004	0.00103	100

ET-lysimeter= Measured ET values were provided by EFFA archive and Fari,2008
ET-PM= ET calculated by FAO Penman-Monteith equation
AE= The Absolute Error.
RE= The Relative Error.
A= Difference ET$_{(PM)}$ / ET $_{(LYSI)}$ (inear regression coefficient).
NE= Normalized error was calculated as 100*Difference

The ET estimated by the lysimeter water balance ET method versus ET estimated by traditional (FAO Penman-Monteith) method at EFFA weather stations on the 2006

wheat crop growing season is shown in Table 5.5 . The correlation coefficient does not indicate a strong relationship between the lysimeter water balance ET and the traditional ET method. However, after a close inspection of the weighting factors of the stations, an excessive low ET value was found at station EFFA. Station EFFA was located at the southern tip of the EFFA to the Sana'a basin. Due to the low values of the crop, the crop coefficient used in the EFFA lysimeter ET model was much lower than the crop coefficient used for crops in traditional FAO-PM ET calculation. As shown in Table 5.5, the average error of lysimeter and calculated by FAO Penman-Monteith equation recorded ET was 13.5 percent for EFFA. The largest Relative error estimation (19.6%) was with the lysimeter on Sep. 07, 2006.

5.4. **Comparison of surface parameter and surface heat fluxes estimating from NOAA-AVHRR and Landsat-TM Images with modified SEBAL**

In this section the comparison of application modified SEBAL from NOAA-AVHRR and Landsat-TM Images will be discussed. Additionally, the section will also discuss the comparison of ET by Remote Sensing models, hydrological models and water balance (lysimeter) model, the comparison estimates of actual evapotranspiration from Satellites, Hydrological Models, and also the comparison between evapotranspiration value by remote sensing SEBAL model and different traditional models: A Case Study from mountains region Yemen.

The figures 5.33 to 5,35 show maximum and minimum values of surface parameters and land surface heat over the study area (Sana'a, Basin), which comprises arid and semi arid conditions.

By comparing figures 5.33 and 5.34 it was found that areas which have a high vegetation index have a low surface temperature; the other land areas which have low vegetation indices tend to have high surface temperature. This is seen in figure 5.33a especially the part near the valley which represents the high vegetation density, while the part further from the valley area face the opposite situation.

Figure 5.33 (c) shows that daily ET is increased from bare soil to where Vegetation indices are high, the daily ET distribution by NOAA- AVHRR (0.6 -16.8mm/day) and from LANDSAT 5 TM (0.02–9.32 mm/day) .

The figures 5.34 below show maximum and minimum results of the estimated of surface heat fluxes over the study area (Sana'a, Basin), which comprises arid and semi arid conditions. from LANDSAT 5 TM (left) and from NOAA- AVHRR(right) (w m^{-2}). The figures (5.35) below show comprise of surface parameters: Albedo, vegetation index (NDVI), surface Temperature (Ts) and Evapotranspiration averaged over 24 hours(ET$_{24}$), and surface heat flux parameters over selected point in the study area (Sana'a, Basin), which comprises arid and semi arid conditions.
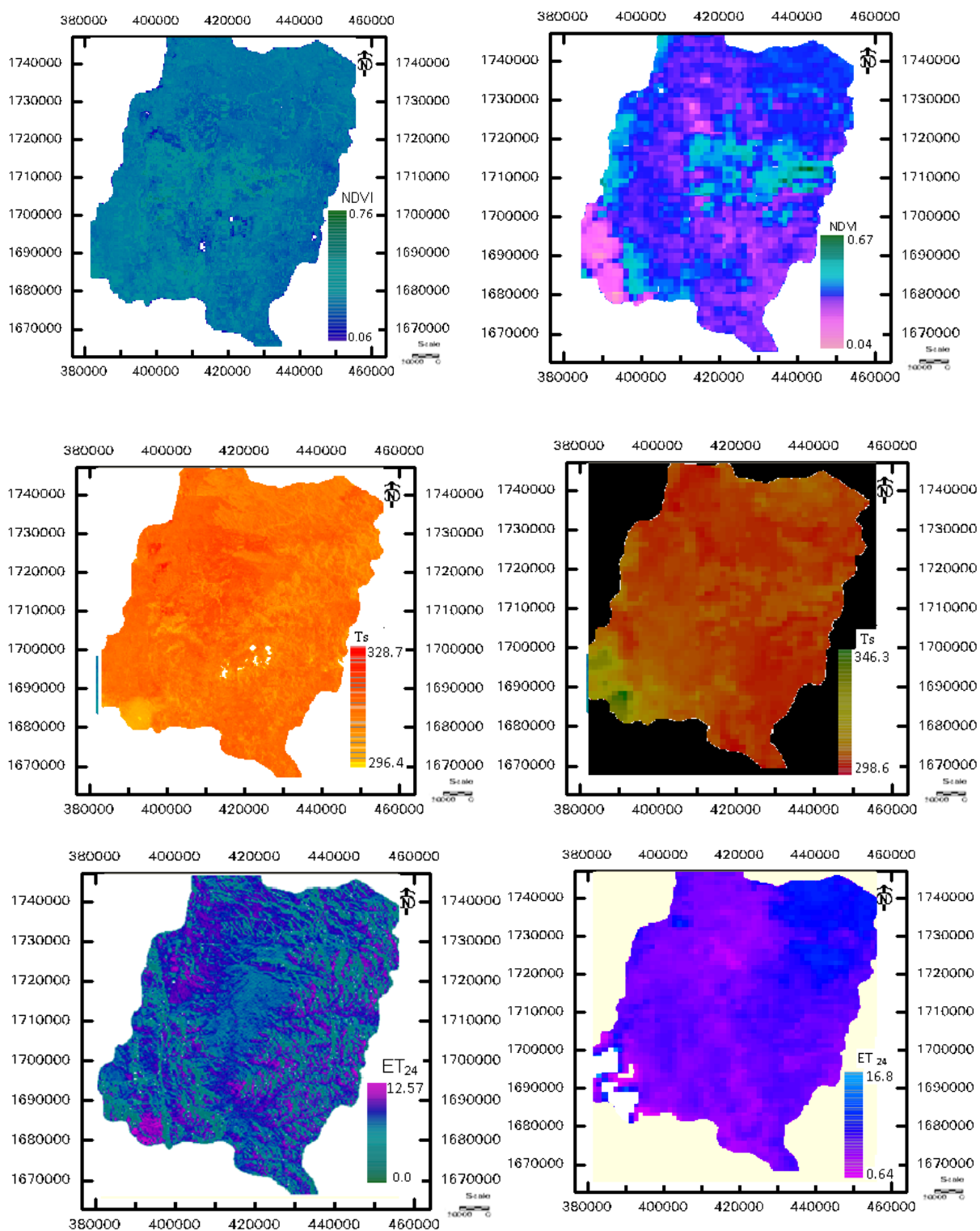
Figure 5.33 Comparison of vegetation index (NDVI), surface Temperature (Ts) and Evapotranspiration averagedover 24 hours(ET$_{24}$) derived from LANDSAT 5 (left) and TM NOAA-AVHRR (right) for Sana'a basin Yemen.
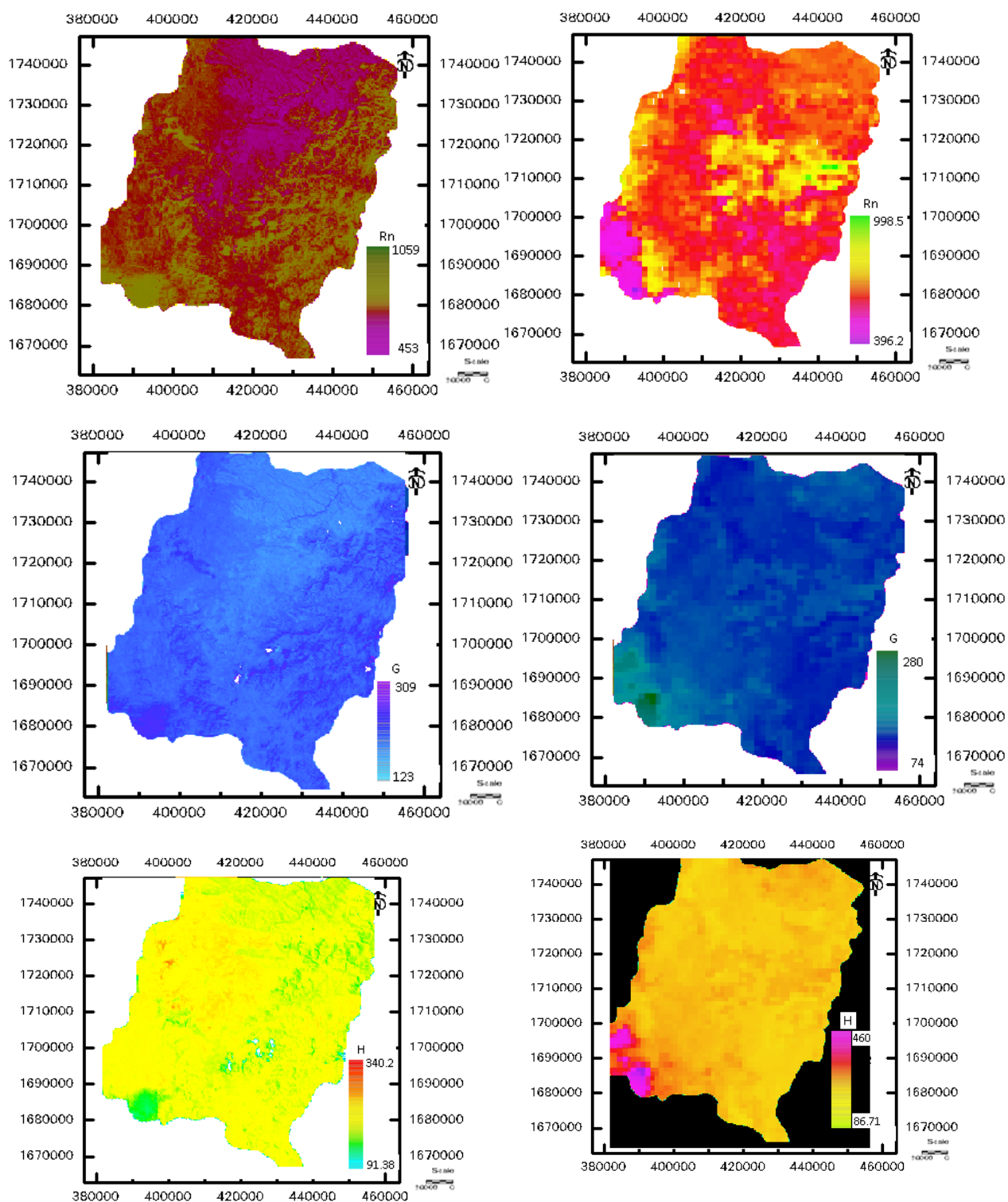
Figure 5.34   Comparison of Net radiation(Rn), Soil heat flux(G), and Sensible heat flux(H) derived from LANDSAT 5 TM(left)and NOAA-AVHRR (right)for Sana'a basin Yemen.
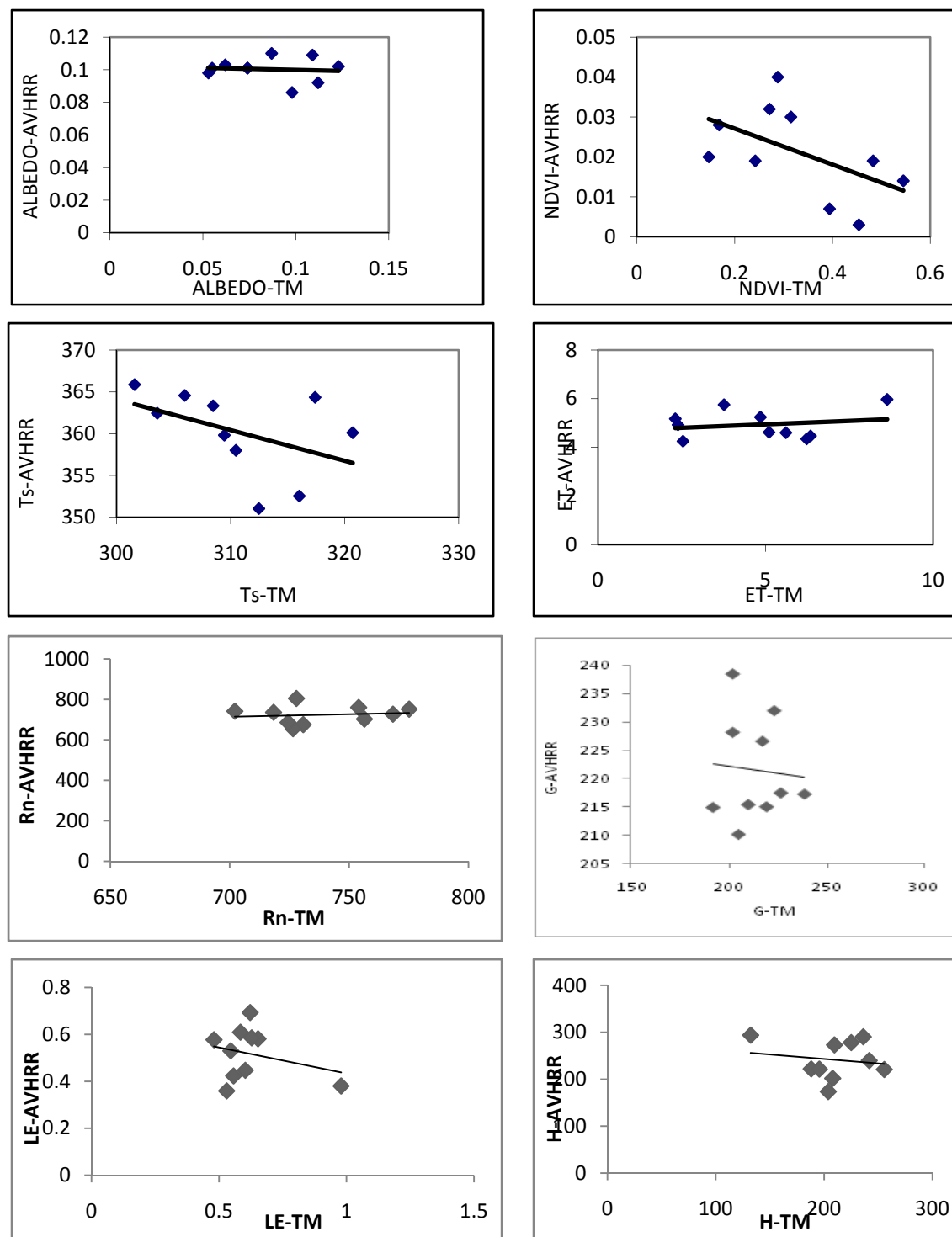
Figure 5.35 Comparison of surface parameters: Albedo, vegetation index (NDVI), surface Temperature (Ts) and Evapotranspiration averaged over 24 hours(ET_{24}), and surface heat fluxes: Net radiation(Rn), Soil heat flux(G), and Sensible heat flux(H) derived from LANDSAT 5 TM(X axis) and NOAA-AVHRR (Y axis)for Sana'a basin Yemen.

Figure 5.36 to 5.39 presents the results of the estimated surface parameters and surface heat fluxes over the study area from NOAA- AVHRR and from LANDSAT 5 TM (W m^{-2}). The latent heat flux (LE) is increased from bare soil to the vegetated area as ET.
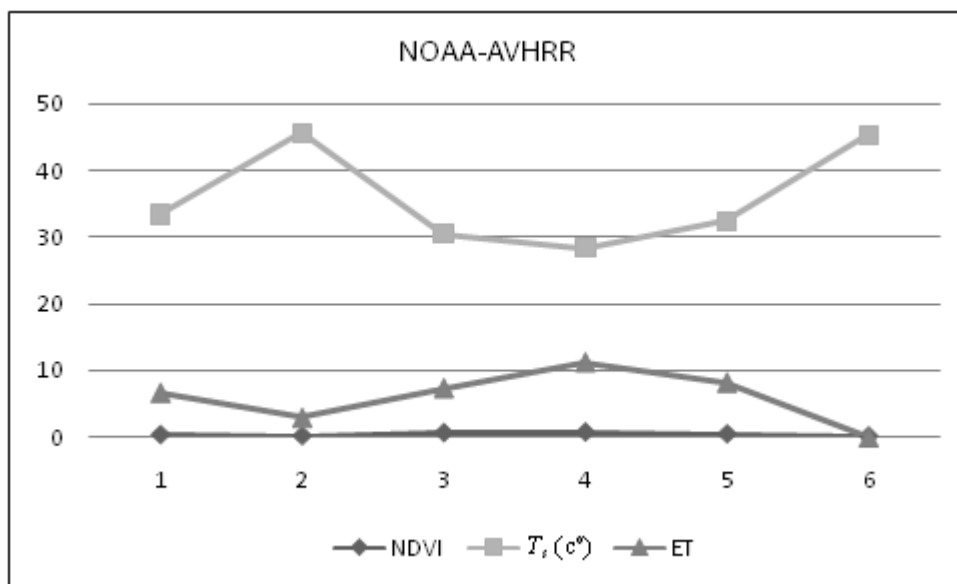
Figure 5.36 . Estimated the surface parameter derived from NOAA-AVHRR on Sana'a Basin from TM, on 10th June 1998, T_s surface temperature(°c), *NDVI* vegetation indices, ET_{24} evapotranspiration from satellite overpass time.
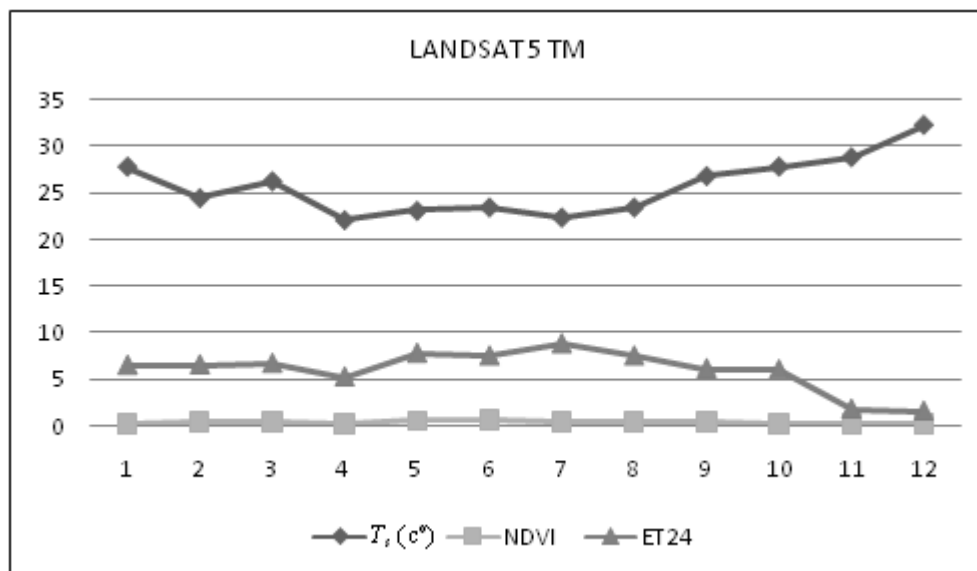
Figure 5.37 . Estimated the surface parameter derived from LANDSAT-5 on Sana'a Basin from TM, on 1st June 1998, T_s surface temperature(°c), *NDVI* vegetation indices, ET_{24} evapotranspiration from satellite overpass time.
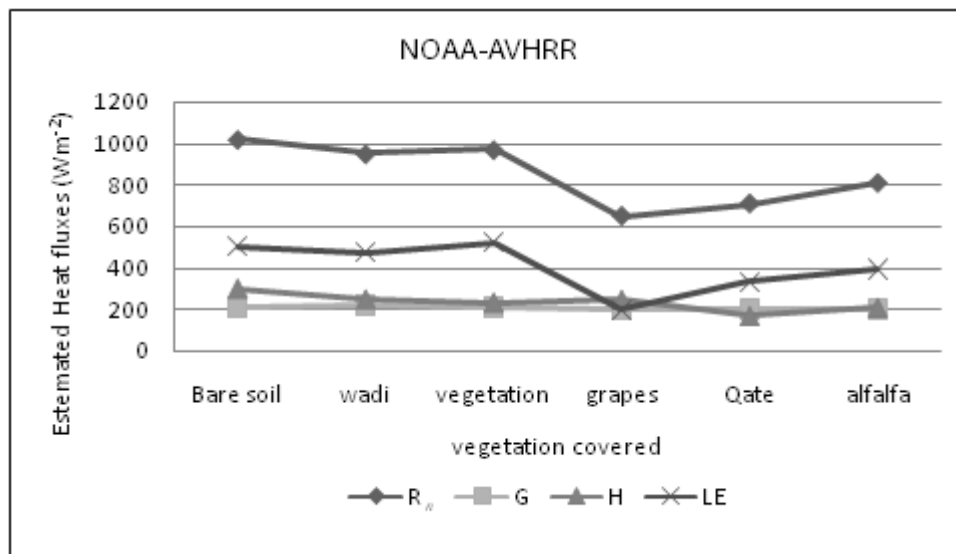
Figure 5.38 Estimated surface heat fluxes over arid and semi-arid region of Sana'a Basin from NOAA-AVHRR. LE = latent heat flux, R_n = net radiation, G = soil heat flux, H = sensible heat flux.
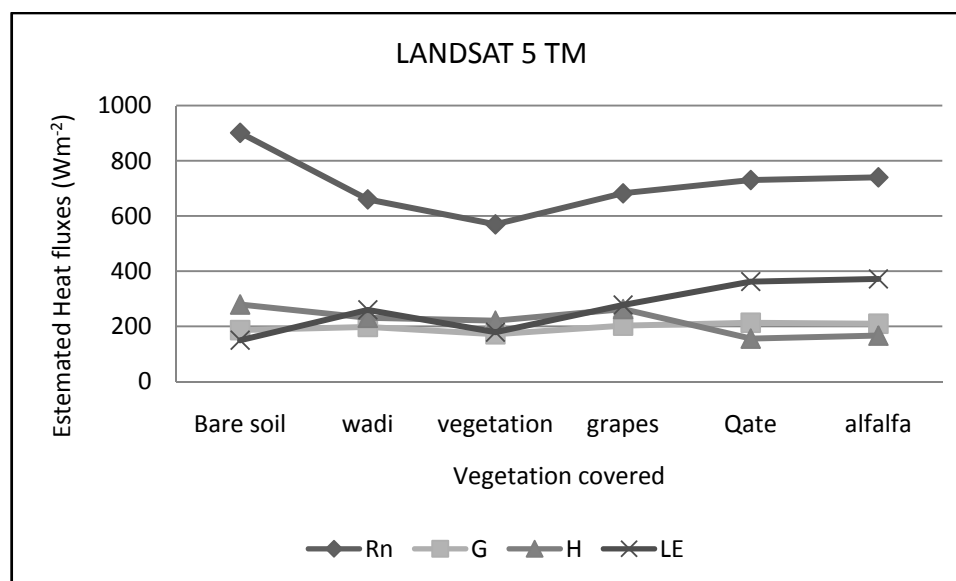
Figure 5.39 Estimated surface heat fluxes over arid and semi-arid region of Sana'a Basin from LANDSAT-5 TM. LE = latent heat flux, R_n = net radiation, G = soil heat flux, H = sensible heat flux.

5.5 Fusions of Landsat TM and NOAA-AVHRR data for generating ET maps

In this section the results from the methodologies of fusion SEBAL is discussed. The result of the daily measured ET was compared with the SEBAL Landsat ET on four different dates during the growing season. Two out of four days show good agreement: the difference between measured and estimated daily ET is 0.1 mm on December 24th and 0.5 mm on June 1st 1998(see Fig.5.40). On the Landsat image of June 1st some haze was present above a large part of the Sana'a basin irrigation district including the measurement site. Due to haze an area appears colder on the satellite image than it actually is, causing higher SEBAL ET values. On March 26, the measured value is 1.0 mm higher than the SEBAL ET. This difference for the Landsat day appears consistent with the NOAA-AVHRR results: june 10 NOAA-AVHRR and both estimates are higher than the landsat TM and measured values.
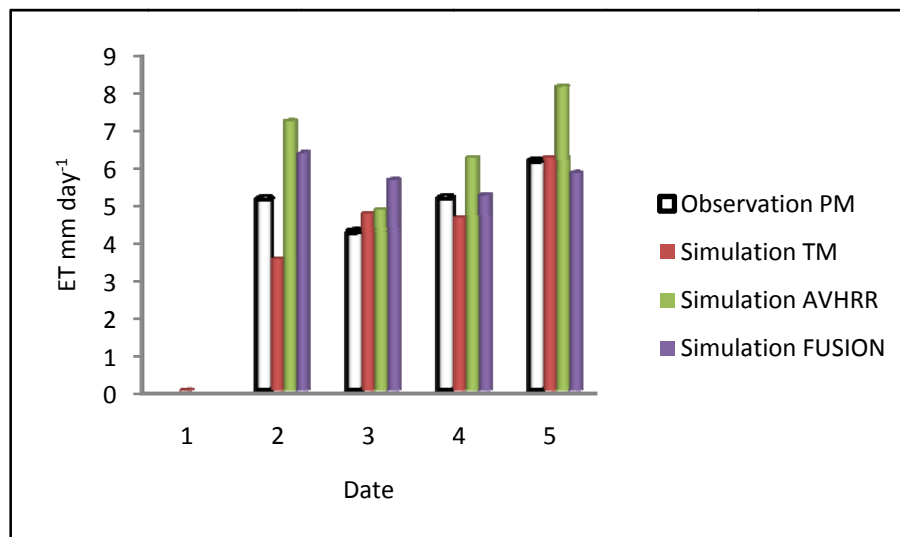
Figure. 5.40   Measured daily ET plotted against M-SEBAL daily ET of four TM & AVHRR and Fusion the two.

In this study, for the purpose of validation, the classified image of - Landsat TM, NOAA-AVHRR and fused image using the SEBAL method was compared with classified image of Landsat TM data acquired at the same time as NOAA-AVHRR. Figures 5.41 to 5.43 respectively demonstrate classification result of ET from NOAA-

AVHRR composite image, NOAA-AVHRR-Landsat TM fused image and Landsat TM image acquired during early January 1998. The comparison of images covering part of the Sana'a basin clearly shows the spatial improvement in the classification accuracy in the fused image.
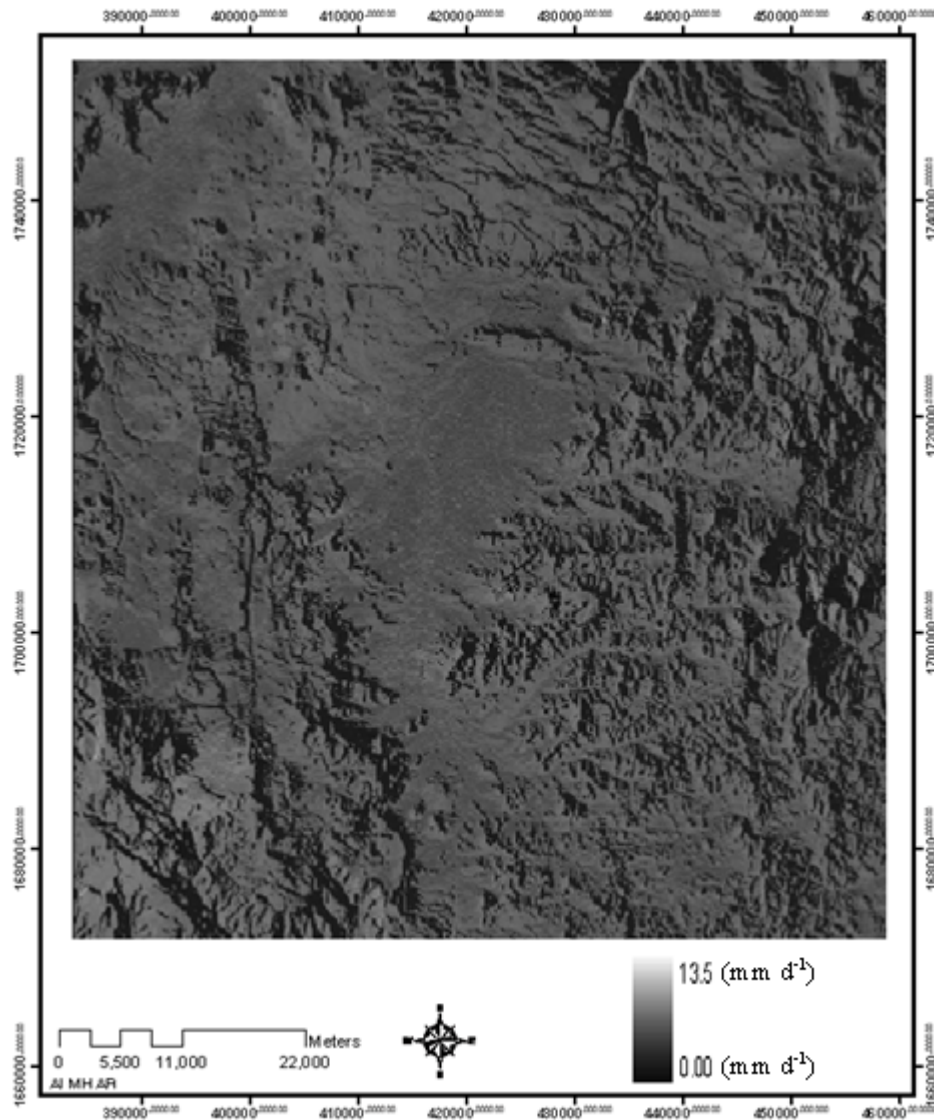
Figure 5.41   Evapotranspiration Landsat TM image 1st June 1998)
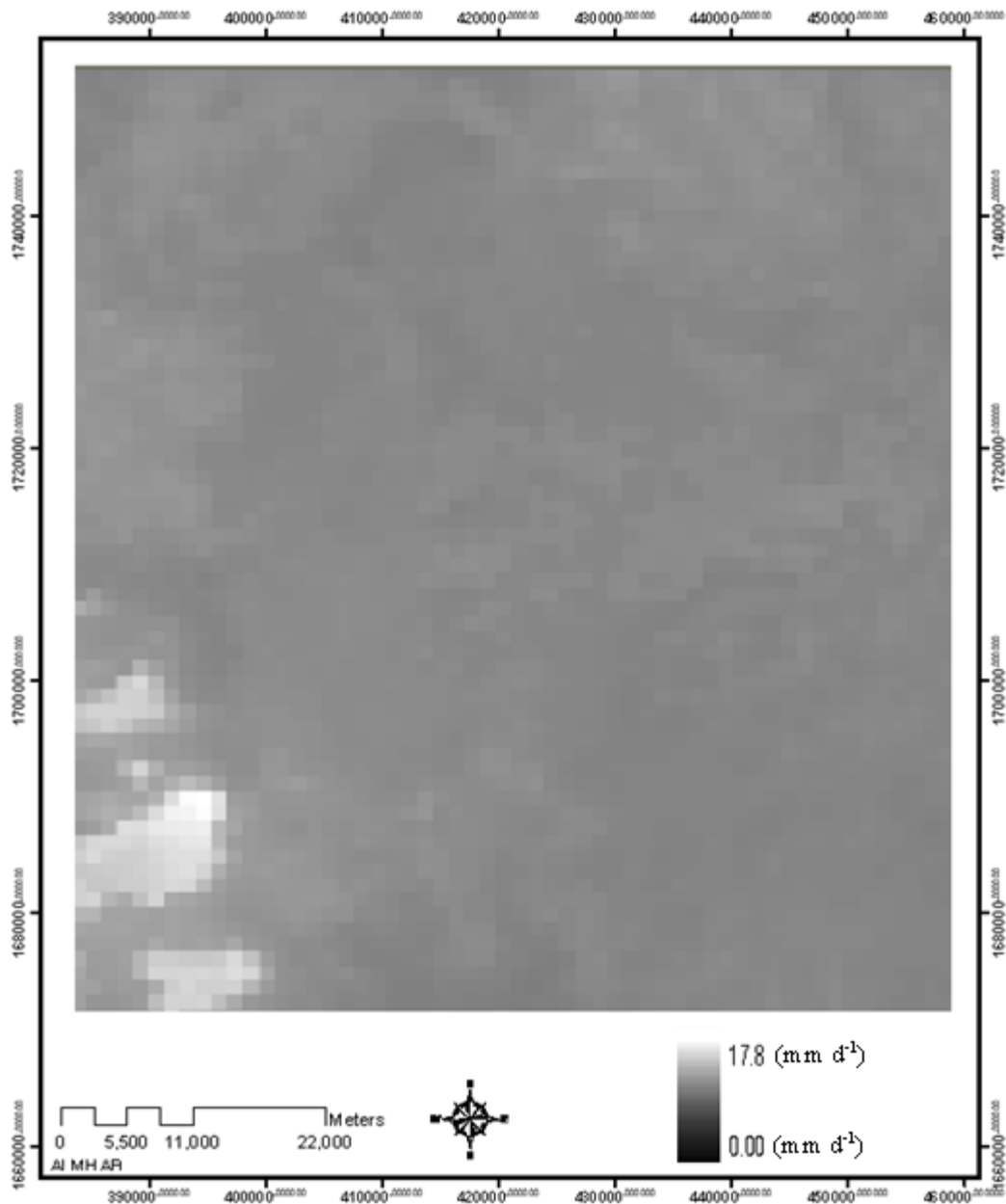
Figure 5.42 Evapotranspiration NOAA-AVHRR composite image (1st to 10 June 1998)
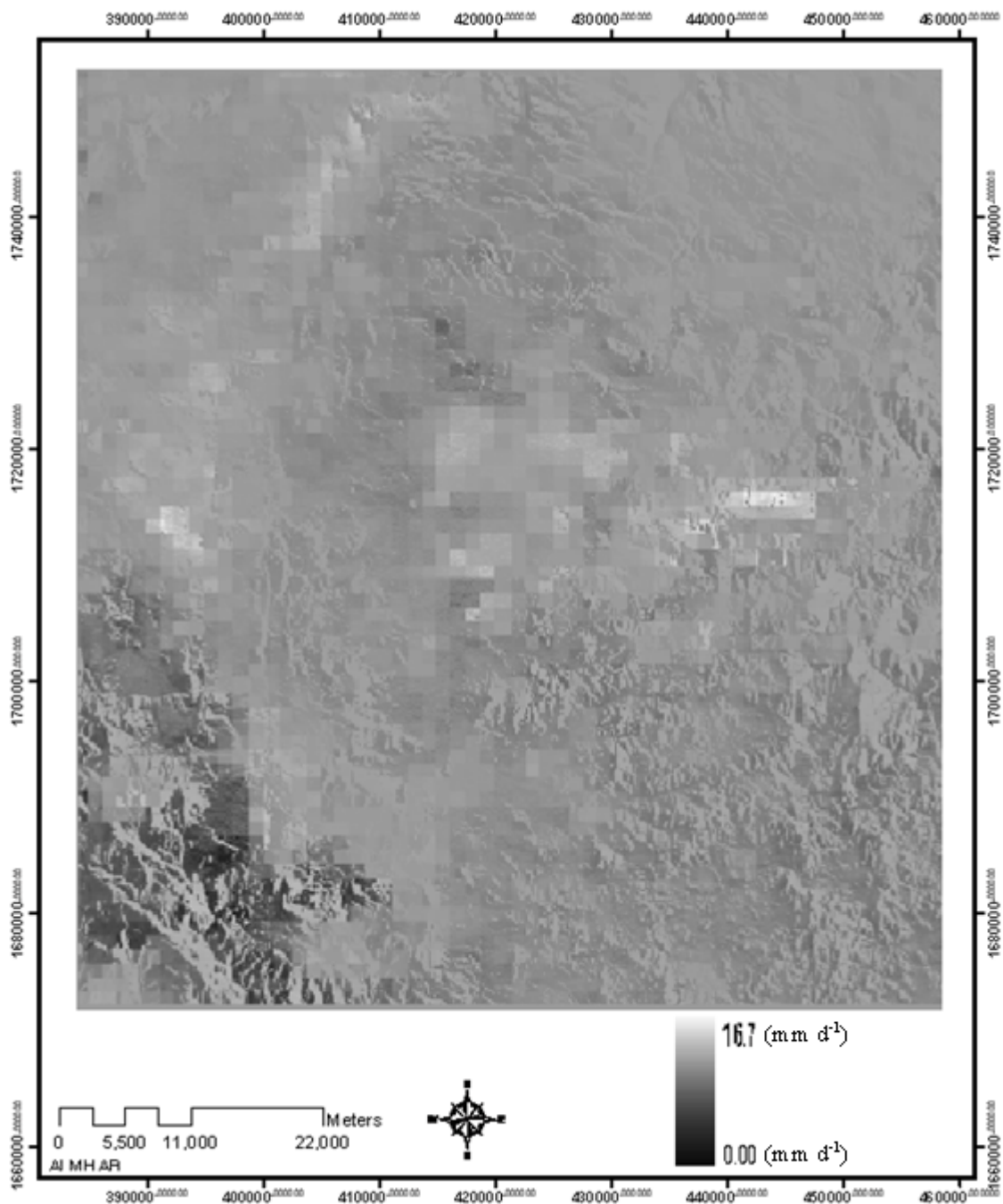
Figure 5.43 Evapotranspiration fusion image

For numerical comparison, the statistics of ET derived from the NOAA-AVHRR composite image, fused image and Landsat image are given in Table 5.6. This shows a slight improvement in the classification result of fused data. Further detailed

comparison will be made using better ground truth data, which is being collected in the

Landsat images in Sana'a basin.

Table 5.6 : Observation ET for grape fields using FAO Penman Monteith Eq (PM) and Simulation ET from TM and AVHRR and Fusion images with M-SEBAL over Sana'a basin area

Observation PM	Simulation TM	Simulation AVHRR	Simulation FUSION	SEE
5.1	3.5	7.2	6.32	0.93
4.2	4.7	4.8	5.6	1.12
5.1	4.6	6.2	5.2	0.59
6.1	6.2	8.1	5.8	0.95

Where: SEE is the standard error of the estimate Eq. (4.16)

5.6. Analysis of the Behavior of modified SEBAL in different study Areas

For the result of the analysis, it could be concluded that , all the values of surface parameters and surface fluxes are in the normal ranges expected for agricultural fields.

5.6.1 Analysis of the Behavior of modified SEBAL in mountainous areas

The Site of the study area in the mountain, Sana'a Basin figure 5.44. comprises of a wide range of area which is made up from different type of land covers and land uses. However, it is mostly an intermountain plain surrounded by highlands from the west, south and east. It also covers (1) agriculture areas, (2) volcanic areas, (3) basalt areas and (4) urban areas figure 5.45 below. This research analyses the behavior of modified SEBAL model in four sample in agriculture areas, four sample for bare areas, four sample for volcanic areas, four sample for basalt areas and four sample for urban areas. The predominant climate is arid, particularly along the western highlands.

Figure 5.44 Sana'a basin area contains the (1) agricultural areas, (2)volcanic area, (3) basalt areas and (4) urban areas for the image date of 06/01/1998.

5.6.1.1 Analysis of the behavior of modified SEBAL in agricultural areas

In Fig. 5.45 a true color close-up of some agricultural fields in the Sana'a area for image acquired on 01/6/1998 is displayed where some individual fields are labeled. Table 5.7 shows surface parameters and fluxes corresponding to sub samples from the four fields in Fig. 5.45. Sample 4 represent full-covered vegetated surfaces with the highest values of NDVI (see NDVI map in the figure5.46b).
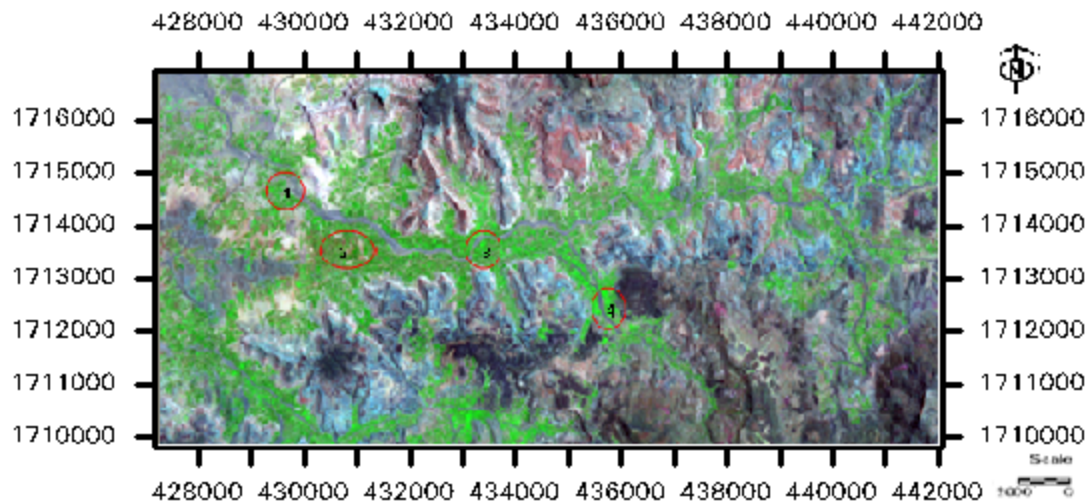
Figure 5.45 four samples on the agricultural areas, Sana'a basin for the Scene of 06/01/1998

According to Fig. 5.45 and Table 5.7, sample 1 is likely to be a seasonally crop, sample 2 is a Plum tree plantation, sample 3 is an alfalfa and sample 4 is grape plantation.

The color of the parameters and fluxes for the samples shown in figure 5.46 area (a), Albedo (b) vegetation indices (NDVI);(c) Surface Temperature in Kelvin; (d) aerodynamic resistance (e) Sensible heat flux; (f) evapotranspiration 24 hours derived from LANDSAT 5 TM for wadi asser Sana'a basin Yemen. Predicted Table 5.7 shows that the surface having the lower temperature (sample 2 T_s=306.9 K) is the one having the lowest predicted H, and the highest predicted ET (7.8 mm/day). On the other hand,

samples 1 and 3 which have higher temperatures show the highest values of H, resulting in lowest predicted ET.

In conclusion, all the values of surface parameters and surface fluxes are in the normal ranges expected for agricultural fields.

Table 5.7 : Surface Parameters and Fluxes for Samples of agriculture areas Pixels
Taken from the 06/01/1998 Image

Sample	1	2	3	4
Probable crop	seasonally crop	Plum	alfalfa	Grape
Albedo	0.107	0.068	0.077	0.069
NDVI	0.384	0.492	0.291	0.495
z_{om}(m)	0.54	0.413	0.190	0.912
T_S(K)	315.797	306.960	311.475	307.899
Rn (Wm^{-2})	716.668	772.196	732.700	756.893
G (Wm^{-2})	203.291	215.06	215.662	218.158
H (Wm^{-2})	252.353	219.102	237.629	213.995
r_{ah}	42.997	34.859	38.944	37.577
$\lambda(ET_{ins})$	0.471	0.605	0.542	0.578
ET24 (mm/day)	4.560	7.799	4.868	6.842
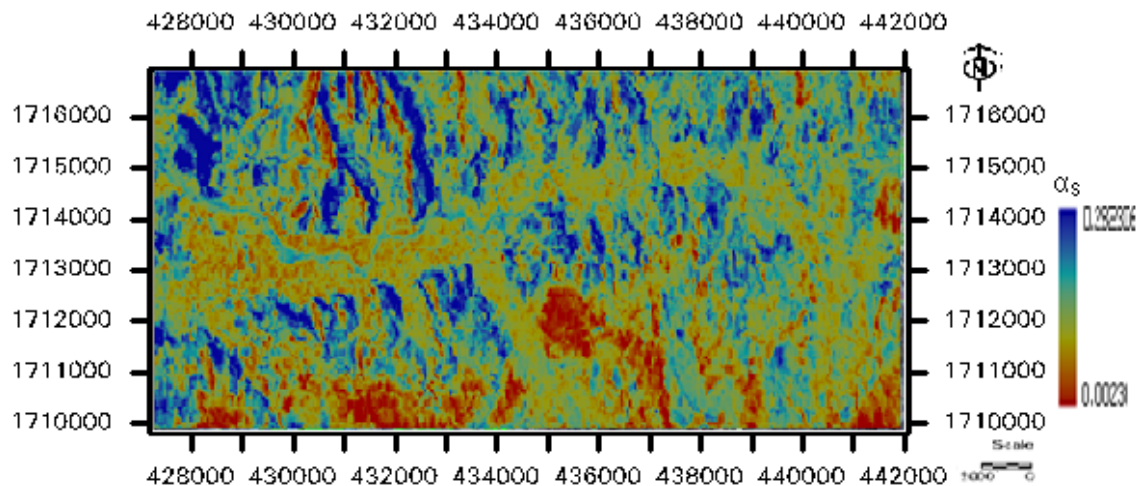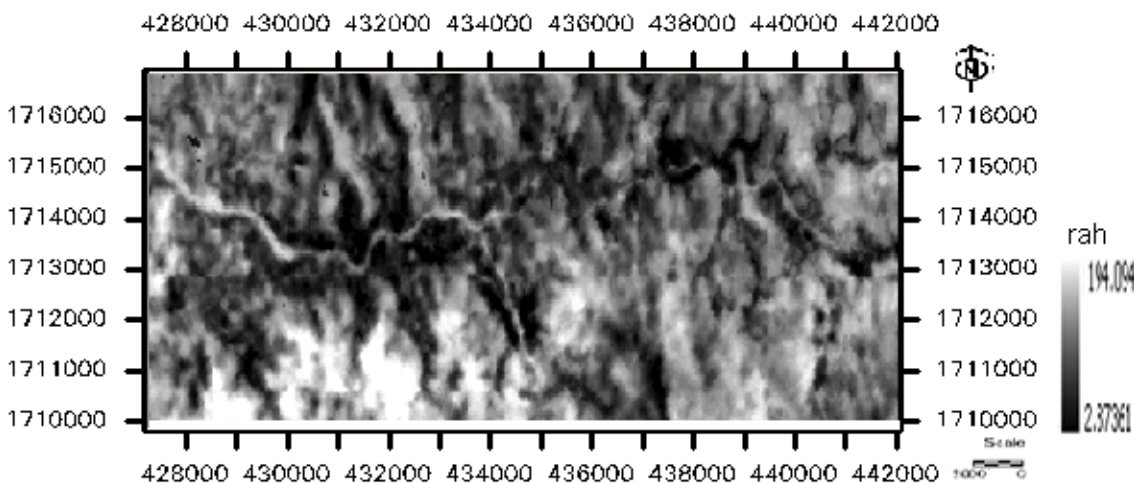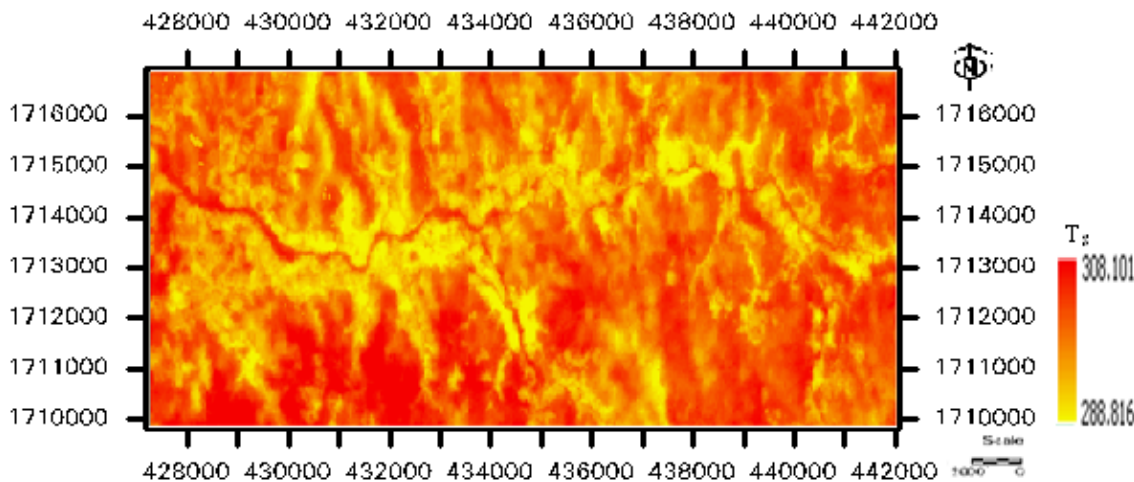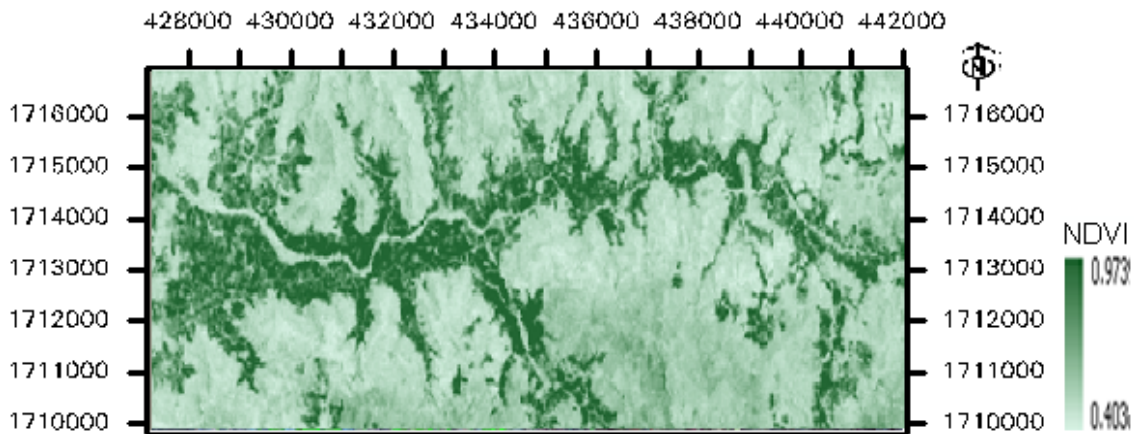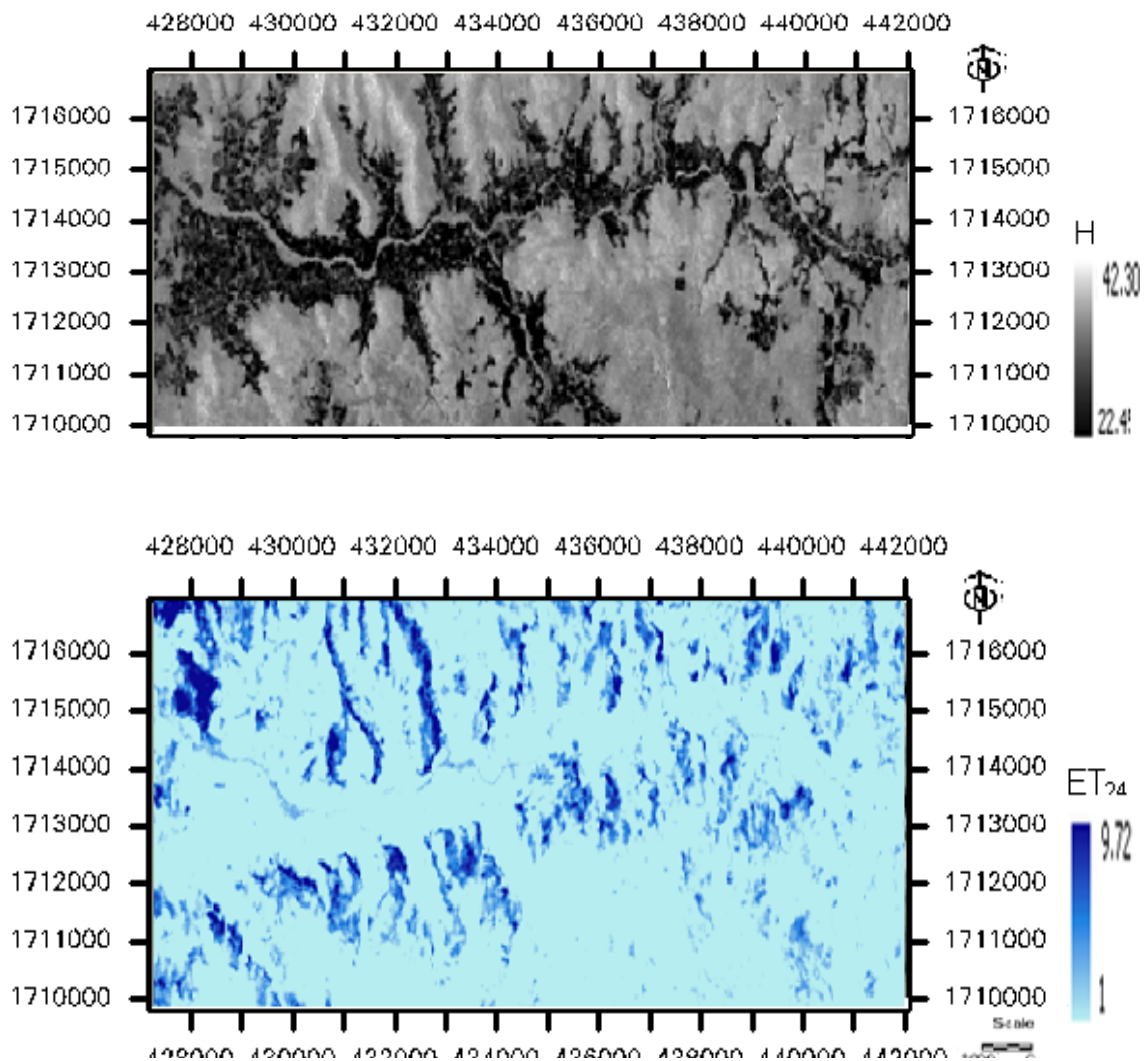
Figure 5.46 .(*a*) Estimated surface Albedo; (NDVI)vegetation indices ;(Ts) Surface Temperature in Kelvin; (r_{ah}) aerodynamic resistance (H) Sensible heat flux; (ET_{24}) evapotranspiration 24 hours derived from LANDSAT 5 TM for wadi asser Sana'a basin Yemen.

5.6.1.2   **Application of modified SEBAL for Volcanic areas**

The estimation of evaporation from volcanic areas depends greatly on the correct estimation of G for the volcanic areas. Since this study focused on the estimation of ET for agricultural fields, G for volcanic rock was roughly estimated as Eg.(3.49).

Figure 5.47   Four samples on the volcanic areas, Sana'a basin for the Scene of
06/01/1998

The ratio of G/R_n in volcanic areas is complicated to determine, and depends on several parameters including topographic, currents, and season. Values of surface parameters and fluxes are included in Table 5.8 for several samples of volcanic areas (reservoirs) in the region. The 4 samples are located around Jabal Nugom, Sana'a, Yemen.

Table 5.8 : Surface Parameters and Fluxes for Samples of volcanic areas Pixels Taken
from the 06/01/1998 Image

Sample	1	2	3	4
Albedo	0.058	0.056	0.046	0.051
NDVI	0.217	0.225	0.213	0.184
z_{om}(m)	0.114	0.134	0.123	0.114
T_S(K)	314.324	311.579	310.738	314.460
Rn (Wm^{-2})	759.302	862.600	760.358	795.809
G (Wm^{-2})	226.442	238.010	229.952	229.971
H (Wm^{-2})	242.898	233.078	212.027	337.958
r_{ah}	44.402	43.464	44.756	44.828
$\lambda(ET_{ins})$	0.541	0.597	0.605	0.557
ET24 (mm/day)	2.441	0.00	0.104	3.311

The low Albedo predicted for volcanic areas (around 0.046) makes volcanic areas a good
absorber of both incoming short wave ($R_{s\downarrow}$) and incoming longwave radiation ($R_{L\downarrow}$).
This tends to make net radiation a large component in the energy balance for volcanic
area. In the cases shown in Table 5.8, the amount of sensible heat, predicted for volcanic
areas using the dT function is low, so that almost all net radiation is partitioned into G
and $\lambda(ET_{ins})$.

 Due to the uncertain prediction of G/R_n in this study, the results of ET for volcanic areas
are questionable, even though they appear to be reasonable values. More research needs to
be done on this issue to help modified SEBAL predict accurate values of evaporation of
volcanic areas in the study area.

5.6.1.3 Application of modified SEBAL in Basalt Areas

In this study area, there are a significant areas covered by basalt rock that originated from volcanic activity. These areas are portrayed in Figure 5.48. One of them is part of the Wadi Alkhared, northern Sana'a basin , Yemen.
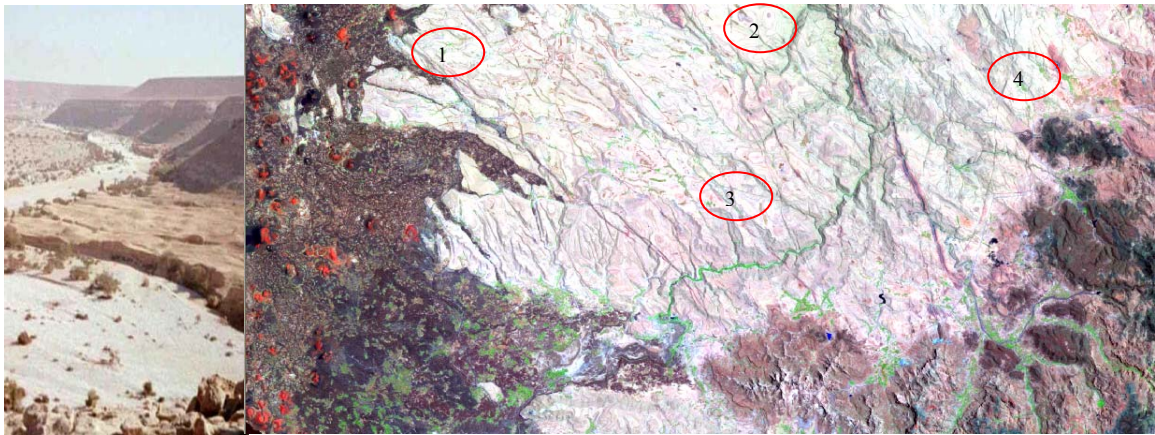
Figure 5.48   four samples on the basalt areas, and typical area wadi alkhared southern Sana'a basin (right) , picture from wadi alkhared(left), Yemen

Table 5.9 shows surface parameters and fluxes corresponding to sub samples from the four fields in Fig.5.48

Table 5.9 : Surface Parameters and Fluxes for Samples of basalt areas Pixels Taken from the 06/01/1998 Image

Sample	1	2	3	4
Albedo	0.165	0.165	0.163	0.176
NDVI	0.214	0.215	0.212	0.223
z_{om}(m)	0.127	0.126	0.123	0.126
T_S(K)	310.703	308.088	308.566	311.441
Rn (Wm^{-2})	669.017	662.128	672.96	635.532
G (Wm^{-2})	196.848	202.685	201.319	192.432
H (Wm^{-2})	210.641	194.549	202.943	207.476
r_{ah}	43.850	43.850	43.919	43.541
$\lambda(ET_{ins})$	0.543	0.589	0.569	0.539
ET24 (mm/day)	2.48	0.57	4.921	0.00

5.6.1.4 Application of modified SEBAL in Urban Areas

In this study area, there are a significant areas covered by urban area that originated from human activity. These areas are portrayed in Figure 5.49. is part from the western Sana'a City, around Aldaery street.
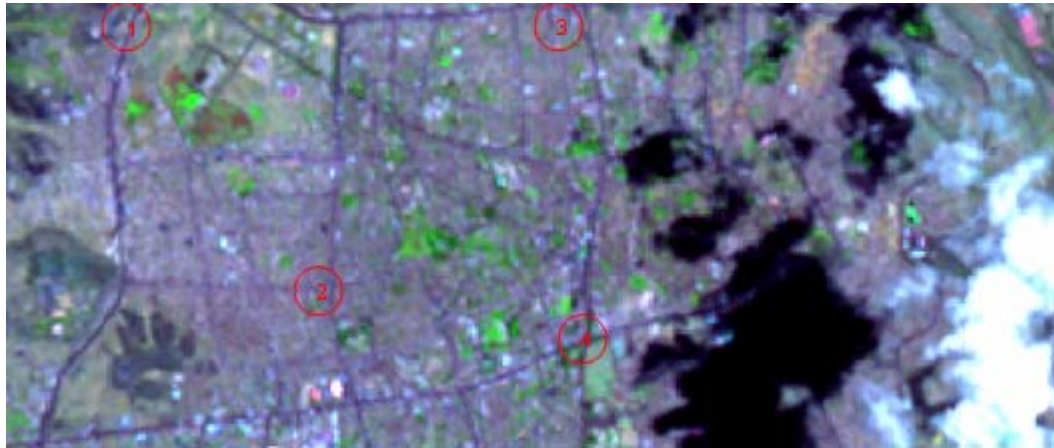
Figure 5.49   Four samples on the urban areas, western Sana'a city, Yemen

Table 5.10 shows surface parameters and fluxes corresponding to sub samples from the four fields in Fig.5.49.

Table 5.10 : Surface Parameters and Fluxes for Samples of urban areas Pixels Taken from the 06/01/1998 Image

Sample	1	2	3	4
Albedo	0.147	0.093	0.088	0.125
NDVI	0.157	0.138	0.145	0.125
z_{om}(m)	0.092	0.082	0.086	0.076
T_S(K)	315.505	312.346	312.146	313.176
Rn (Wm^{-2})	711.667	727.661	731.841	688.647
G (Wm^{-2})	213.372	218.220	219.456	206.545
H (Wm^{-2})	237.457	209.091	207.950	213.217
$\lambda(ET_{ins})$	0.523	0.590	0.594	0.558
ET24 (mm/day)	6.982	4.753	4.805	4.412

5.6.2　Application of modified SEBAL in oasis Desert Areas

In Eastern Yemen, Wadi Hadramout areas are characterized predominantly by desert climate, and have two types of vegetation: desert grass and Pennisetum divisum . In many areas only one of these vegetation types is predominant, but a combination of both is also commonly encountered. Photos of desert vegetation are shown in Fig. 5.50

A　　　　　　　B

Figure 5.50　　Desert wadi hadramout in the Study Area:　satellite images (B) and picture in the started of the wadi hadramout (A).

In most of the images processed in 1995 and 1998, the radiometric surface temperature of desert areas was consistently higher than dry bare soil surfaces in agricultural environments. Since in this study, hot pixels were taken from agricultural bare soil pixels in order to insure good estimates of dT for the range of agricultural conditions, the surface temperature (T_s) of desert pixels was often greater than the T_s of the hot pixel. Since in SEBAL the hot pixel is considered to have zero ET, the estimated ET in desert areas are often estimated to be negative, depending on R_n, G, and surface roughness.

Table 5.11 shows results obtained from the date 08/24/98 Landsat 5 scene. This table includes surface parameters and fluxes corresponding to the cold and hot pixels selected for the image, and a representative desert grass sample and Pennisetum divisum sample.

Table 5.11 : Surface Parameters and Fluxes for Several Desert Samples

Sample	Cold Pixel	Hot Pixel	Pennisetum	Grass
Albedo	0.076	0.075	0.055	0.058
NDVI	0.478	0.188	0.194	0.191
z_{om}(m)	0.139	0.011	0.122	0.130
T_S(K)	306.499	315.743	315.125	316.053
Rn (Wm^{-2})	772.856	713.715	850.572	750.383
G (Wm^{-2})	209.063	217.116	238.812	224.919
H (Wm^{-2})	215.694	255.0743	253.483	257.324
r_{ah}	35.012	44.723	44.516	44.622
$\lambda(ET_{ins})$	0.615	0.00	-0.545	-0.510
ET_{24} (mm/day)	5.6	0.00	-2.215	-1.941

Table 5.11 shows that the surface temperature of the Pennisetum divisum sample (T_s = 315.1 K), and the grass sample (316.0 K) are greater than the temperature for the hot pixel (315.7 K). The final daily evapotranspiration for the hot pixel was 0 mm/day (which is the main assumption of modified SEBAL for a dry hot pixel, and the corresponding ET_{24} for the Pennisetum divisum and grass sample (was -2.2 and - 1.9 mm/day) respectively. These negative ET_{24} values are obviously erroneous. If one considers the satellite overpass time (around 11:30 am) and the season of the year (mid-summer), one should expect ET values from desert areas to be zero or slightly positive, since essentially no rain occurs during May-September in eastern Yemen.
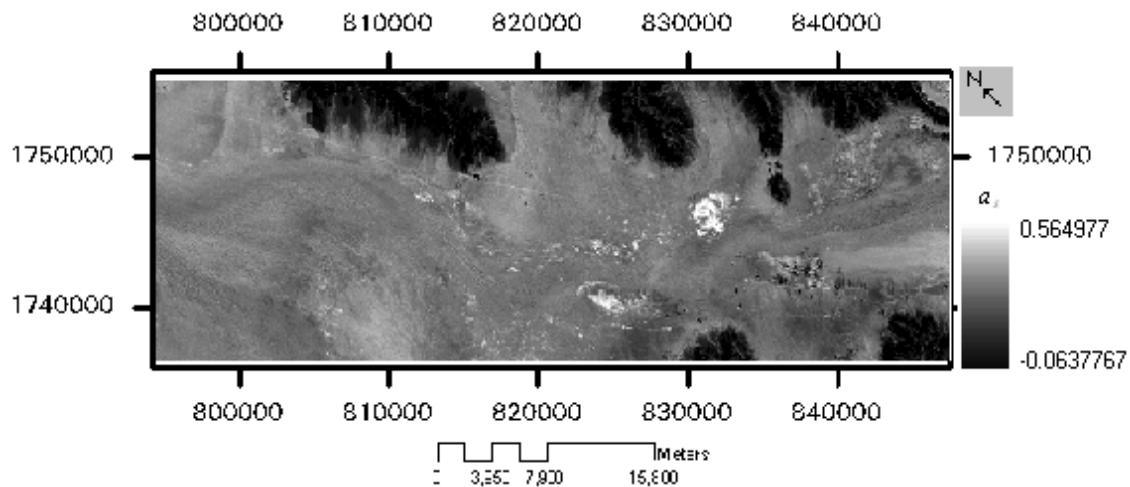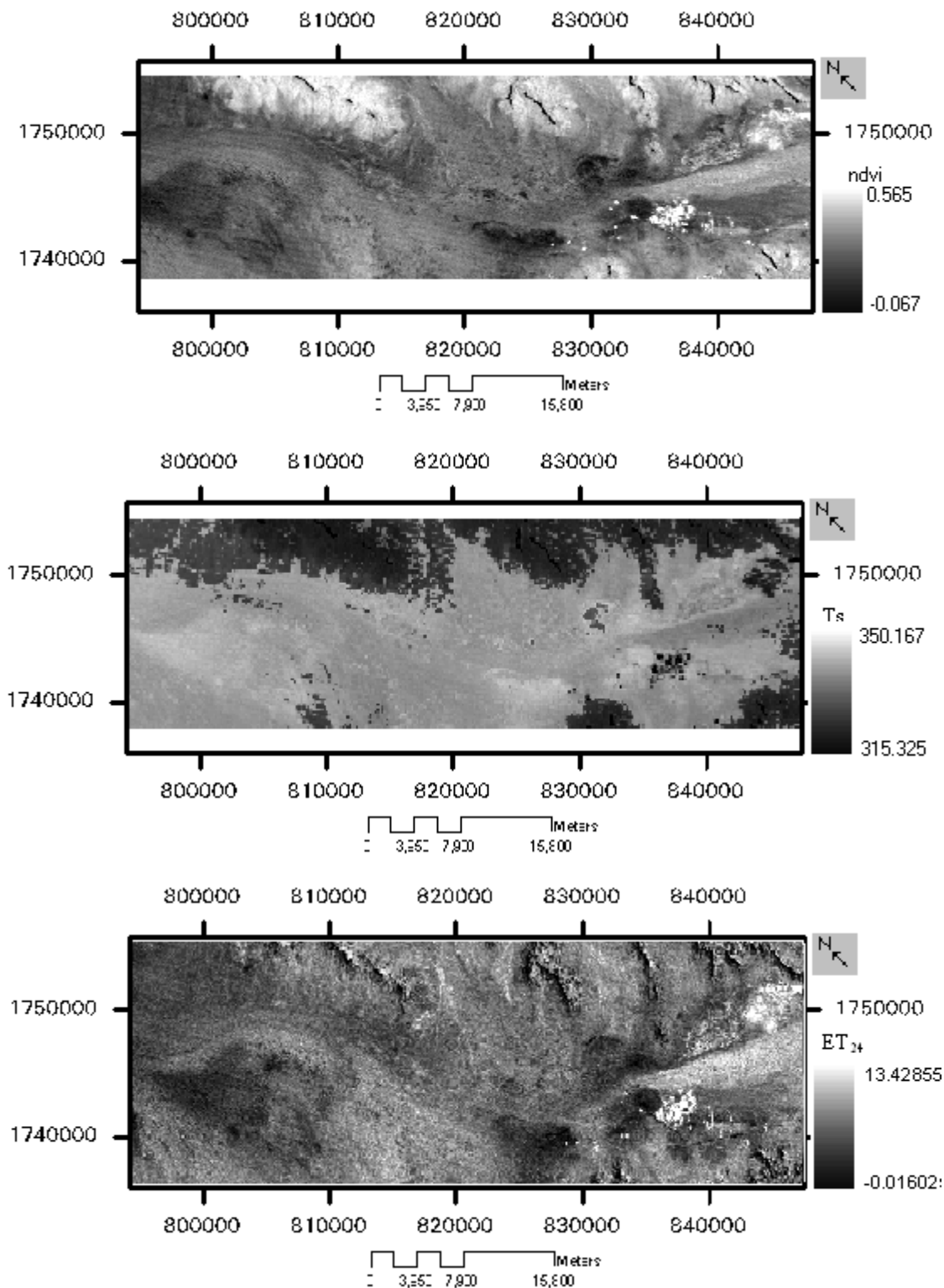
Figure 5.51 (*a*) Estimated surface Albedo; (ndvi)vegetation indices (NDVI);(Ts) Surface Temperature in Kelvin; (ET$_{24}$) evapotranspiration ET$_{24}$ hours derived from LANDSAT 5 TM for Desert wadi Hadramout, Hadramout, Yemen.

5.6.3 Application of modified SEBAL in arid coastal Areas

In this study area, there are a significant areas covered by arid coastal areas. Two of these areas are portrayed in Fig. 5.52. One of them is part of the Wadi Tuban, Lahj, Yemen.
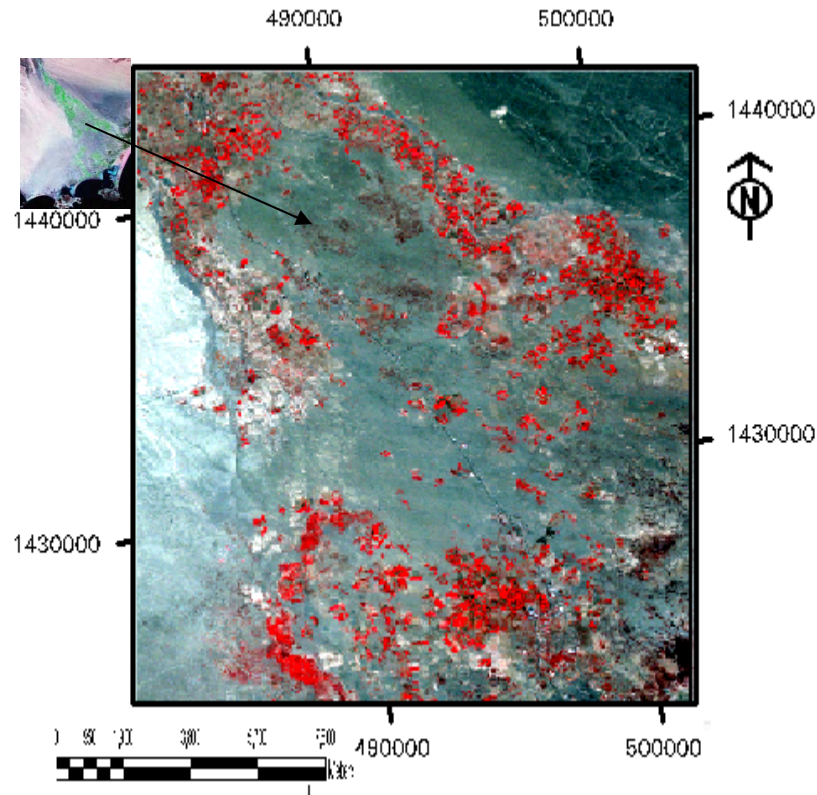
Figure 5.52 coastal Area in Wadi Tuban, Lahj , Yemen for the Scene of 06/21/1989
LANDSAT TM image true color

Figure 5.53 show the result of application modified SEBAL on Wadi Tuban , Lahj, Yemen. the methodology can be very valuable to assist SEBAL in the prediction of ET from no irrigated areas as rangeland or bare soils.
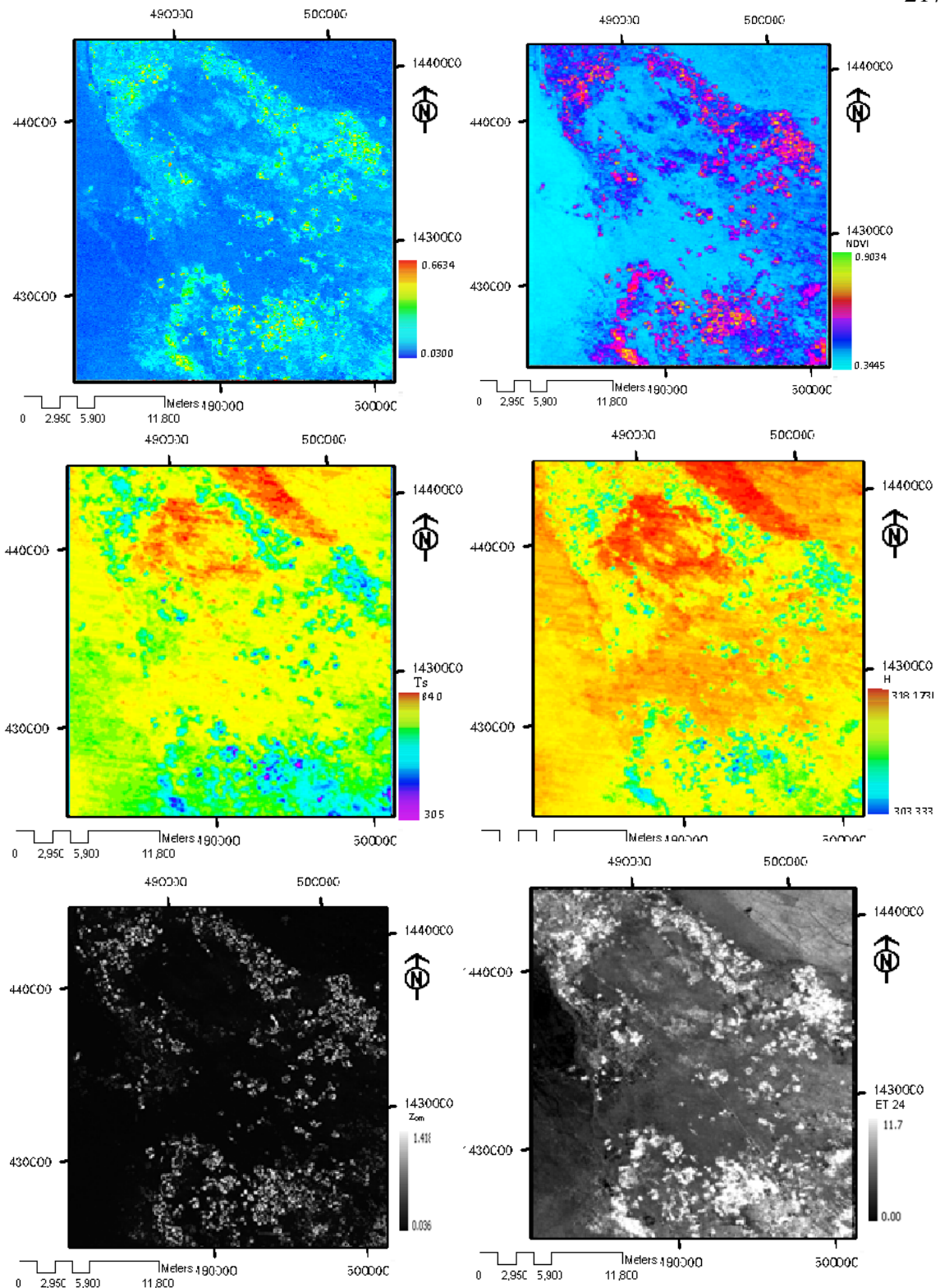
Figure 5.53 (*a*) surface Albedo; (NDVI)vegetation indices ;(Ts) Surface Temperature in Kelvin; (H) Sensible heat flux; (z_{om})surface roughness (ET_{24}) evapotranspiration 24 hours derived from LANDSAT 5 TM for wadi Tuban Lahj, Yemen.

5.7 Difference between modified SEBAL, SEBAL and other SEBAL's variants

The major extensions in modified SEBAL from SEBAL are the mountain correction procedures including radiation and surface temperature corrections and calibration of energy balance to cold pixel and for the 24-hour ET estimation. In this section, some of the differences between the Modified SEBAL, SEBAL and SEBAL$_{ID}$ are discussed in tables 5.12 below. The other general comparison between Modified SEBAL, SEBAL and other SEBAL variants is showed in table 5.13.

Table 5.12 : Comparison between Modified SEBAL, SEBAL and other SEBAL variants

parameter	SEBAL	SEBAL-ID	Modified- SEBAL (this study)
reflectance correction by DEM	No	No. in general model Yes in the mountain model	Yes
Surface parameter estimation	From the image	From the image	From reflectance correction by DEM
Surface temperature to estimation long wave radiation	From the metrological station	From the metrological station	From cold pixel in the image
Ground heat flux	F(Ts, a, NDVI)	F(LAI)	F(NDVI)
Sensible Heat flux estimation	Experimentally Repeat five time	no	yes
u* coefficient correction	no	no	Yes
surface roughness z_{om}		F(LAI)	F(NDVI)
height z_1	0.01	0.1	0.01
height z_2	2	2	2
Wet Pixel	Cool water	Agriculture land	Agriculture Land
Hot Pixel	Poor land	Poor land	Desert Area
ET type focuses	Actual ET	Actual ET	Actual ET Potential ET
Fraction evaporation FE	From satellite image	From metrological data and reference evapotranspiration	From satellite image
Based on	ILWIS	ERDAS	ERDAS& Arc GIS
Database	access	Excel	Excel &Geo-database
Number models use	12	24	46
ET	From satellite image	EF*ETr	From satellite image

Table 5.13 below shows the basic difference regarding data source, the calculation of reflectance and satellite data used.

Table 5.13   General difference between Modified SEBAL, SEBAL and other SEBAL variants

No.	SEBAL variants	University	Type of research	Program	Satellite Image	Reference
1	SEBAL	W.U ITC	PhD	ILWIS	Multi Sensors	Bantiaanssen,1995
3	SEBAL-ID	UID	2PhD	ERDAS, Excel	ETM+	Terazz, 2002& Tasumi, 2003
2	Modified-SEBAL	UTM	PhD	ERDAS, Excel	TM, AVHRR	Almhab,2008
4	SEBAL^{NM}	UNM	PhD	C++	ASTER	Wing, 2006
5	SEBAL$_{FLORED}$	UFL	Project	-	MODIS	Sahra.com, 2006
6	SEBAL $_{SP}$	Project	Project	Spatial program	-	Project, 2006

5.8   Regional DSS-ET maps for Sana'a basin, Yemen

5.8.1   Overview

The chosen weather stations CAMA, NWRA and AREA (Al-Irra) are situated in the middle of the basin. The stations are located in an arid region, and for these station the DSS has selected the M-SEBAL as the best method for estimating ET when available metrological data is only daily mean of metrological parameters, as in the case of CAMA and NWRA stations. However, the SEBAL-$_{ID}$ and SEBAL were selected as the best methods for estimating ET, when all the metrological data available, with good accuracy and instantaneous data as in the case of Al-Irra station. In order to verify the decisions of the DSS, the model was run using all available data except wind speed. In this case, the DSS chose the simplified method as the best ET estimation method because the data needed was only the temperature (see Table 5.14 to 5.17). Values of ET estimated by different methods versus FAO Penman-Monteith for **CAMA** station Sana'a basin. Wind speed is required for applying any combination, SEBAL, SEBA-$_{ID}$, M-SEBAL and Biophysical method. For more detail on this section is provided in appendix B

The hydrological models based on GIS have identified FAO Penman-Monteith as the best method for estimating ET. In order to verify the decisions of the DSS, the model was run using all available data except wind speed. It is also found that the DSS selected the Hargreaves method as the best ET estimation method because it can accommodates all the available data. The DSS has selected the FAO Penman-Monteith method as the best method for CAMA, when it uses estimated net radiation from extraterrestrial radiation and sunshine hours. The model selected the FAO 24 radiation method as the best in the absence of wind speed data. However, the Hargreaves method was the best method when the maximum and minimum temperatures, maximum and

minimum relative humidity, and wind speed were used as input to the model. This is because solar radiation or sunshine hours are essential for applying all combination and radiation methods as well as the SCS Blaney-Criddle method.

The model selected the FAO Penman-Monteith method for stations located in the regions and monthly temperature, relative humidity, wind speed, and sunshine hours were used as input. The Hargreaves method was the best method when temperature, relative humidity, and wind speed or temperatures alone were used as input to the model. Apart from that, when the model was used with temperature, relative humidity, and solar radiation, the DSS has selected the FAO24 Radiation method as best. All these decisions made by the DSS coincide exactly with ASCE rankings (ASCE, 2002 and Jensen et al. 1990

5.8.2   Comparison of Methods: Daily Estimates on CAMA station

The ET values estimated by all the eleven chosen methods were compared with the FAO Penman-Monteith estimates. Summary statistics of daily ET for the entire period is shown in Table 5.14. The SEBAL and Biophysical methods gave a high daily mean of ET for the full period. They are 5.8 and 5.6 mm/day respectively. Standard error estimates of the different methods ranged from 0.792 mm/day for the SEBAL to 1.46 mm/day for the SCS-BC method for the full time period. However, it varies from 0.79 mm/day for the Simplified method to 1.46 mm/day for FAO24 Penman in the peak month. During the peak month SEE estimate was greater than that for all periods estimate for all methods except the Hargreaves and Priestley-Taylor.

Table 5.14 Statistical Summary of daily ET Estimates for CAMA Stations

Statistical	ET method										
parameter	FAO56 PM	FAO24 P	FAO-R	PT	HG	SCS -BC	SEBAL	SEBAL -ID	M-SEBAL	Bio	Simp
Mean ET mm/day	3.2	4.1	3.4	3.9	4.6	3.0	5.8	-	4.8	5.6	3.8
Weight Ranking	38	37	33	33	19	28	68	69	62	46	27
Normalized weight	2.53	2.467	2.2	2.2	1.26	1.85	4.533	4.9	4.1	3.06	1.80
Reciprocal weight	6.16	5.66	5.17	5.17	3.5	4.7	11	11.17	10.33	7.5	5.25
Weight (n-rj+1)^p, p=2	158	149	133	133.	91	116	290	297	272	192	2.34
SEE mm/day	1.411	1.175	1.35	1.22	1.05	1.46	0.792	-	1.009	0.83	1.25
WSEE mm/day	1.044	0.870	1.00	0.91	0.78	1.09	0.586	-	0.747	0.62	0.93
b	1.00	1.281	1.06	1.22	1.44	0.94	1.813	-	1.500	1.75	1.19
%PM	100	128	106	122	144	94	181	-	150	175	119

Note: SEE standard The latter method predicted similar values of SEE for all periods and the peak error estimate; WSEE =weighted standard error estimates calculated as 0.74 SEE ; R^2 = coefficient of determination; b=regression coefficient; and % of PM percentage of FAO Penman-Monteith value.
- mean meteorological data not available during the time of satellite overpass on the study area.

The SEBAL yielded very high values of the coefficient of determination when compared with the FAO Penman- Monteith estimates when using parameter values extracted from remote sensing data. The simplified methods have over predicted the daily ET for all periods. These two methods over predicted daily ET value when the wind velocity was very high which ultimately affected the wind function component of these two ET estimation methods.

The combination equation made up of the FAO-R and FAO-24 Penman yielded very good values of the coefficient of determination when compared with the FAO Penman-Monteith estimates. The SEBAL and Biophysical methods over predicted daily ET for all periods and the peak month. These two methods over predicted when the wind velocity was very high which ultimately affected the wind function component of these two ET estimation methods.

5.8.3 Comparison of Methods: Daily Estimates in NWRA station

Summary statistics of daily ET in NWRA station for the entire period is given in Table 5.15. The FAO56 PM and SCS-BC methods gave the maximum mean daily ET for the full period 5 and 4.9 mm/day respectively. Standard error estimates of the different methods ranged from 0.964 mm/day for the FAO56 PM to 1.303 HG method.

Table 5.15 : Statistical Summary of daily ET Estimates for NWRA Station

Statistical	ET method										
parameter	FAO56 PM	FAO24 P	FAO-R	PT	HG	SCS-BC	SEBAL	SEBAL ID	M-SEBAL	Bio	Simp
Mean ET mm/day	5.0	4. 0	3.9	3.9	3.6	4.9	4.6	-	3.8	4.6	3.7
Weight Ranking	38.0	37	33	33	19	28	68	69	62	46	27.0
Normalized weight	2.533	2.467	2.2	2.2	1.27	1.86	4.533	4.9	4.1	3.06	1.8
SEE mm/day	0.964	1.200	1.23	1.23	1.3	0.99	1.055	-	1.251	1.06	1.28
WSEE mm/day	0.713	0.888	0.91	0.91	0.96	0.73	0.781	-	0.925	0.781	0.95
b	1	0.8	0.78	0.78	0.72	0.98	0.92	-	0.76	0.92	0.74
%PM	100	80	78	78	72	98	92	-	76	92	74

- mean metrological data not available during the time of satellite overpass on the study area.

The SEBAL down predicted daily ET by 8, but gave the SEE 1.055 mm/day. The HG method lower estimated 72 and the other methods underestimated -18% Mean daily ET. Overall, the SCS-BC and SEBAL methods predicted the FAO Penman-Monteith ET the best and other methods were ranked in a descending order are M-SEBAL, FAO-Penman Monteith, FAO Penman, FAO radiation, Priestley-Taylor, SCS- Blany Creadel, simplified, and Hargreaves.

As discussed earlier, the purpose of standardization of the methods is to have equivalent evaporation estimates from all methods when they are applied as a single evaporation estimating method. As FAO Penman-Monteith equation is universally

established and accepted method for estimating evaporation, it was nominated as the basis of standardizing other methods. All stations which contain parameters for FAO Penman-Monteith method was selected and FAO Penman evaporation was also estimated.

5.8.4 Comparison of Methods: Daily Estimates in Al-irra station

Table 5.16 shows the comparison of daily ET estimates for Al-Irra Station, between the FAO Penman-Monteith and all the combination, radiation, Temperature and Remote Sensing methods in A-Irra station Sana'a basin Yemen. The Hargreaves method yielded the minimum mean daily ETo of 3.2 mm/day, The SEE of different methods ranged from 0.92 mm/day for the SEBAL to 1.75 mm/day for the SEBAL-$_{ID}$ method a displayed in table 5.16.

The SEBAL over predicted mean monthly ET by 20, but gave the lowest SEE 0.920 mm/day. The simplified method estimated 15% lower and the other methods underestimated ±12.5% Mean monthly ET Table 5.16, the FAO-24 radiation method overestimated ET especially during the first three months when satellite image captured. The Hargreaves method lower predicted ET by about 20%, and yielded the SEE 1.41. Since the maximum and minimum temperature difference is very high in this station, these deviations are expected, because the Hargreaves method is the only method that requires measurement of only one daily parameter, and air temperature. Additionally SEBA$_{ID}$ yielded the maximum SEE 1.75. Overall, the SEBAL-$_{ID}$ method predicted the FAO Penman-Monteith ET as best. The SEBAL method has the lowest SEEs and ranked second, SEBAL-$_{ID}$ the ranking first, and other methods which are ranked in a descending order are M-SEBAL, FAO-Penman Monteith, FAO Penman, FAO radiation, SCS- Blany Creadel, Priestley-Taylor, simplified, and Hargreaves.

Table 5.16 : Statistical Summary daily ET Estimates for Al-Irra Station

Statistical parameter	ET method										
	FAO56 PM	FAO24 P	FAO-R	PT	HG	SCS-BC	SEBAL	SEBAL ID	M-SEBAL	Bio	Simp
Mean ET mm/day	4.0	3.5	3.5	3.5	3.2	4.1	4.8	4.0	3.6	4.6	3.4
Weight Ranking	38.00	37	33	33	19	28	68	69	62	46	27.0
Normalized weight	2.533	2.467	2.2	2.2	1.27	1.86	4.533	4.9	4.1	3.06	1.8
SEE mm/day	1.079	1.329	1.33	1.33	1.41	1.18	0.920	1.751	1.303	1.06	1.36
WSEE mm/day	0.798	0.984	0.98	0.98	1.04	0.87	0.681	1.296	0.964	0.78	1.004
b	1	0.875	0.875	0.875	0.8	1.025	1.2	1	0.9	1.15	0.85
%PM	100	87.5	87.5	87.5	80	102.5	120	100	90	115	85

5.8.5   Comparison of Methods: monthly Estimates in Al-irra station

Summary statistics of monthly ET for the entire period **in Al-irra station** are given in Table 5.17. The simplified and biophysical methods gave the maximum mean monthly ET for the full period 5.8 and 5.6 mm/day. Standard error estimates of the different methods ranged from 0.792 mm/day for the simplified to 1.47 Hargreaves (HG) method.

The method was found to over predict during the period of satellite image available tables B1 to B14 appendex B, when the solar radiation values were high in comparison to other months. The SEE of this method was found to be higher than that of the FAO24R method for all periods and the peak month. The Hargreaves (HG) method under predicted ET for all periods 18% and gave a lower value of SEE for the peak

month compared to other periods. The SCS Blaney-Criddle method (SCS BC) gave a high coefficient of determination of 0.95 for all periods, but ET values that were overestimated for both all periods was 14%.

The Priestley-Taylor (PT) method under predicted ET by 13% compared to the standard estimate. The regression coefficient was close to unity and the SEE was found to be 0.97 and 0.65 mm/day, respectively, for all periods and the peak month. This may be because the data from the Al-Irra site were used to derive the coefficients of the Hargreaves method. Based on the weighted average SEE, the different methods ranked in decreasing order are SEBAL$_{ID}$, SEBAL, M-SEBAL, Biophysical , FAO Penman Monteith. FAO Penman, FAO-24 radiation, Priestley-Taylor, SCS Blaney-Criddle, Hargreaves and simplified method.

Table 5.17 : Statistical Summary of monthly ET Estimates for Al-Irra Station

Statistical	ET method										
parameter	FAO5 6 PM	FAO2 4 P	FAO -R	PT	HG	SCS -BC	SEBAL	SEBAL $_{-ID}$	M- SEBAL	Bio	Simp
Mean ET mm/day	4.1	3.1	3.2	3.4	3.0	3.9	5.1	4.9	4.2	5.6	5.8
Weight Ranking	38.00	37	33	33	19	28	68	69	62	46	27.0
Normalize d weight	2.533	2.467	2.2	2.2	1.27	1.86	4.53	4.9	4.1	3.06	1.80
SEE mm/day	1.175	1.439	1.41	1.36	1.47	1.23	0.942	0.986	1.151	0.83	0.79
WSEE mm/day	0.870	1.065	1.04	1.004	1.09	0.91	0.697	0.730	0.851	0.62	0.59
R^2	0.99	0.966	0.85	0.93	0.57	0.95	0.842	0.872	0.897	0.64	0.59
b	1	0.756	0.78	0.8	0.73	0.95	1.243	1.195	1.02	1.36	1.41
%PM	100	75.6	78.0	82.9	73.2	95.1	124.39	119.51	102.4	136.6	141.5

The regression coefficient (b) used to adjust to Penman Monteith estimates, on average, is increased from 0.73 to 1.41 for all stations. However, no apparent trend exists in other methods. The typical plots estimated for Sana'a Basin, NWRA, CAMA and Al-Irra.

Regional ET in Sana'a basin, Yemen was calculated by using the all the combination, radiation, Temperature and Remote Sensing methods (SEBAL, SEBAL$_{ID}$, M-SEBAL, Biophesical and simlifield methods) some of the ET maps plotted in figure5.54 and

5.55, the ET layers from the combination, radiation, and also temperature based in the GIS. ET contour map of interpolated ET shown in figure 5.56.

A   B
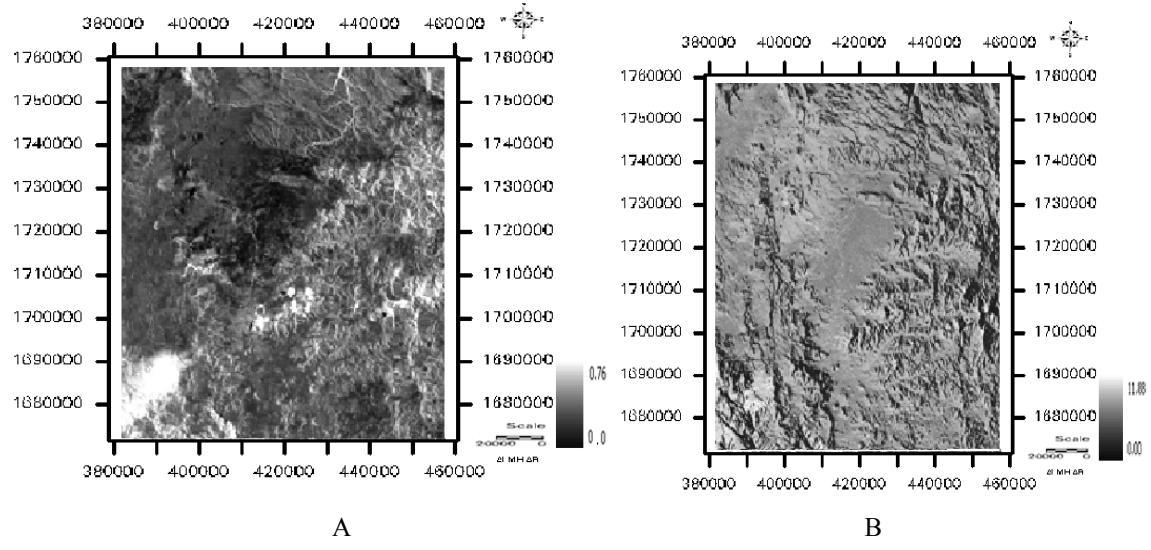
Figure 5.54   Instantaneous EF(at satellite image time) values(A) and 24-hour ET values(B) for the Sana'a basin, Yemen.

A   B
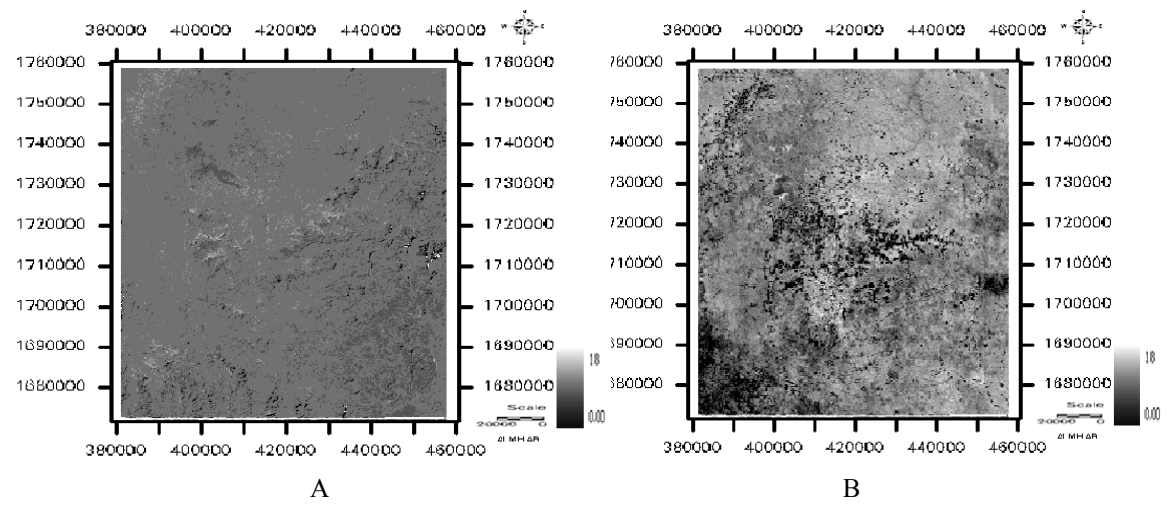
Figure 5.55   24-hour ET using simplified method (A) and biophysical model (B) for the Sana'a basin, Yemen.
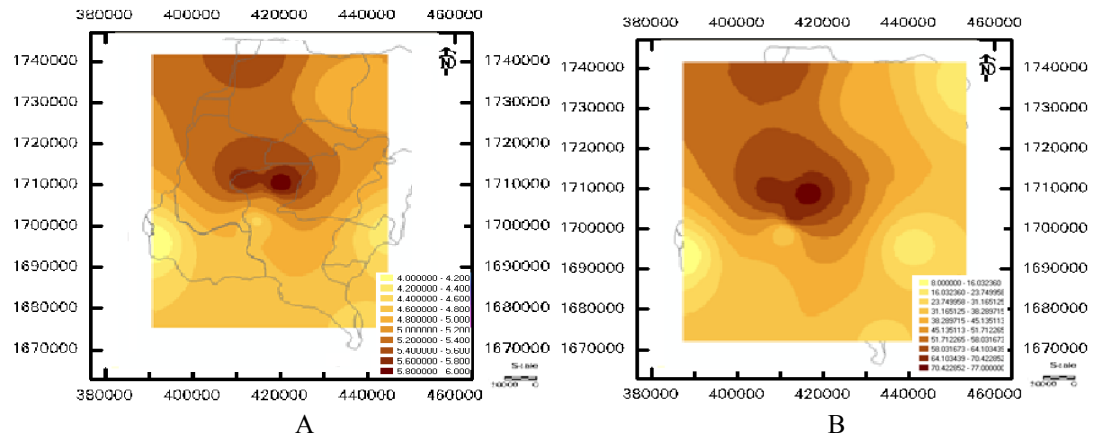
Figure 5.56 24-hour ET using FAO Penman Montaith model monthly(A) and daily (B) by DSS-ET for Sana'a basin, Republic of Yemen.

As shown in both Figures 5.54 to 5.56, display the highest ET rate appears over the western watershed. However, the interpolated ET in traditional method displays a higher value along the zones boundary due to the extrapolation from further distance away.

ET maps as remote sensing methods, on the other hand, displays a more evenly distributed and detailed contour due to the spatially distributed ET from remote sensing method. The pattern of excessive values along the extrapolating boundary is more noticeable if there are fewer weather stations in the region.

Using all the combination, radiation, and Temperature and Remote Sensing methods in the available satellite image data and climate data for Sana'a basin Figure 5.57 show the contrast between the daily ET value for Al-Irra (A) and CAMA (B) station Sana'a **b**asin-Yemen.
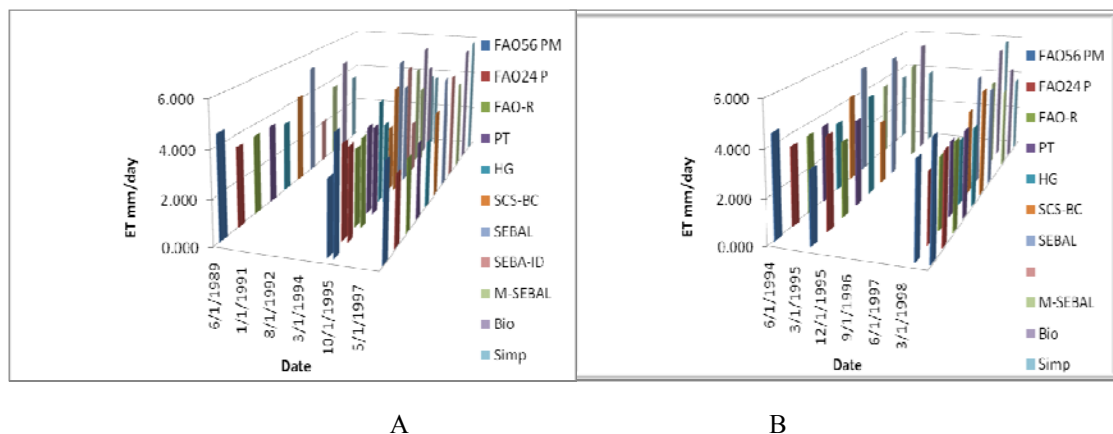
Figure 5.57 Compeering ET value for Al-Irra (A) and CAMA (B) station Sana'a **b**asin-Yemen

5.8.6 Comparison between DSS-ET with other works

Table 5.18 show comparison between DSS-ET developed during this research with other works in the field of decision support system for estimation of Evapotranspiration.

Table 5.18 : Comparison between DSS-ET with other works

parameter	Biju A. et al 2002	EVAPDSS Moges,S.A,et al,2002	DSS-ET (this study)
ET type focuses	Reference ET	Potential ET	Actual ET
Based on	User-defined option	– Arc View GIS	ERDAS& Arc GIS
Database	access	HEC-HMS	Geo-database
No. Models use	6	8	11
Method of sitting	ranking	Stochastic modeling	Rank weight MCDM-GIS
Layout preparation	Point ETr	Plot regional PET	Raster &image Regional ET
Type Models use	Traditional method	Traditional method and confer grid GIS	Remote sensing Method, Traditional method on GIS grid
Spatial functions supported	None	-	Buffer, reselect,
Result	Number point	Map grid	Map grid , raster, image
Running different scenarios with different criteria	no	no	yes

5.9. Regional Water balance propose model

5.9.1   Regional Water balance monthly.

The final produce of propose model in this study consisted of maps that represent the water storage depth which occurred on basin or regional gauging station zone as a result of the heavy precipitation events between the images dates . Each day's maps represent a snapshot of how much precipitation occurred in the study area, and how it affected the land surface. Although the GIS can perform many of the tasks necessary to determine water storage, a final step remains in order to fully understand the temporal aspects of the safely groundwater observation from the basin. This visualization step involves the use of various computer software packages, colouring, and animation procedures and output types.

Based on section 2.2.6 and section 4.10 equations, water balance was computed for regional watershed irrigated lands in the study areas. Table 5.19 represents the calculated water balances in millimeters (mm/month). As the equation 4.23 indicates, there are eight different components. Based on the concept of water balance modeling, the analysis showed the following results:

The total precipitation was divided into two main parts, which are the effective rainfall that is taken in account in the model to estimate the remaining part of precipitation appears as runoff and evaporation and infiltration. The direct evaporation from rainfall is relatively small, so it was considered to be zero. The infiltration that reaches the groundwater increases the storage.

It can be seen that as a result of precipitation caused an increasing irrigation water demand.

These issues will together make more press on groundwater as the only type of available water. This point (loss of groundwater) is clearly shown in the column no.8. the calculated storage loss due to agricultural demands. As it is shown, at the beginning of analyzed period the amount of storage loss is 43 mm while in the second half of this period it has increased to 82 mm and in the last few years it decreased to 76 mm. It

means that the annual storage loss has been around several tens of mm in the dry years in the Sana'a basin area.

At the beginning of the analysed period, due to proper and adequate amount of precipitation, the required irrigation water has been supplied by precipitation and inflow discharges. In the last few years, because of rainfall shortage, the total amounts of rainfall and inflow discharges do not meet the net irrigation water requirement. For instance, in the year (1995-1998) the total irrigation water requirement was about 201mm but the total rainfall and inflow discharges are about 121 mm. It shows a great amount of water deficit in Sana'a basin. Looking at the problem from another angle, it means that, in the existing conditions, there is a great amount of extra lands irrigated extra to the potential provided by the water resources, in both of the study areas. This is expressed in columns no.2 in the table 19. The summary of these columns show that in the year, the irrigated land exceeds the potentially possible by 48.68% in the basin area.

Table 5.19 : Computed monthly water balance mm/month for Sana'a basin

	1	2	3	4	5	6	7	8
Date water balance	Area in km^2	Irrigation Areas km^2	%Irrigation Areas	Precipitation (P) mm/month	Q_{in}	Q_{out}	Evapotranspiration (ET) mm/month	$\pm\Delta S$ mm/month
Jun-98	3239.9	207.354	6.4	37	0	0	113	-76
May-95	3239.9	139.316	4.3	59	0	0	107	-43
Dec-95	3239.9	191.154	5.9	25	0	0	102	-82

Description for columns in table 5.19

- Column 1and 2: Determined by applying Landsat image for 1995 and 1998 based on ERDAS Imagine software
- Column 4: Calculated based on interpolated rainfall data from point to polygon grid by Arc GIS software
- Columns 5and 6 considered zero in the date of this study because no record for runoff during this time and all the precipitation for the basin was infiltration that reaches the groundwater to increases the storage by the dams which built in the basin.
- Column 7: Estimated by modified SEBAL model which developed during

this study to estimate the ET in the mountain arid areas in ERDAS Imagine software (the data mean in (mm) can be change to million cubic meter(MCM) by multiplied it by the area km^2 divided by one thousand)

- Column 8: Calculated based on difference between input and output in the water balance model.

Rainfall is the source of runoff in the Wadis and recharge of ground water in Sana'a basin. which is characterized by convective rainfalls that are localized and having intensive precipitation events of short duration.

The spatial pattern of annual rainfall varies from interannually. It ranges between 250 mm at the plain areas to more than 300 mm at the south-western mountains .

The result of the summation of the ET made by this study for each individual crop type provides the total evapotranspiration in the Sana'a basin. The white regions in this map show the areas where no vegetation was observed during the investigated year. Here an ET value of zero was assigned. This map might give the first impression that the abundance of vegetation is not high in the Sana'a basin.

However, one has to consider that the simulations were done on a raster cell of 90 m by 90m (1 ha) using subpixel information. For each raster cell the percentage of each crop type is considered in the simulation. It is sufficient that one (full resolution) 10m by 10m pixel within each model raster cell of 1 ha was classified as crop to calculate its contribution to the evapotranspiration in the respective hectare.

Table 5.19 lists the area of irrigated area and the ET results in mm/month. Both ways of looking at the ET of the basins reveal that the distribution of ET varies considerably from sub-basin to sub-basin. Wadi al Furs has (south of the basin) the highest relative value, whereas Wadi bani Huwat (north of the basin) has the highest absolute value of actual evapotranspiration.

It should be mentioned that because of lack of reliable data for groundwater flow it was decided that as a first step, input and output of groundwater consider as equal in this research. It is obvious that this assumption introduces some inaccuracies, so further investigations will be needed in the future on this topic for a more accurate approach.

CHAPTER 6

DISCUSSION AND CONCLUSION

6.1 Introduction

This chapter presents the discussion and concludes the outcome of this study; Besides that, recommendations for future work are also discussed in order to provide a better work flow. The chapter is into different sections, which are discussion as well as limitation and future work.

6.2 Discussion

This section provides and brief summary of the strategies and basic approaches adopted for the study with respect to the main objectives of the research.

The **first objective** of the research was to investigate the capability of existing SEBAL models for calculation ET in mountainous arid areas. This thesis has presented literature review of the almost of the important methods and techniques used

to estimate ET by different approaches including the models depending of full energy balance method like SEBAL and other SEBAL variants. The literature review provides and showing confident that existing SEBAL and other SEBAL variants is not suitable for arid and semi arid mountainous areas. This is due to different in climatic conditions and other condition parameters like different in land use and land scope characterizes has made existing SEBAL model and its variants less effective for calculating ET in the arid and semi arid areas.

The **second objective** of the research was to develop a new SEBAL variant for calculating evapotranspiration in mountainous arid areas. This thesis has presented methods and tools for facilitating estimation of evapotranspiration in mountainous arid areas. The new SEBAL variant is specially developed for the arid and semi arid areas, in order to have an estimation of evapotranspiration become more accurate than the one estimated using existing SEBAL model. In the period of developing the new SEBAL variants, the following activites are involved; correction of the slope and mountainous area by calibration with the solar zenith angle and DEM data, calculation of surface reflectance and other surface parameters using remote sensing data. The new SEBAL model was accurately developed and validated using metrological and ground truth data.

The **third objective** of the research was to study the reliability of each medium and low spatial resolution remote sensing data for calculating evapotranspiration using new SEBAL variance model. This thesis has presented that the modified SEBAL is capable calculating the spatial crops daily water use (ET). Different characterizations of remote sensing data , image data from NOAA-AVHRR and Landsat-TM have been used for estimate some surface parameters to be used in new SEBAL model for estimating ET for the study area. Conclusively medium spatial resolution image data from Landsat TM provide a more accurate information compare to the low spatial resolution image data is much larger, this will enable estimation of ET to be done over a large area.

In general the simulation is accurate compared with measurement under both stressed and no stressed conditions. The developed modified SEBAL model accurately estimates 24-hour and seasonal ET, especially for mountain arid regions. In addition,

application for agricultural areas, basalt areas, volcanic areas, desert areas and arid coastal areas, showed reasonable results.

The study has shown that it is possible to calibration the parameters of the model to increase the accuracy of estimate regional ET using remote sensing data. Besides it also has shown that it is possible to replace the mathematical model for estimate regional ET using remote sensing with the computerized models, using ERDAS IMAGINE spatial modeler.

The **fourth objective** of the research was to investigate the new SEBAL variant with remote sensing and GIS techniques for a water management. This thesis has presented a new method to model Decision Support System (DSS) tool that able to simulate regional ET. The DSS-ET can be regarded as a tool for waleing make estimation of ET at any place in the region.

Conclusively the results obtained by the application of modified SEBAL in mountains showed that the modifications made to the original SEBAL algorithm accounted for the variation of some components of the surface energy balance (i.e. incoming solar radiation, net radiation, soil heat flux, surface roughness, and LE) in a correct direction, so that the refinements of the model produced adaptation of SEBAL for mountains, hill foot agriculture and sloping surfaces.

The largest advantage of the modified SEBAL is that the model is an operationally usable model that can be applied with a minimum amount of ground data. The data requirement of modified SEBAL is lower than the original SEBAL model and SEBAL$_{ID}$ to increase the widely estimation ET, when still limited data which obtained from weather stations.

Even though modified SEBAL was just partially validated in this study, it can be concluded that the application of modified SEBAL is promising for the operational estimation of ET, especially in hill foot agricultural areas and mountain basin in Yemen. modified SEBAL has been developed in such a way that the need for extensive ground measurements is partly eliminated, and an accurate atmospheric corrected surface temperature is not a strong requirement.

During the sensitivity analyses, it was confirmed that the internal calibration of modified SEBAL by the given energy balance at cold and the hot pixels, effectively

eliminated the errors and biases generated in Albedo, surface temperature and surface roughness predicted by relatively simple methods. The resulting ET information has a great potential to the water management, especially irrigation management. Although some uncertainties and problems remain to be solved for ET estimation, for areas other than agricultural areas, the modified SEBAL model is a useful tool for regional water resources and field management.

The results have shown that all methods could compute evapotranspiration for the two study sites on two specified days and that some methods also have wider applicability. It was pointed out in the conclusions that there is a range of computed values and that no method is regarded as ideal; one; all have their advantages and disadvantages. Evapotranspiration is generally computed not for its own sake but for some other purpose, and each method can be assessed for its usefulness in this regard. To make some general recommendations, several important topics have been identified where knowledge of evapotranspiration is required.

Fusion of parameters estimated from NOAA-AVHRR composite and those from Landsat TM image data is an effective method in image processing which improves spatial detail whilst maintaining the spectral signature very close to the original. Therefore one can clearly identify the textural and structural features of land cover as well as the agricultural activities at the period of NOAA-AVHRR data acquisition. Moreover, it improves classification accuracy. The technique is seen as the first stage of a process in which free, coarse resolution NOAA-AVHRR composites can be analyzed using a variety of multi-temporal techniques, ranging from characteristic signature extraction or through non-parametric approaches such as decision trees. This is the focus of continuing work to evaluate appropriate and affordable methods of regional ET. The technique is amenable to automation as the co-registration between NOAA-AVHRR composite data and the LANDSAT TM images is very good. The costs of image processing for time series data using automation should be investigated as part of the future activity.

In desert areas, volcanic areas and arid coastal areas results were realistic for much of the year. Modified SEBAL consistently predicted negative values of latent heat flux in these areas. Here the problem of applying a single-source model to sparse vegetation, where sources and sinks of momentum and heat are significantly different from soil and vegetation was one of the possible explanations for the negative values of ET predicted at desert areas. In addition, uncertainties in soil heat flux and extrapolation of the agricultural-calibrated Ts versus dT function are also possible explanations for the unrealistic results.

A Decision support system (DSS -ET) that can effectively use the state of the art technology of GIS, combination of various spatial and stochastic time series modeling technique was developed to effectively use the available limited climatic data to estimate Potential Evaporation. The model has demonstrated its applicability in data scarce area and can be used to fill missing data.

In general, the study has revealed some of the potentials of the modified SEBAL model for estimation of ET in arid and semi arid areas.

The results of this study will be start to be distributed by NWRA and MAI through the next cropping season , to enable land and water managers, engineers and researchers to use the ET information for field water management in Yemen.

6.3 Limitations and Future Work

In this section, the major limitations of this work are listed. Most of these limitations are addresses with the ideas of future works and suggest several directions for future explorations including improvements in accuracy of estimation of ET, improvements in validations and sensitivity model parameters under mountain arid condition. The most obvious direction for the future is to continue to improve the

accuracy of the modified SEBAL model. A number of limitations and problems with this current work provide goals for future work.

Due to the limited time and unavailability of satellite data for this study, some problems remain to be solved and work remains to be done in the future. This study was primarily focused on mountain and agricultural areas, as irrigation water management is one of the major issues in water resources management in Yemen.

In view of all the previous considerations, it is recognized the value of SEBAL and modified SEBAL to estimate evapotranspiration for large areas in an operational manner. Furthermore, works are needed to refine several components of SEBAL that introduce uncertainties into the results, especially for the non-agricultural areas.

First the estimation of incoming solar radiation needs refinement to account for the topographic interactions among pixels. In modified SEBAL the value of Rn (for clear sky days) is calculated assuming the slope of the pixel is infinite; therefore the presence of shaded areas produced by the other surface features is not taken into account. The wind correction applied in modified SEBAL has to be further investigated. Better functions need to be developed to incorporate factors such as wind direction, mountain shape and variation in surface roughness. The lapse correction applied in modified SEBAL to convert radiometric surface temperatures to "equivalent" surface temperatures at a given reference level, for the application of the near surface temperature difference (dT) versus surface temperature (Ts) relationship, also needs more verification through field measurements.

Validation and verification for application in agricultural areas are requirement needed, especially for different climate/land conditions to ensure the model applicability. Also, more sensitivity analyses on important assumptions in modified SEBAL will provide valuable information. The important assumptions are: Weather conditions of applied area are similar, and dT is linearly related to the surface temperature. For example, correlations among windspeed, surface temperature and dT would be a very interesting topic for future refinement of modified SEBAL considered as an alternative to fill the information gaps between images. Image data from NOAA-AVHRR and MODIS can be considered for this task, even though the fine spatial resolution of surface fluxes obtained from application of SEBAL with Landsat TM images data, will be jeopardized due to the lower spatial resolution of these sensors. Other alternatives would be the use of numerical models to

predict the spatial variation of ET in the area. However the significant number of inputs parameters that those models require would hamper the operational characteristics of SEBAL.

In order to establish reliable ratios of actual to potential ET, long term ET study of wetland vegetation is recommended. These parameters should be developed locally and are important for the accurate application of remote sensing methods for the determination of regional ET estimation in Yemen.

References

Ahmad, M.D. (2002). *Estimation of net groundwater use in irrigated river basins using geoinformation techniques: A case study in Rechna Doab, Pakistan*. Ph.D. Thesis, Wageningen,The Netherlands.

Allen R.G. and Pruitt, W.O. (1986). Rational Use of the FAO Blaney-Criddle Formula. J Irrig Drain Eng 112(IR2):139–155

Allen, R.G., Jensen, M.E., Wright, J.L. and Burman, R.D. (1989). Operational Estimates of Reference Evapotranspiration. *Agronomy Journal*, 81:650-662

Allen,R.G., Pruitt, W.O, Businger, J.A, Fritschen, LJ., Jensen, M.E. and Quinn, F.H. (1996). *Evaporation and Transpiration*. Chapter 4, pp. I2S-252 in: Wootton et al. (Ed.). ASCE Handbook of Hydrology. American Society of Civil Engineers. NY.

Allen R.G., Pereira, L.S., Raes, D., Smith, M. (1998). *Crop evapotranspiration. Guidelines for computing crop water requirements*. FAO Irrigation and Drainage Paper no.56. F AO, Rome.

Allen.R.G. (2001). *Manual of RefET: Reference Evapotranspiration Calculation Software for FAO and ASCE Standardized Equations Version 2.0*. University of Idaho (http://www.kimberly.uidaho.edu/ref-et/)

Allen, R. (2005). *Introduction to Remote Sensing for Large Areal Evapotranspiration at High Resolution and Reasons for using METRIC and SEBAL*, the workshop on Evapotranspiration from Remote Sensing Using Surface Energy Balance, which was held in Ft. Collins, CO Feb. 7-8, 2005

Allen R., Tasumi, M., Trezza, R. Bastiaanssen, W. Morse, T., Kramber, W., Wright, J. (2005). METRIC: *High Resolution Satellite Quantification of Evapotranspiration University of Idaho,* Kimberly, Idaho. USA.

Allen, R.G., Tasumi, M., Trezza, R. (2007a). *Satellite-based energy balance for mapping evapotranspiration with internalized calibration (METRIC)*—model. J. Irrig. Drain. Eng. ASCE. 133.

Allen, R.G., Tasumi, M., Morse, A., Trezza, R., Kramber, W., Lorite, I., Robison, C.W.(2007b). *Satellite-based energy balance for mapping evapotranspiration with internalized calibration (METRIC)—application*s. J. Irrig. Drain. Eng. ASCE. 133.

Arthur P. Cracknell and Ibrahim Busu (1997). *Calibration of AVHRR data Generated By The Instrument on-Board Tiros-N Using Ocean and Cloud views*, IEEE, PP, 1386 – 1400.

ASCE-EWRI. (2005) ASCE-EWRI, 2005. The ASCE *standardized reference evapotranspiration equation*. Environmental and Water Resources Institute of the ASCE Standardization of Reference Evapotranspiration Task Committee. American Society of Civil Engineers, Reston, Virginia, p. 216.

ASCE-EWRI. (2002). *The ASCE Standardized Reference Evapotranspiration Equation*, Draft. 2001, Environmental and Water Resources Institute of the American Society of Civil Engineers.

Almhab A. A. (2003). *Water Management in Microwtershed a case study in Sawan area*, MSc Theses, Sana'a University, Yemen.

Almhab A. A., Bamatraf A. M., Bamaga O. (2004a). *Assessment of Water Budget of Sawan small watershed-Sana'a basin*, the science conference-2004, Yemen Sciences Research Foundation(YSRF), Yemen.

Almhab A. A. (2004b). *Participatory Management & Use Water Resources*, Athawabit a Quarterly journal vol.38 p41-52dec.2004, Yemen.

Almhab A. A., Yaya A. M., Bamaga O. (2004c). *Relevance of GIS and RS in national resources study and planning in Yemen*, the first conference about the education agriculture development in Yemen, Sana'a University, Yemen Sana'a.

Almhab A.A. (2004). Estimation of crop water requirement for Coffee crop in different regions of Yemen, the first national workshop about Coffee in Yemen, Ministry of Agriculture and Sana'a University, Sana'a Yemen

Almhab A.A. (2005b).*Technical Information(TI) practical on agricultural plan for example Geographic Information System(GIS)*, International symposium on technical information practical, Sana'a university, Sana'a Yemen.

Almhab A. A., Bamatraf A. M., Bamaga O. (2005). *Assessment of water budget in small watershed a case study Sawan area-Sana'a basin*. The Third Conference of Environment and National Resources 2005. Taiz University, Yemen.

Alterra, 2003. http://www.alterra.dlo.nl/models/swap/index.htm

Amayreh, J.A. (1995). *Lake evaporation: a model study*. Ph.D. dissertation, Dept. Biological and Irrigation Engineering, Utah State University, Logan, UT. 178

AREA. (2006). Metrological data for several gauge stations in Yemen, Dhamar , Yemen.

Bastiaanssen, W.G.M. (1995). "*Regionalization of surface flux densities and moisture indicators in composite terrain.*" Ph.D. thesis, Agricultural University, Wageningen, The Netherlands, p. 288.

Bastiaanssen, W.G.M, Menenti,M, Feddes, R.A., Holtslag, A.A.M. (1998a). *A remote sensing surface energy balance equation for land (SEBAL). 1. Formulation,* Journal of Hydrology vol.212-213, 198-212.

Bastiaanssen, W.G.M, Pelgrum, H, Wang, J:, Ma,JI:,Moreno,J:F., Roerink, G.J., yander Wal, T. (1998b). A remote sensing surface energy balance equation for land (SEBAL). 2. Validation. Journal of Hydrology vol.212-213, 213-229.

Bastiaanseen.W.G.M. and M.G.Bos (1999). *Irrigation performance indicators based on remotely sensed data: a review of literature*. Irrigation and Drainage Systems 13:291-311.

Bastiaanseen.W.G.M., (2000). *SEBAL-based sensible and latent heat fluxes in theirrigated Gediz Basin*, Turkey. J. of Hydr. 229:87-100.

Bowen, I. S.(1926). *The ratio of heat losses by conduction and by evaporation from any water surface*. Physics Review, 27(6):779-787.

Blaney, H. F. and Criddle, W. D. (1966). Determining consumptive use for water developments. *ASCE Irrigation and Drainage Special Conference Proceedings*, Nov. 2-4, pp. 1-34.

Brutsaert, W. (1986). *Catchment-scale evaporation and atmospheric boundary layer*. Water Resources Research, 22(9):39-46.

Bruggeman H.Y. (1997). *Agro-climatic Resources of Yemen. Part 1. Agro-climatic Inventory*. FAO proj. GCP/YEM/021/NET, Field doc. 11. Ministry of Agri. & Irrigation., Agri. Res. & extension Authority, Dhamar, Yemen.

Brutsaert, W.H.(1982). *Evaporation Into the Atmosphere,* p. 199, D. Reidel, Norwell, Mass.

Brutsaert, W.H., M. (1992). Sugita, Regional surface fluxes from satellite-derived surface temperatures (AVHRR) and radiosonde profiles. *Boundary-Layer Meteorology, 58,* pp. 355-366, 1992.

Brutsaert, W., and Sugita, M. (1992). Application of self-reservation in diurnal evolution of the surface budget to determine daily evaporation. J. Geophys. (Res. 97(D170, 18 377-18 382).

Burba,G.G., Verma, S.B.and Kim, J. (1999). *Surface energy fluxes of Phragmites australis in a prairie wetland*. Journal of Agricultural and Forest Meteorology, 94:31-51.

Busu. I. (1997). Calibration of visible and near-infrared channels from the early AVHRRs using ocean and cloud views, PhD thesis, University of Dundee. U.k.

CAMA. (2006) metrological data for several year and gauge stations in Yemen, Sana'a Yemen.

Campbell, G.S.and Norman, J.M., 1998, *An Introduction to environmental biophysics* (New York: Springer).

Campbell, G.S. (1977). *An Introduction to environmental biophysics*. Heidelberg Science Library, SpringerVerlag (Eds.), New York, 157pp.

Chandrapala, L., and Wimalasuriya, M. (2001). Satellite measurements supplemented with Meteorological data to operationally estimate Actual Evapotranspiration over Sri Lanka.

Carlson, T. N.,. Perry, E. M and Schmugge, T. J. (1990). *Remote estimation of soil moisture availability and fractional vegetation cover for agricultural fields*. Agricultural and Forest Meteorology, 52:45-69.

Caselles, V., Sobrino, J. A. and Coll, C. (1992). *On the use of satellite thermal data for determining evapotranspiration in partially vegetated areas*, International Journal of Remote Sensing, 13(14):2669-2682.

Chemin, Y., and Ahmad, M.D. (2000). *Evaporation calculation from an Energy Balance model (SEBAL)* A manual. IIMIPakistan Blue Report N° 102, Lahore, Pakistan, 27p.

Chemin, Y., and Alexandridis, T. (2001). Improving spatial resolution of ET seasonal for irrigated rice in Zhanghe, China. 22nd *Asian Conference of Remote Sensing*, November 59, 2001, National University of Singapore, Singapore, 6p.

Chemin, Y., Alexandridis, T., and Loeve, R. (2003). *Water productivity at different spatial scales from remote sensing. Zhanghe Irrigation Distric*t, Hubei Province, China. Journal of Irrigation Science. Forthcoming.

Chen, Y., Li, X. and Shi, P. (2001). *Estimation of regional evapotranspiration over Northwest* China by using remotely sensed data.

Choudhury, B.J., Ahmed, N.U., Idso, S.B., Reginato, R.J., and Daugthry, C.S.T. (1994). *Relations between evaporation coefficients and vegetation indices studied by model simulations*. Remote. Sensing. Environment. 50(1): 117.

Choudhury, F.J., Idso, S.B., Reginato, R.J. (1986). *Analysis of an empirical model for soil heat flux under a growing wheat crop for estimating evaporation by an infrared-temperature based energy balance equation*. Agric. Forest Meteorol. 39, pp. 283-97, 1986.

Chow, V. T., Maidment, D. R. and Mays, L. W. (1988). *Applied Hydrology,* Mc-Graw Hill, New York.

Cracknell, S. P. (1990). *The Advanced Very High Resolution Radiometer (AVHRR)*. Taylor & Francis Ltd, London, 1990.

Curran, P. J. (1983). Multispectral remote sensing for the estimation of green leaf index. *Philosophical Transactions of the Royal Society of London,* A, 309:257-270.

Curran, P. J. and Foody, G. M. (1994). Environmental issues at regional to global scales. In *Environmental Remote Sensing from Regional to Global Scale* (G. Foody and P. Curran, editors). John Wiley & Sons, New York. pp. 1-7.

Doorenbos, J., and Pruitt, W. O. (1977). *Guidelines for Predicting Crop Water Requirements*. FAO Irrigation And Drainage Paper No. 24, 2nd ed., FAO, Rome, Italy, 156 pp.

Dingman, S.L., 2002: Physical Hydrology, 2nd Ed.: Upper Saddle River, New Jersey.Prentice Hall.

Doran, J. C. (1993). The sensitivity of flux parameterizations to surface characteristics. Proceedings of the *Third Atmospheric Radiation Measurement Science Team Meeting*, March 1-4, Norman, Oklahoma. U.S. Department of Energy, Washington, DC. pp. 73-76.

Droogers, P., and Bastiaanssen, W.G.M. (2001). *Combining remote sensing and hydrological models to enhance spatial and temporal variability*. Submitted to IAHS Red Books.

DuffieJ, A. and Beckman, W.A. (1991). Solar engineering of thermal process. 2nd Ed. John Wiley and sons, NY

Engman, E.T. and Gurney, R.J. (1991). *Remote Sensing in Hydrology*. Chapman and Hall, London 225 pp., 1991

EFFA-SUY, Tahir. N. (2006). Archive the experimental farming – faculty of agriculture: research projects during 1995 to 2006, doing by under and post graduate student, Sana'a university, Sana'a , Yemen

ERDAS. (1995). ERDAS Field Guide, 3rd ed. Atlanta, Georgia, pp.628.

Farah, H.O. (2000). *Estimation of regional evaporation under different weather conditions from satellite and meteorological data:* a case study in the Navaisha Basin, Kenya. Doctoral Thesis Wageningen University and ITC, CIPData Koninklijke Biblotheek, Den Haag, The Netherlands, 170pp.

Feddes, R.A., Kowalik, P.J., and Zaradny, H. (1978). *Simulation of water use and crop yield*. Simulation Monography, Pudc, Wageningen, 188pp.

Feddes, R.A., Kabat, P., Bakel, P.J.T., Bronswijk, J.J.B., and Halbertsma, J. (1988). Modellingsoil water dynamics in the unsaturated zone – state of the art. Journal of Hydrology, 100:69111.

Fontenot, R. (2004). An Evaluation of Reference Evapotranspiration Models in Louisiana. M.N.S. Thesis, Department of Geography and nthropology,Louisiana State University.

Gao, Y.C., Long, D. and Li, Z.L. (2008). Estimation of daily actual evapotranspiration from remotely sensing data under complex terrain over the upper Chao river basin in north China," *International Journal of Remote Sensing*, 29, 3295-3315.

Gandin, L.S. (1970). The planning of meteorological station networks. WMO Tech Note, 1. NM.111.

Gieske, A. (2001). *Short energy balance algorithm – NOAA AVHRR,* version of December 2001.

Gillespie.A.R., S.Rokugawa, Hook, S.J., Matsunaga, T.and Kahle A.B. (1999). *Temperature/Emissivity Separation Algorithm Theoritical Basis Document.* Version 2.4. *NASA EOS Algorithm Theoretical Basis Document*, (http://eospso.gsfc.nasa.gov/atbd/astertables.html)

Goward, G. Cruickshanks and Hope, A. (1985): Observed relation between thermal emission and reflected spectral radiance from a complex vegetated landscape. *Remote Sens. Environ*., 18, 137-146.

Hashmi, M.A., Garcia, L.A., Fontane, D.G. (1994). *Spatial estimation of regional evapotranspiration*. Trans. Am. Soc. Agric. Engr. 38, 1345-1351.

Hargreaves, G. H. (1994). Defining and using reference evapotranspiration. *Journal of Irrigation and Drainage Engineering*. 12O(6):1132-1139.

Harrison, B.A. and Jupp, D.L.B. (1989). *Introduction to Remotely Sensed Data*, CSIRO Publications.

Harrison LP (1963) *Fundamental concepts and definitions relating to humidity*. In: Wexler, A (eds) Humidity and Moisture. vol. 3. Reinhold, New York

Heliman, J. L., E. P., Kanwmasu, N. J., Rosenberg, and B. L. Blad (1976). Thermal scanner measurement of canopy temperature to estimate evapotranspiration, *Remote Sensing of Environment*, 5:13 7-145.

Holben, B. N., C. J. Tucker, and C. J. Fan (1980). Spectral assessment of soybean leaf area and leaf biomass. Photogrammetric Engineering and Remote Sensing, 46:651-656.

Huete.A.R . (1988). A Soil-Adjusted Vegetation Index (SAVI). *Remote Sensing of Environment*, 25:295-309

Huete.A.R., H.Q.Liu, K.Batchily and W.vanLeeuwen (1997). A comparison of vegetation indices over a Groval Set of TM Images for EOS-MODIS. *Remote Sensing of Environmen*t, 59:440-451.

Humes.K.S., Kustas, W.P.and Moran M.S. (1994). Variability of emissivity and surface temperature over a sparsely vegetated surface. *Water Resources Research*, 30:5:1299-1310.

Hope, A. S., and McDowell, T. P. (1992). The relationship between surface temperature and a spectral vegetation index of a tallgrass prairie: effects of burning and other landscape controls. *international Journal of Remote Sensing*, 13:2849-2863.

Horler, D. N. H., Dockray, M., Barber, J. and Barringer A. R. (1983). Red edge measurements for remotely sensing plant chlorophyll content. *Advanced Space Research*, 3:273-277.

Idso, S. B., Jackson, R. D., Reginato, R. J. (1975). *Estimating evaporation: a technique adaptable to remote sensing*. Science, 189:991-992.

International Service for Agricultural Research (ISNAR). (1993). *A Review of the Agricultural Research System in the Republic of Yemen*. ISNAR, The Netherlands.

Jarvis, P.G. (1976). *The interpretation of the variations in leaf water potential and stomatal conductance found in canopies in the field*. Philosophical transactions of the Royal Society of London B273: 593610.

Jackson, R.D. (1985). Estimating evapotranspiration at local and regional scales. *IEEE Trans. Geosci. Remote Sensing, GE-73,* pp. 1086-1095, 1985.

Jensen, J. R. (1983): Biophysical remote sensing. *Ann. Assoc. Amer. Geogr*, 73(1), 111-132.Jackson, R. D., R. J. Reginato, and S. B. Idso, (1977). *Wheat canopy temperature: a practical tool for evaluating water requirements. Water Resource*s Research, 13:651.

Jensen, M.E., Burman, R.D. and Allen, R.G. (1990). *Evapotranspiration and irrigation water requirements.* Irrig. Drainage Div. American Society of Civil Engineers. New York. NY. p. 360.

Jensen, M. E., R. D. Burman, and R. G. Allen (1990). *Evapotranspiration and Irrigation Water Requirements*. ASCE Manuals and Reports on Engineering Practice No. 70, American Society of Civil Engineering, New York.

Jensen, D.T., G.H. Hargreaves, B. Temesgen, and R.G. Allen. 1997: Computation of ETo under Nonideal Conditions. *Journal of Irrigation and Drainage Engineering* 123(5):394-400.

Jensen,J.R. (2000). *Remote Sensing of the Environment*: An Earth Resource Perspective. Prentice Hall. Upper Saddle River. New Jersey.

Kabart, P., Hutjes, R.W.A., Feddes, R.A. (1997). The scaling characteristics of soil parameters: From plot scale heterogeneity to subgrid parameterization. *Journal of Hydrology,*190:363396.

Kerr, Y.H., Imbernon, J., Dedieu, G., Hautecoeur, O., Langouarde J.P. and Seguin, B. (1989). NOAA AVHRR and its uses for rainfall and evapotranspiration monitoring. *International Journal of Remote Sensing,* 10(4):847-854.

Kerr, Y. H., J. P. Lagouarde, and Imbernon, J. (1992). Accurate land surface temperature retrieval from AVHRR data with use of an improved split window algorithm. *Remote Sensing of Environment,* 41:197-209.

Kidwell, C. B. (1991). *NOAA Polar Orbiter Data User's Guide*. NOAA/NESDIS NCDC/SDSD, Washington, DC.

Khorasani , M. A. (2005). Agro climate guide in Yemen (1881-2004), AREA, Dhamar, Yemen

Kustas, W.P., and C.S.T. (1990). Daughtry, Estimation of the soil heat flux/net radiation ratio from multispectral data. *Agric. For. Meteorol., 49,* pp. 205-223, 1990.

Kustas, W.P., Moran, M.S., Jackson, R.D., Gay, L.W., Duell, L.F.W., Kunkel, K.E. and Matthias, A.D. (1990). Instantaneous and daily values of the surface energy balance over agricultural fields using remote sensing and a reference field in an arid environment. *Remote Sens. Environ., 32,* pp. 125-141, 1990.

Kustas, W.P., Moran, M.S., Humes, K.S., Stannard, D.I., Pinter, P.J., Hipps, Jr., L.E. Swiatek, E. and Goodrich, D.C. (1994). Surface energy balance estimates at local and regional scales using optical remote sensing from an aircraft platform and atmospheric data collected over semiarid rangelands, *Water Resources Research, Vol. 30,* No. 5, pp. 1241-1259, 1994.

Kustas, W. P. and Norman, J. M. (1996). "*Use of remote sensing for evapotranspiration monitoring over land surfaces.*" Hydrological Sciences 41(4): 495-515.

Landsat 7 Science Data Users Handbook (2002). *Landsat Project Science Office. NASA* Goddard Space Flight Center in Greenbelt, Maryland, http://ltpwww.gsfc .nasa.gov/l AS/handbook/handbook_toc .htm I

IDWR. (2002). *SEBAL Idaho Implementation Advanced Training and Users* Manual version 1. Idaho Dept. Water Resources, Boise, ID, http://www.idwr.state.id.us/gisdata/ET/final_sebal_page.htm

Markham.B.L. and Barker, J.L. (1986). Landsat MSS and TM Post-Calibration Dynamic Ranges, Exoatmospheric Reflectances and At-Satellite Temperatures. EOSAT Landsat Technical Notes 1:3-8. *Earth Observation Satellite Company*, Lanham, Maryland.

Markham.B.L and Barker, J.L. (1987). Thematic Mapper bandpass solar exoatmospherical radiances. *Int. J. of Remote Sensing* 8(3):517-523

Mekonnen, G.M and Bastiaanssen, W.G.M. (2000). *Anew simple method to determine crop coefficients for water allocation planning from satellites: results from Kenya*. Irrigation and drainage Systems vol. 14, 2000, p 237-256.

Menenti, M. (1984). Physical aspects and determination of evaporation in deserts applying remote sensing techniques. Report 10 (special issue). Institute of Land and Water Resources Management, Wageningen, The Netherlands: 202p.

Menenti, M. (2000). *Evaporation. In Remote Sensing in Hydrology and Water Management*, Gert A. Schultz and Edwin T. Engman (Eds.), Springer Verlag, Berlin, Heidelberg, NewYork: 157188.

Ministry of Agriculture and Irrigation (MAI). (2005). *Agricultural statistics year- book 2000*. MAI, Sana'a, ROY.

MAI. Central Unit Water monitoring (2006). metrological data for several year and gauge stations in Yemen, Sana'a Yemen.

Ministry o planning and Development (MPD). (2005). *Statistics year-book 2005*. Central Stat. Organisation. Sana'a, Yemen.

Mitchel, A. (1999). *The ESRI guide to GIS Analysis*, Volume I: Geographic Patterns and Relationships. ESRI. CA.

Moghaddam (2000). Fusion of AirSAR and TM data for variable classification and estimation in dense and hilly forests. *3rd International Conference of Fusion of Earth Data*, 2628 January, Sofia Antipolis, France (Nice: SEE GreCA):161166.

Mogaes,S.A,,Katambara,Z.nad Bashar,K. (2002). Decision Support System for estimation of Potential Evapotranspiration in Pangani Basin, 3rd WaterNetWarfasa "Water Demand Management for Sustainable Development", Dar es Salaam, 30-31 October 2002.

Monteith.J.L., and Unsworth,M.H. (1990). Principles of Environmental Physics, Edward Arnold, London.

Monteith, J. L. (1973). *Principles of Environmental Physics,* American Elsevier Pub. Co., New York, 241 pp.

Monteith, J. L. (1981). Evaporation and surface temperatue. Quarterly *Journal of Royal Meteorological Society*, 107:1 -27.

Moran, S.M., Clarke, T.R., Inoue, Y., and Vidal, A. (1994). Estimating crop water deficit using the relation between surface air temperature and spectral vegetation index. *Rem. Sens. Environ*. 49(3): 246263

Moran, M. S., Jackson, R. D., Raymond, L. H., Gay, L. W. and Slater P. N. (1989). Mapping surface energy balance components by combining Landsat Thematic Mapper and ground-based meteorological data. *Remote Sensing of Environment*, 30:77-87.

Moran, M. S., Clarke, T. R., Inoue, Y. and Vidal A. (1994). Estimating crop water deficit using the relation between surface-air temperature and spectral vegetation index. *Remote Sensing of Environment*, 49:246-263.

Murtha, P. A. (1978). Remote sensing and vegetation damage: a theory for detection and assessment. *Photogrammetric Engineering and Remote Sensing*, 44:1147-1158.

Morse,A., Tasumi, M., Allen R.G.and Kramber, W.J. (2000). *Application of the SEBAL Methodology for Estimating Consumptive Use of Water and Streamflow Depletion in the Bear River Basin of Idaho through Remote Sensing*: Final Report. Idaho Department of Water Resources, Idaho, http://www.idwr.state.id.us/gisdata/ET/final_sebal_page.htm .

Morse.A.,.Allen, R.G, Tasumi, M..Kramber, W.J, Trezza R. and Wright, J.L. (2001). *Application of the SEBAL Methodology for Estimating Evapotranspiration and Consumptive Use of Water Through Remote Sensing*: Final Report. Idaho Department of Water Resources, Idaho.

N0AA-Class website.

http://www.class.ncdc.noaa.gov/saa/products/welcome;jsessionid=6EA776EC5E73948 DEE97BAA543085436

Nemani, R. R. and Running, S. W. (1989). Estimation of regional surface resistance to evapotranspiration from NDVI and thermal-IR AVHRR data. *Journal of Applied Meteorology,* 28:276-284.

Nieuwenhuis, G.J.A., Smidt E.H. and Thunnissen, H.A.M. (1985). Estimation of regional evapotranspiration of arable crops from thermal infrared images. *International Journal of Remote Sensing,* 6(8): 1319-13 34.

Norman,J.M., Kustas, W.P. and Humes, K.S. (1995). Source approach for estimating soil and vegetation energy fluxes in observations of directional radiometric surface temperature. Agricultural and Forest Meteorology, 77:263-293.

Norman,J.M, Kustas, W.P., Prueger, J.H. and Diak, G.R. (2000). Surface Flux Estimation using Radiometric Temperature: A Dual-Temperature-Difference Method to Minimize Measurement Errors. *Water Resources Research*, 36(8):2263-2274

NWRA. (2001). National Strategy for Water Resources Development in Yemen, Sana'a, Yemen.

NWRA. (2006). Metrological data for several years and gauge stations in Yemen, Sana'a Yemen.

Oke.T.R, 1987. Boundary Layer Climates. Routledge, NY

Ormsby, J. P., Choudhury, B. J. and Owe, M. (1987). Vegetation spatial variability and its effect on vegetation indices. *International Journal of Remote Sensing,* 8:1301 -1306.

Owe, M. and van de Griend A.A. (1990). Daily surface moisture model for large area semi-arid land application with limited climate data. *J. Hydrol., 121,* pp. 119-132, 1990.

Parodi, G. (2000). *AVHRR Hydrological Analysis System – Algorithms and theory –* Version 1.0. WRES, ITC, The Netherlands.

Penman, H.L. (1948). *Natural evaporation from open water, bare soil and grass.* Proc. Roy. Soc. London. A193:129-145, 1948.

Phillips, R. (1990). *Commercial Production of Asparagus in New Mexico.* NMSU. NM, http://www.cahe.nmsu.edu/pubs/_h/h-227.html. September 2002.

Pohl, C., and Touron, H. (2000). Issues and challenges of operational applications using multisensor image fusion. 3rd International Conference of Fusion of Earth Data, 2628 January, Sofia Antipolis, France (Nice: SEE GreCA):5358.

Pohl, C., and Van Genderen, J.L. (1998). Multisensor image fusion in remote sensing: concepts, methods and applications. *International Journal of Remote Sensing,* 19:823854.

POD Guide, (1998). Edition of the NOAA Polar Orbiter Data User's Guide , http://www.ncdc.noaa.gov/oa/pod-guide/ncdc/docs/podug/amendmnt.htm.

Price, J.C. (1982). Estimation of regional scale evapotranspiration through analysis of satellite thermal-infrared data. *IEEE Trans. on Geosci. and Rem. Sensing. GE-20:*286-292, 1982.

Price, J.C. (1990). Using spatial context in satellite data to infer regional scale evapotranspiration. IEEE Trans. Geosc. Rem. Sens. 28(5): 940948.

Price, J. C (1992). Estimating vegetation amount form visible and near infrared reflectances. *Remote Sensing of Environment,* 41:29-34.

Priestley, C. H. B., and Taylor, R. J. (1972). *On the assessment of surface heat flux and evaporation using large scale parameters*. Monthly Weather Review, 100:81-92, 1972.

Penman, H. L. (1948). *Natural evaporation from open water, bare soil, and grass*, Proceedings of the Royal Society. A, 193(1032): 120-145.

Penman, H. L., Angus D. E. and van Bavel C. H. M. (1967). *Microclimatic factors affecting evaporation and transpiration.* Chapter 26, In American Society of Agronomy Mo. II, Irrigation of Agricultural Lands. Madison, WI.

Richard Tutwiler. (1990). Agricultural *labour and Technological Change in the Yemen Arab Republic*; pp 229-251 In: Labor and Rainfed Agriculture in West Asia and North Africa., Eds., Dennis Tully. Publ. Kluwer Academic, London.

Roerink, G.J. (1995). *SEBAL estimations of the areal patterns of sensible heat fluxes over the HAPEXSahel* grid – a case study on 18 September 1992. DLOStaring center, Wageningen, The Netherlands, September 1995, 61p.

Roerink G.J, Z. Su and M. Menenti (2000). S-SEBI: a simple remote sensing algorithm to estimate the surface energy balance, Phys. Chem. Earth B 25 (2000) (2), pp. 147–157.

Rosenberg, N. J., B. L. Blad, and S. B. Verma (1983). *Microclimate - The Biological Environment.* John Wiley and Sons, New York, pp. 495.

SCS. (1967). *Irrigation Water Requirements*. U.S. Department of Agriculture, Soil Conservation Service TR-21, April 1967, 88 pp.

Seguin, B. and B. Itier (1983). Using midday surface temperature to estimate daily evaporation from satellite thermal IR data. *International Journal of Remote Sensing*, 4:371-383.

Shuttleworth, W. J. (1993). *Evaporation. In Handbook of Hydrology,* (D. R. Maidment, ed), McGraw-Hill Inc., New York, pp.4.1-4.35.

Shuttleworth, W. J., Gurney, R. J., & Hsu, A. Y., Ormsby, J.P. (1989). FIFE: the variation in energy partitioning at surface flux sites, remote sensing and large scale global processes. Proceedings at the *Baltimore Symposium IAHS publication* no 186, IAHS Press, Oxfordshire, p. 67-74.

Shuttleworth, W. J. and Wallace, J. S. (1985). Evaporation from sparse crops-An energy combination theory. *Quarterly Journal of the Royal Meteorological Society,* 111:839-855.

Smith, R. C. G., and Choudhury, B. J. (1991). Analysis of normalized difference and surface temperature observations over southeastern Australia. International Journal of Remote Sensing, 12(10):2021-2044.

Su, Z. (2002). The Surface Energy Balance System (SEBS) for estimation of turbulent heat fluxes, *Hydrology and Earth System Sciences*, 6(1), 85-99.

SWAP user's manual (2006). DLOWinand Staring Centre, Wageningen, The Netherlands.

Tasumi, M. masahiro (2003). *Progress in Operation Estimation of Regional Evapotranspiration Using Satellite Imagery. PhD Theses* , Colleg of Graduat Studies University of Idaho, University of Idaho, USA.

Tasumi, M., Allen R.G. and Bastiaanssen, W.G.M. (2000a). *The Theoretical Basis of SEBAL*. Appendix A of Morse etal. (2000). Idaho Department of Water resources, Idaho ,http://www.idwr.state.id.us/gisdata/ET/final_sebalj)age.htm

Tasumi.M., Bastiaanssen W G.M. and Allen, R.G. (2000b). *A Step-by-Step Guide to Running SEBAL*. Appendix C of Morse et al. (2000). Idaho Department of Water Resources, Idaho, http://www.idwr.state.id. us/gisdata/ET/final_sebal_page.htm

Trezza, R. (2002). *Evapotranspiration using a satellite-based surface energy balance with standardized ground control*. Ph.D. Dissertation, Utah State University, Logan, Utah.

Thornthwaite, C. W., and Holzman B. (1939). *The determination of evaporation from land and water surfaces*. Monthly Weather Review, 67:4-11.

Thornthwaite, C.W. (1948). An approach toward a rational classification of climates. *Geophys. Rev. 38:*55-94, 1948.

Thornthwaite, C.W. and Mather, J.R. (1957). *Instruction and tables for computing potential evapotranspiration and the water balance*. Publications in climatology X, pp 183-243.

Tucker, C. J. and Maxwell, E. L. (1976). *Sensor design for monitoring vegetation canopies. Photogrammetric Engineering and Remote Sensing*, 42:1399-1410.

Tucker, C. J. (1979): Red and photographic infrared linear combinations for monitoring vegetation. *Remote Sens. Environ.,* 8, 127-150.

Turc, L., 1961: *Evaluation des besoins en eau d'irrigation, evapotranspiration potentielle, formule climatique simplifee et mise a jour*. (In French). Annales Agronomiques 12(1):13-49.

UNESCO. (1977). Impact of urbanization and industralization on water resources planning and management : report of the Unesco/IHP Workshop on impact of urbanization and industrialization on regional and national water planning and management, at Zandvoort, Netherland, October 1977 .

USGS (2001). The Radiance by Band of NLAPS processed Landsat Data, USGS Online Description, http://edcdaac.usgs.gov/pathfindcr/faq_pathfinder.html

USGS. (2002). MRLC 2000 *Image Preprocessing Procedure*. USGS Online Document. http://landcover.usgs.gov/pdf/image_preprocessing.pdf

U.S. Department of Agriculture, Soil conservation Service (1972). *National Engineering Handbook,* Section 4, HYDROLOGY. U.S. Govt. Printing Office, Washington, DC 544 pp., 1972

Van Dam, J.C., Huygen, J., Wesseling, J.G., Feddes, R.A., Kabat, P., and Van Walsum, P.E.V. (1997). Simulation of transport processes in the SoilWaterAirPlant environment.

Van de Griend, A.A. and Owe, M. (1993). On the relationship between thermal emissivity and the normalized difference vegetation index for natural surfaces. *Int. J. of Rem. Sens.* vol 14(6):1119-1131.

Van der Gun, Jac A.M. and Adul Aziz Ahmed, ed. with Abdullah Saleh Saif, dr Abdul Majid Mohamed, Salim Ba-Shueib and Ton Negenman (1995). Report WRAY-35, "*The Water Resources of Yemen*" a summary and digest of the available information. Ministry of Oil and Mineral Resources, General Department of Hydro-geology, and TNO Institute of applied Geo-science P.O. Box 6012, 2600 JA Delft the Netherlands.

Wing J, Sammis T.W, Meier C.A, Simmons L.J, Miller D.R, Samani Z. (2006). A Modified SEBAL model for spatially estimating pecan consumptive water use for las cruces, New Mexico, Agronomy and Horticaulture Departement, New Mexico State Univ. Las Cruses, New Mexico, USA.

Whittingham, C. P. (1974). The Mechanisms of Photosynthesis, Edward Arnod, London.

World Meteorological Organization (WMO). (1992). Simulated real-time intercomparison of hydrological models operational hydrology report no. 38. World *Meteorological Organization,* Geneva Switzerland, 241 pp., 1992

Wright, J. L. (1982). New evapotranspiration crop coefficients. *Journal of Irrigation and Drainage* Division, ASCE, 108(IR2):57-74.

Wright.J L, Allen, R.G. and Howell T. A. (2000). Comparison between evapotranspiration references and methods. Pp 251-259 in Evans, R.G.,

Woolley, J. T. (1971). Reflectance and transmittance of light by leaves. *Plant Physiology,* 47:656-662.

Wukelic, G.E., D.E. Gibbons, Martucci L.M. and Foote, H.P. (1989). Radiometric calibration of Landsat Thematic Thermal Band, Remote Sensing of Environment 28: 339-347

Yamamoto, G. and Kondo J. (1968). Evaporation from Lake Nojiri. J. *Meteor. Soc. Japan*. 46:166-176.

Zarkesh, M,K. (2005). *Decision Support System for Floodwater Spreading Site Selection in Iran*, PhD Thesis, Wgeningen University, itc, Enschede. Netherlands.

Publication during this research work from 2005 to 2008

a) International journals

Almhab, Ayoub and Ibrahim Busu (2008). Estimation of Evapotranspiration with modified SEBAL model using landsat-TM and NOAA-AVHRR images in arid mountains area, EMS2008, *IEEE computer society ,pp350-355, 2008 IEEE.*

http://ieeexplore.ieee.org/iel5/4530427/4530428/04530501.pdf?tp=&arnumber=453050 1&isnumber=4530428

Almhab, A. and Ibrahim Busu (2008). the approaches for oasis desert vegetation information abstraction based on medium -resolution Lansat TM image: A case study in desert wadi Hadramut Yemen, EMS2008, *IEEE computer society ,pp356-360, 2008 IEEE*

http://ieeexplore.ieee.org/iel5/4530427/4530428/04530502.pdf?tp=&arnumber=453050 2&isnumber=4530428

Almhab Ayoub, Ibrahim Busu and Arthur Cracknell (2008). Estimation of evapotranspiration using fused remote sensing image data and energy balance model for improving water management in arid mountains area. *International Journal of Remote Sensing. (under publish).*

Almhab A., Ibrahim B. (2008). Evapotranspiration of Grape vines Plantation by remote sensing using the energy balance based algorithms and Landsat TM Images in Arid mountainous Areas . *International Journal of Geoinformation. (under publish).*

Almhab A., Ibrahim B. (2008). Decision Support System for Estimating Actual crop Evapotranspiration using Remote Sensing, GIS and Hydrological Models. *Asian Journal of Geoinformation. (under publish).*

Almhab Ayoub, Ibrahim Busu and Arthur Cracknell (2007). Comparison of evapotranspiration using NOAA-AVHRR and LANDSAT-TM images over Sana'a basin, republic of Yemen, *IIUM Engineering Journal (under publish)*.

Ayoub Almhab (2005). Consequence of Remote Sensing Data for National Resources Management in Yemen, 2006. *Athawabit journal*, vol.44, pp59-86, Foundation Athwabit , Sana'a, Republic of Yemen.

Ayoub Almhab (2005). Relevance of Geographic Information System (GIS) to administrated planning &development in Yemen,2005. *Athawabit journal*, vol.39, pp59-86, Foundation Athwabit , Sana'a, Republic of Yemen.

b) *International conferences Publication*

Almhab A., Ibrahim B., (2008), Estimation of evapotranspiration using fused remote sensing image data and energy balance model for improving water management in arid area. ICECS2008, Singapor .

Almhab A., Ibrahim B., (2008), *Estimation of evapotranspiration using fused remote sensing image data and m-sebal model for improving water management in arid mountainous area.* ACRS2008, Sere lank.

Almhab A., Ibrahim B., (2008), *Regional Water Balance Visualization Using Remote Sensing And Gis Techniques with Application to the Arid Watershed Are*a . ACRS2008, Sere lank.

Almhab A., Ibrahim B., (2008), *Remote sensing of available solar energy modelling in mountainous areas*. Post graduate seminar alam bena 2008,UTM, Skudai Johor, Malaysia.

Almhab A., Ibrahim B., (2008), *Application of remote sensing data for environmental monitoring in semiarid mountain areas: a case study in yemen mountains*. post graduate seminar alam bena 2008,UTM, Skudai Johor, Malaysia.

Almhab A., Ibrahim B., (2008), *Regional Water Balance Visualization Using Remote Sensing And Gis Techniques with Application to the Arid mountain basin area* . IPGCES 2008,UTM, Skudai Johor, Malaysia.

Almhab Ayoub, Ibrahim Busu (2008). *Decision Support System for Estimating Actual crop Evapotranspiration using Remote Sensing, GIS and Hydrological Models*, MRSS2008, Kula Lumpur , Malaysia.

Almhab Ayoub, Ibrahim Busu and Arthur Cracknell (2008). *Fusion of landsat tm, noaa-avhrr and dem data for generating evapotranspiration maps in mountainous-arid regions,* MRSS2008, Kula Lumpur , Malaysia.

Almhab Ayoub and Ibrahim Busu Arthur Cracknell (2008). *Prediction of Groundwater availability in arid areas using Integration of Remote Sensing, GIS and DSS mapping,* ICEEMAT2008, Kula Lumpur , Malaysia.

Almhab Ayoub, Ibrahim Busu (2008). *Evapotranspiration Estimation using A Normalized Difference Vegetation Index Transformation of two Satellites data in Arid Mountain Areas,* ISG2008, Kula Lumpur , Malaysia.

Almhab Ayoub, Ibrahim Busu (2008). *Predicting evapotranspiration from MODIS vegetation indices and meteorological data in arid regions: A case study in Republic of Yemen*, ISG2008, Kula Lumpur , Malaysia.

Almhab Ayoub, Ibrahim Busu (2008). Decision Support System for Estimating Actual crop Evapotranspiration using Remote Sensing, GIS and Hydrological Models, *MAPASIA2008*, Kula Lumpur , Malaysia.

Almhab Ayoub and Ibrahim Busu (2008). Decision Support System for Estimating of Regional Evapotranspiration in Yemen mountainous, *Mountain GIS e-Conference, 14-24 january 2008, online.*
http://www.mtnforum.org/rs/ec/index.cfm?act=cres&econfid=15&startPage=11

Almhab, Ayoub, Ibrahim Busu (2008). A simple method for estimating of evapotranspiration using remotely sensed data in arid regions: a case study in Yemen Mountains , *MAP Middle East 2008*, Dubai , UAE.
http://gisdevelopment.net/proceedings/mapmiddleeast/2008/index.htm

Almhab, Ayoub, Ibrahim Busu (2008). *Remotely-sensed Evapotranspiration of arid regions in the central Yemen Mountains with a simple energy balance method ,*

The Postgraduate Annual Research Seminar 2008 (PARS08), UTM, skudai, johor, Malaysia.

http://www.pps.fsksm.utm.my/pars08/pars08.htm

Almhab, Ayoub And Ibrahim Busu (2008). Fusion of landsat tm, noaa-avhrr and dem data for generating evapotranspiration maps in semi-arid regions , 5th international conference on gis *(ICGIS-2008)*, Istanbul/Turkey.

http://icgis2008.fatih.edu.tr/?Bilpos&Lang=En

Almhab A., Ibrahim B. (2008). *Regional Water Balance Visualization Using Remote Sensing And Gis Techniques with Application to the Arid area* . IPGCES 2008,UTM, Skudai Johor, Malaysia.

Almhab Ayoub, Ibrahim Busu (2007).Estimation of regional scale evapotranspiration for arid area using NOAA-AVHRR application in republic of Yemen, *MAPASIA2007*, Kula Lumpur , Malaysia.

http://www.gisdevelopment.net/proceedings/mapasia/2007/PosterSession/ma072 26.pdf

Almhab Ayoub, Ibrahim Busu and Norkhair ibrahim (2007).Estimation of regional evapotranspiration for Arid Areas Using LANDSAT Thematic Mapper Images data: A Case Study for Grape Plantation, *ISG & GPS/GNSS 2007*, Johor, Malaysia. http://eprints.utm.my/4681/

Almhab Ayoub, Ibrahim Busu and Arthur Cracknell (2007).Comparison of regional evapotranspiration using NOAA-AVHRR and LANDSAT-TM images: a case study in an arid area in the Sana'a basin, republic of Yemen, *The 28th Asian Conference on Remote Sensing (ACRS) 2007P*.N. 93, Kuala Lumpur, Malaysia. http://www.ionicsoft.com/images/gallery/mest2007finalannouncement11948571 07.pdf

Almhab Ayoub and Ibrahim Busu (2007). *Application of remote sensing data for environmental monitoring in semiarid mountain areas: a case study in Yemen mountains*, Asian post graduate seminar in built environment 2007, 3–5 December 2007, Faculty of the built environment, university of Malaya, Kuala Lumpur, Malaysia. full paper pdf

Almhab Ayoub and Ibrahim Busu (2007). Comparison of regional evapotranspiration using NOAA-AVHRR and LANDSAT-TM images: a case study in an arid area in the Central of Yemen mountains , *Middle East spatial technology 4th conference & exhibition,* Al- Bahrain Kingdom.

http://www.ionicsoft.com/images/gallery/mest2007finalannouncement11948571 07.pdf

Almhab Ayoub, Ibrahim Busu and Kalifa Alromathi (2007). Fusion of Landsat TM, NOAA-AVHRR and DEM data For generating evapotranspiration Maps In Semi-Arid Regions, 3rd International Conference " *Earth from Space – the Most Effective Solutions*" December, 4-6, 2007. Moscow Region Vatutinki recreation center of the Russian, Russian.

http://scanex.com/ru/news/News_Preview.asp?id=n21793201

Almhab Ayoub, Ibrahim Busu and Norkhair ibrahim (2006). Development of Vegetation and Land Use By Remote Sensing Method in Wadi Tuban Abyan Area - Yemen, *1st Regional Postgraduate Conference on Engineering and Science (RPCES 2006)*, Johore, 26-27 July, Johor ,Malaysia.

APPENDIXES:

APPENDIX A: ERDAS IMAGINE SPATIAL MODELER AND OTHER SOFTWARE

The implementation of the soil energy balance algorithm for land model was carried out using spatial modeler facility of ERDAS imagine version 8.5. Spatial modeler is a unique module which has graphical editing capabilities that allow access to spatial analysis modeling of the soil energy balance algorithm for land SEBAL model. A graphic model of the desired process can be developed by defining input variables, analysis operations and output format.

 Usage of the spatial modeler involves a number of steps i.e. graphical design, data input and output and execution of the model. Upon invoking the 'Model Maker' icon, a blank 'sheet' appears on the screen, together with window showing various 'objects' including raster data sets, tables and scalars, criteria, mathematical functions, operators and connectors. Some of the most commonly used 'objectives' are shown in figure 4.5. To create a model, the user chooses and defines the objects and places them on the sheet. A model must contain at least the basic structure: an input object, an operator and output object (figure A1). All components must be connected to another before the model can be executed.

A.1 Modified SEBAL ET Estimation Spatial Model

As a product of this study, the modified SEBAL model was developed using model maker in ERDAS Imagine. This model does all of the calculations explained earlier, above. The operated modified SEBAL model for Yemen mountain applications is composed of 14 sub-models. However, the number of sub models is not a fixed value. For purpose of a clear presentation, the model is broken up into seven parts as showing in figure A2 to A14 , some parts is double because we have used two satellite images AVHRR and TM. The separation of the sub-models depends on the users' preference.

For operational purposes, many calculations are contains in one sub model, thereby reducing the total number of sub-models. Also, for operational purposes, a very large model which cannot be shown on one computer screen might be subject to more human errors. This section presents the series of sub-models used for the Yemen Mountain application Model.

A.2   ERDAS Imagine Model Maker

ERDAS Imagine Model Maker is a user-friendly model development tool. In the Model Maker, model components (inputs, calculations, and outputs) are visualized so that the model compositions and computational flows are easily tracked. Figure A1 shows the primary dialogs used in ERDAS Imagine Model Maker. The "Raster Object" represents raster data, either for input/output images and for storage of intermediate calculation results. For input data, the data name and the stored location are specified. For output data, data type and names are specified. The "Scalar Object" is used for scalar data input (i.e. constants), and the "Table Object" is used for input of a series of scalars as a table. The "Function Definition" is for defining the calculation equations and programming functions. These dialogs are sequentially connected by arrows.
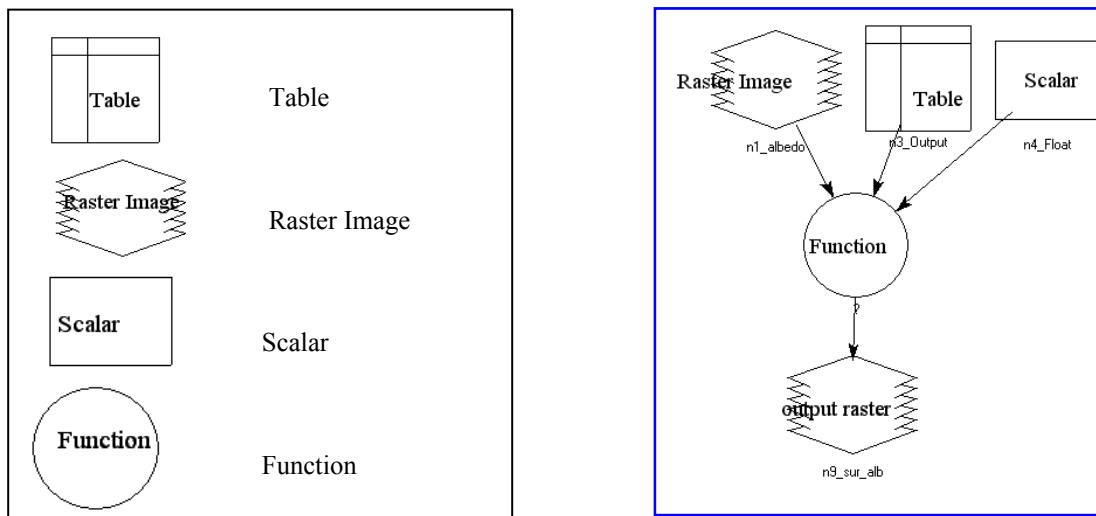
Figure A1 Shapes of primary dialogs in ERDAS Imagine Model Maker (right), and Model example in ERDAS Imagine Model Maker (left)

A3. Modified SEBAL pre-calculations

Before starting the land surface energy balance calculation, incoming solar radiation related calculations are carried out. This Pre-Calculation process is for the Mountain Model.

M-S-01: Generation of DEM Calculations of sine and cosine of slope, aspect and cosine θ theta:

Input Images: Surface slope and aspect images derived by DEM

Input Values: calculated δ (declination), ɸ (latitude), and ω (solar angle) values for the image

Output Images: sin(slope), sin(aspect), cos(slope), cos(aspect) and cos(θ)

Description: This model is for calculating sine and cosine of surface slope equation 3.18 and aspect equation 3.19. These four outputs are used in calculating cosine of solar incident angle for each pixel equation 3.13. Because modified SEBAL application on the Mountain to calculates all components of the energy balance in W m^{-2}, for a horizontal equivalent surface, the calculated cos(θ) by this model has been divided by cosine of surface slope. Therefore the resulting cos(θ) values can be more than 1 due to the effect of area differences for a sloped surfaces. In the graphical model, function 1 to 8 which executes equations 3.18, 3.19, 3.13, and 3.17 thus produce images sin(slope), sin(aspect), cos(slope), cos(aspect) and cos(θ) is given by:

Table A1cod snippet for calculation DEM generation

1. DEGREE SLOPE ($n1_00sanaa_dem_sq , "meters")*PI/180
2. ((ASPECT ($n1_00sanaa_dem_sq) -180)*PI/180)
3. sin($n12_temp)
4. cos($n12_temp)
5. SIN($n2_temp)
6. COS($n2_temp)
7. (cos($n41_Float) *
   pi/180)*$n14_001sin_slop*$n3_004cos_aspect)+((cos($n40_Float) *
   pi/180) * (cos($n41_Float) *
   pi/180)*$n13_002cos_slop*cos($n42_Float)) + ((cos($n40_Float)*
   pi/180)* (sin($n41_Float)* pi/180)
   *$n14_001sin_slop*$n3_004cos_aspect*cos($n42_Float))+(
   (cos($n40_Float)* pi/180) * (sin($n41_Float)*
   pi/180)*$n14_001sin_slop*sin($n42_Float))
8. ($n35_memory/$n13_002cos_slop).
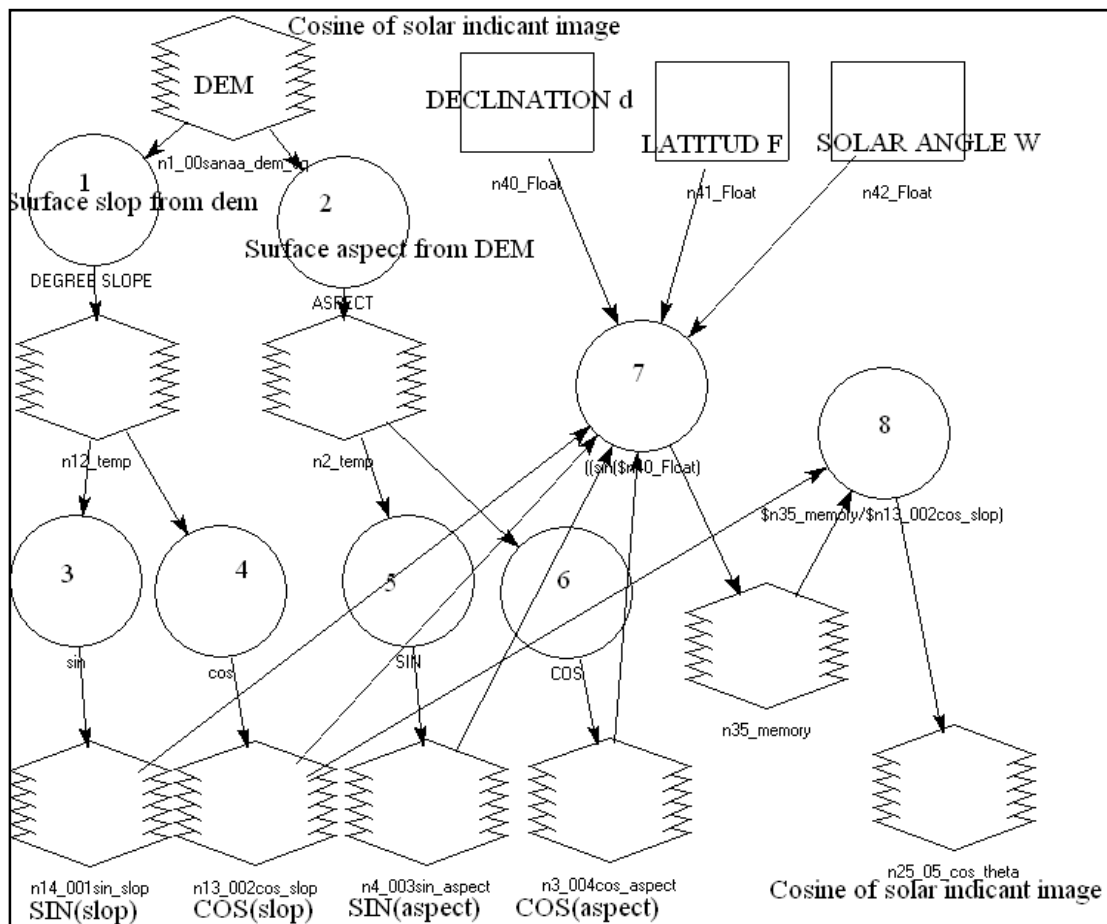
Figure A2 cosine slop, sine slop, cosine aspect, sine and cosine solar indicant angle

M-S02: Calculation of Radiation Correction Surface Reflectance LANDSAT TM,

Input Images: Landsat TM/ETM+, $\cos\theta$ and DEM

Input Values: Image specific constants (L_{MIN}, L_{MAX}, ESUN$_A$,

Output Images: R1,R2,R3,R4,R5,R7,(R=reflectance correction for band number 1to2and7)

Description: This model derives the basic information from the satellite image. In the graphical model, function 1 to 7 which execties Correction Surface Reflectance thus produce images R1,R2,R3,R4,R5,R7 is given by:

Table A2 cod snippet for calculation Radiation Correction Surface Reflectance Landsat TM,

1. (($n19_Custom_Float - $n18_Custom_Float) / 255)* $n16_000sanaa_basin_98sq + $n18_Custom_Float

2. (((-0.15+(15.21+0.15)*$n2_02spectral_rad_foreachband(1)/255))*PI)/(195.7* $n1_005_cos_theta_sub *0.9762)

3. (((-0.28+(29.68+0.28)*$n2_02spectral_rad_foreachband(2)/255))*PI)/(182.9* $n1_005_cos_theta_sub *0.9762)

4. (((-0.12+(20.43+0.12)*$n2_02spectral_rad_foreachband(3)/255))*PI)/(155.7* $n1_005_cos_theta_sub *0.9762)

5. (((-0.15+(20.62+0.15)*$n2_02spectral_rad_foreachband(4)/255))*PI)/(104.7* $n1_005_cos_theta_sub *0.9762)

6. (((-0.037+(2.72+0.037)*$n2_02spectral_rad_foreachband(5)/255))*PI)/(21.93* $n1_005_cos_theta_sub *0.9762)

7. (((-0.015+(1.44+0.015)*$n2_02spectral_rad_foreachband(7)/255))*PI)/(7.452* $n1_005_cos_theta_sub*0.9762)
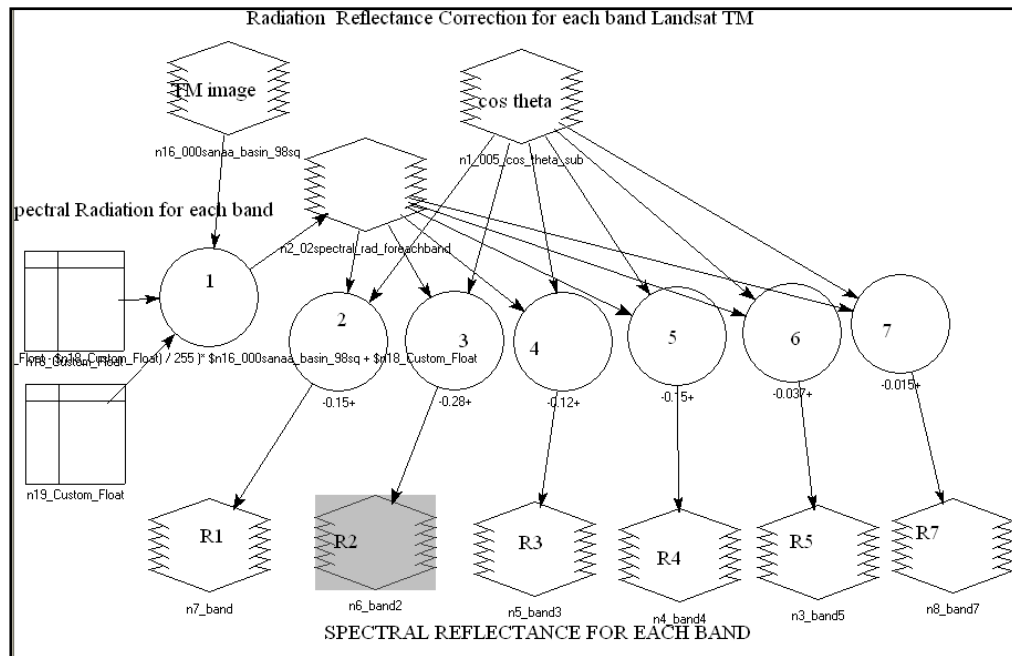
Figure A3 Radiation and reflectance Correction LANDSAT TM,

M-S03: : Generating model parameters Landsat TM,

The following models are required in modified SEBAL to perform the surface parameter for each pixel.

Input Images: Landsat TM/ETM+ , cosθ, and DEM

Input Values: d_r, Ra, Image specific constants (G_S, W_A, C_1 and C_2 for Band 6 calibration), and representative elevation

Output Images: a_{TOA}, $\tau_{SW,}$ a, NDVI, ε, T_s, and $T_{S(DEM)}$

Table A3 cod snippet for calculation Generating model parameters Landsat TM,

1. $n7_r_band1* 0.293 + $n6_r_band2* 0.274 + $n5_r_band3 * 0.233 + $n4_r_band4 * 0.157 + $n3_r_band5 * 0.033 +$n8_r_band7 * 0.011
2. 0.75 + (2 * (10 ** (- 5)) *$n38_00sanaa_dem_sq)
3. ($n26_1_albedo_toa - 0.03) /($n39_2_transmittance ** 2)
4. ($n4_r_band4 - $n5_r_band3) / $(n4_r_band4 + $n5_r_band3)
5. 1.009 + 0.047 * LOG ($n42_4_ndvi)
5b. EITHER 1 IF ($n34_3_surface_albedo>0.47) OR $n69_memory OTHERWISE
5c. EITHER 1 IF ($n42_4_ndvi<0) OR $n64_memory OTHERWISE
5d. EITHER $n68_memory IF ($n68_memory>0.9) OR 0.9 OTHERWISE

6a. 0.1238+((1.56 - 0.1238) * $n16_01sanaa_basin_98sq(6)/255)
6b. 1260/(LOG (61.6/$n51_memory + 1))
6c. $n52_memory / (($n60_5_emissivity) ** 0.25)
7. ($n38_00sanaa_dem_sq - 2150) * 0.0065 + $n53_6_surface_temperature.
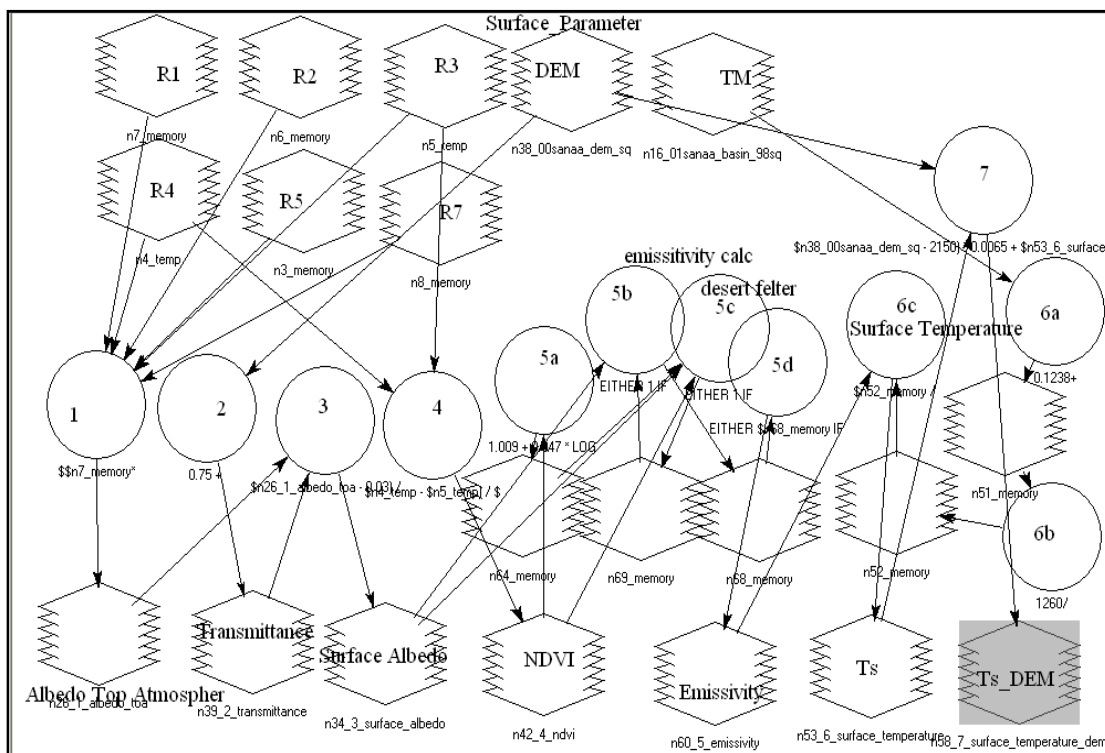
Figure A4 Surface Parameter LANDSAT TM,

M-S03: Generating model parameters NOAA-AVHRR

M-S03: Calculation of Surface Reflectance and Generating model parameters

The following models are required in modified SEBAL to perform the surface parameter for each pixel.

Input Images: NOAA-AVHRR , $\cos\theta$, and DEM

Input Values: d_r, Ra, T_{NB}, Image specific constants (G_S, W_A, C_1 and C_2 for Band 4 and 5 calibration), and representative elevation

Output Images: a_{TOA}, τ_{SW}, a, NDVI, ε, T_s, and T_S(DEM)

Description: This model derives the basic information from the satellite

Image. E_{NB} and SAVI are internally used and are not output. The surface temperature correction terms (Ra and ε_{NB}) can be set as 0,0,1 respectively if the decision is to use uncorrected temperature. . In the graphical model, function 1 to 12 which executes equations 3.23, 3.24, 3.25, 3.26, 3.36 TO 3.43 and 3.44 thus produce images a_{TOA}, τ_{SW}, a, NDVI, ε, T_s, and T_S(DEM)is given by:

Table A4 cod snippet for calculation Radiation Correction and Generating model parametersNOAA-AVHRR,

1. (0.1090 * $n1_noaa49sub(2) + (- 3.6749))
2. (0.1081 * $n1_noaa49sub(1) + (- 3.8648))
3. (0.035 + (0.545 * $n3_temp)+ (0.32 * $n5_temp)) / 100
4. 0.75 + (2 * (10 ** (- 5)) *$n11_000sanaa_dem_sq)
5. ($n9_1_albedo_toa - 0.015) /($n12_2_transmittance ** (2))
6. ($n5_temp - $n3_temp) / ($n5_temp + $n3_temp)
7. 1.009 + 0.047 * LOG ($n20_4_ndvi)
7b. EITHER 1 IF ($n20_4_ndvi<0) OR $n27_memory OTHERWISE
7c. EITHER $n29_memory IF ($n29_memory>0.9) OR 0.9 OTHERWISE
7d. EITHER 1 IF ($n16_3_surface_albedo>0.47) OR $n28_memory OTHERWISE
8. (1.438833 * 929.5878) / LOG (((1.1910659 * 10 ** (- 5) * 929.5878 ** 3) / $n1_noaa49sub(5)) + 1)
9. (1.438833 * 929.5878) / LOG (((1.1910659 * 10 ** (- 5) * 929.5878 ** 3) / $n1_noaa49sub(4)) + 1)
10. (0.39*($n47_memory) ** 2) + (2.34 * $n47_memory) - (0.78 * $n47_memory * $n48_memory) - (1.34 * $n48_memory) + (0.39 * ($n48_memory) ** 2) + 0.56
11. ($n11_000sanaa_dem_sq - 2150) * 0.0065 + $n52_6_surface_temperature
12. ($n50_memory** 4 / $n30_5_surface_emisitivity) ** 0.25
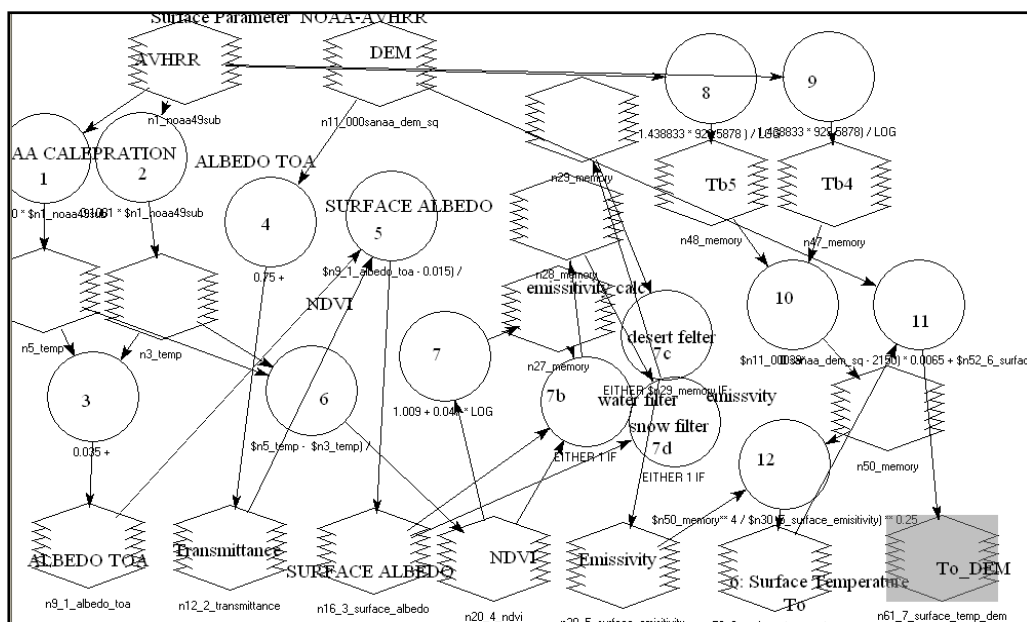
Figure A5 Radiation Correction and Surface Parameter LANDSAT TM,

M-S04: Determination of radiations

M-S04-1 Net Radiation *Rn and Soil Heat Flux G calculations*

Input Images: $\cos\theta$, τ_{sw}, a, ε, T_s, NDVI, and DEM

Input Values: d_r, $T_{S(DEM\ cold\ pixel)}$ and representative elevation

Output Images: R_n, and G

Description: This model calculates R_n and G values. The land use map is used for indicating special surfaces such as water and snow, for application of different G equations. If a land use map is not available, negative values of NDVI may be used as an indicator of the presence of water. DEM is used to adjust the value of R_{Lin} for differences in pixel elevation. The $T_{S(DEM\ cold\ pixel)}$ and the representative elevation are used for R_L in calculation instead of $T_{s(cold\_pixel)}$ and elevation of the cold pixel, so that the user does not have to read the elevation value of the cold pixel for each image. In the Flat Model, R_{Lin}, $\cos\theta$, and τ_{sw} are taken as constants. In the graphical model, function 1 to 5 which executes equations 3.44, 3.46, 3.49 and 3.50 thus produce images Rn and G is given by:

Table A5 cod snippet for Determination of radiations calculation Rn and G

1. 1.08 * ((- LOG ($n16_2_transmittance)) ** 0.265) * 5.67 * (10 ** (- 8)) * (289 ** 4)
2. ((1 - $n4_3_surface_albedo) *1367*$n19_005_cos_theta_sub*0.9762*$n16_2_transmittance) + $n17_memory - ($n2_5_emissivity* (5.67 * (10 ** (- 8))) * ($n15_6_surface_temperature ** 4)) - ((1 - $n2_5_emissivity) * $n17_memory)
3. 0.3*(1 - (0.98 * ($n22_4_ndvi ** 4)))*$n6_10_net_radiation
4. EITHER (1*$n6_10_net_radiation-90) IF ($n22_4_ndvi<0) OR ($n27_memory) OTHERWISE
5. EITHER (EITHER (0.5*$n6_10_net_radiation) IF ($n15_6_surface_temperature<277) OR($n26_memory)OTHERWISE) IF ($n4_3_surface_albedo>0.47) OR ($n26_memory) OTHERWISE
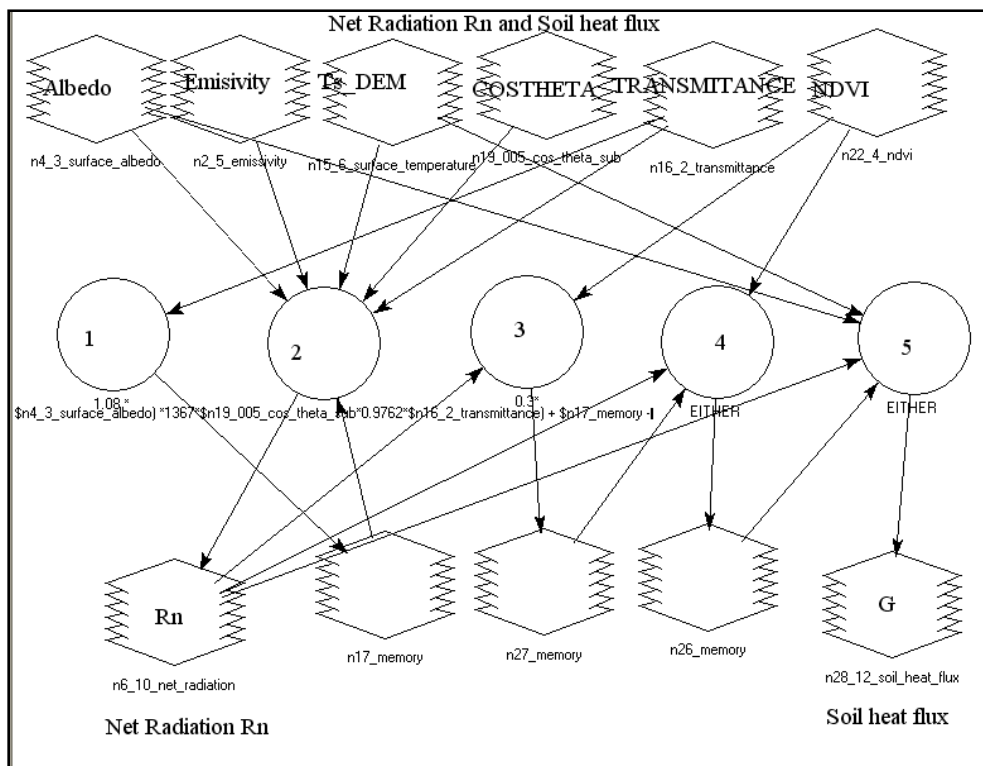
Figure A6 Net radiation R_n and soil heat flux G

M-S04-2: z_{om}, u_{200}, $H_{(ist)}$ and $rah_{(1st)}$ calculations

Input Images: LAI, Slope (derived by DEM), Land use Map, and DEM Input
Values: u_{2oo} at weather station, Elevation at weather station

Output Images: z_{om}, u_2oo- H-(1st). r_{ah}(ist).

Description: This model calculates z_{omi} u_2oo- u*(ist) and r_{ah}(ist)for each pixel. z_{om} values are basically assigned by the Landuse Map, and LAI is used to estimate z_{om} for agricultural areas only. Slope map and DEM are used for mountain correction of Zo_m and u_2oo. In the graphical model, function 1 to 8 which executes equations 3.63, 3.46, 3.55 and 3.57 thus produce images z_{om}, u_2oo- r_{ah}(ist). and H-(1st) is given by:

Table A6 cod snippet for Determination of radiations calculation H1

```
1. EITHER ( EITHER (EXP ($n46_Float * $n4_4_ndvi - $n47_Float))
IF ((EXP ($n46_Float * $n4_4_ndvi -
$n47_Float)) < 0.246) OR (0.246) OTHERWISE ) IF
($n37_000sanaa_dem_sq < 5) OR ( EITHER (EXP (5.5895 *
$n4_4_ndvi -3.2705)) IF ((EXP (5.5895 * $n4_4_ndvi - 3.2705)) < 4)
OR (4) OTHERWISE ) OTHERWISE
2. EITHER $n6_memory IF ($n4_4_ndvi> 0.0 ) OR 0.001 OTHERWISE
3. 5.3*0.41/(log(200/$n7_13surface_roughness_zom))
4. log(2 / 0.01)/($n14_14_friction_velosity_u1*0.41)
5. $n42_Float * $n19_7_surface_temperature_dem - $n43_Float
6. $n18_6_surface_temperature - $n21_temp
7. 349.467*((($n20_memory-
0.0065*$n37_000sanaa_dem_sq)/$n20_memory)**5.26)/$n20_memory
8. $n22_16_air_density_p1 * 1004 * $n21_temp /
$n13_15_airodynamice_to_heat_transport_rah1
```
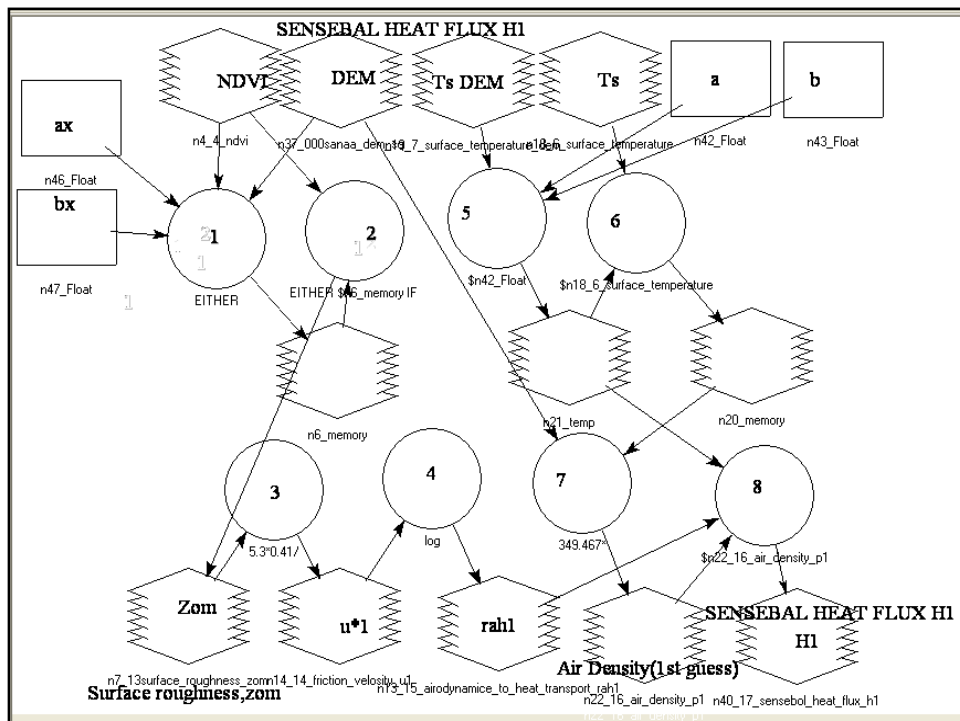
Figure A7 Sensible heat flux H1

M-S04-3: H calculation

Input Images: T_s, $T_{S(DEM)}$, z_{om}, u_{2oo}. $u^*(ist)$. $r_{ah}(ist)$. and DEM Input Values: The final "a" and "b" for developed dT function. Output Images: H

Description: The shortcut method described in Section 4.7 of the main text was applied. In the Model, u_2oo is not a mapped value but a constant value for the entire

image. Function 1 to 8 which executes equations 3.68 to 3.76 thus produce images z_{om}, $u_2$oo- r_{ah}. and H is given by:

Table A7 cod snippet for Determination of radiations calculation repeat H2 toH5

1. EITHER (- 1004 * $n2_302friction_velosity_u1 * ($n5_304air_density ** 3) * $n4_06surface_temperatur) / (0.41 * 9.81 * $n3_3_sensebol_heat_flux_h1) IF ($n3_3_sensebol_heat_flux_h1 ne 0) OR - 1000 OTHERWISE
2. EITHER ((1 - 16 * (200 / $n9_temp)) ** 0.25) IF ($n9_temp< 0) OR 1 OTHERWISE
3. EITHER (2 * LOG ((1 +$n6_temp ** 2) / 2)) IF ($n9_temp< 0) OR (- 5*2 /$n9_temp)OTHERWISE
4. EITHER (2 * LOG ((1 + $n10_memory) / 2) + LOG ((1 + $n10_memory ** 2) / 2) - 2 * ATAN ($n10_memory) + 0.5 * PI) IF ($n9_temp< 0) OR (-5*2 /$n9_temp) OTHERWISE
5. ($n57_Float*0.41)/(log(200/$n1_301surface_roughness_zom)-$n8_memory)
6. (log(2 / 0.01)-$n6_temp)/(0.41 * $n11_401_u_star2)
7. $n52_Float * $n31_06_1surface_temperatur_dem - $n53_Float
8. $n4_06surface_temperatur-$n45_404_dt2
9. 349.467*((($n44_405_air_temp-0.0065*$n32_wadi_asser_sanaadem)/$n44_405_air_temp)**5.26)/$n44_405_air_temp)
10. $n43_403air_density * 1004 * $n44_405_air_temp / $n51_402rah2
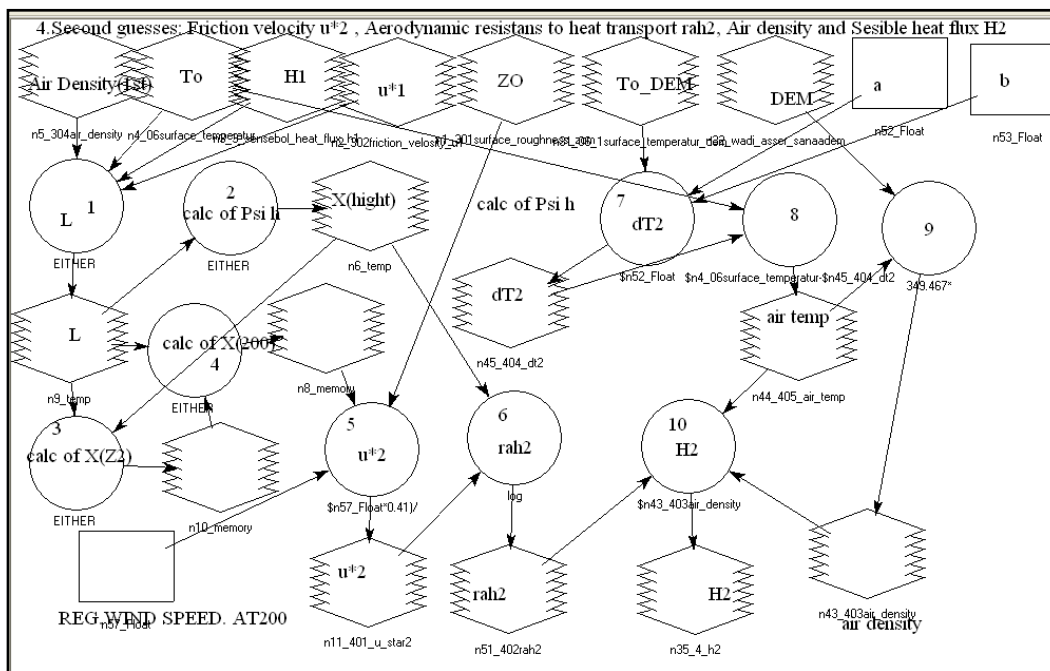
Figure A8 Sensible heat flux repeat H

M-S05: Calculation of ET: daily

M-S05- EF instantaneous evaporative fraction.

Input Images: Rn, G and H5

Output Images: Image of the instantaneous evaporative fraction EF

Description: This model calculates the instantaneous evaporative fraction EF. for sloped land surfaces. Function 1 and 2 which executes equations 3.77 and 3.78 thus produce images EF is given by:

Table A8 cod snippet for estimation of instantaneous evaporative fraction

1. ($n3_10_net_radiation - $n2_17_sensebol_heat_flux_h1 - $n1_12_soil_heat_flux) / ($n3_10_net_radiation - $n1_12_soil_heat_flux)

2. EITHER 0.0 IF ($n4_memory<0.0) OR $n4_memory OTHERWISE
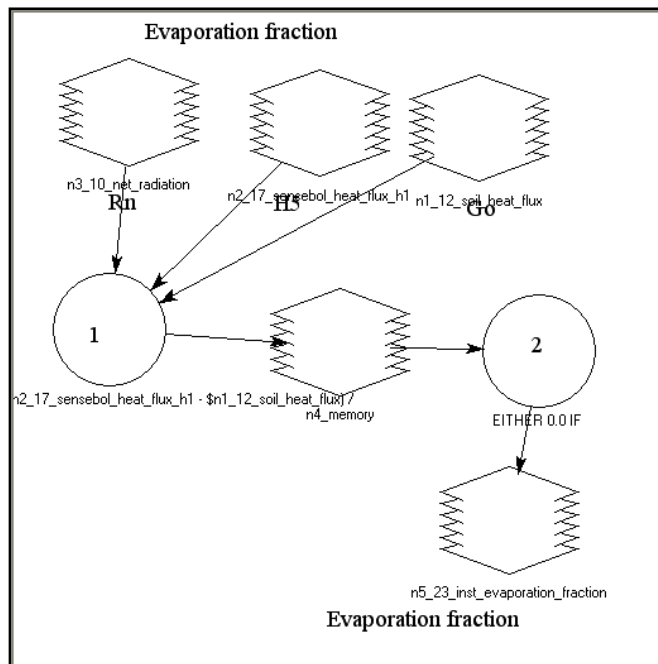
Figure A9 instantaneous evaporation fraction

M-S05-2: ET24 calculation

Input Images: a, R_{a24}, cos slop , τ_{sw}, T_s, NDVI, EF

Input Values: Instantaneous and 24-hour ET_r

Output Images: $FET_{(24)}$

Description: In this model, the cumulative ET24 for each sub-period is directly assigned in the equation in function definition dialog. Therefore, these values are not shown in the model. Function 1 to 4 which executes equations 3. 81 and 3.82 thus

produce images ET24 is given by:

Table A9 cod snippet for estimation of *twenty four* Evaptranspiration

1. (1 - $n7_3_surface_albedo) * ($n6_22_ra24) /($n5_002cos_slop) *
$n4_2_transmittance -(110
*$n4_2_transmittance)
2. (2.501 - 0.002361 * ($n3_6_surface_temperature)) * (10 ** 6)
3. EITHER (1*$n8_25_le-100) IF ($n16_4_ndvi<0) OR (0) OTHERWISE
4. $n1_23_inst_evaporation_fraction* (($n8_25_le - $n10_24_g24) * 86400) /
($n9_memory)
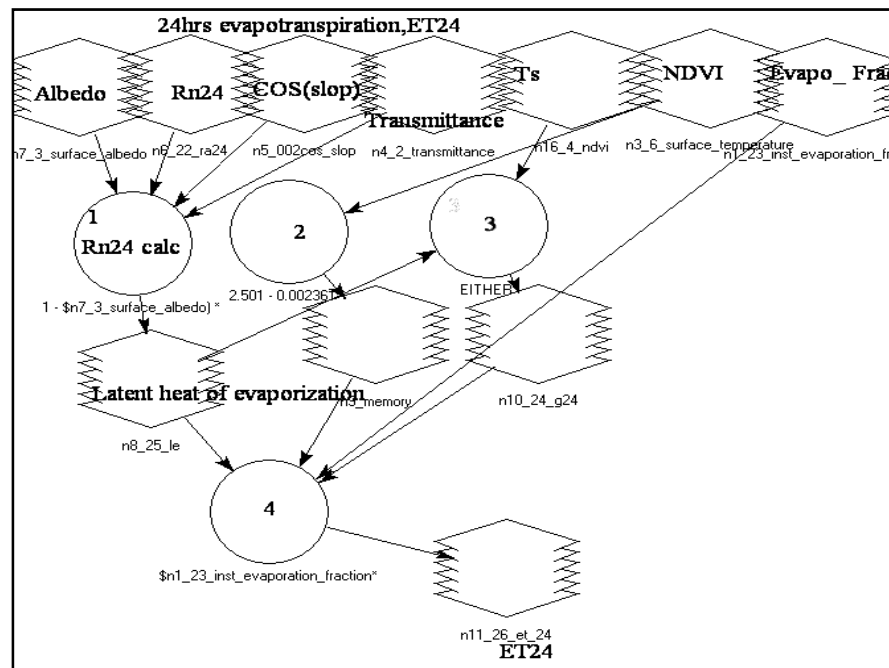
Figure A10 ET24

M-S01-2: twenty four (24) hour R_a calculation

Input Images: sin(slope), sin(aspect), cos(slope), and cos(aspect)

Input Values: calculated sinδ sin φ, sin5cosφ, cosδ sinφ, cosδ, ω (Sunrize), ω (sunset)' and
G_{sc}_related_constant Output Images: R_a(24)

Description: This model is for calculating 24-hour R_a for sloping surfaces, which is
later used in 24-hour R_{so} estimation. This model is the most complicated model in

modified SEBAL. The "G$_{sc}$_related_constant" in the Input Value is G$_{sc}$. d$_r$/2л ($W\ m^{-2}$), where G$_{sc}$ is 1367 $W\ m^{-2}$. This G$_{sc}$_related_constant is calculated outside of the model to simplify the equations in the function definition dialogs used in this model.
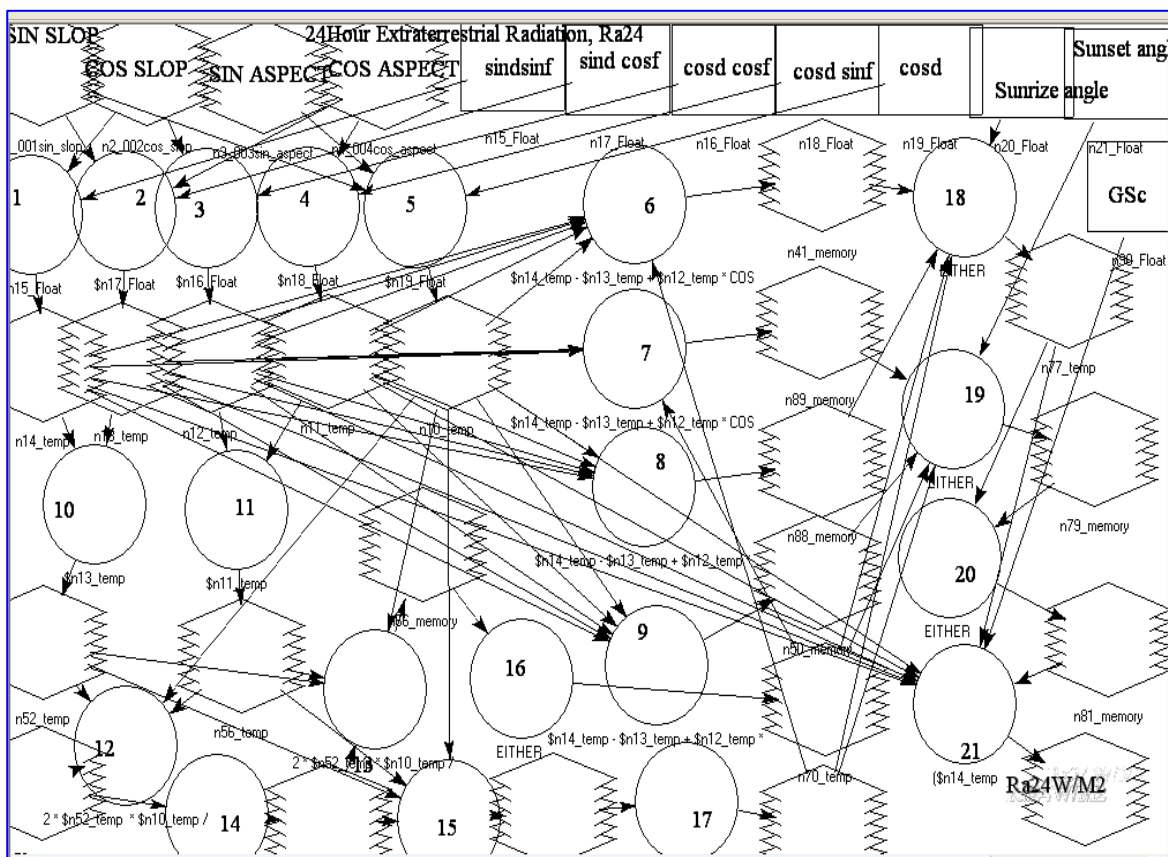
Figure A11 Ra24

Table 3.14 cod snippet for estimation of *twenty four* solar extraterrestrial radiation

1. $n15_Float * $n2_0012cos_slop_rad
2. $n17_Float * $n1_0012sin_slop_rad * $n4_0013cos_aspect_rad
3. $n16_Float * $n2_0012cos_slop_rad
4. $n18_Float * $n4_0013cos_aspect_rad

5. $n19_Float * $n1_0012sin_slop_rad * $n3_0013sin_aspect_rad
6. $n14_temp - $n13_temp + $n12_temp * COS ($n71_temp + 0.0218166) + $n11_temp * COS ($n71_temp + 0.0218166) + $n10_temp * SIN ($n71_temp + 0.0218166)
7. $n14_temp - $n13_temp + $n12_temp * COS ($n70_temp - 0.0218166) + $n11_temp * COS ($n70_temp - 0.0218166) + $n10_temp * SIN ($n70_temp - 0.0218166)
8. $n14_temp - $n13_temp + $n12_temp * (- 0.1980) + $n11_temp * (- 0.1980) + $n10_temp * (- 0.9802)
9. $n14_temp - $n13_temp + $n12_temp * (- 0.1980) + $n11_temp * (- 0.1980) + $n10_temp * (0.9802)
10. $n13_temp - $n14_temp
11. $n11_temp + $n12_temp
12. ((2 * $n52_temp * $n10_temp /($n56_temp ** 2)) ** 2) - 4 * (1 +($n10_temp ** 2) / ($n56_temp ** 2)) * (($n52_temp ** 2) / ($n56_temp ** 2) - 1)
13. (2 * $n52_temp * $n10_temp / ($n56_temp ** 2) + ($n64_temp ** 05)) / (2 * (1 +($n10_temp ** 2) / ($n56_temp ** 2)))
14. EITHER($n59_memory) IF ($n59_memory>0.0001) OR (0.0001) OTHERWISE
15. (2 * $n52_temp * $n10_temp / ($n56_temp ** 2) - ($n64_temp ** 0.5)) / (2 * (1 + ($n10_temp ** 2) / ($n56_temp ** 2)))
16. EITHER (- 1.5708) IF ($n66_memory<(-1)) OR(EITHER (1.5708) IF ($n66_memory >1) OR (ASIN($n66_memory)) OTHERWISE) OTHERWISE
17. EITHER (- 1.5708) IF ($n69_memory<(-1)) OR(EITHER (1.5708) IF ($n69_memory >1) OR (ASIN($n69_memory)) OTHERWISE) OTHERWISE
18. EITHER ($n20_Float) IF ($n88_memory >0) OR (EITHER ($n71_temp) IF ($n41_memory >0) OR($n70_temp) OTHERWISE) OTHERWISE
19. EITHER ($n21_Float) IF ($n50_memory >=0) OR (EITHER ($n70_temp) IF ($n89_memory >0) OR ($n71_temp) OTHERWISE) OTHERWISE
20. EITHER ($n79_memory) IF ($n79_memory >$n77_temp) OR ($n77_temp) OTHERWISE
21. ($n14_temp * ($n81_memory - $n77_temp) - $n13_temp * ($n81_memory - $n77_temp) + $n12_temp * (SIN($n81_memory) - SIN($n77_temp)) + $n11_temp * (SIN ($n81_memory) - SIN ($n77_temp)) - $n10_temp * (COS ($n81_memory) - COS ($n77_temp))) * $n90_Float
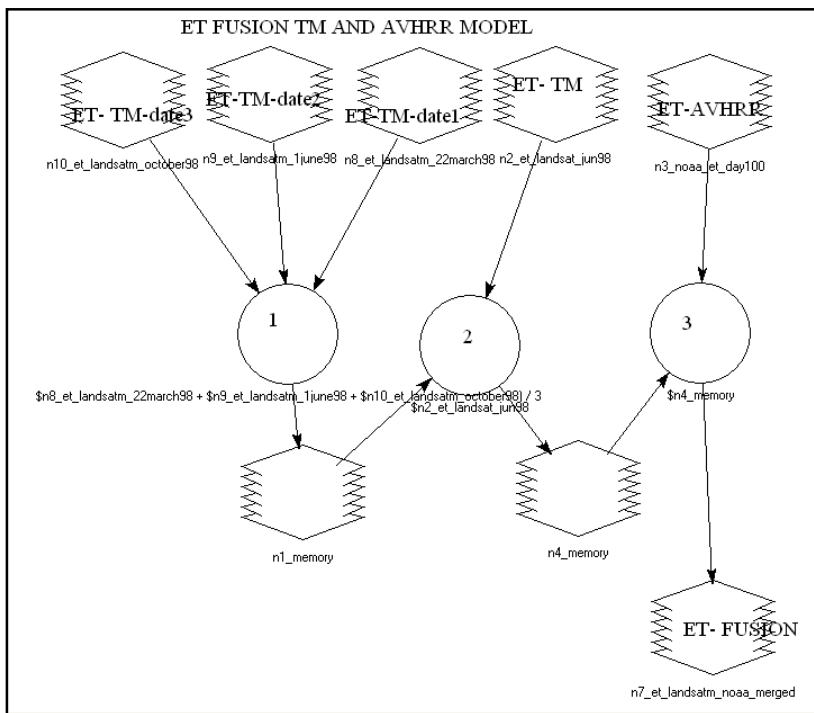
Figure A12 Fusion evaptranspiration from AVHRR-TM

1. ($n8_et_landsatm_22march98 + $n9_et_landsatm_1june98 + $n10_et_landsatm_october98) / 3
2. $n2_et_landsat_jun98 / $n1_memory
3. $n4_memory * $n3_noaa_et_day100

A4. Evaporation daily by simplified method

ET BY SIMPLEFIELD METHOD

A

n2_Float

B

n3_Float

dT

n1_dt

1

$n2_Float

ET

n5_et_simple
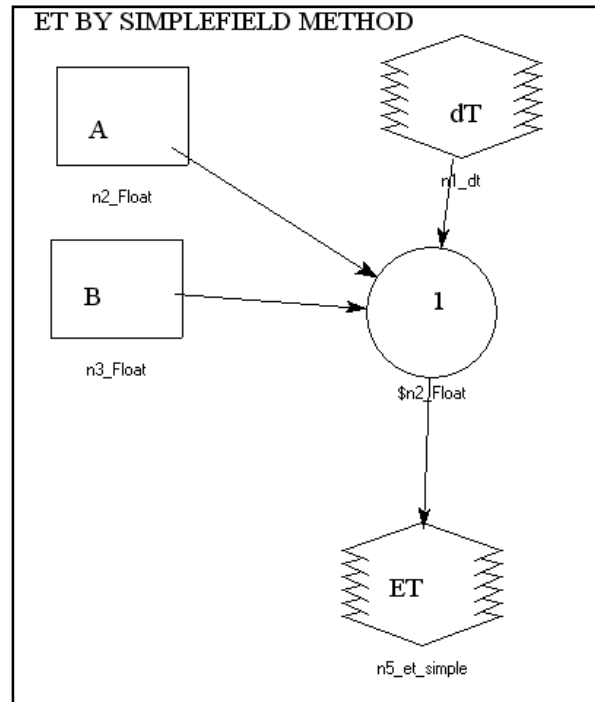
Figure A13 Evaporation daily by simplified method

$n2_Float * $n1_dt + $n3_Float

A5 Evaporation daily by biophesical method
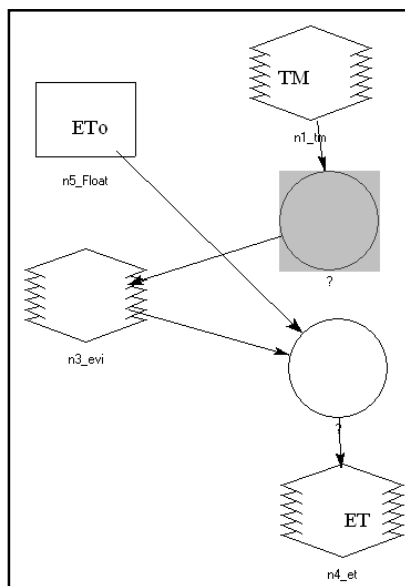
Figure A14 Evaporation daily by biophesical method

A6. Remote Sensing and GIS for water management software.

This programme develop during this research study but due to the limited time and original software, the programme not complete. need more future work and developing to produce it to the practical work.
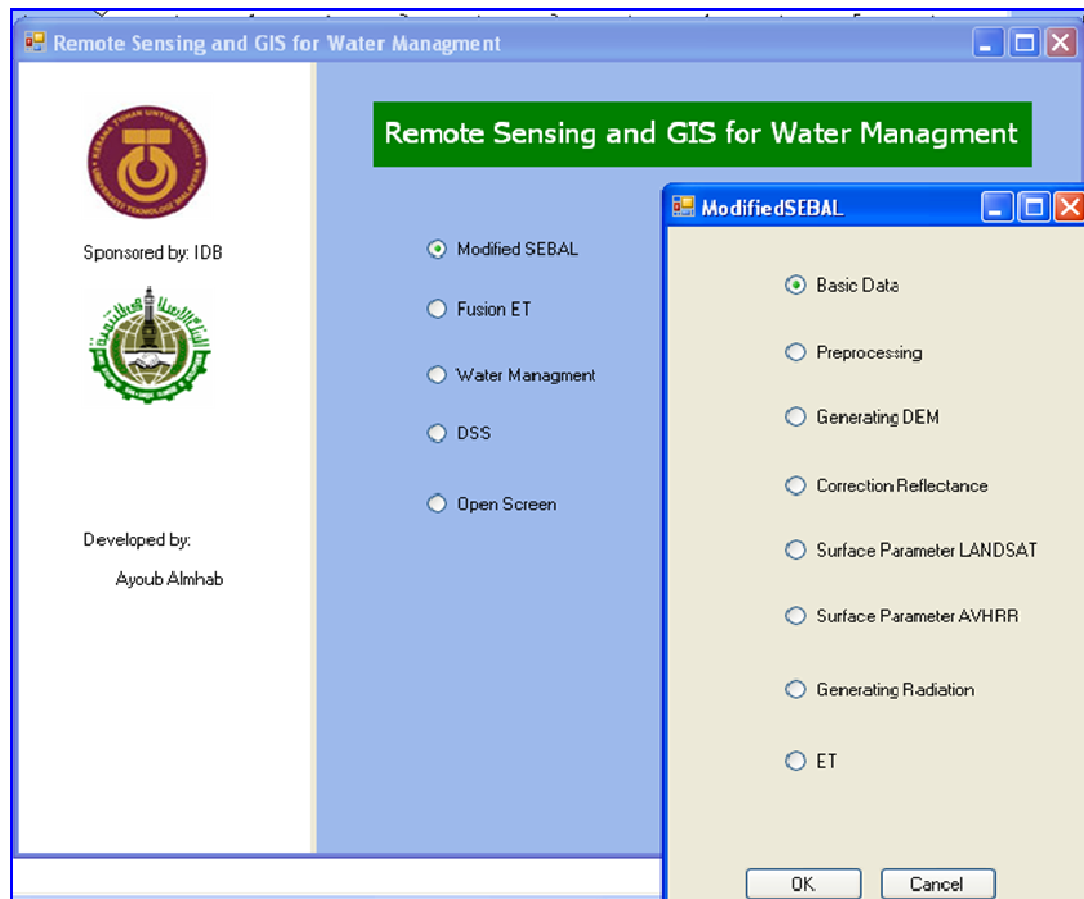
Figure A15 the mean face of the proposed programm

Appendices B

Decision Support System DSS Model Design (Planning Model)

The decision support system (DSS) is an integrated assemblage of models, data, interpretative routines, and other relevant information that efficiently processes input data, runs the models, and displays the results in an easy to interpret format. The system makes the support accessible to decision-makers. The DSS developed for ET estimation includes a model base with decision making capabilities, Microsoft excel, ArcGIS software and a database management system DBMS.

B1 Description of Data

Five climatologically stations in Sana'a basin, namely, CAMA, NWRA, AREA, and Sana'a Airport figure 4.2, were selected for this study based on the location characteristics and data availability. The selected sites ranged in elevation from 1900 to 3600 m above mean sea level. The latitude and the longitude of these stations showing in table 4.5. All the stations are located in the arid region. Daily minimum and maximum temperatures, minimum and maximum relative humidity, solar radiation, and wind velocity collected by the NWRA, AREA and CAMA in Yemen. The description of the different weather stations along with the data available and time scale is given in Table 4.5.

Table B.1.ranking weight of the paramete for different ET methods use in this study.

Ranking Number

N	parameter	Description	FAO56 PM2	FAO24 Penman	FAOR	PT	HG	SCS-BC	SEBAL	SEBA-ID	M-SEBAL	Bio	Simp
1	Ta	Average temperature	A^2	A^2	A^2	A^2		A^2	A^2	A^2	-	A^2	A^1
2	Ta-max/min	temperature Max. and Min.	A^2	A^2	A^2	A^2	A^1	A^1	-	A^2	-	A^2	-
3	RH	Average relative humidity	A^3	A^3	A^3	A^3	-	-	A^3	A^3	A^3	A^3	-
4	RH-max/min	Relative humidity Max. and Min.	A^3	A^3	A^3	A^3	-	A^1	-	A^3	-	A^3	-
5	u	Total wind speed	A^1	A^2	-	-	-	-	-	-	-	A^1	-
6	u*	Daytime wind speed	A^1	A^1	A^1			A^2	A^1	A^1	A^2	A^1	-
7	n	Sunshine hours	A^4	A^4	A^4	A^4		A^4	A^4	A^4	A^4	A^4	-
8	Rs	Solar radiation	A^4	A^4	A^4	A^4		A^4	A^4	A^4	A^4	A^4	-
	Kc	Crop Coefficient	A^2	A^2	A^2	A^2	A^2	A^2	-	-	-	-	-
9	GIS data	GIS A. Raster	A^1	A^1	A^1	A^1	A^1	A^1	-	-	-	-	-
10	RSdata	Satellite Image	-	-	-	-	-	-	A^1	A^1	A^1	A^1	A^1
11	DEM	Digital Elevation Model	-	-	-	-	-	-	A^3	A^2	A^1	A^4	A^4
12	a	Surface Albedo	-	-	-	-	-	-	A^1	A^1	A^1	-	-
13	NDVI	Normalize difference Vegetation Index	-	-	-	-	-	-	A^1	A^1	A^1	A^1	A^2
14	ε	Emisvity	-	-	-	-	-	--	A^1	A^1	A^1	-	A^1
15	Ts	Surface Temperature	-	-	-	-	-	-	A^1	A^1	A^1	-	A^1
16	Rn	Net Radiation	-	-	-	-	-	-	A^2	A^2	A^2	-	-
17	dT	Difference Surface Temperature	-	-	-	-	-	-	A^1	A^1	A^1	-	-
18	H	Sensible heat flux	-	-	-	-	-	-	A^2	A^2	A^2	-	-
19	Go	Ground Heat Flux	-	-	-	-	-	-	A^2	A^2	A^2	-	-
20	LE	Latent heat flux	-	-	-	-	-	-	A^2	A^2	A^2	-	-
		Ranking Total	21	22	20	19	2	15	31	35	28	26	10

Note: A^1 either maximum and minimum temperatures or average temperature is required; A^2 either maximum and minimum relative humidity or average RH is required; and A^3 either sunshine hours or solar radiation is required.

a)Penman-Monteith. B)FAO-24 Penman. c)FAO-24 Radiation. d).Priestley-Taylor. e)Hargreaves. f)SCS Blaney-Criddle. g)original SEBAL. h) SEBAL-ID . i) Modified SEBAL. j) Biophysical model. k)Simplified energy balance model.

* Notes: the metrological date for the remote sensing method (last five methods in the table4.13) shod be instantaneous data at the same date of the satellite images used.

B2. Assigning weights

Criterion weights are usually determined in the consultation process with decision makers (DM) which results in ratio value assigned to each criterion map. They reflect the relative preference of one criterion over another. In such a case, they can be expressed in a cardinal vector of normalized criterion preferences:

$$w = (w_1, w_2, ..., w_j) \text{ and } 0 <= w_j <= 1 \qquad (2.31)$$

Normalization implies that the numbers sum up to 100 or to 1, depending on whether they are presented in percentage or ratio. Another way to express preferences is in regard to criterion scores. Then, they have a form of cut-off values (minimum and maximum threshold) or desired aspiration levels Jankowski (1995). The second approach is more preferable in formulating location constraints. The task of assigning weights (deciding the importance of each factor) is usually performed outside GIS software; unless such a module is specially programmed or embedded in the proprietary GIS (compare Carver 1991, Jankowski 1995, Rapaport and Snickars 1998, Grossardt et al. 2001). The values of weights are then incorporated into the GIS-model. There are several techniques for assigning criterion weights. Some of the most popular include: ranking methods, rating methods, and pairwise comparison method. A common characteristic of them is that they imply subjective judgment of the decision maker about relative importance of the decision factors. The basic idea of rating methods is to arrange the criteria in order according to its relative importance. In straight ranking criteria are ordered from most important to least important, in inverse ranking it is done the other way round. After the ranks are established, several procedures for calculating numerical weights can be used.

One of the simplest methods is rank sum, in the following formula.

$$w_j = (n - r_j + 1) / \sum (n - r_k + 1) \qquad (2.32)$$

Where:

w_j is the normalized weight for $_j$ the factor, n is number of factors under consideration (k= ,2,…,n), and r_j is the rank position of the criterion. Each criterion is weighted *(n - r_j + 1)*and then normalized by the sum of all weights that is $\sum (n - r_k + 1)$.

Rank reciprocal weights are derived from the normalized reciprocals of a criterion's rank. The following formula is used to calculate the weights:

$$w_j = (1/r_j) / \sum(1/r_k) \qquad (2.33)$$

The rank exponent method requires an additional piece of information. The decision maker is required to specify the weight of the most important criterion on a 0-1 scale. This weight is entered into the formula:

$$w_j = (n - r_j + 1)^p / \sum(n - r_k + 1)^p \qquad (2.34)$$

which may then be solved for *p* by an iterative procedure. Once *p* is determined, weights for the remaining criteria can be calculated. This approach is characterized by several interesting properties. For *p=0* equation (2.34) assigns equal weights to the evolution criteria. For *p=1* the method results in rank sum weights. As *p* increases, normalized weights gets steeper and steeper (Stillwell et al. 1981).The example of how the weighted ranked values are calculated is shown in Table 2.2 below.

Table 2.2: Example of straight rank weighting procedure

Criterion	Straight Rank	Rank sum		Rank Reciprocal		Rank Exponent	
		Weight (n-rj+1)	Normalized weight	Reciprocal weight (1/rj)	Normalized weight	Weight (n-rj+1)p, p=2	Normalized weight
1	4	2	0.133	0.25	0.110	4	0.073
2	2	4	0.267	0.5	0.219	16	0.291
3	5	1	0.067	0.2	0.088	1	0.018
4	1	5	0.333	1	0.438	25	0.455
5	3	3	0.200	0.333	0.146	9	0.164
		15	1.000	2.283	1.000	55	1.000

Ranking method is the simplest criterion weighting methods. It is though criticized for its lack of theoretical foundations in interpreting the level of importance of a criterion Malczewski (1999). Second group of weighting methods are rating methods. There are two most commonly used approaches: point allocation and ratio estimation procedure. The common characteristic is that the decision maker has a total amount of points,

usually 100 that he or she needs to distribute among the decision criteria depending on their importance. More important factors get higher scores and factors that are of no importance to the decision would be assigned zero value. These methods are compared to budget allocation. In the point allocation approach one assigns points among criteria according to its importance. Commonly used scale is 0 to 100 or 0 to 10. The points are then transformed into weights summing sum up to 1. The ratio estimation procedure is a modification of point allocation method. Here, the most important criterion is assigned value of 100 and rest of the attributes is given smaller values, proportionally to their importance. The smallest ration is used as an anchor point for calculating the ratio. Every criterion value is divided by the smallest value and then the weights are normalized by dividing each weight by total. Similarly to ranking methods, rating methods lack theoretical and formal foundations, thus the meaning of weights is difficult to justify Malczewski (1999)

Table 2.3: Assessing weights by ratio estimation procedure

Rank	Ratio estimation scale	original weight	Normalized weight
1	30	2	0.133
2	60	4	0.267
3	15	1	0.067
4	75	5	0.333
5	45	3	0.200
		15.000	1.000

The main steps for working DSS-ET on GIS to produce the ET contour maps and the suitable method

| Metrological Data | → | DBMS database | → | Raster point | → | Future point |

| Future contour |

| DSS select the suitable method | ← | Comparison between diff. methods. | ← | Select comparison area in diff. method |
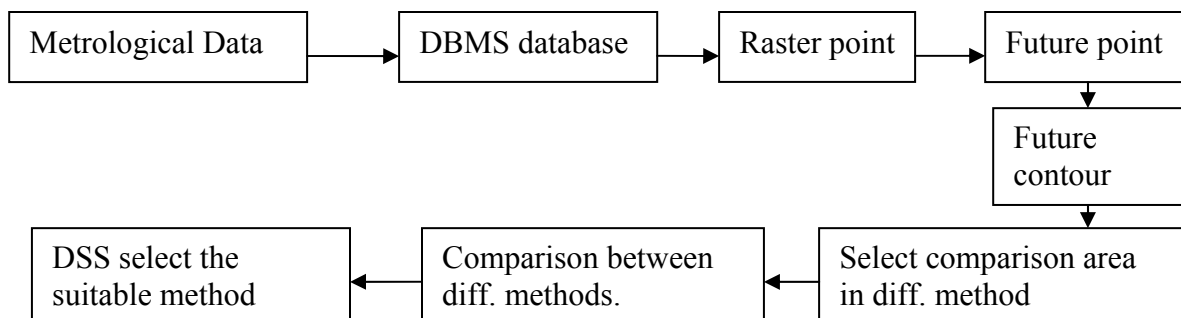
B3. Result Ranking weight tables of DSS-ET modell

Table (B1) Assessing Weights by Ranking Procedures FAO-PM method

Criterion	Straight Rank	Rank sum		Rank Reciprocal		Rank Exponent	
		Weight (n-rj+1)	Normalized weight	Reciprocal weight (1/rj)	Normalized weight	Weight (n-rj+1)p, p=2	Normalized weight
Ta	2	4	0.267	0.5	0.219	16	0.291
Ta-max/min	2	4	0.267	0.5	0.219	16	0.291
RH	3	3	0.200	0.3333333	0.146	9	0.164
RH-max/min	3	3	0.200	0.3333333	0.146	9	0.164
u	1	5	0.333	1	0.438	25	0.455
u*	1	5	0.333	1	0.438	25	0.455
n	4	2	0.133	0.25	0.110	4	0.073
Rs	4	2	0.133	0.25	0.110	4	0.073
Kc	1	5	0.333	1	0.438	25	0.455
GIS data	1	5	0.333	1.000	0.438	25	0.455
		38	2.533	6.167	2.701	158	2.873

Ratio estimation scale	original weight	Normalized weight
60	4	0.267
60	4	0.267
45	3	0.200
45	3	0.200
75	5	0.333
75	5	0.333
30	2	0.133
30	2	0.133
75	5	0.333
75	5	0.333
	38.000	2.533

Table (B2) Assessing Weights by Ranking Procedures FAO-P method

Criterion	Straight Rank	Rank sum		Rank Reciprocal		Rank Exponent	
		Weight (n-rj+1)	Normalized weight	Reciprocal weight (1/rj)	Normalized weight	Weight (n-rj+1)p, p=2	Normalized weight
Ta	2	4	0.267	0.5	0.219	16	0.291
Ta-max/min	2	4	0.267	0.5	0.219	16	0.291
RH	3	3	0.200	0.333333	0.146	9	0.164
RH-max/min	3	3	0.200	0.333333	0.146	9	0.164
u	2	4	0.267	0.5	0.219	16	0.291
u*	1	5	0.333	1	0.438	25	0.455
n	4	2	0.133	0.25	0.110	4	0.073
Rs	4	2	0.133	0.25	0.110	4	0.073
Kc	1	5	0.333	1	0.438	25	0.455
GIS data	1	5	0.333	1.000	0.438	25	0.455
		37	2.467	5.667	2.482	149	2.709

Ratio estimation scale	original weight	Normalized weight
60	4	0.267
60	4	0.267
45	3	0.200
45	3	0.200
60	4	0.267
75	5	0.333
30	2	0.133
30	2	0.133
75	5	0.333
75	5	0.333
	37.000	2.467

Table (B3) Assessing Weights by Ranking Procedures FAO-R method

Criterion	Straight Rank	Rank sum		Rank Reciprocal		Rank Exponent	
		Weight (n-rj+1)	Normalized weight	Reciprocal weight (1/rj)	Normalized weight	Weight (n-rj+1)p, p=2	Normalized weight
Ta	2	4	0.267	0.5	0.219	16	0.291
Ta-max/min	2	4	0.267	0.5	0.219	16	0.291
RH	3	3	0.200	0.333333	0.146	9	0.164
RH-max/min	3	3	0.200	0.333333	0.146	9	0.164
u*	1	5	0.333	1	0.438	25	0.455
n	4	2	0.133	0.25	0.110	4	0.073
Rs	4	2	0.133	0.25	0.110	4	0.073
Kc	1	5	0.333	1	0.438	25	0.455
GIS data	1	5	0.333	1.000	0.438	25	0.455
		33	2.200	5.167	2.263	133	2.418

Ratio estimation scale	original weight	Normalized weight
60	4	0.267
60	4	0.267
45	3	0.200
45	3	0.200
75	5	0.333
30	2	0.133
30	2	0.133
75	5	0.333
75	5	0.333
	33.000	2.200

Table (B4) Assessing Weights by Ranking Procedures PT method

Criterion	Straight Rank	Rank sum Weight (n-rj+1)	Normalized weight	Rank Reciprocal Reciprocal weight (1/rj)	Normalized weight	Rank Exponent Weight (n-rj+1)p, p=2	Normalized weight
Ta	2	4	0.267	0.5	0.219	16	0.291
Ta-max/min	2	4	0.267	0.5	0.219	16	0.291
RH	3	3	0.200	0.333333	0.146	9	0.164
RH-max/min	3	3	0.200	0.333333	0.146	9	0.164
u*	1	5	0.333	1	0.438	25	0.455
n	4	2	0.133	0.25	0.110	4	0.073
Rs	4	2	0.133	0.25	0.110	4	0.073
Kc	1	5	0.333	1	0.438	25	0.455
GIS data	1	5	0.333	1.000	0.438	25	0.455
		33	2.200	5.167	2.263	133	2.418

Ratio estimation scale	original weight	Normalized weight
60	4	0.267
60	4	0.267
45	3	0.200
45	3	0.200
75	5	0.333
30	2	0.133
30	2	0.133
75	5	0.333
75	5	0.333
	33.000	2.200

Table (B5) Assessing Weights by Ranking Procedures HG method

Criterion	Straight Rank	Weight (n-rj+1)	Normalized weight	Rank Reciprocal Reciprocal weight (1/rj)	Normalized weight	Rank Exponent Weight (n-rj+1)p, p=2	Normalized weight
Ta	2	4	0.267	0.5	0.219	16	0.291
Ta-max/min	1	5	0.333	1	0.438	25	0.455
RH-max/min	1	5	0.333	1	0.438	25	0.455
Kc	1						
GIS data	1	5	0.333	1.000	0.438	25	0.455
		19	1.267	3.500	1.533	91	1.655

Ratio estimation scale	original weight	Normalized weight
60	4	0.267
75	5	0.333
75	5	0.333
75	5	0.333
	19.000	1.267

Table (B6) Assessing Weights by Ranking Procedures SCS-BC method

Criterion	Straight Rank	Rank sum Weight (n-rj+1)	Normalized weight	Rank Reciprocal Reciprocal weight (1/rj)	Normalized weight	Rank Exponent Weight (n-rj+1)p, p=2	Normalized weight
Ta	2	4	0.267	0.5	0.219	16	0.291
Ta-max/min	1	5	0.333	1	0.438	25	0.455
RH-max/min	5	1	0.067	0.2	0.088	1	0.018
u*	2	4	0.267	0.5	0.219	16	0.291
n	4	2	0.133	0.25	0.110	4	0.073
Rs	4	2	0.133	0.25	0.110	4	0.073
Kc	1	5	0.333	1	0.438	25	0.455
GIS data	1	5	0.333	1.000	0.438	25	0.455
		28	1.867	4.700	2.059	116	2.109

Ratio estimation scale	original weight	Normalized weight
60	4	0.267
75	5	0.333
15	1	0.067
60	4	0.267
30	2	0.133
30	2	0.133
75	5	0.333
75	5	0.333
	28.000	1.867

Table (B7) Assessing Weights by Ranking Procedures SEBAL method

Criterion	Straight Rank	Weight (n-rj+1)	Normalized weight	Reciprocal weight (1/rj)	Normalized weight	Weight (n-rj+1)p, p=2	Normalized weight
Ta	**2**	**4**	**0.267**	**0.5**	**0.219**	**16**	**0.291**
RH	3	3	0.200	0.333333	0.146	9	0.164
RH-max/min	3	3	0.200	0.333333	0.146	9	0.164
u*	1	5	0.333	1	0.438	25	0.455
n	4	2	0.133	0.25	0.110	4	0.073
Rs	4	2	0.133	0.25	0.110	4	0.073
RSdata	1	5	0.333	1	0.438	25	0.455
DEM	3	3	0.200	0.333333	0.146	9	0.164
a	1	5	0.333	1	0.438	25	0.455
NDVI	1	5	0.333	1	0.438	25	0.455
ε	1	5	0.333	1	0.438	25	0.455
Ts	1	5	0.333	1	0.438	25	0.455
Rn	2	4	0.267	0.5	0.219	16	0.291
dT	1	5	0.333	1	0.438	25	0.455
H	2	4	0.267	0.5	0.219	16	0.291
Go	2	4	0.267	0.5	0.219	16	0.291
LE	2	4	0.267	0.5	0.219	16	0.291
		68	4.533	11.000	4.818	290	5.273

Ratio estimation scale	original weight	Normalized weight
60	4	0.267
45	3	0.200
45	3	0.200
75	5	0.333
30	2	0.133
30	2	0.133
75	5	0.333

Table (B8) Assessing Weights by Ranking Procedures SEBAL-ID method

Criterion	Straight Rank	Weight (n-rj+1)	Normalized weight	Reciprocal weight (1/rj)	Normalized weight	Weight	Normalized weight
Ta	2	4	0.267	0.5	0.219	16	0.291
Ta-max/min	2	4	0.267	0.5	0.219	16	0.291
RH	3	3	0.200	0.333333	0.146	9	0.164
RH-max/min	3	3	0.200	0.333333	0.146	9	0.164
u*	1	5	0.333	1	0.438	25	0.455
n	4	2	0.133	0.25	0.110	4	0.073
Rs	4	2	0.133	0.25	0.110	4	0.073
RSdata	1	5	0.333	1	0.438	25	0.455
DEM	2	4	0.267	0.5	0.219	16	0.291
a	1	5	0.333	1	0.438	25	0.455
NDVI	1	5	0.333	1	0.438	25	0.455
ε	1	5	0.333	1	0.438	25	0.455
Ts	1	5	0.333	1	0.438	25	0.455
Rn	2	4	0.267	0.5	0.219	16	0.291
dT	1	5	0.333	1	0.438	25	0.455
H	2	4	0.267	0.5	0.219	16	0.291
Go	2	4	0.267	0.5	0.219	16	0.291
LE	2	4	0.267	0.5	0.219	16	0.291
		69	4.600	11.167	4.891	297	5.400

Ratio estimation scale	original weight	Normalized weight
60	4	0.267
60	4	0.267
45	3	0.200
45	3	0.200
75	5	0.333
30	2	0.133
30	2	0.133
75	5	0.333
60	4	0.267
75	5	0.333
75	5	0.333
75	5	0.333
75	5	0.333
60	4	0.267
75	5	0.333
60	4	0.267
60	4	0.267
60	4	0.267
	69.000	4.600

Table (B9) Assessing Weights by anking
Procedures Modified SEBAL model

Criterion	Straight Rank	Weight (n-rj+1)	Normalized weight	Reciprocal weight (1/rj)	Normalized weight	Weight (n-rj+1)p, p=2	Normalized weight
RH	3	3	0.200	0.333333	0.146	9	0.164
u*	2	4	0.267	0.5	0.219	16	0.291
n	4	2	0.133	0.25	0.110	4	0.073
Rs	4	2	0.133	0.25	0.110	4	0.073
RSdata	1	5	0.333	1	0.438	25	0.455
DEM	1	5	0.333	1	0.438	25	0.455
a	1	5	0.333	1	0.438	25	0.455
NDVI	1	5	0.333	1	0.438	25	0.455
ε	1	5	0.333	1	0.438	25	0.455
Ts	1	5	0.333	1	0.438	25	0.455
Rn	2	4	0.267	0.5	0.219	16	0.291
dT	1	5	0.333	1	0.438	25	0.455
H	2	4	0.267	0.5	0.219	16	0.291
Go	2	4	0.267	0.5	0.219	16	0.291
LE	2	4	0.267	0.5	0.219	16	0.291
		62	4.133	10.333	4.526	272	4.945

Ratio estimation scale	original weight	Normalized weight
45	3	0.200
60	4	0.267
30	2	0.133
30	2	0.133
75	5	0.333
75	5	0.333
75	5	0.333
75	5	0.333
75	5	0.333
75	5	0.333
60	4	0.267
75	5	0.333
60	4	0.267
60	4	0.267
60	4	0.267
	62.000	4.133

Table (B10) Assessing Weights by Ranking Procedures Biophysical model

Criterion	Straight Rank	Rank sum Weight (n-rj+1)	Normalized weight	Rank Reciprocal Reciprocal weight (1/rj)	Normalized weight	Rank Exponent Weight (n-rj+1)p, p=2	Normalized weight
Ta	2	4	0.267	0.5	0.219	16	0.291
Ta-max/min	2	4	0.267	0.5	0.219	16	0.291
RH	3	3	0.200	0.333333	0.146	9	0.164
RH-max/min	3	3	0.200	0.333333	0.146	9	0.164
u	1	5	0.333	1	0.438	25	0.455
u*	1	5	0.333	1	0.438	25	0.455
n	4	2	0.133	0.25	0.110	4	0.073
Rs	4	2	0.133	0.25	0.110	4	0.073
RSdata	1	5	0.333	1	0.438	25	0.455
DEM	3	3	0.200	0.333333	0.146	9	0.164
a	1	5	0.333	1	0.438	25	0.455
NDVI	1	5	0.333	1	0.438	25	0.455
		46	3.067	7.500	3.285	192	3.491

Ratio estimation scale	original weight	Normalized weight
60	4	0.267
60	4	0.267
45	3	0.200
45	3	0.200
75	5	0.333
75	5	0.333
30	2	0.133
30	2	0.133
75	5	0.333
45	3	0.200
75	5	0.333
75	5	0.333
	46.000	3.067

Table (B11) Assessing Weights by Ranking Procedures Simplified energy balance model

Criterion	Straight Rank	Rank sum		Rank Reciprocal		Rank Exponent	
		Weight (n-rj+1)	Normalized weight	Reciprocal weight (1/rj)	Normalized weight	Weight (n-rj+1)p, p=2	Normalized weight
Ta	1	5	0.333	1	0.438	25	0.455
RSdata	1	5	0.333	1	0.438	25	0.455
DEM	4	2	0.133	0.25	0.110	4	0.073
NDVI	1	5	0.333	1	0.438	25	0.455
ε	1	5	0.333	1	0.438	25	0.455
Ts	1	5	0.333	1	0.438	25	0.455
		27	1.800	5.250	2.300	129	2.345

Ratio estimation scale	original weight	Normalized weight
75	5	0.333
75	5	0.333
30	2	0.133
75	5	0.333
75	5	0.333
75	5	0.333
	27.000	1.800

For more refer the below paper publishing during this research :

1. Ayoub Almhab, Ibrahim Busu,2007. Decision Support System for Estimating Actual crop Evapotranspiration using Remote Sensing, GIS and Hydrological Models, MAPASIA2008, Kula Lumpur , Malaysia.

2. Ayoub Almhab and Ibrahim Busu , 2008. Decision Support System for Estimating of Regional Evapotranspiration in arid areas: Application to the Republic of Yemen, GIS86 Conference Along with ISPRS Workshop on Geoinformation and Decision Support Systems, Tahran, Iran.
http://en.gis86sdss.ir/Home/tabid/36/Default.aspx

3. Ayoub Almhab and Ibrahim Busu , 2008. Decision Support System for Estimating of Regional Evapotranspiration in Yemen mountainous, **Mountain GIS e-Conference, 14-24 january 2008, online.**
http://www.mtnforum.org/rs/ec/index.cfm?act=cres&econfid=15&startPage=11

APPENDICES C

Lysimeter Data and picture

The integrity of the lysimeter data was evaluated using the known methodology. Table c1 provides comments on the general soil and crop conditions present in Lysimeter .

Most of the dates included in Table c1 correspond to 2006, where lysimeter field EFFA was planted to wheat. The wheat was planted on Jun 12 and was harvested on November 8. Full cover conditions for the wheat were reached around September 12. The September 7 and September 25 dates represent full-cover conditions.

Table c1.   General Crop and Soil Conditions at the Lysimeter

Date	Lysimeter	
	Crop and stage	Soil Wetness Condition
06/18/2006	bare. Wheat planted later on June 27	Dry. 8 days since slight rain
07/04/2006	One week after planting of wheat, no vegetation	wet. 1 day after irrigation
07/20/2006	Wheat emerged May 8^m on field, May I Ith on lysimeter 2	dry. 5 days since 12 mm rain, > 8 days since Irrigation
08/05/2006	Wheat partial cover	most dry. 3 days since 3 mm P, > 15 days since irrigate.
08/21/2006	Wheat. Intermediate cover	Dry. 8 days since irrigation
09/07/2006	Wheat -full cover	Dry. 9 days since Irrigation
09/23/2006	Wheat -full cover	some moist. 3 days since 3 mm P, 5 days since Irr.
11/25/2006	Wheat (harvested 10/11-18)	Dry. 6 days since Irrigation. Weather data was lost due to lightning damage on datalogger

With regard to image dates for the other crops, potatoes (1985), peas (1996), and alfalfa (1998), all were in full cover condition for the considered dates.

The accuracy of modified SEBAL strongly depends on the quality of the thermal information which is used to retrieve the radiometric surface temperature of the pixel. Table c2. shows a summary of the results obtained in the model validation. ET values from modified SEBAL were obtained averaging results from four 30 m x 30 m pixels approximately centered at the lysimeter site. Table c2 includes the values of instantaneous ET (corresponding to the satellite overpass time) estimated from modified SEBAL, and corresponding instantaneous ET measured at the lysimeter site. In addition, the corresponding values of reference ET are included for comparative purposes.

Table c2.   Summary of Instantaneous ET Comparison for 1988 (alfalfa), 1995 (peas), 1998 (sorghum), and 2006 (wheat)

Satellite Date	Crop	Reference	Measured ET[1]		M-SEBAl ET[2]		Difference	Normalize Error[4]
		mm/hr	mm/hr		mm/hr		mm/hr	%
3/21/95	alfalfa	0.84	0.84	1.00				
06/24/95	Peas	0.81	0.78	0.96				
07/29/98	sorghum	0.75	0.63	0.84	0.57	0.76	-0.055	-7.4
06/18/2006	Wheat	0.72	0.05	0.07				
07/04/2006	Wheat	0.68	0.60	0.88				
07/20/2006	Wheat	0.71	0.10	0.14				
08/05/2006	Wheat	0.71	0.18	0.25				
08/21/2006	Wheat	0.60	0.21	0.35				
09/07/2006	Wheat	0.74	0.70	0.95				
09/23/2006	Wheat	0.67	0.67	1.00				
11/25/2006	Wheat	0.87	0.53	0.61				

(1) Measured ET values were provided by NWRA

(2) The modified SEBAL ET is the average of (bur 30m x 30m pixels that were centered at the lysimeter

(3) In "Difference" column, negative values indicated that modified SEBAL ET was lower than Lysimeter ET.

(4) Normalized error was calculated as $100*\text{Difference ET}_{(Inst)} / \text{ETr}_{(inst)}$
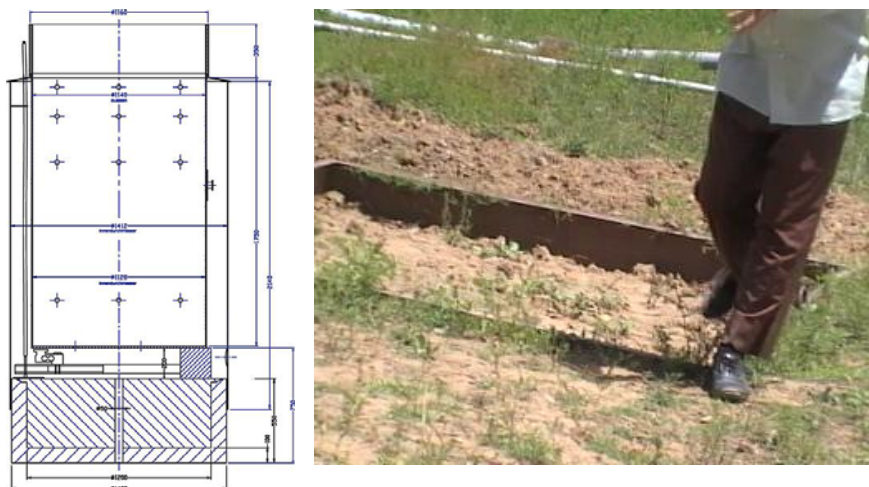
Figure C1 the lysimeters in the field experiment in farm of the faculty of agriculture Sana'a University.

The general formula used on the lysimeters measurement of ET as the fallowing:

$$P + 1 = ET + D \pm \Delta W \qquad\qquad \text{Eq. c.1}$$

Where:

P is the Precipitations, *I is the irrigation ,ET* is the Evapotranspiration, *D* is the deep percolation, $\pm \Delta W$ is the change soil moisture.

Figure C2 experiment farm of the faculty of agriculture Sana'a University,map from SPOT satellite

Figure C3 pictures for the lysimeters and field work in EFFA, 2006

APPENDIX D

Worksheet for calculation ET by eight traditional method

YEMEN: RIYAN
YEMEN: SANA'A
YEMEN: SOCOTRA
YEMEN: TAIZ
YEMEN: WADI-ZABID
Uzbekistan: POICAZAM
321 [201]

YEMEN: RIYAN
YEMEN: SANA'A
YEMEN: SOCOTRA
YEMEN: TAIZ
YEMEN: WADI-ZABID
UZBEKISTAN: POICAZAM
321 [202]

YEMEN: RIYAN
YEMEN: SANA'A
YEMEN: SOCOTRA
YEMEN: TAIZ
YEMEN: WADI-ZABID
UZBEKISTAN: POICAZAM
343 [203]

TURKEY: URFA
TURKEY: VAN
YEMEN: ADEN-KHORMAK
YEMEN: KAMARAN
YEMEN: RIYAN
UZBEKISTAN: POICAZAM
61 [258]

Lat(de   41
Lat(ra   0.721
Alt   525
Press   952
C_Rad   70

YEMEN: SOCOTRA
YEMEN: TAIZ
YEMEN: WADI-ZABID
UZBEKISTAN: POICAZAM
316 [295]

YEMEN: SOCOTRA
YEMEN: TAIZ
YEMEN: WADI-ZABID
UZBEKISTAN: POICAZAM
318 [296]

YEMEN: SOCOTRA
YEMEN: TAIZ
YEMEN: WADI-ZABID
UZBEKISTAN: Poiceam
316 [297]

Calibration constant for Priestly-Tay   1.28

Country: Uzbekistan   Stati: POICAZAM

MEASURED VARIABLES

Month	Oct	Nov	Dec	Jan	Feb	Mar	Apr	May	Jun	Jul	Aug	Sep
Daynum	289	320	350	15	47	75	106	136	167	197	228	259
Tmax [201]	17.6	12.4	9.2	4.9	10.9	18.1	24.1	32.1	36.3	33.6	32.2	28.8
Tmin [202]	7.0	2.9	1.8	-3.8	1.3	6.4	10.5	17.0	19.2	16.9	16.2	11.4
Tmean [203]	9.7	6.1	5.5	0.6	6.1	12.3	17.3	24.6	27.8	25.3	24.2	20.1
Rhmax [258]	48.0	68.0	75.0	72.0	66.0	55.0	53.0	40.0	29.0	35.0	41.0	42.0
Speed [297]	1.6	0.9	0.6	0.7	1.4	2.7	3.9	5.6	7.1	6.8	5.6	4.5
SUNR [296]	0.5	0.6	0.3	0.4	0.4	0.6	0.7	0.7	0.8	0.8	0.7	0.8
Rad [295]	888	888	888	888	888	888	888	888	888	888	888	888

CALCULATED VARIABLES

	Oct	Nov	Dec	Jan	Feb	Mar	Apr	May	Jun	Jul	Aug	Sep
Vap_Tmax	20.13	14.40	11.64	8.67	13.04	20.78	30.03	47.83	60.41	52.04	48.10	39.61
Vap_Tmin	10.02	7.53	6.96	4.61	6.71	9.62	12.70	19.38	22.26	19.26	18.42	13.48
Vap_Tmean	12.04	9.42	9.04	6.38	9.42	14.31	19.76	30.94	37.37	32.26	30.21	23.54
Act_Vap	5.78	6.40	6.78	4.60	6.22	7.87	10.47	12.38	10.84	11.29	12.39	9.88
Vap_Dif	6.26	3.01	2.26	1.79	3.20	6.44	9.28	18.56	26.54	20.97	17.82	13.65
RHmax	57.7	85.1	97.4	99.6	92.6	81.8	82.4	63.8	48.7	58.6	67.2	73.8
RHmin	28.7	44.5	58.2	53.0	47.7	37.9	34.9	25.9	17.9	21.7	25.7	25.0
DECL	-0.18	-0.34	-0.41	-0.37	-0.22	-0.04	0.17	0.33	0.41	0.37	0.23	0.03
COSDECLAT	0.74	0.71	0.69	0.70	0.73	0.75	0.74	0.71	0.69	0.70	0.73	0.75
SINDECLAT	-0.12	-0.22	-0.26	-0.24	-0.15	-0.03	0.11	0.22	0.26	0.24	0.15	0.02
DAYLENGTH	10.9	9.7	9.1	9.4	10.6	11.8	13.3	14.5	15.1	14.8	13.7	12.3
SUNH	1.41	1.26	1.18	1.22	1.37	1.54	1.72	1.88	1.96	1.92	1.78	1.60
DAYLH	10.8	9.6	9.0	9.3	10.5	11.7	13.2	14.4	15.0	14.7	13.6	12.2
MODAYS	31	30	31	31	28	31	30	31	30	31	31	30
MLTDLIGHT	338	291	283	293	296	367	398	448	452	458	425	369	4417
xDAYHRS	7.65	6.58	6.40	6.62	6.69	8.30	9.02	10.15	10.24	10.37	9.62	8.35	100
SUNx	0.47	0.57	0.30	0.38	0.42	0.62	0.67	0.69	0.75	0.77	0.72	0.84
SUNSHINE	5.1	5.5	2.7	3.6	4.4	7.3	8.9	10.0	11.3	11.4	9.9	10.3
RELDIST	1.008	1.023	1.032	1.032	1.023	1.009	0.992	0.977	0.968	0.968	0.977	0.992
EXRAD	8.78	6.24	5.20	5.79	8.10	10.98	14.10	16.22	17.10	16.61	14.78	11.90
RNS	3.28	2.57	1.60	1.96	2.87	4.73	7.43	8.23	8.12	6.94	6.14	
RNL_SP	2.48	2.68	1.58	1.94	2.11	2.96	3.05	3.20	3.81	3.71	3.30	3.95
RNL_FAO&PI	1.57	1.70	1.01	1.22	1.34	1.89	1.98	2.10	2.48	2.42	2.17	2.55
RN_SP	0.80	-0.11	0.02	0.02	0.76	1.78	3.30	4.23	4.42	4.41	3.65	2.19
RN_FAO&PM	1.71	0.87	0.60	0.74	1.53	2.84	4.37	5.33	5.75	5.70	4.78	3.58
Uday	2.1	1.2	0.8	0.9	1.9	3.6	5.2	7.5	9.5	9.1	7.5	6.0
DELTA	0.808	0.651	0.628	0.462	0.651	0.941	1.248	1.848	2.178	1.916	1.810	1.455
GAMMA	0.628	0.628	0.628	0.628	0.628	0.628	0.628	0.628	0.628	0.628	0.628	0.628
GAMMOD	0.970	0.820	0.756	0.778	0.927	1.205	1.461	1.824	2.144	2.080	1.824	1.589
ADJUST	0.830	0.936	0.967	0.975	0.937	0.890	0.895	0.781	0.660	0.729	0.779	0.823
MHI	2.727	1.351	1.155	0.040	1.351	3.907	6.549	11.159	13.429	11.644	10.886	8.219	72.418	1.642

PET METHOD	Oct	Nov	Dec	Jan	Feb	Mar	Apr	May	Jun	Jul	Aug	Sep
ET0_PEM	1.3	0.5	0.4	0.4	1.1	2.7	4.7	8.1	10.9	9.6	7.5	5.2	4.4
ET0_FAO	2.3	1.1	0.7	0.7	1.6	3.6	5.9	8.9	10.5	10.1	8.4	6.5	5.0
ET0_HON	1.9	0.8	0.5	0.5	1.2	2.9	4.6	8.1	11.1	9.5	7.6	5.6	4.5
ET0_RAD	1.5	0.8	0.4	0.4	1.0	2.6	4.2	6.2	7.8	7.3	5.7	4.6	3.5
ET0_PR/TT	1.2	0.6	0.4	0.4	1.0	2.1	3.7	5.0	5.6	5.4	4.5	3.2	2.8

APPENDIXES E

Evapotranspiration Estimation by other Remote Sensing Methods

More detail about the two models please refer to the bellow publishing paper for it

E1-Simplified energy balance model

Almhab, Ayoub, Ibrahim Busu, 2008. A simple method for estimating of evapotranspiration using remotely sensed data in arid regions: a case study in Yemen Mountains , MAP Middle East 2008, dubai , UAE.(full paper pdf)
http://www.mapmiddleeast.org/2008/organiser.htm

Almhab, Ayoub, Ibrahim Busu, 2008. Remotely-sensed Evapotranspiration of arid regions in the central Yemen Mountains with a simple energy balance method , The Postgraduate Annual Research Seminar 2008 (PARS08), UTM, skudai, johor, Malaysia.
http://www.pps.fsksm.utm.my/pars08/pars08.htm

E2- Biophysical estimation evapotranspiration model

Ayoub Almhab, Ibrahim Busu,2008. Evapotranspiration Estimation using A Normalized Difference Vegetation Index Transformation of two Satellites data in Arid Mountain Areas, ISG2008, Kula Lumpur , Malaysia.

Ayoub Almhab, Ibrahim Busu,2008. Predicting evapotranspiration from MODIS vegetation indices and meteorological data in arid regions: A case study in Republic of Yemen, ISG2008, Kula Lumpur , Malaysia.

APPENDIXES F

Regional water balance estimation

More detail about the two models please refer to the bellow publishing paper for it

Almhab A., Ibrahim B., (2008),   Regional Water Balance Visualization Using Remote Sensing And Gis Techniques with Application to the Arid Watershed Area . ACRS2008, Sere lank.

Almhab A., Ibrahim B., (2008),   Regional Water Balance Visualization Using Remote Sensing And Gis Techniques with Application to the Arid mountain basin area . IPGCES 2008,UTM, Skudai Johor, Malaysia.